



## AVERTISSEMENT

Ce document est le fruit d'un long travail approuvé par le jury de soutenance et mis à disposition de l'ensemble de la communauté universitaire élargie.

Il est soumis à la propriété intellectuelle de l'auteur. Ceci implique une obligation de citation et de référencement lors de l'utilisation de ce document.

D'autre part, toute contrefaçon, plagiat, reproduction illicite encourt une poursuite pénale.

Contact : [ddoc-theses-contact@univ-lorraine.fr](mailto:ddoc-theses-contact@univ-lorraine.fr)

## LIENS

Code de la Propriété Intellectuelle. articles L 122. 4

Code de la Propriété Intellectuelle. articles L 335.2- L 335.10

[http://www.cfcopies.com/V2/leg/leg\\_droi.php](http://www.cfcopies.com/V2/leg/leg_droi.php)

<http://www.culture.gouv.fr/culture/infos-pratiques/droits/protection.htm>

---

## Thèse

présentée pour l'obtention du titre de

**Docteur de l'Université de Lorraine**

GEOSCIENCES

par

**Mariam MOUSSA**

---

### **Loading of dendrimer nanoparticles into layer-by-layer assembled Poly(diallyl dimethyl ammonium) chloride- (Poly(acrylic acid))<sub>n</sub> Multilayer Films: Particle Electrokinetics, Film Structure Dynamics and Elasticity**

---

Soutenue Publiquement le 04.12.2017 à l'Université de Lorraine, Nancy, France  
devant la commission d'examen

Bruno LARTIGES  
Claudine FILIATRE  
Gregory FRANCIUS  
Jérôme DUVAL  
Vincent BALL

Rapporteur  
Rapporteur  
Examineur  
Examineur  
Membre Invité

GET, Toulouse  
Institut UTINAM, Besançon  
LCPME, Nancy  
LIEC, Nancy  
Inserm, Strasbourg



Laboratoire Interdisciplinaire des Environnements Continentaux  
UMR7360 CNRS-Université de Lorraine



Laboratoire de Chimie Physique et Microbiologie pour l'Environnement  
UMR7564 CNRS-Université de Lorraine



# Acknowledgments



This PhD work was realized in Laboratoire Interdisciplinaire des Environnements Continentaux (**LIEC**), UMR 7360 CNRS-Université de Lorraine, as a part of *Erasmus* ELEMENT program. For this, I would like to thank Mr. **Fabien THOMAS**, director of LIEC, for accepting me as a PhD student at LIEC. I would like to thank in parallel Mr. **Stephane DESOBRY**, director of the doctoral school **RP2E** and the coordinator of *Erasmus* ELEMENT program at Université de Lorraine, for his availability and help throughout my PhD period.

I am deeply indebted for a number of people for making this thesis a reality, for their individual and collaborative efforts to guide and shape my research and professional development during my PhD period.

An enormous thank you to Mr. **Jérôme DUVAL**, my PhD supervisor, for his availability despite of his busy schedule, his valuable advices, his guidance throughout my PhD period, and for his always open door. Thank you Jérôme for all the efforts you paid for the completion of this PhD thesis. I consider myself extremely lucky to have had the opportunity to be one of your students. Merci Jérôme.

I would like to deeply thank the committee members Madame **Claudine FILIATRE**, Professor, Université de Franche-Comté, and Mr. **Bruno LARTIGES**, Professor, Université Paul Sabatier, for taking the time to assess this work and be part of the Jury. I appreciate all your efforts in evaluating this work.

Thanks to Mr. **Gregory Francius**, CR at LCPME, for all his help especially in Atomic Force Microscopy. Thank you Gregory for your helpful assistance and guidance.

Special thanks to Mr. **Vincent BALL**, Professor, Université de Strasbourg, Thank you Vincent not only for being a part of the Jury, but also for your availability, for the fruitful discussions, and for your generosity in sharing information. Merci Vincent.

I would like to thank too Mme. **Catherine SOMMIER**, former International Relations Officer at Université de Lorraine, for her valuable help and support in all the administrative procedures at my arrival to Nancy, and Mrs. **Delphine LAURANT**, International Relations Officer- ENSAIA / ENSTIB, for all her support, sympathy and help. Merci Delphine. Thanks also to Mrs. **Anna DUKES**, Senior International Development Officer at Cardiff Metropolitan University, for always making sure that everything went well during my Erasmus mobility period.

Special thanks to Mr. **Christian POIRSON**, of service of Accueil International de l'Université de Lorraine, for all his efforts in making the administrative procedure of the stay of foreign PhD students at University of Lorraine as simple as possible. Many thanks for the orientation and advices.

Special thanks also to Mrs. **Aude Martinez** and Mrs. **Aurore Binet**, secretariat of RP2E, for their help in all the administrative procedure from registration to dissertation.

Pour tout ce qu'elle a fait pour moi, pour son aide inestimable, ses conseils précieux, son compréhension, son hospitalité, encouragement et soutien, je suis très reconnaissante à Madame **Christine FIVET**. Merci Christine d'être toujours là pour m'aider. Merci d'être ma deuxième maman.

A huge thank you to **Hussein Kanbar** for providing me with great entertainment on daily basis, thanks Hussein for the long bike rides and for your unique sense of humor. Thanks man.

For the people of LIEC, I owe a particular debt of gratitude for all they have taught me through our numerous interactions and friendships. In particular I would like to thank **Celine CAILLET**, Merci Celine, for your help in DLS, for your time and valuable advices, things would have been much difficult without your presence. Thank you **Renaud** for your help and for your touch in making my French better. I am grateful to all the technicians, support staff and secretaries of the LIEC. Merci **Pabla, Manuel, Nicole, Tiffany, Delphine, Pierre-Yves, Allan, Yves**. Thank you to all the former and current PhD students, **Romain, Sandotin, Jean-Aimé, Jennifer, Noemie, Jenny**.

Egalement J'adresse ma profonde gratitude à **Lise SALSI, Audile BARRE, Isabelle BIHANNIC, Fabrice FRAYSSE**, and **Manuel DOSSOT**.

Special thanks to **Tareq** and **Bouchra**, and their lovely family, for the good times we spent together, Shoukran Ktirrrr.

I will treasure more than anything else the friendships that have arisen as a result of my time spent here. A big thank you to **Rasha**, thanks for the delicious treats, late night chats, care and valuable advices. Merci **Farah**, baby **Julia**, and **Fattoum** for being by my side and tolerating me at my worst. Thanks **Habiba** and **Sirina**, words can never explain my love and gratitude, thanks **Karaky, Badrano**, and **Yara**. Shoukran **Zannuba, Moma, Sara, Rima, Maya, Ayat, Alaa, Hala**. I am lucky to have you in my life. Special thanks to Youssef for his support and help, thanks zouzou for always saving me at the last minute. Merci Alex (Batman dark knight).

Last but not least, I acknowledge the love and support of my family. To my parents, **Zahra** and **Ali** I offer my loving thanks for their unconditional support, for their love and financial support as well. I thank my sisters **Doha** and **Fatima**, and my niece baby **Allen** ☺, for their love and for tolerating an often annoying weird big sister, **Reda, Hassan, Ali** and **Ali**. I love you all. I thank my grandparents, **Tata** em Ucef for her lovely prayers and **Jeddo** bu Ucef. My Khaltu's Maryam, Layoula, Fatima, Emneh,, ammtu's, khalou's, My precious Amtu Zahra, Zainab and Aniseh, Ibtihal, Nahed, and khaltu Zainab, Kalu Ucef and Auntie Janes, Khalus' Ali, Ahmad, Mustafa, and the best Ammo Ghassan, my cousins. Special thanks for Ammou Qassem and Uté fo their unvaluable support throughout my dissertation, أجيبكم جدا جدا وجدا

Et enfin, pour ce qui le liront et apprécier les informations fournies dans ce rapport toute ma remerciement.

*To Bassel who left this world to a better place, perhaps, I address this work.*

**Mariam**



## Table of Contents

<b>Index.....</b>	<b>VI</b>
<b>Table of figures.....</b>	<b>VIII</b>
<b>French summary .....</b>	<b>1</b>
 <b><u>GENERAL INTRODUCTION</u>.....</b>	 <b>6</b>
 <b><u>CHAPTER I. LITERATURE REVIEW</u> .....</b>	 <b>11</b>
I. Polyelectrolyte multilayer (PEM) films.....	12
I.1. Polyelectrolyte multilayer (PEM) films obtained by electrostatic interactions.....	12
I.1.1. Properties of polyelectrolytes.....	12
I.1.2. Strong polyelectrolytes versus weak polyelectrolytes.....	13
I.1.3. History of polyelectrolyte multilayer films.....	13
I.1.4. Principles of the Layer by Layer (LBL) deposition of PEM films.....	15
I.1.5. Interactions in multilayer LBL films.....	16
I.1.6. Charge balance in polyelectrolyte multilayers.....	18
I.1.7. Growth modes of multilayer films.....	20
I.1.7.1. Films with linear growth.....	20
I.1.7.2. Films with exponential growth.....	21
I.1.8. Physico-chemical parameters affecting the growth of PEM films.....	23
I.1.8.1. Solution pH.....	23
I.1.8.2. Ionic strength of the buffer and polyelectrolyte solutions.....	25
I.1.8.3. Buildup temperature.....	27
I.1.8.4. Effect of salt anion on the film construction.....	28
I.1.9. Mechanical properties of PEM films.....	31
I.1.10. Water content in PEM films.....	32
I.2. Polyelectrolyte multilayer films obtained by hydrogen bonding.....	32
I.3. Electrochemical properties of polyelectrolyte multilayers.....	33
I.3.1. Ion Permeability of polyelectrolyte multilayers.....	33
I.3.2. Donnan Potential in PEM films.....	34
I.4. Applications of PEM films.....	36
I.5. Incorporation of Nanoparticles and Biomolecules into PEM Films.....	37
I.5.1. Incorporation of bioactive molecules and ions.....	37
I.5.2. Incorporation of Nanocolloids.....	41
I.5.3. Incorporation of proteins and peptides.....	44
I.5.4. Loading with Multivalent ions.....	45
I.5.5. Loading of nanoparticles in PEM films.....	46
II. Electrokinetic Investigations of Nanodendrimers.....	48
II.1. Concept of soft particles.....	50
II.2. Electrokinetics of soft particles.....	52
II.3. Polyamidoamine (PAMAM) carboxylated nanodendrimers.....	59
II.3.1. Synthesis and structure.....	59
II.3.2. Advances in nanodendrimers research and applications.....	61
II.3.3. Investigations of dendrimer toxicity.....	64
III. References.....	66

<b>CHAPTER II. MATERIALS AND CHARACTERIZATION METHODS</b>	<b>79</b>
I. Materials and samples preparation	80
I.1. The polyelectrolyte solutions	80
I.2. Construction of the PEI – (PDADMAC/PAA) films	81
I.3. Heating and aging of the films	83
I.4. Electrokinetics of the nanodendrimers	83
I.5. Loading the films with nanodendrimers	83
II. Characterization Methods	84
II.1. Atomic force microscopy (AFM)	84
II.1.1. AFM technique and principles	85
II.1.2. AFM cantilevers and probes	87
II.1.3. Different AFM modes	89
II.1.4. Force measurements	95
II.1.5. Determining film elastic modulus using AFM	99
II.2. Quartz Crystal microbalance-dissipation (QCM-D)	105
II.3. Confocal Raman Spectroscopy (CRS)	110
II.4. Dynamic light scattering (DLS) and Phase Analysis light Scattering (PALS)	113
II.4.1. Size measurements by DLS	113
II.4.2. Electrophoretic mobility measurements by PALS	117
III. References	122
<b>CHAPTER III. REMARKABLE ELECTROKINETIC FEATURES OF CHARGE-STRATIFIED SOFT NANOPARTICLES: MOBILITY REVERSAL IN MONOVALENT AQUEOUS ELECTROLYTE</b>	<b>128</b>
<b>CHAPTER IV. REMARKABLE STRUCTURE AND ELASTICITY RELAXATION DYNAMICS OF POLY(DIALLYLDIMETHYLAMMONIUM CHLORIDE)-POLY(ACRYLIC ACID) MULTILAYER FILMS</b>	<b>157</b>
<b>CHAPTER V. LOADING OF PAMAM G6.5 DENDRIMERS IN (PDADMAC-PAA) MULTILAYER FILMS</b>	<b>199</b>
I. Characterization of (PDADMAC-PAA) films	201
II. Loading of the films with G6.5 PAMAM nanodendrimers	204
II.1. Effect of G6.5 dendrimers concentration on the morphology of P A MAC – PAA) films	206
II.2. Effect of G6.5 concentration on Young modulus of P A MAC – PAA) films	209
III. Conclusions	211
III. References	213
<b>GENERAL CONCLUSION AND PERSPECTIVES</b>	<b>214</b>

## Index

Å	Angstrom
AFM	Atomic force microscopy
ATR-IR	Attenuated Total Reflection Infrared Spectroscopy
Br <sup>-</sup>	Bromide ion
Cl <sup>-</sup>	Chloride ion
CCD	Charge-Coupled Device
CdTe	Cadmium telluride
ClO <sub>4</sub> <sup>-</sup>	Perchlorate ion
CLSM	Confocal Laser Scanning Microscopy
COO <sup>-</sup>	Carboxylate ion
CPM	Carboxymethylpullulan
CuPc	Copper (II) phtalocyanines
D <sub>2</sub> O	Deuterium oxide
DC	Direct Current
DLS	Dynamic light scattering
DMT	Derjaguin-Muller-Toropov
DNA	Deoxyribonucleic acid
ESEM	Environmental scanning electron microscopy
F <sup>-</sup>	Fluoride ion
FITC	Fluorescein isothiocyanate
FTIR	Fourier Transform Infrared Spectroscopy
HA	Hyaluronic acid
K <sup>+</sup>	Potassium ion
KSCN	Potassium thiocyanate
Li <sup>+</sup>	Lithium ion
LBL	Layer-by-layer
LDE	Laser Doppler Electrophoresis
LDV	Laser Doppler Velocimetry
LSPR	Localized Surface Plasmon Resonance
M	Molar
Na <sup>+</sup>	Sodium ion
NaBr	Sodium bromide
NaCl	Sodium chloride
NMR	Nuclear Magnetic Resonance
NP	Nanoparticles
NWs	Nanowires
O <sup>-</sup>	Hydioxide ion
P <sub>2</sub> O <sub>5</sub>	Phosphorus pentoxide
PAA	Poly(acrylic acid)
PAH	Poly(allylamine hydrochloride)
PALS	Phase analysis light scattering
PAMAM	Poly(amidoamine)
PCS	Photon Correlation Spectroscopy
PDADMAC	Poly(diallyl dimethyl ammonium) chloride
PdI	Polydispersity Index
PEI	Poly(ethyleneimine)
PEM	Polyelectrolyte multilayers
PGA	Polyglutamic acid
pKa	Acid dissociation constant
PLL	Poly-L-Lysine
POMs	Polyoxometalates
PSS	Poly(styrenesulfonate)
QCM-D	Quartz crystal microbalance with dissipation

QELS	Quasi-Elastic Light Scattering
QNM	Quantitative Nanomechanical Mapping
RCM	Raman confocal microscopy
SANS	Small Angle Neutron Scattering
SDS	Sodium dodecyl sulfate
SERS	Surface-enhanced Raman scattering
SNOM	Scanning Near-Field Optical Microscope
SPM	Scanning-Probe Microscopes
STM	Scanning Tunneling Microscopy
SWNTs	Single Walled Carbon Nanotubes
Te	Tellurium
Tris	Tris(hydroxyaminomethane)
UV-vis	Ultraviolet–visible spectroscopy



## Table of figures

### Figures Chapter I

<b>Figure 1.1.</b> Principle of transfer of a lipid monolayer into a solid substrate by the Langmuir-Blodgett method...	1
<b>Figure 1.2.</b> Principle of polyelectrolyte multilayer films construction .....	1
<b>Figure 1.3.</b> Buildup techniques: (a) dip coating, (b) spin coating, and (c) spray coating.....	1
<b>Figure 1.4.</b> Interactions that govern the buildup of polyelectrolyte multilayer films and applications of PEMs...	1
<b>Figure 1.5.</b> Evolution of the $\zeta$ potential during the buildup of PEI – (PSS/PAH) $_n$ multilayer film. ....	1
<b>Figure 1.6.</b> Intrinsic and extrinsic charge compensation in a PEM film. ....	1
<b>Figure 1.7.</b> Evolution of the thickness of PEI – (PSS/PAH) $_n$ films and poly(L-glutamic acid)/poly(L-lysine) films denoted by PEI – (PGA/PLL) $_n$ as a function of the number of deposited layers.. ....	1
<b>Figure 1.8.</b> The three zone model of polyelectrolyte multilayer films with linear growth. ....	1
<b>Figure 1.9.</b> The buildup mechanism of (PLL/HA) films. ....	1
<b>Figure 1.10.</b> Average thickness contributions by PAA and PHA adsorbed layer as a function of solution pH. ....	1
<b>Figure 1.11.</b> Evolution of the absorbance at $\lambda=217$ nm maximum absorption for PSS) by visible UV spectrophotometry during the construction of (PDADMAC/PSS) $_n$ films at different molar concentrations of NaCl.....	1
<b>Figure 1.12.</b> The evolution of the growth of (PDADMA/PSS) films followed by QCM-D as a function of the temperature of the polyelectrolyte solution. ....	1
<b>Figure 1.13.</b> “Salting-in” and “salting-out” effects.....	1
<b>Figure 1.14.</b> Hofmeister series of classification of some monovalent anions .....	1
<b>Figure 1.15.</b> a) The thickness of (PDADMA/PSS) film measured by ellipsometry. b) The thickness of (PAH/PSS) followed by QCM-D. ....	1
<b>Figure 1.16.</b> Cyclic voltammograms (Fe(CN) $_6^{3-}$ at 0.005 M, pH=6.3) at a gold electrodes coated with a (●)(PAH/PSS) $_{20}$ prepared with no supporting salt (thickness of 16 nm); (dotted line) (PAH/PAA) $_5$ film prepared with supporting salt (thickness of 44 nm); (◆) (PAH/PAA) $_9$ film prepared with no supporting salt (thickness of 15 nm); (×) (PAH/PSS) $_4$ film prepared with supporting salt (thickness of 15 nm). ....	1
<b>Figure 1.17.</b> Cyclic voltammograms measured at a gold electrode coated with a (PAH – Os/PVS) $_4$ – PAH – Os constructed under different conditions. ....	1
<b>Figure 1.18.</b> Confocal laser scanning (CLSM) images (A) (PLL/HA) $_{30}$ /paclitaxelGreen 488/PSSMRho/PAHMRho/PSSMRho film section, (B), HT29cell section 24 h after seeding on a (PLL/HA) $_{30}$ /paclitaxelGreen 488/PSSMRho/PAHMRho/PSSMRho film and (C), top view (x,y) of the same cell. ....	1
<b>Figure 1.19.</b> UV-vis absorbance of curcumin loaded into PEM thin films with an increasing number of deposited layers as a function of time.....	1
<b>Figure 1.20.</b> Permeation kinetics of P8W48 in PEI – (PLL/HA) $_9$ /HA films followed by UV/Vis spectroscopy as a function of the concentration in the solution .....	1
<b>Figure 1.21.</b> (A) PDDA – PAA film on a glass substrate (B) Film loaded with negatively charged SWNTs for 1 day. (C) Side view of PDDA – PAA coated glass slide. (D) Side-view of swollen PDDA – PAA film loaded with negatively charged SWNTs. (E) Cross-section of the (PDDA – PAA) $_{200}$ film (F) Schematics of incorporation of SWNTs in the films. ....	1
<b>Figure 1.22.</b> (A) Top view of (PDADMAC/PAA) $_{200}$ film infused with negatively charged SWNT (B) Zoom-in image for negatively charged SWNT (C) Top view of LBL film infused with multi-walled carbon nanotubes. (D), (E) Top view of LBL film infused with CdTe and Te NWs. The NW samples did not show any swelling and incorporation inside the films. ....	1
<b>Figure 1.23.</b> Absorption spectra of CuPc – SO $_4$ at $5 \times 10^{-4}$ M in the Tris-NaCl buffer (black line) and of a PEI-(PGA/PLL) $_{10}$ films put in contact with a $10^{-3}$ M CuPc – SO $_4$ containing buffer after 15 (blue line), 60 (green line), 120 (red line), and 180 (pink line) min of contact with the film. ....	1
<b>Figure 1.24.</b> Schematic representation of the reversible loading of (PDDA/PAA) $_n$ PEM films with NPs. ....	1

<b>Figure 1.25.</b> (a) Loading and unloading of (PDDA/PAA) <sub>45</sub> films (pH 9) with green fluorescence-emitting NP <sub>1</sub> as followed by UV-vis absorbance at 530 nm. The insets are fluorescence photographs of the filled (top) and empty (bottom) films. (b) Confocal microscopy images of (PDDA/PAA) <sub>100</sub> films loaded by 6h of exposure to NP <sub>1</sub> solution and (c) empty films after 24h exposure at pH 9. The right panels show white light images. ....	1
<b>Figure 1.26.</b> UV-vis spectra of e-LBL AgNP films as a function of immersion time of the e-LBL film in a silver colloid dispersion. Inset: digital photographs of films after 12 and 24h immersion. ....	1
<b>Figure 1.27.</b> Schematic representation of the EDL around a solid particle.....	1
<b>Figure 1.28.</b> A soft particle becomes a hard particle in the absence of the surface charge layer, while it tends to form a spherical polyelectrolyte in the absence of the particle core. ....	1
<b>Figure 1.29.</b> Schematic representation of a soft particle.....	1
<b>Figure 1.30.</b> Schematic representation of a soft particle, composed of a rigid hard core and a permeable charged polymeric layer, moving with a velocity $U^*$ in a nonbound electrolyte subjected to a dc electric field $E^*$ . ....	1
<b>Figure 1.32.</b> The Two principle synthetic methods for constructing dendrimers .....	1
<b>Figure 1.33.</b> PAMAM dendrimers Structure .....	1
<b>Figure 1.34.</b> Effect of pH on dendrimers conformation.....	1
<b>Figure 1.35.</b> Effect of ionic strength on dendrimers conformation. (A) Hollow core, dense shell picture. (B) Dense core picture. ....	1
<b>Figures Chapter II</b>	
<b>Figure 2.1.</b> Automated dip coating (Dipping robot, Riegler and Kirstien, GmbH, Berlin, Germany).....	1
<b>Figure 2.2.</b> Schematic diagram of atomic force microscopy.....	1
<b>Figure 2.3.</b> Dimension FastScan AFM setup .....	1
<b>Figure 2.4.</b> Schematic representation of an AFM probe .....	1
<b>Figure 2.5.</b> Scanning Electron Microscopy of AFM cantilevers.....	1
<b>Figure 2.6.</b> Different modes of AFM operation .....	1
<b>Figure 2.7.</b> Real time QNM data obtained from different measurement channels for a (PDADMAC – PAA) <sub>30</sub> film at pH 3 in 10mM NaNO <sub>3</sub> , and details on the parts of the approach/retract curves from which each parameter can be obtained (upper right). ....	1
<b>Figure 2.8.</b> Force volume mapping: Force volume data set can be seen as a stack of horizontal slices, each representing the array of force data at a given height Z. A single force volume image represents one of these slices, showing the X,Y distribution of the force data over the scan area at that height. The value at a point (X,Y,Z) in the volume is the deflection (force) of the cantilever at that position in space. ....	1
<b>Figure 2.9.</b> Force volume data for (PDADMAC/PAA) multilayer films at pH 6 acquired from NanoScope Analysis software .....	1
<b>Figure 2.10.</b> The sketch of forces of interaction ( $F_{int}$ ) as a function of tip-sample separation distance ( $z_t$ ).....	1
<b>Figure 2.11.</b> Typical AFM force curve .....	1
<b>Figure 2.12.</b> Deflection of the cantilever during force measurement.....	1
<b>Figure 2.13.</b> Left: Sketch of an indentation experiment. Right: The correction of the height for the cantilever deflection ( $x$ ) to derive the tip sample separation .....	1
<b>Figure 2.14.</b> Force versus indentation curves: comparison between the shape of the curve of a rigid (PDADMAC – PAA) <sub>30</sub> film denoted by $J_0$ and a soft film after thermal treatment denoted by ( $J_0+60^\circ\text{C}$ ). ....	1
<b>Figure 2.15.</b> Sneddon model versus Hertz model .....	1
<b>Figure 2.16.</b> Data presented in NanoScope Analysis software: Height image of a (PDADMAC – PAA) <sub>30</sub> multilayer film (left), and a force plot displaying the associated force curve for the selected pixel chosen in the height image (deflection error versus Z piezo position) (right). ....	1
<b>Figure 2.17.</b> Data presented in NanoScope Analysis software: Height image of a (PDADMAC – PAA) <sub>30</sub> polyelectrolyte film (right), and force plot region (deflection error versus Z piezo position) displaying 50 of all the force curves (256x256) corresponding to all the selected pixels in the height image (left).....	1
<b>Figure 2.18.</b> Raw force curves (spm files) exported as ASCII files (text files) to be loaded into Matlab editor. ...	1
<b>Figure 2.19.</b> Matlab editor with the main parameters used for the derivation of Young modulus data .....	1
<b>Figure 2.20.</b> Deflection versus time, force versus distance and force versus indentation data obtained from the analysis of the measured force curves. ....	<b>Error! Bookmark not defined.</b>

<b>Figure 2.22.</b> QCM-D setup .....	1
<b>Figure 2.23.</b> Geometry of a quartz crystal microbalance (QCM) covered by a double-layer viscoelastic film. The QCM system oscillates in a bulk liquid .....	1
<b>Figure 2.24.</b> Schematic depiction of the Voight viscoelastic element consisting of a spring and a dashpot .....	1
<b>Figure 2.25.</b> Right: QCM-D3 setup (Qsense, Göteborg, Sweden); Left: real-time data of the variation in frequency (blue) and in dissipation (red) as function of time during the in situ deposition of a (PDADMAC-PAA) film .....	1
<b>Figure 2.27.</b> Results obtained from QCMD data analysis: graphs showing the properties of the constructed film (shear modulus, viscosity, and thickness) versus the number of deposited layers. ....	1
<b>Figure 2.28.</b> Schematic representation of a confocal Raman microspectrometer .....	1
<b>Figure 2.29.</b> Typical intensity fluctuations of large and small particles .....	1
<b>Figure 2.30.</b> Setup of DLS system of Zetasizer Nano ZS .....	1
<b>Figure 2.31.</b> The correlation function .....	1
<b>Figure 2.32.</b> Number, volume and intensity distributions of a bimodal mixture of 5 and 50nm particles present in equal number. ....	1
<b>Figure 2.33.</b> Zetasizer Nano ZS electrophoretic mobility measurement set up .....	1
<b>Figure 2.34.</b> The measurement principle of electrophoretic mobility of charged particles in a capillary cell or zeta cell (Malvern Instruments Ltd, UK) .....	1

### **Figures Chapter III**

<b>Figure 1.</b> Schematic representation of carboxylate-terminated poly(amido)-amine (PAMAM) dendrimers with ethylenediamine core. ....	1
<b>Figure 2.</b> Electrophoretic mobility of G6.5 PAMAM-COOH dendrimer as a function of NaNO <sub>3</sub> electrolyte concentration at several pH values (indicated). ....	1
<b>Figure 3.</b> Electrophoretic mobility of G6.5 PAMAM-COOH dendrimer as a function of pH at several NaNO <sub>3</sub> electrolyte concentrations (indicated). ....	1
<b>Figure 4.</b> Comparison between the Point of Zero Mobility (PZM) of G6.5 PAMAM-COOH dendrimer measured at several NaNO <sub>3</sub> concentrations (symbols) and that evaluated from theory (solid curve (a)). Model parameters: as in Figure 2 with $\alpha_H \rightarrow 0$ .....	140
<b>Figure 5.</b> Theoretical dependence of the Point of Zero Mobility (PZM) on monovalent salt concentration for various values of $1/\lambda_o$ (A), $pK_{1,2}$ (B) and $r_{1,2}$ (C) (indicated). ....	142
<b>Figure 6.</b> Electrophoretic mobility of G6.5 PAMAM-COOH dendrimer as a function of NaNO <sub>3</sub> electrolyte concentration at several pH values (indicated). ....	1
<b>Figure S1.</b> Variations of the volume charge density $\rho_2$ with $1/r_2$ , where $r_2$ was adjusted to best fit the measured salt concentration dependence of the point of zero mobility for G6.5 PAMAM-COOH dendrimer. ....	1
<b>Figure S2.</b> Comparison between the Point of Zero Mobility (PZM) measured for G6.5 PAMAM-COOH at various NaNO <sub>3</sub> concentrations (symbols) and that evaluated from theory with $-\rho_2/F = 10.5 \times 10^3$ mM at $r_2$ values (indicated) that best bracket the overall dependence of the PZM on salt concentration. Other model parameters: as in Figure 2 with $\alpha_H \rightarrow 0$ .....	1

### **Figures Chapter IV**

<b>Figure 1.</b> Quantitative analysis of QCM-D results. ....	181
<b>Figure 2.</b> Effect of aging and heating treatment on film morpholog. ....	182
<b>Figure 3.</b> Effect of natural aging on the film mechanical properties. ....	183
<b>Figure 4.</b> Effect of heating treatment delay on the film mechanical propertie. ....	185
<b>Figure 5.</b> Effect of natural aging and heating treatment on film surface roughness and Young modulus. ....	185
<b>Figure 6.</b> Confocal Raman spectroscopy on freshly built (PDADMAC-PAA) <sub>30</sub> film. ....	186
<b>Figure 7.</b> Schematics summarizing the structure-mechanics-molecular organization features of freshly built (PDADMAC-PAA) <sub>30</sub> film .....	187

<b>Figure 8.</b> Effect of laser printing/heating on film Raman signature.....	188
<b>Figure S1.</b> Morphological analysis of the freshly built film.....	194
<b>Figure S2.</b> Detailed analysis of mechanical heterogeneities of a freshly built (PDADMAC-PAA) <sub>30</sub> film.....	195
<b>Figure S3.</b> Confocal Raman spectroscopic mapping of donut-like structures in freshly built (PDADMAC-PAA) <sub>30</sub> film.....	196
<b>Figure S4.</b> Representative snapshots of DFT-derived structures for (A) PDADMAC, (B) PAA and (C) PDADMAC-PAA complexes .....	197
<b>Figure S5.</b> Comparison between DFT-derived and experimentally measured Raman spectra .....	197
<b>Figure S6.</b> Raman spectra measured for a 22-day old (PDADMAC-PAA) <sub>30</sub> film.....	198

### **Figures Chapter V**

<b>Figure 5.1.</b> P A M AC – PAA) at pH=3 (pH of PAA solution adjusted with HCl, see Chapter 2, and 10mM NaNO <sub>3</sub> ) (A) native films; (B), (C), and (D): films after exposure to 0.5 g/l G6.5 solution for 24 hrs .....	1
<b>Figure 5.2.</b> P A M AC – PAA) at pH=3 after 6 hours of heating (60°C) (A) unloaded films; (B) and (C): films loaded with G6.5 ( 0.5 g/L solution, 24 hrs exposition time). .....	1
<b>Figure 5.3.</b> Thickness of P A M AC – PAA) films constructed with PAA solution @ pH=3 and (A) 50 mM and (B) 100 mM NaNO <sub>3</sub> concentration.....	1
<b>Figure 5.4.</b> Thickness of P A M AC – PAA) at pH=6 (pH of PAA solution adjusted with Tris buffer, see chapter 2) and NaNO <sub>3</sub> 10 mM. ....	1
<b>Figure 5.5.</b> G6.5 immobilized on a glass substrate (image in air). (A) AFM height image (in air), (B) image captured by the AFM scanner camera, (C) Zoomed section showing G6.5 particle size (zoom of section located in between the fractal structures displayed in (A)), (D) 3-D film surface topography .....	1
<b>Figure 5.6.</b> The different modes of adsorption of nanoparticles/molecules, as suggested by Salloum and Schlenoff, (a) and (b) schematically represent particles adsorbing to the surface either (a) uniformly (monolayer formation) or according to (b) island-like distribution, (c) this case represents the formation of aggregates on the surface, and (d) the sorption throughout bulk film. ....	1
<b>Figure 5.7.</b> Effect of G6.5 concentration on the morphology of (PDADMAC-PAA) <sub>30</sub> films; (A) Control films, (B) Films loaded with 0.5 g/L G6.5, and (C) films loaded with 0.8 g/L G6.5 .....	1
<b>Figure 5.8.</b> (Left) Surface topography in AFM contact mode for (PDADMAC – PAA) <sub>30</sub> loaded with 0.2 g/L G6.5 dendrimers; Right: section of the same film showing a thickness of 4.5 μm.....	1
<b>Figure 5.9.</b> Force-indentation curves on (PDADMAC-PAA) <sub>30</sub> loaded with G6.5 present in different concentrations (indicated) in the exposure medium .....	1
<b>Figure 5.10.</b> Distribution of Young Modulus (kPa) for (PDADMAC-PAA) <sub>30</sub> loaded with different concentrations of G6.5 nanodendrimers .....	1
<b>Figure 5.11.</b> Variation of Young modulus as a function of G6.5 concentration .....	1

## Résumé

Depuis son introduction par Decher au début des années 1990 (Decher et al, 1992), l'assemblage couche par couche « layer by layer » (LBL) s'est avéré être une technique peu coûteuse et respectueuse de l'environnement qui permet la fabrication de films minces nanométriques. En raison de la simplicité de cette technique, les domaines de la construction et de l'investigation des films LBL sont devenus populaires et des recherches approfondies ont été réalisées pour dévoiler les propriétés des blocs de films produits en fonction de leurs conditions de dépôt. Particulièrement, de nombreux travaux effectués sur les multicouches de polyélectrolytes (PEM) ont porté sur l'analyse de leurs propriétés et de leurs structures et réactivités. Les PEM sont traditionnellement construits par un dépôt LBL de polyélectrolytes. La perméabilité, l'épaisseur ou l'élasticité mécanique des films peuvent être maîtrisées avec un bon contrôle des propriétés physico-chimiques du milieu où les polyélectrolytes sont initialement dispersés, à savoir ; le pH de la solution, la concentration en sel et la nature des ions en solution ou encore la température. Avec un léger changement d'une ou plusieurs de ces propriétés, un film polyélectrolyte multicouche peut prendre la forme d'une membrane mince et rigide, ou épaisse, ductile et hautement perméable. Cette polyvalence est extrêmement attrayante car les caractéristiques de film PEM peuvent en principe être ajustées pour répondre aux exigences spécifiques de certains types d'applications, par exemple l'inhibition de l'adhésion de bactéries aux surfaces ou l'incorporation de drogues. La compréhension des propriétés des films PEM est requise pour optimiser leur capacité par exemple piégé des colloïdes ou des nanoparticules pour des applications de filtration, par exemple. Par ailleurs, une connaissance pointue des propriétés interfaciales de ces (nano) colloïdes à incorporer dans les films PEM est nécessaire pour une analyse adéquate de leur sort dans la matrice de PEM et, en particulier, leur action sur les propriétés mécaniques des films et sur l'organisation structurale des polymères constitutifs du film. En raison de leurs propriétés uniques, en termes de structure hautement ramifiée, taille ajustable, composition chimique réglable et caractéristiques dispersives remarquables même dans des conditions physiologiques, les dendrimères ont reçu une attention croissante dans

divers domaines de recherche, ex. science des matériaux et biomédecine, en particulier pour encapsuler des composés pharmaceutiquement actifs ou pour la liaison de surface d'espèces chimiques ciblant par exemple Radioligands ou agents d'imagerie. L'utilisation significative de ces particules dendritiques et leur relargage dans les écosystèmes aquatiques ont également conduit les chercheurs à s'intéresser à leur toxicité vis-à-vis des microorganismes aquatiques, ce qui a donné lieu à des recherches sur les méthodes et les techniques pour diminuer leur présence en milieu aqueux.

L'objectif général du travail de ce doctorat concernait initialement l'étude des processus physico-chimiques menant à l'incorporation de poly (amido) -amine (PAMAM) starburst (nano) dendrimers dans les films multicouches de poly (chlorhydrate de diallyldiméthylammonium) (PDADMAC) -poly (acide acrylique) (PAA). Au-delà de leur pertinence dans de nombreuses applications, certaines d'entre elles mentionnées ci-dessus, le choix de ces systèmes a été motivé par (i) les études antérieures dans la littérature sur l'utilisation des films PDADMAC-PAA comme réservoir de piégeage pour les colloïdes (par exemple nanoparticules de  $\text{TiO}_2$ ) et (ii) la facilité à contrôler la composition chimique des dendrimères et leur versatilité en termes de propriétés de surface. Ces éléments rendaient à priori possible l'élaboration de connaissances génériques sur les interactions PEM film-colloïdes avant et après le processus d'incorporation, un problème qui est souvent entravé par le mauvais contrôle des caractéristiques physico-chimiques des systèmes particuliers (et des PEM<sub>s</sub>) utilisés dans la littérature. Du point de vue application, l'utilisation des films PDADMAC-PAA comme «éponges» à dendrimères (potentiellement toxiques pour les microorganismes aquatiques) dans les unités de filtration offre une solution prometteuse pour diminuer le relargage de ces nanomatériaux dans les environnements aquatiques.

Compte tenu de l'objectif ci-dessus, mes travaux de PhD consistaient, d'abord, à (i) analyser la structure et les propriétés mécaniques (élasticité) des films PDADMAC-PAA et leur évolution en fonction du temps dans des conditions de vieillissement naturelles ou après traitement thermique, puis (ii) effectuer une étude détaillée de la taille et des propriétés électrostatiques des dendrimères PAMAM en fonction de la composition du milieu physico-chimique (pH, salinité), et, enfin (iii) fournir des données préliminaires sur le chargement possible de dendrimères dans les films PEM fabriqués et analysés en

---

(i). Le manuscrit de ce doctorat est organisé selon 6 chapitres, dont le contenu est brièvement décrit ci-dessous.

Le chapitre 1 est une revue de la littérature couvrant la fabrication, les propriétés et les applications des films polyélectrolytes multicouches, particulièrement ce qui concerne leur chargement avec différents types de molécules et de particules. Le chapitre rappelle également les bases de l'électro-cinétique des particules molles et une description du type de nanodendrimères utilisés dans ce travail.

Dans le chapitre 2, nous examinons les différentes méthodes physico-chimiques utilisées pour mesurer les propriétés recherchées de nos PEMs et dendrimères. Cela comprend une description détaillée de la synthèse des films et l'explication des principes de fonctionnement des équipements utilisés pour réaliser le travail expérimental. Principalement, les expériences de dynamic light scattering (DLS) et phase analysis light scattering (PALS) ont été utilisées, respectivement, pour évaluer le diamètre hydrodynamique et la mobilité électrophorétique des nanodendrimères. Quartz-crystal microbalance with dissipation (QCM-D) a été utilisé pour suivre la cinétique d'accumulation in situ des PEMs et pour étudier leurs propriétés rhéologiques (viscosité dynamique et module de cisaillement). La spectroscopie confocal Raman (RCS) a permis de suivre les changements structuraux et chimiques dans les organisations (empilement) des films en fonction du temps. Enfin, la microscopie à force atomique (AFM) pour aborder les propriétés mécaniques des films multicouches et leur morphologie de surface dans différentes conditions, leur évolution au cours du temps en l'absence de dendrimères et après incorporation de ces particules.

Dans le chapitre 3, nous reportons une étude électrocinétique systématique des nanodendrimères poly (amido) -amine carboxylés (PAMAM-COOH) (5 à 8 nm de diamètre) et, pour la première fois, une preuve directe est amenée concernant le changement non conventionnel du signe de leur mobilité électrophorétique en changeant la concentration de l'électrolyte monovalent en solution. L'origine physique pour les caractéristiques électrocinétiques remarquables des nanodendrimères s'explique quantitativement au moyen du modèle électrocinétique standard avec prise en considération de (i) la distribution non uniforme des charges intraparticulaires cationiques

amine) et anioniques (carboxylate), et ii) la présence d'un gradient de densité de segment fini à l'interphase dendrimère/solution. En outre, une démonstration claire est donnée pour la dépendance observée du point de zéro mobilité des nanodendrimères en fonction de leur taille. Ce chapitre a abouti à la publication *Moussa, et al.* 'Remarkable electrokinetic features of charge-stratified soft nanoparticles: mobility reversal in monovalent aqueous electrolyte', *Langmuir* **2015**, 31, 5656-5666.

Le chapitre 4 rapporte l'analyse de la morphologie, de la structure et de l'élasticité des films PDADMAC-PAA en l'absence de dendrimères. La littérature abondante sur les polyélectrolytes multicouches suggère une forte différenciation entre les propriétés des films à croissance linéaire et à croissance exponentielle construits à partir du dépôt alternatif de polyanions et de polycations. Il existe de nombreuses études montrant en effet que les films à croissance linéaire sont hors équilibre, dans un «état figé», et leur transition vers un état d'équilibre est extrêmement lente en raison de la réduction de la mobilité des chaînes polyélectrolytes. En revanche, les films de PEM à croissance exponentielle sont plus proches de l'équilibre thermodynamique et leurs chaînes constitutives polyélectrolytes sont a priori bien inter-mélangées, comme l'ont confirmé diverses mesures de microscopie et de spectroscopie, la mobilité des chaînes pointues dans une matrice de film comparable à celle obtenue dans des conditions aqueuses. Conformément à cela, les modules de Young de films linéaires peuvent être un à deux ordres de grandeur supérieurs à ceux de leurs homologues exponentiels. Dans ce chapitre 6, nous démontrons pour la première fois que la différenciation dichotomique ci-dessus entre les films hors équilibre à croissance linéaire et les films à croissance exponentielle en équilibre n'est pas une règle générale. Sur la base de la microscopie à force atomique et (AFM) des analyses de microspectroscopie Raman complétées par des calculs moléculaires basés sur la théorie fonctionnelle de Densité, on montre que le polychlorure Les films exponentiel multicouches de poly (diallyldiméthylammonium) (PDADMAC) - poly (acide acrylique) (PAA) représentent des caractéristiques de relaxation de structure et mécaniques qui sont généralement observées pour les systèmes linéaires PEM. En particulier, les films de poly électrolyte (PDADMAC-PAA)<sub>n</sub> se comportent comme des matériaux vitreux avec des modules de Young aussi grands que 2 MPa et leur relaxation à un état d'équilibre se produit sur quelques jours, accompagnée d'une diminution de trois



fois du module d'Young. L'étude démontre que cet adoucissement du film est considérablement accéléré après un chauffage à 60 ° C avec une relaxation qui prend effet sur quelques heures seulement. Cette stabilité unique et ces propriétés mécaniques proviennent de la présence de domaines bien définis de type "donuts" dans des films fraîchement construits, des domaines appauvris en l'eau, enrichis en PDADMAC et constitués de complexes PDADMAC-PAA stabilisés électrostatiquement et solidement compactés. La dynamique lente de relaxation de la structure du film est intrinsèquement liée à l'instabilité de ces domaines de type donuts, dont la disparition progressive a été mesurée au cours du temps avec une résolution spatiale nanométrique par AFM. Enfin, nous prouvons que cette transition de structure atypique de films à croissance exponentielle peut être utilisée pour des applications microscopiques d'impression réversibles assistées par laser. Les résultats présentés dans ce chapitre ont été publiés dans l'article *The Journal of Physical Chemistry C*, **2016**, 120, 5599–5612.

Le chapitre 5 présente des données préliminaires sur la modification de l'élasticité du film PDADMAC-PAA chargé avec des nanodendrimères en fonction de la concentration des particules dans la solution à laquelle les films PEM ont été exposés. Enfin, le chapitre 6 résume les conclusions générales de ce travail et une description brève des études à entreprendre dans un futur proche afin de comprendre/optimiser les processus régissant les mécanismes d'absorption/relargage des nanodendrimères par les films multicouches PDADMAC-PAA.

# General Introduction

Since its introduction by Decher in the early 1990's (Decher et al., 1992), layer by layer (LBL) assembly has proven to be a low-cost and environmentally friendly technique that allows the fabrication of nanostructured thin films. Because of the simplicity of this technique, the fields of LBL films construction and investigation have become popular and extensive research has been conducted to unveil the properties of films building blocks in relation to film deposition conditions. In particular, much work has been reported on so-constructed polyelectrolyte multilayers (PEM) with a special focus on their intertwined reactivity-structure properties. Polyelectrolyte multilayer films are traditionally constructed from the LBL deposition of oppositely charged polyanionic and polycationic polyelectrolytes. Films properties such as permeability, thickness or mechanical elasticity can be tailored upon proper control of the physico-chemical properties of the medium where polyelectrolytes are initially dispersed, namely solution pH, salt concentration and ion nature in solution or temperature. With a slight change of one or several of these medium properties, a polyelectrolyte multilayer film may turn from a rigid thin membrane into a thick, soft and highly permeable one. This versatility is extremely attractive as PEM film features can in principle be adjusted to match requirements specific for certain types of applications, *e.g.* the inhibition of bacterial adhesion to surfaces or the incorporation of drugs. The understanding of PEM film properties is a mandatory requirement for further optimizing their ability to *e.g.* trap colloids or nanoparticles of specific interest. In addition, a basic knowledge of the interfacial properties of these (nano)colloids to be incorporated in PEM films is of utmost importance for adequate analysis of their fate within the soft PEM matrix and, in particular, their effect on films mechanical properties and on the structural organization of the film constitutive polymers.

Due to their unique properties including a highly branched structure, a size that can be varied at will, a tunable chemical composition and marked dispersive features even

---

under physiological medium conditions, dendrimers have attracted increasing attention in research fields as diverse as material science or biomedicine, especially for encapsulating pharmaceutically active compounds or for surface conjugation of chemical species targeting *e.g.* radioligands or imaging agents. The significant use of these dendritic particles and their accompanied release in aquatic ecosystems also led researchers to define their toxicity toward aquatic microorganisms and this gave rise to investigations about methods and techniques for decreasing their availability in aqueous environment.

The general objective of this PhD work was initially to address the basic physico-chemical processes leading to the incorporation of poly(amido)-amine (PAMAM) starburst (nano)dendrimers into poly(diallyldimethylammonium chloride) (PDADMAC)-poly(acrylic acid) (PAA) multilayer films. Beyond their relevance in numerous applications, some of them being mentioned above, the choice of these systems was motivated by (i) prior studies given in literature on the use of PDADMAC-PAA films as trapping reservoir for colloids (*e.g.*  $\text{TiO}_2$  nanoparticles) and (ii) the highly-controlled dendrimer chemical composition and the versatility for tailoring their surface properties. These elements made *a priori* possible the derivation of generic knowledge on PEM film-colloids interactions before and after incorporation process, an issue that is often hampered by the poor control of the physico-chemical characteristics of the particulate (and PEM) systems employed in literature. From an application point of view, the use of PDADMAC-PAA films as ‘sponges’ for dendrimers toxic for aquatic microorganisms within filtration units offers a promising solution for decreasing the release of these nanomaterials in environmental aquatic media.

In view of the aforementioned objective, my PhD work consisted, first, in (i) analyzing the structure and mechanical properties (elasticity) of PDADMAC-PAA films, and their evolution over time under natural aging conditions or after thermal treatment, then (ii) performing a detailed investigation of the size and electrostatic properties of PAMAM dendrimers as a function of physico-chemical medium composition (pH, salinity) and, finally (iii) providing preliminary data about the feasible loading of dendrimers within the PEM films fabricated and analyzed in (i). The PhD manuscript is organized according to 6 chapters, the content of which is briefly outlined below.

**Chapter 1** is a literature review covering the fabrication, properties and applications of polyelectrolyte multilayer films, in particular with respect to their loading with different types of molecules and particles. The chapter further recalls basics of electrokinetics of soft particles and a description of the type of nanodendrimers used in this work.

In **chapter 2**, we review the various physico-chemical methods employed to address the relevant properties of our PEM and dendrimer materials. This includes a detailed description of the films synthesis, and the explanation of the working principles of the equipment used to carry out the experimental work. In particular, dynamic light scattering (DLS) and phase analysis light scattering (PALS) experiments were used to evaluate hydrodynamic diameter and electrophoretic mobility of the nanodendrimers, respectively. Quartz-crystal microbalance with dissipation (QCM-D) was used to monitor the *in-situ* buildup kinetics of the PEMs of interest and to investigate their rheological properties (dynamic viscosity and shear modulus). Raman confocal spectroscopy (RCS) allowed the monitoring of the changes in structural and chemical organizations of the films with time. Finally, Atomic force microscopy (AFM) was employed to address the mechanical properties of the multilayer films and their surface morphology under different conditions, their evolution with time in the absence of dendrimers and after incorporation of the latter.

In **chapter 3**, we provide a systematic electrokinetic study on poly(amido)-amine carboxylated (PAMAM-COOH) nanodendrimers (5 to 8 nm in diameter) and, for the first time, a direct evidence is given for the unconventional change in sign of electrophoretic mobility for PAMAM-COOH nanodendrimers with changing monovalent electrolyte concentration in solution. The physical origin for the remarkable electrokinetic features of nanodendrimers are quantitatively explained by means of the standard electrokinetic model with accounts of (i) the nonuniform distribution of intraparticle cationic (amine) and surface anionic (carboxylate) charges, and (ii) the presence of a finite segment density gradient at the dendrimer/solution interphase. We demonstrate that mobility reversal originates from the interplay between the Debye length and the thickness of the carboxylic surface layer. The non-monotonous electrokinetic response at low salt

concentrations and/or high pH is further shown to stem from subtle changes in dendrimer compactness/size due to Coulombic interactions between intraparticulate functional groups. In addition, a clear demonstration is given for the observed dependence of nanodendrimer point of zero mobility on particle size. This chapter lead to the publication Moussa, *et al.* ‘Remarkable electrokinetic features of charge-stratified soft nanoparticles: mobility reversal in monovalent aqueous electrolyte’, *Langmuir*, **2015**, 31, 5656-5666.

**Chapter 4** reports the analysis of PDADMAC-PAA films morphology, structure and elasticity in the absence of dendrimers. The abundant literature on polyelectrolyte multilayers suggests a strong differentiation between properties of linearly and exponentially grown films constructed from the alternate deposition of polyanions and polycations. There is plethora of studies showing indeed that linearly growing films are out of equilibrium, in a ‘frozen state’, and their transition to an equilibrium state is extremely slow due to the reduced mobility of the polyelectrolyte chains. In contrast, exponential PEM films are thought to be closer to thermodynamic equilibrium and their constitutive polyelectrolyte chains are supposedly well inter-mixed, as confirmed by various microscopy and spectroscopy measurements pointing chains mobility in film matrix that is comparable to that achieved in bulk aqueous conditions. In line with this, Young moduli of linear films may be one to two orders of magnitude larger than that of their exponential counterparts. In this chapter 6, we demonstrate for the first time that the above dichotomous differentiation between non-equilibrated linearly growing films and equilibrated exponentially growing films is not a general rule. Based on in-situ Atomic Force Microscopy (tens of nanometer resolution) and Raman microspectroscopy analyses complemented by Density Functional Theory-based molecular computations, it is shown that exponential poly(diallyldimethylammonium chloride) (PDADMAC)-poly(acrylic acid) (PAA) multilayer films depict mechanical and structure relaxation features that are typically observed for linear PEM systems. In particular, (PDADMAC-PAA)<sub>n</sub> polyelectrolyte films behave as glassy materials with Young moduli as large as 2 MPa and their relaxation to an equilibrium state occurs over few days, accompanied by a three-fold decrease of the Young modulus. The study demonstrates that this mechanical softening of the film is significantly accelerated after heating treatment at 60°C with a relaxation that then operates over few hours only. These unique stability and mechanical

properties are shown to originate from the presence of well-defined donut-like domains in freshly built films, domains depleted in water, enriched in PDADMAC and consisting of electrostatically-stabilized and tightly compacted PDADMAC-PAA complexes. The slow structure relaxation dynamics of the film is shown to be inherently connected to the instability of the donut-like domains, the gradual disappearance of which is addressed here over time with nanometer spatial resolution by AFM. Finally, we evidence that such atypical structure transition of exponentially-grown films can be used for reversible laser-assisted printing applications at microscales. Results reported in this chapter had been published in *The Journal of Physical Chemistry C*, **2016**, 120, 5599–5612.

**Chapter 5** presents preliminary data on the modification of PDADMAC-PAA film elasticity loaded by nanodendrimers as a function of particles concentration in solution PEM films were exposed to. Finally, **chapter 6** provides the general conclusions of this work and a description of the studies to undertake in the near future in order to understand/optimize the processes governing nanodendrimers uptake/release mechanisms by PDADMAC-PAA multilayer films.

# **Chapter I**

## **Literature Review**

Understanding PEM film properties (structure, organization, and mechanics) is essential for studying their ability to trap molecules and nanoparticles. Moreover, assessment of the interfacial properties of particles to be incorporated within PEM films is mandatory for evaluation of their behavior within the soft film matrix and the various effects they induce on the polymeric cushion structural features.

In the first part of this chapter, we present an overview on the polyelectrolyte multilayer films, their physico-chemical properties and applications. Next, we describe the nature of the interactions governing their buildup and the external parameters affecting those interactions. This is followed by a brief history covering the work on loading of multilayer films with different molecules, ions or nanoparticles. In the second part, we provide a brief summary of soft particles electrokinetic properties/theory. Finally, we provide a description of the structure and other relevant characteristics of the nanodendrimers used in my PhD work.

## **I. Polyelectrolyte multilayer (PEM) films**

### **I.1. Polyelectrolyte multilayer films obtained by electrostatic interactions**

Several types of interactions potentially drive the assembly of polyelectrolytes within multilayer films. The most widely occurring assembly is based on the sequential deposition of charged polymer species whose electrostatic interactions trigger the buildup of the multilayer film. Although the interactions in LBL films are primarily governed by electrostatics, other types of interactions may occur, *e.g.* hydrogen bonding, charge transfer, specific biological recognition, hydrophobic attraction or covalent bonding. In this section an overview of the literature on PEM films obtained by electrostatic interactions is presented. Other types of interactions driving polyelectrolytes assembly are subsequently discussed.

#### **I.1.1. Properties of polyelectrolytes**

Polyelectrolytes are a class of macromolecules or polymers with high molecular weight and whose repeating unit bears an electrolyte group that dissociates in a suitable polar solvent (usually water) giving the polyelectrolyte its charge. Despite their widespread presence and use, polyelectrolytes remain among the least understood materials in soft condensed matter.



In particular, difficulty arises from the correlation between chain configuration and polyelectrolyte charges [1].

The chemical properties of a polyelectrolyte play a major role in the design of PEM films. Polyelectrolytes may differ in terms of structure, charge densities, hydrophobicity, and stiffness all of which have a significant impact on the design and structure of PEMs.

### **I.1.2. Strong polyelectrolytes versus weak polyelectrolytes**

In analogy to acids, one can distinguish between weak polyelectrolytes and strong polyelectrolytes. The interaction between two polyelectrolytes used for a given PEM film construction is mainly governed by electrostatics, and therefore it depends on the charged groups carried by both polyelectrolytes. The degree of ionization of a polyelectrolyte in an aqueous solution depends on the protolytic features of these groups and on solution's  $p$ . Weak and strong polyelectrolytes differ according to their degree of dissociation/ionization in the solution. Strong polyelectrolytes completely dissociate in solution and are thus completely ionized regardless of solution pH. In case of weak polyelectrolytes, the degree of dissociation is pH-dependent, and in principle maximum ionization occurs at a pH equal to the  $pK_a$  of the ionogenic groups the polyelectrolyte carries [2].

### **I.1.3. History of polyelectrolyte multilayer films**

"Langmuir" or "Langmuir-Blodgett" thin films were the first nanostructured films to be prepared at the beginning of the last century. Langmuir-Blodgett films were prepared from the building of a monolayer of tensioactive or amphiphilic molecules at an air/water interface upon compression transfer to a solid substrate (Figure 1.1) [3, 4]. The adsorption is based on hydrophilic/hydrophobic type of interactions and the thickness of such films may range from few Angstroms to several nanometers.

Langmuir-Blodgett films were known for their low resistance to extreme changes in physico-chemical parameters such as temperature and type of solvent used during the deposition process. Additional disadvantages include films instability, limitation in terms of topography (*i.e.* the substrate must necessarily be planar), necessity to work in a controlled atmosphere, and the occurrence of undesired parasitic reactions between solvent and film molecules. In addition, desorption becomes more favorable than adsorption after the deposition of just a few layers, which makes difficult the build-up of thick films.

In the early 1980s, the concept of self-assembled monolayers was developed. This method involves the covalent attachment of an amphiphilic molecule to a solid surface, implying that the polar head of the amphiphilic molecule must possess a group capable of forming covalent bonds with the chemical groups of the substrate [5]. Other self-assembly methods have been developed to form structured organic films based on coordination chemistry of metal/phosphonate system [6] and covalent chemistry [7]. Studies where these methods were applied classically deal with protein adsorption [8, 9] or synthesis of metallic colloids [10]. However, these methods remain restricted to certain molecules and do not generally provide high quality films.

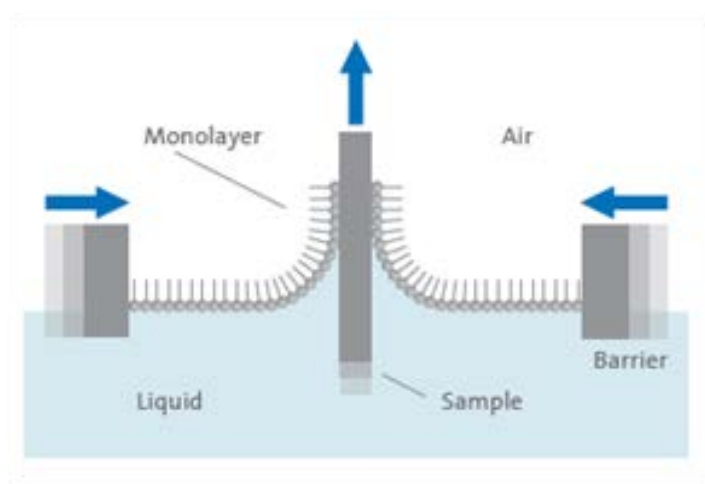


**Figure 1.1.** Principle of transfer of a lipid monolayer into a solid substrate by the Langmuir-Blodgett method.

The principle of polyelectrolyte multilayer films was first introduced by Iler in 1966 based on mixing oppositely charged polyelectrolyte solutions to form colloidal complexes [11]. Iler showed that it was possible to create multilayer films by successive adsorption of cationic and anionic colloids. Yet this work did not raise much attention by the community due to the lack -at that time- of experimental techniques required to characterize these assemblies. Furthermore, it was recorded that the deposition of oppositely charged materials stopped as soon as the cationic species had exactly compensated the charge stemming from the anionic species, and *vice-versa*.

It was only in the early 1990 that Decher introduced the layer by layer assembly and set assembly methods [12, 13]. In forefront of polymer literature, Decher applied the layer by layer (LBL) method on particular charged polymers or polyelectrolytes based on the sequential adsorption of species bearing oppositely charged functional groups.

#### I.1.4. Principles of the Layer by Layer (LBL) deposition of PEM films

The LBL technique is based on the sequential deposition of oppositely charged polyelectrolytes (a polyanion and a polycation) on a charged substrate (Figure 1.2). Charged substrates include metals, and glasses that carry a net negative charge in solution due to surface oxidation and hydrolysis. Successive deposition steps of the polycation and the polyanion are usually followed by a minimum of one rinsing step by an aqueous electrolyte solution in order to remove excess of the poorly bound polyelectrolyte molecules [14]. Thus a multilayer film can be constructed by repeating the sequence of the deposition cycle polycation/rinsing/polyanion/rinsing, thus resulting in quasi-unlimited thickness of polyelectrolyte films. After  $n$  deposition cycles the film is denoted (polycation-polyanion) $_n$ . The advantage of the LBL technique is that it allows a complete control over the sequence in which multiple functional elements are incorporated into a growing film [15].

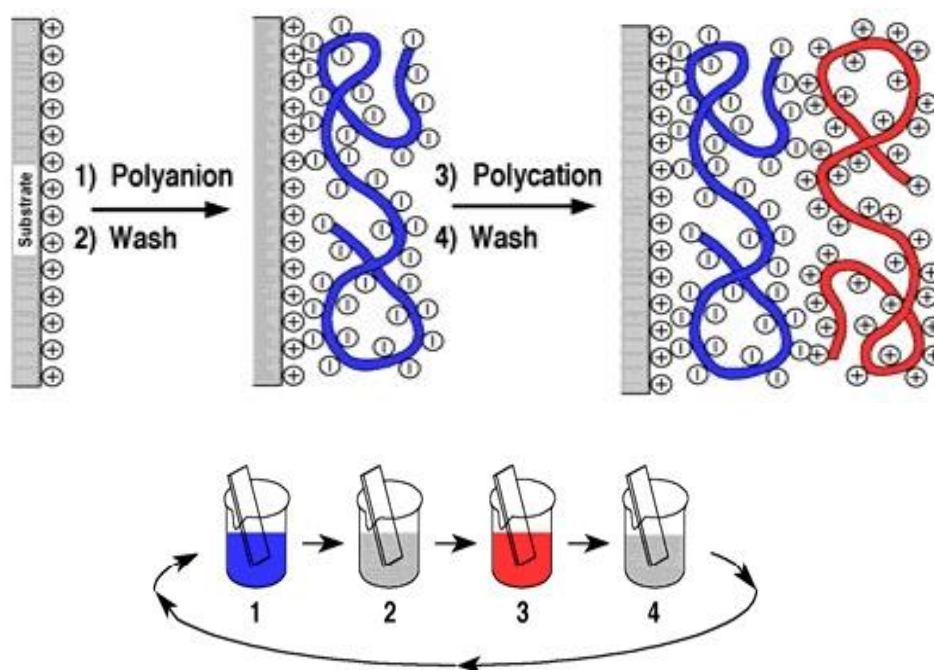
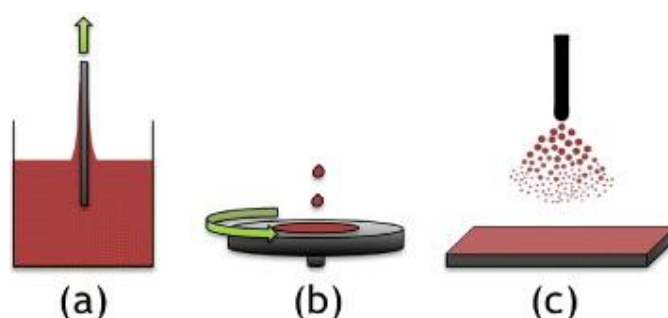


Figure 1.2. Principle of polyelectrolyte multilayer films construction [13]

### I.1.4.1. Buildup Techniques

The support can be brought into contact with polyelectrolyte solutions either by dipping it into the polyelectrolyte solutions, by spraying the solutions on the surface, or by spin coating. Although dip coating is relatively slow (~20 hours per 30 deposition cycles), it remains the most used method due to its simplicity, low polyelectrolyte solutions consumption, and the wide variety of substrates that can be potentially used. Spin coating offers a rapid method of construction but it is limited to flat substrates [16].



**Figure 1.3.** Buildup techniques: (a) dip coating, (b) spin coating, and (c) spray coating.

Besides the conventional manual method consisting in the dipping of the substrates, there has been a surge for deposition methods in order to shorten deposition time. For example, Clark and coworkers [17] have employed an automated programmable dipping system allowing for highly reproducible LBL films. The automated dipping also makes it possible to control accurately the parameters relevant for the film construction process.

### I.1.5. Interactions in multilayer LBL films

The most widely studied multilayer assembly is based on the sequential deposition of oppositely charged polyelectrolytes. The strong electrostatic interaction between the oppositely charged species is the basis of the multilayer film construction [18]. The LBL assembly is not limited to electrostatic interactions since hydrogen bonding and Van der Waals interactions may also contribute to the stabilization and corresponding variation in free energy of the polyelectrolyte multilayer system (Figure 1.4. *Interactions that govern the buildup of polyelectrolyte multilayer films and applications of PEMs.*). We first focus below on electrostatic interactions, and other types of interactions are discussed afterwards.

The key feature in the adsorption of polyelectrolyte films is charge overcompensation [19, 20]. The initial layer adsorbs onto the substrate either by electrostatic or hydrophobic interactions and creates a surface layer with charge sign opposite to that of the deposition substrate, and since each subsequently deposited molecule carries more than one charge, there can be charge overcompensation at each deposition step. Adsorption of subsequent layers again overcompensates the charge on the surface to reverse the net charge and allow the adsorption of the next layer. To remove excess polyelectrolyte, the PEM is typically

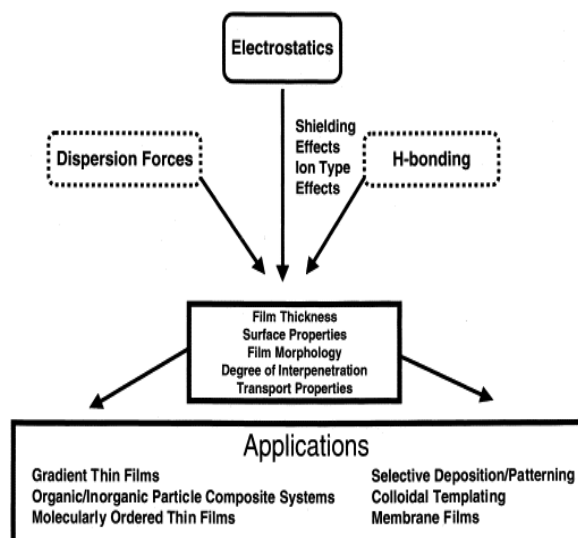


**Figure 1.4.** Interactions that govern the buildup of polyelectrolyte multilayer films and applications of PEMs.

rinsed by a salt solution after being deposited on the substrate. The charge overcompensation after each deposition step is classically monitored by zeta potential measurements and an example is provided in Figure 1.5 for the system PEI – (PSS/PAH) LBL films constructed from a poly(styrene sulfonate) (PSS) as a polycation, poly(allylamine hydrochloride) (PAH) as a polyanion, and with a first layer of cationic poly(ethyleneimine) (PEI) [20]. The surface of the substrate becomes positive after the deposition of the first PEI layer (Figure 1.5). This is followed by the deposition of the first polyanion layer. The adsorption of the polyanionic chains on the PEI cationic monolayer is ensured by the attractive electrostatic interactions between the two species. Those interactions take place between the negatively charged groups of the polyanion and the positively charged groups of the polycation adsorbed on the surface. Zeta potential measurements revealed that the surface charge becomes negative.

Thereby, the polyanion overcompensated the positive charge of the PEI monolayer. This overcompensation occurs after each polyelectrolyte deposition step.

A minimum charge density is required for the formation of multilayers. Below this critical charge density limit, charge reversal may not be sufficient for proper film construction. Schoeler and coworkers used UV-visible spectroscopy (UV-vis), quartz crystal microbalance (QCM), and atomic force microscopy (AFM) to demonstrate the existence of a critical charge density limit, or charge overcompensation threshold, between 50% and 75% below which no significant layer growth occurs [21, 22].

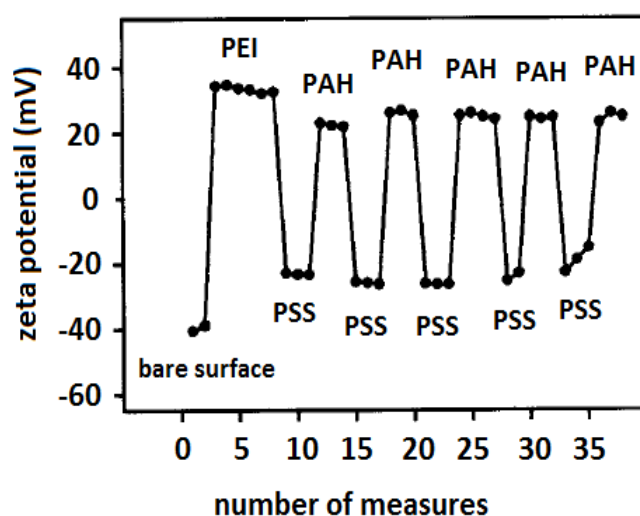


**Figure 1.5.** Evolution of the  $\zeta$  potential during the buildup of  $PEI - (PSS/PAH)_n$  multilayer film. [20]

#### I.1.6. Charge balance in polyelectrolyte multilayers

The combination of polyelectrolyte units and salt ions can explain the maintenance of net charge neutrality. We can distinguish here between two types of charge compensation. In one case hereafter termed intrinsic compensation, polyelectrolyte positive charge is balanced by another polyelectrolyte's negative charge. In extrinsic charge compensation, the polyelectrolyte charge is balanced by salt counterions from the solution used to construct the multilayers (Figure 1.6). A continuum of intrinsic-extrinsic composition is obvious, with the

idea that fully extrinsic multilayers are not realistic since, in the absence of other interaction mechanisms, the PEMs would decompose back into isolated molecules [23].

The properties of the constructed films are directly connected to the conformation and the nature of the polyelectrolyte chains, which includes the density of ionic functional groups they carry and their distribution along the polyelectrolyte chains. The conformation of a polyelectrolyte chain results from the balance between the electrostatic repulsive forces that favors chain elongation upon minimizing the interaction between monomers, and the elastic forces that favors the opposite by a gain in entropy.

Moreover, the counterions of the polyelectrolyte chains play a key role in electrostatic interactions. The complexation reaction between a polycation and a polyanion induces the release of counterions [24], which results in a gain of entropy [25]. Schlenoff et al. [26, 27] precisely defined the nature of the pairing of charges within polyelectrolyte multilayer films. This is to differentiate the charges in the film or intrinsic loads (carried by polyelectrolytes) or extrinsic (provided by the counterions from the solution). It is possible to describe the alignment forming between two polyelectrolytes sites  $Pol^+$  and  $Pol^-$  and associated release of the counterions  $C^-$  and  $C^+$  by the reaction:

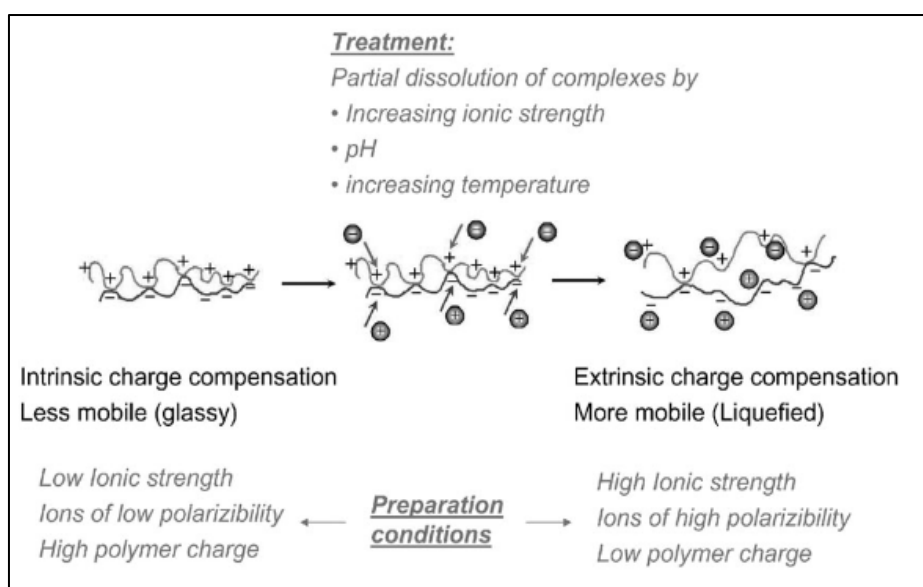
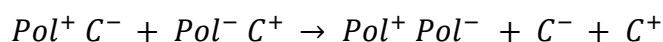


**Figure 1.6.** Intrinsic and extrinsic charge compensation in a PEM film.

### I.1.7. Growth modes of multilayer films

PEM films grow in thickness as a function of the number of deposited layers following two possible regimes, the so-called linear or exponential growth regime. In the linear mode, the film thickness increases linearly with the number of deposited layers, unlike the exponential mode. Depending on the combination of polyelectrolytes and on the preparation conditions, some films may show a transition between the two types of growth.

#### II.1.7.1. Films with linear growth

In films with linear mode of growth, the increase in the thickness of the constructed film is always constant per number of deposited layers. In the linear growth, a polyelectrolyte interacts only with the last deposited polyelectrolyte layer [13] and cannot diffuse into the film, and at each deposition step the same amount of polyelectrolytes is adsorbed. In general, linearly growing films are thinner than exponentially growing ones.

It has been shown that there is a correlation between the complexation heat and the mode of growth of a PEM film. For linearly growing films, the polycation/polyanion complex has a negative enthalpy of complexation [28].

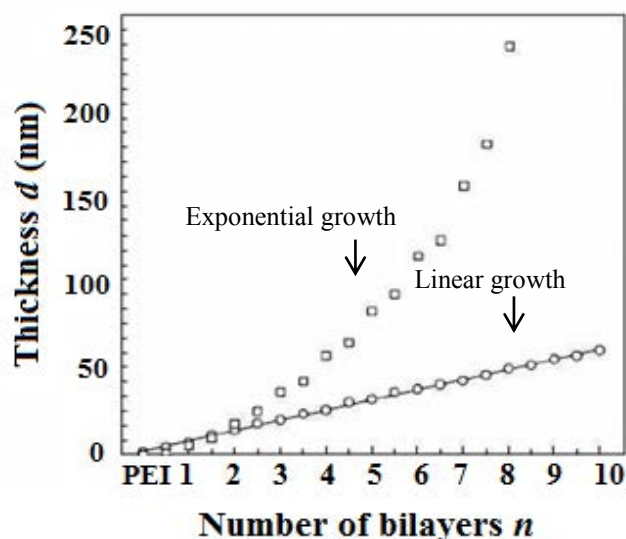


**Figure 1.7.** Evolution of the thickness of (○)  $\text{PEI} - (\text{PSS}/\text{PAH})_n$  films and (□) poly(L-glutamic acid)/poly(L-lysine) films denoted by  $\text{PEI} - (\text{PGA}/\text{PLL})_n$  as a function of the number of deposited layers. Data determined by optical spectroscopy. [32]



The poly(styrene sulfonate)/poly(allylamine hydrochloride) (PSS/PAH) system is a reference example for linear growth mode (Figure 1.7). X-ray reflectometry and neutron reflectivity results showed that in (PSS/PAH) films, polyelectrolyte layers only penetrate the adjacent layers constituting a pseudo-layer structure called “fuzzy layers” [13]. This gives the film certain homogeneity in structure and charge distribution [29, 30, 31].

Ladam et al. proposed a mechanism for the linear growth of multilayer films [20]. This model divides the film into three zones. Zone I, called the “precursor zone”, at the substrate/film interface and its vicinity, corresponds to the film precursor and is strongly influenced by the substrate. Zone III, at the interface film/solution, is called “external area”. Zone II is the intermediate zone and separates the two other zones and is not influenced by the interfaces. The boundaries between zones I and II and zones II and III are diffuse. The precise number of component layers of the zones I and III is not known but depends largely on the substrate, chemical structure of the used polyelectrolytes, and the physico-chemical parameters adopted for the film buildup. The model of the three zones is valid until a sufficient number of layers are deposited on the substrate.

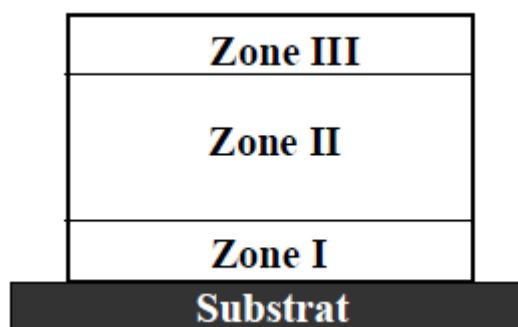


**Figure 1.8.** *The three zone model of polyelectrolyte multilayer films with linear growth.* [20]

#### **I.1.7.2. Films with exponential growth**

Such growth regime was first evidenced in 1990 with polypeptides- and polysaccharides-based films [32, 33]. Actually, most of biologically relevant films built from polypeptides and polysaccharides show an exponential growth. The mechanism leading to exponential growth is totally different from that which led to films with a linear growth. In

exponentially growing films, at least one of the two polyelectrolytes has the ability to diffuse “in” and “out” of the core of the polyelectrolyte multilayer during its buildup [32, 33]. Such films possess physico-chemical properties similar to those of a hydrogel due to their high water content [34, 35]. The thicknesses of such films may reach several micrometers after the deposit of twenty layer pairs. Comparatively, a film with a linear growth has a typical thickness in the order of ten nanometers for 15 constructed bilayers under the same conditions of pH and ionic strength.

Isothermal titration microcalorimetry experiments revealed that the enthalpy of complexation of the polyelectrolytes in exponentially growing films is positive. Therefore, exponential growth is mainly driven by the entropy and is temperature sensitive [28]. The mechanism of construction of the exponentially growing hyaluronic acid/poly(L-lysine) (PLL/HA) films were described by Lavalle et al. (Figure 1.9) [36]. The (PLL – HA)

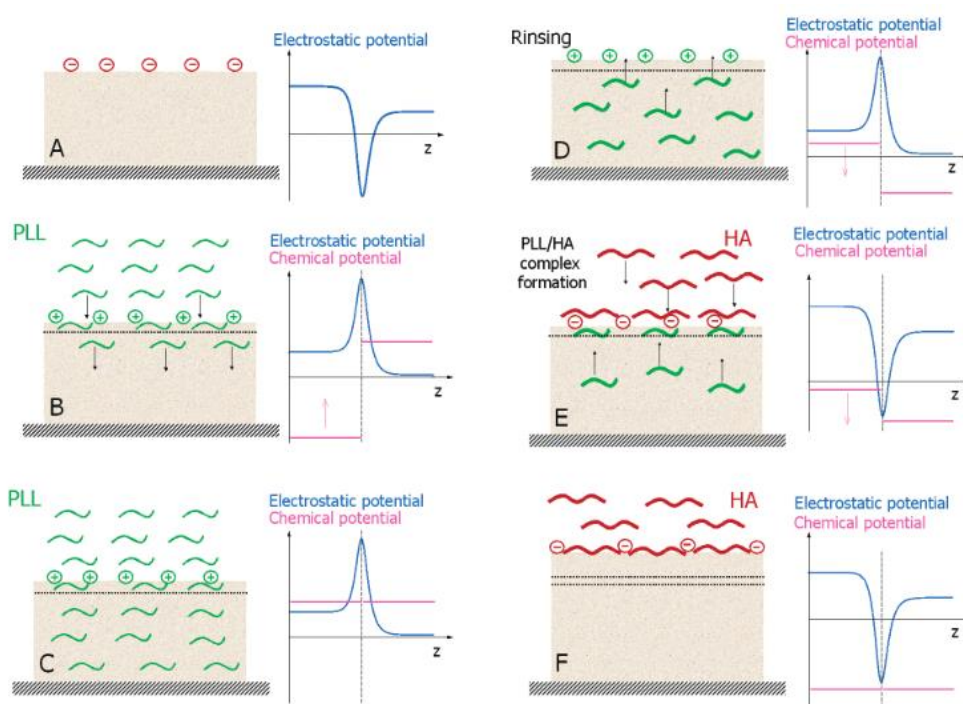


**Figure 1.9.** The buildup mechanism of (PLL/HA) films. [196]

multilayer film, terminated by a layer of polyanions HA (panel A in Figure 1.9), is brought into contact with the polycation PLL solution (panel B). The polycations form a layer at the surface creating a positive charge excess and diffuse at the same time into the film forming a reservoir of free polycations (panel C). During the rinsing phase, only a part of the free

polycations leaves the film because of the barrier of positive charges at the surface (panel D). The ability of the film to store part of PLL chains is explained by excess loads of positive charges to the film surface, which creates an electrostatic potential barrier preventing the diffusion of all of the polycations in the film. When the film is then brought into contact with the polyanion solution, polyanions complex with the excess positive charges on the surface changing the sign of the potential barrier which becomes negative (E). The free polycations previously confined in the film then diffuse outwardly and interact with polyanions forming an additional deposit to the surface. During this single application process continues until the depletion of the polycations reservoir is reached (F). The mass of the layers formed is proportional to the amount of free polycations remaining in the film after the rinsing phase.

During the construction of multilayer films, a transition from exponential to linear growth may occur. Hübsh et al. were the first to observe such a transition [37]. They studied the growth of a multilayer film based on a polycation, poly(allylamine hydrochloride) (PAH), and a binary mixture of polyanions, poly(glutamic acid) (PGA) and poly(styrene sulfonate) (PSS). These polyanions were chosen because PGA induces exponential growth with PAH while PSS causes a linear growth is solely interacting with PAH. Other studies have also described this transition in the case of (PLL/HA) system. This film reaches a critical thickness at which free polyelectrolytes stop diffusing into the film. After constructing a large number of layers, a structure comprising the three zones of the linear model would be obtained. This transition phenomenon would be established when the film thickness is between 150 and 200 nm.

### **I.1.8. Physico-chemical parameters affecting the growth of PEM films**

The physico-chemical parameters defining the conditions of the deposition cycle such as the pH, the ionic strength, and the temperature of the polyelectrolyte solutions mainly determine the structural, morphological and mechanical properties of the deposited PEMs.

#### **I.1.8.1. Solution pH**

The pH of the polyelectrolyte solutions plays a key role especially in cases where at least one of the two polymers used for constructing the PEM is a weak polyelectrolyte. The degree of charge dissociation or the polyelectrolyte ionization is pH-sensitive in the case of weak polyelectrolytes, thus the charge density can be regulated by a simple change of the pH of the polyelectrolyte solutions [2]. The total charge density determines the degree of

interaction between the two polyelectrolyte solutions used in the film deposition as well as the ions permeability within the films. This degree of interaction in turn greatly affects the structural and mechanical properties of the deposited films.

Studies showed that the young modulus of PEM films is tunable upon simple adjustment of pH. Lulevich and Vinogradova showed that the swelling and the stiffness of polyelectrolyte multilayer capsules are pH-controlled processes. For (PSS/PAH) multilayer capsules, the stiffness (young modulus) can be adjusted by changing the pH. The Young modulus varies dramatically from 70-100 MPa at a neutral pH to the order of 10-20 MPa at pH 10 [38]. These results were confirmed by Kim and Vinogradova [39]. This shift in Young modulus is explained by the fact that PAH is a weak polycation, so its linear charge density is pH sensitive. The charge density of PAH decreases at high pH where the ammonium groups are deprotonated. This affects the PAH conformation and reduces the density of ionic cross-links resulting in a smaller Young modulus.

Rubner also showed that the pH-controlled LBL assembly of weak polyelectrolytes yields a huge flexibility for controlling the molecular organization and the properties of PEM films [40]. For (PAA/PAH) multilayer film of weak polyelectrolytes, poly(acrylic acid) (PAA) and poly(allylamine hydrochloride) (PAH), it is possible to shift the thickness of a deposited polyelectrolyte layer from 0.5 nm to 8 nm just by changing the pH of the polyelectrolytes solutions used for film construction (Figure 1.10). At pH=7 the polymeric chains are significantly ionized and exhibit an elongated conformation due to strong intra-chains charges repulsion and thus the process ends up with thinner films [41]. Assembling PAA and PAH with strong polyelectrolytes led to similar results. In both cases, the dramatic change in thickness and the transition from thin to much thicker layers occurred when the charge density of the weak polyelectrolyte decreased from its fully charged state to 70-90% charged units. Moreover, FTIR analyses of the pH-dependent degree of ionization of the weak polyelectrolyte showed that the ionization behavior of a weak polyelectrolyte can differ substantially from the solution state when it is incorporated into a multilayer film [42].

In addition, the ion permeability of polyelectrolyte films varies significantly depending on the pH of the polyelectrolyte solutions. Harris and Bruening showed that the ion permeability in the poly(sterene sulfonate)/poly(allylamine hydrochloride) (PSS/PAH) multilayer system does not vary in the pH range between 3.2 and 6.3, but it increases significantly at basic pH values [43].

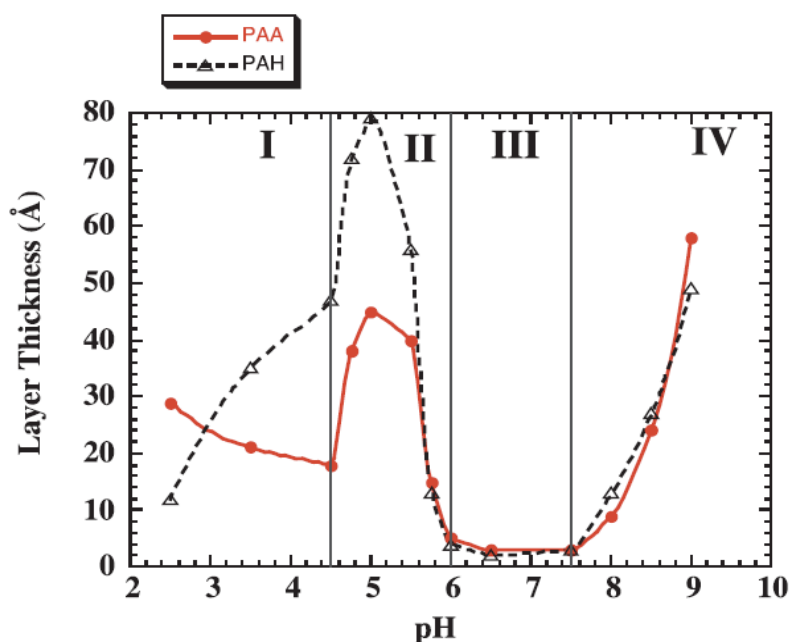


**Figure 1.10.** Average thickness contributions by PAA and PHA adsorbed layer as a function of solution pH. [41]

### I.1.8.2. Ionic strength of the buffer and polyelectrolyte solutions

Solution ionic strength plays a major role in the PEM films construction mechanism. In general, the increase in ionic strength is accompanied by an increase in the multilayer thickness (at least up to a certain ionic strength, which is specific for each multilayer system) and by an increase in film roughness [12, 18, 20].

Above the charge overcompensation threshold, the film thickness can be tuned by increasing the ionic strength of the rinsing solution, which enhances adsorption of polyelectrolytes due to charge screening. The presence of the charges along the chain changes its flexibility, so the role of the counterions in the configuration of a polyelectrolyte chain is essential. The electric Debye length is fixed by the ionic strength of the solution wherein the polyelectrolyte is dissolved. Thus, the higher the ionic strength, the lower is the Debye length, the greater the screening is, and the polyelectrolyte chain adopts an intertwined conformation. On the contrary, the lower the ionic strength, the less significant is the screening and the polymeric chain then adopts a linear conformation. The space occupied by a compact conformation is more important. Thus the film thickness increases with the ionic strength of the solutions. This phenomenon has been observed for (PAH/ PSS) films [20].

The change in multilayer structure due to variations in the solution ionic strength depends on the types of the polyelectrolytes and on the type of adopted salt as well. Dubas and Schlenoff observed completely different behavior for three different multilayer systems with respect to changes in thickness and surface roughness. While the poly(acrylic acid)/poly(diallyldimethylammonium chloride) (PAA/PDADMAC) multilayer film shows a strong swelling with increasing salt concentration, the (PSS/PDADMAC) multilayer swells slightly at a sodium chloride (NaCl) concentration above 1 mol/L (Figure 1.11. *Evolution of the absorbance at  $\lambda=217$  nm (maximum absorption for PSS) by visible UV spectrophotometry during the construction of (PDADMAC/PSS)<sub>n</sub> films at different molar concentrations of NaCl.* ). Below this concentration a slight shrinking of the (PSS/PDADMAC) multilayer is observed. The (PSS/PAH) multilayer is not sensitive to changes in NaCl concentration below 2 mol/L [44]. (PSS/PAH) capsules are also reported to be stable at even higher salt concentrations for several weeks.

At salt concentrations higher than 2 mol/L, the (PSS/PAH) films starts to swell and it is dissolved in NaCl of about 4 mol/L. The minimum NaCl concentration for multilayer decomposition depends on the type of polyelectrolyte and is about 0.3 mol/L for the (PAA/PDADMAC) and 2 mol/L for (PSS/PDADMAC). The minimum salt concentration that is required for decomposition increases with increasing polymer charge density and is slightly lower if the multilayer is exposed to a sodium bromide (NaBr) solution in comparison to NaCl solution [45]. The mobility of polyelectrolyte chains in PEM films can also be tuned after the adsorption process is finished. The diffusion coefficient shows the same dependence on ionic strength as during the preparation. Moreover, ions with a smaller hydration shell, i.e. larger polarizability, are more efficient. The diffusion coefficient increases by about one order of magnitude when NaCl is replaced by NaBr in the outer solution. This is due to the stronger interaction between Br ions and the polycation as compared to interactions with NaCl. The mobility of polyelectrolyte chains in the multilayer increases with increasing salt concentration until the multilayer is destroyed. It is assumed that the salt ions compete with the oppositely charged polyelectrolytes and break the complexes. This might explain the observed annealing of the (PSS/PDADMAC) multilayer after exposure to salty water [46].

An increase in ionic strength generally reduces the Young modulus. (PSS/PDADMAC) capsules show a continuous softening with increasing NaCl concentration [47]. In contrast to this, the mechanical properties of hollow (PSS/PAH) capsules do not change significantly at a NaCl concentration below 3 mol/L. Above this NaCl concentration a drastic decrease in the elasticity modulus by a factor of 10 (*i.e.* a strong softening of the multilayer capsules) has been observed [48]. This can be explained by the very low mobility of the (PSS/PAH) matrix, which is attributed to the glassy character of this system.

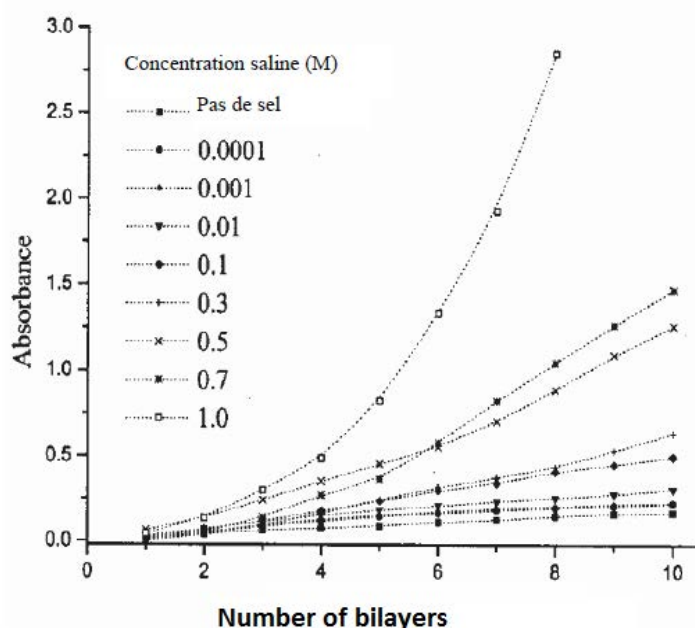


**Figure 1.11.** Evolution of the absorbance at  $\lambda=217$  nm (maximum absorption for PSS) by visible UV spectrophotometry during the construction of  $(PDADMAC/PSS)_n$  films at different molar concentrations of NaCl. [46]

### I.1.8.3. Buildup temperature

The buildup temperature also affects greatly the growth of the PEM films. Buscher et al. showed that for (PSS/PAH) multilayer films, the film thickness increases with the increase of the buildup temperature. In general, the temperature effect depends on the type of polyelectrolytes used [49]. This trend has been confirmed for the (PDADMA/PSS) (PDADMA=Polydiallyldimethylammonium) system where the thickness increases approximately linearly as a function of temperature in a range 10°C to 70°C. The proposed mechanism for this phenomenon is similar to that described for the ionic strength. At high temperatures, polyelectrolytes adopt a compact conformation, which explains the increase in

the thickness and roughness of the film. The effect of temperature is dependent on the type of polyelectrolyte used [50]. More recently, Salomäki et al. have shown that the change in temperature during the construction of (PDADMA/PSS) films induces a change in the growth pattern. At 45°C this film grows exponentially with the number of layers but when the temperature dropped to 25°C, the growth becomes linear (Figure 1.12. *The evolution of the growth of (PDADMA/PSS) films followed by QCM-D as a function of the temperature of the polyelectrolyte solution. The graph shows the increase in the imaginary part of the acoustic wave, represented by the increase in the mass of polyelectrolytes after each deposition step.* [51]. Other factors not detailed here,

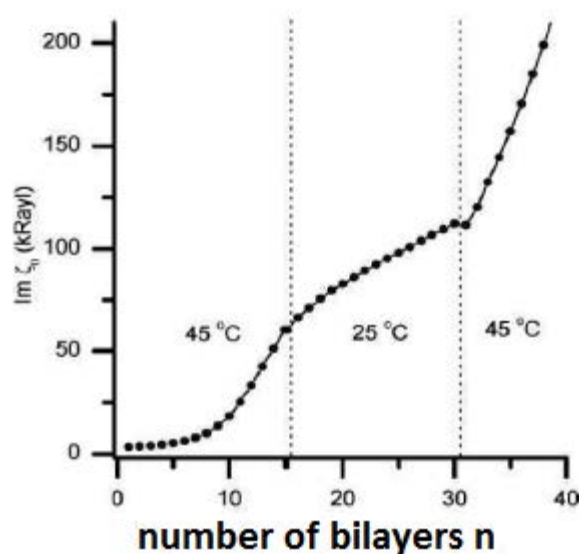


**Figure 1.12.** *The evolution of the growth of (PDADMA/PSS) films followed by QCM-D as a function of the temperature of the polyelectrolyte solution. The graph shows the increase in the imaginary part of the acoustic wave, represented by the increase in the mass of polyelectrolytes after each deposition step.* [51]

influence the growth of multilayer films as the concentration of polyelectrolyte, their molecular weight [52] and their deposition time [44].

#### I.1.8.4. Effect of salt anion on the film construction

Hofmeister was the first to investigate the effect of the nature of the salt anion on the conformation of macromolecules in 1888 [53]. He showed that the solubility of proteins (egg albumin) depends not only on the ionic strength of the electrolyte, but also on the nature of the anion of the electrolyte used. Proteins are usually poorly soluble in pure water. Their solubility in an aqueous solution depends on two antagonist effects illustrated in Figure 1.12.



Their solubility is strongly dependent on the salt concentration (ionic strength) of the medium. At moderate salt concentrations (green zone in Figure 1.12), an increase of the latter is accompanied by an increase in protein solubility. The hydrated salt ions screen by electrostatics the ionic charge of the proteins rendering them more hydrated because more and more of the well-hydrated inorganic ions (blue circles) are bound to the protein's surface, preventing aggregation of the molecules (*salting in*). At very high ionic strengths (pink zone), the salt ions compete with the proteins for hydration, the salt withdraws water from the proteins and thus leads to aggregation and precipitation of the molecules (*salting out*).

This allowed Hofmeister to classify anions according to their ability to precipitate proteins (salting out) in what is called “Hofmeister series” (Figure 1.13). Going from right to left, i.e. from the hydroxide ion ( $\text{OH}^-$ ) to the perchlorate ion ( $\text{ClO}_4^-$ ), the ability of the anion to precipitate a protein decreases [53]. The anions located at the right of the chloride ion ( $\text{Cl}^-$ ) are called cosmotropes. Cosmotropic anions are known for their high level of hydration which makes it difficult to interact with macromolecules. This leads to a decrease in the

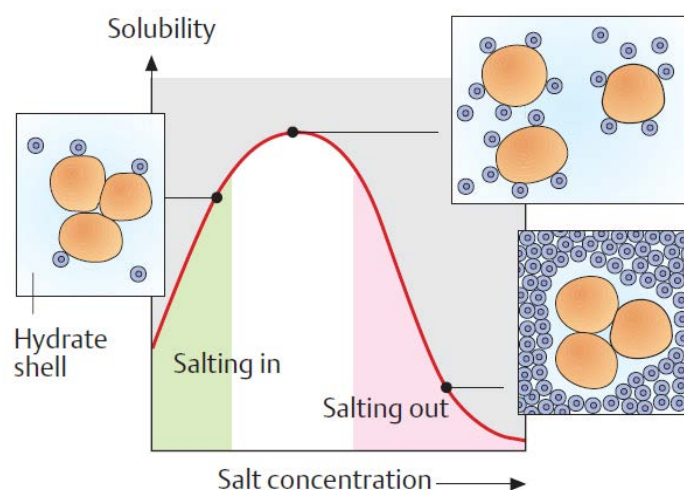


**Figure 1.13.** “Salting-in” and “salting-out” effects [226]

solubility of the macromolecule favoring the “salting-out” process.

The anions at the left of  $\text{Cl}^-$  ion in Hofmeister series are called chaotropic anions and are known for their low degree of hydration. When chaotropes interact with macromolecules, they can easily get rid of their hydration shell, thus favoring a strong interaction with the positively charged groups of the macromolecule. The liberated water allows the hydration of the macromolecule, thereby increasing its solubility.

In general, the Hofmeister effect of anions is greater than that of the cations [54]. With regard to systems of interest in this work, the less the salt ion hydration, the more significant is the interaction between the ions and polyelectrolytes.

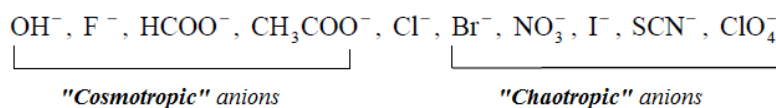


**Figure 1.14.** Hofmeister series of classification of some monovalent anions. From right to left, anions precipitate more proteins. [53]

Salomaki et al. investigated the effect of the salt anion on the growth of PEM films. They showed that the multilayer films growth regime of (PSS/PDADMA) changes from linear to exponential moving from a cosmotropic counterion to a chaotropic one. The thickness of the multilayer films built in various types of salts increase in the following order:  $\text{Li}^+ < \text{Na}^+ < \text{K}^+$  and  $\text{F}^- < \text{Cl}^- < \text{Br}^-$  (Figure 1.15.a) [44, 55, 56]. The films were much thicker when the two counterions of the polyelectrolytes were chaotropes. This is explained by the strong interaction of the chaotropic anions with the ionizable groups of the PDADMA chain, unlike the cosmotropic anions that are usually highly hydrated which makes them less prone to interact with polyelectrolytes chains. A similar study was conducted on (PAH/PSS) system. This multilayer film was shown to be twice thicker than in case of chaotropic ions. In both cases the linear growth of the film is maintained (Figure 1.15.b) [57].

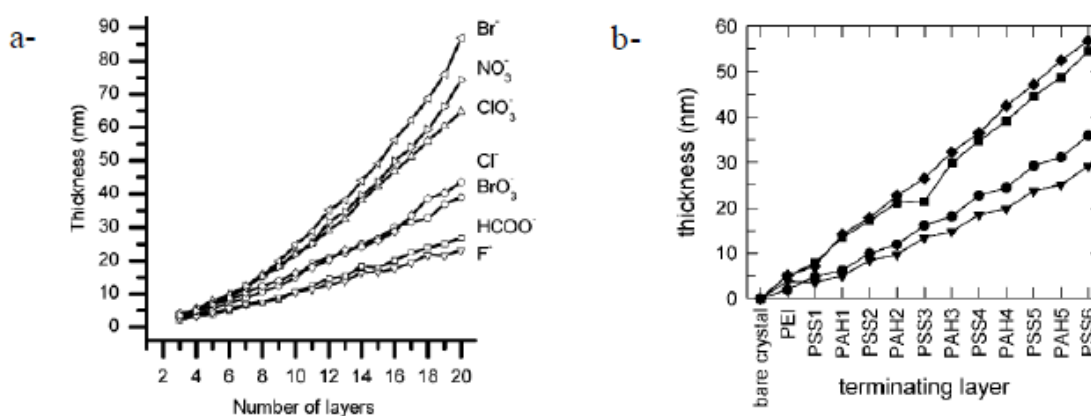


**Figure 1.15.** a) The thickness of (PDADMA/PSS) film measured by ellipsometry. (PDADMA/PSS) films are constructed in different sodium salts at 0.1 M. [55] b) The thickness of (PAH/PSS) followed by QCM-D. [57]

### **I.1.9. Mechanical properties of PEM films**

The knowledge of the mechanical properties of polyelectrolyte multilayer films is of primary importance for their applications, especially with regard to bacterial adhesion prevention as cells prefer to adsorb on “hard” materials. Mechanical properties are studied both at planar films and at PEM capsules. Measurements on planar films are commonly carried out with measuring the indentation of an AFM tip or colloidal probe within the films upon application of a given force (normal to the PEM surface). Capsules elasticity is usually evaluated by osmotic pressure measurements and AFM. In the case of (PSS/PAH) multilayers, both osmotic pressure studies and AFM measurements were carried out at capsules with resulting Young modulus in the range of 300-400 MPa [38, 48]. (PSS/PAH) multilayers are characterized by a Young modulus up to 100 MPa, which is of the same order of magnitude as the value for the capsules.

Hence, crude comparison between different experiments shows that neither the method nor the geometry has an effect on the value of the Young modulus for a given material composition. The relevance of the internal structure in determining the mechanical properties then becomes obvious, especially with respect to the water content. Dried films show a modulus of one to two orders of magnitude higher than their wet homologues. As an example, elasticity of dried (PSS/PAH) films is *ca.* 6 GPa [58] and for (PAA/PAH) about 10 GPa. Another important parameter is the polymer charge density. For instance, if (PAA/PAH) multilayers are prepared at intermediate pH values where both polyelectrolytes are charged, the chains are more or less stretched and the Young modulus is high (more than 10 GPa in the dry state). At lower charged densities (adjusted by pH) the chains are more coiled and can deform to accommodate the moving indenter AFM tip with greater ease. The Young modulus is then reduced to about 50% as compared to that of PEM with higher charge densities. The type of salt has also an effect on the mechanical properties of the multilayers even though opposite conclusion was drawn by Salomaki *et al.* from QCM studies. Multilayers with F ions were rather “rubber-like”, while films with Br are rather glassy. This difference is not clearly understood so far. Exponentially growing films are less structured and much more hydrated than linearly growing films. Therefore their Young moduli are much lower in general than for the linearly growing films. For instance, (HA/PLL) multilayers have only a young modulus in the order of several tens of kPa [34].

### **I.1.10. Water content in PEM films**

Mainly scattering experiments for evaluation of film thickness and polyelectrolyte density were conducted at the solid/air interface. Since polyelectrolyte layers are very sensitive to the water content in the neighboring environment, it is also necessary to conduct structural investigations at solid/liquid interfaces in order to address *in situ* the film internal structure. Employing X-rays at the solid/air and neutrons at the solid/liquid interface of (PSS/PAH) films to probe the structure of films built from bilayer pairs revealed differences between the freshly adsorbed part and the reswollen precursor part of the films at the solid/liquid interface. The analysis of neutron reflectivity data of the swollen film prior and after adsorption of 6 additional (PSS/PAH) bilayers strongly suggested a significantly increased amount of water and thus an increased scattering length density of the adsorbed part of the multilayer. A water volume fraction of 42% found inside the precursor film after moderate swelling (10%) upon exchange of the environment compared well with the value reported for a very similar multilayer examined in a saturated deuterium oxide  $D_2O$  atmosphere [22]. The water volume fraction inside the freshly adsorbed part was much higher. It was estimated to be 56%. This part of the multilayer shrunk upon drying by 50%. The thickness of polyelectrolyte films is further dependent on the amount of adsorbed water from the environment. Dehydration over phosphorus pentoxide ( $P_2O_5$ ) leads to shrinkage of films previously investigated in the ambient laboratory atmosphere due to the evaporation of water from the multilayer structure [59].

### **I.2. Polyelectrolyte multilayer films obtained by hydrogen bonding**

PEM films constructed with non-charged polymers and based on hydrogen bonding were largely studied in the 1990s. Rubner and coworkers had studied the polyelectrolyte system of polyaniline and a water soluble molecule such as poly(acrylamide). The film thickness increased linearly with the number of deposited layers [60].

### **I.3. Electrochemical properties of polyelectrolyte multilayers**

#### **I.3.1. Ion permeability of polyelectrolyte multilayers**

The LBL technique allows control of the net charge density of the film and also its ion permselectivity. Several studies showed that ion permeability of PEM is governed by many factors including deposition conditions, film composition and thickness, and amount of cross-linking in the film. Based on this, films can be highly permeable, selectively permeable, or nearly impermeable to ions. These factors that govern permeability in PEMs also offer a means to control the permeability of these films. This should allow tailoring of PEM for several applications. Studies in this area focus mainly on the movement of highly charged redox couples or redox-active species through PEM films.

Cyclic voltammetry experiments show that the first few layers of (PAH/PSS) and (PSS/PDADMA) film are highly permeable to redox-active species such as  $\text{Fe}(\text{CN})_6^{3-}$  and  $\text{Ru}(\text{NH}_3)_6^{3+}$  [26, 43]. Results of cyclic voltammograms of  $\text{Fe}(\text{CN})_6^{3-}$  at (PAH/PSS)-coated electrodes and of  $\text{Fe}(\text{CN})_6^{3-}$  at rotating disk electrodes coated with (PSS/PDADMA) are consistent with the fact that the first few bilayers on substrates generally have a different structure than layers deposited after the charge distribution of the polymer film is fully established [12]. The first few layers may not fully cover the electrode or they may swell and thus be more permeable. After deposition of four or five bilayers, the blocking ability of PEM films increases slowly with adsorption of additional layers [26]. Experiments were also carried to test the effect of the presence of an electrolyte on the permeability of PEM films. Electrodes coated with films prepared in the absence of salt gave a quasi-reversible  $\text{Fe}(\text{CN})_6^{3-}$  voltammogram with a peak current that was 80-fold larger than that obtained at electrodes coated with films prepared in the presence of salt (Figure 1.16) [43]. Those findings show that the permeability of PEM films can be simply controlled by varying the amount of electrolyte in the deposition solutions. The increased permeability in the absence of a supporting electrolyte is explained by the fact that the salt present during deposition is responsible for the screening of charges on the polyelectrolyte chains resulting in an intertwined structure with many loops and tails [61, 62] which is less permeable than structures in films prepared in the absence of salt.

It has been also shown that the concentration of supporting electrolyte present during electrochemical measurements affects transport of redox-active species through PEM films. Farhat and Schlenoff showed that at rotating-disk electrodes coated with (PDADMA/ PSS)

films, limiting currents increased with the ionic strength [26]. This is explained by the extrinsically charge-compensated sites in films occurring due to high concentrations of  $\text{Na}^+$  and  $\text{Cl}^-$  ions. The transport of  $\text{Fe}(\text{CN})_6^{4-}$  becomes easier by hopping between these sites. Increasing ionic strength might also affect transport by decreasing Donnan exclusion [63] and/or by swelling the film [64].

### I.3.2. Donnan potential in PEM films

The first electrochemical measurements have shown that membrane or Donnan potential differences present at the interface between polyelectrolyte coatings on electrodes and the electrolyte solutions in which they are in contact contribute to the formal potentials measured for redox couples incorporated in the coatings [65, 66]. Findings showed that the nature of the polyelectrolyte capping layer, the electrolyte pH, and ionic strength determine the apparent redox potential of the osmium couple in the film. Doblhofer *et al.* have shown that Donnan exclusion in the polyelectrolyte coatings exposed to electrolytic solutions results in a shift of the apparent formal potentials with electrolyte concentration [67]. The interior of a swollen polymer coating may consist of Donnan domains where counterions are confined by electrostatic forces and regions filled by supporting electrolyte. Organized layer-by-layer polyelectrolytes containing redox groups are therefore attractive for studying the effect of

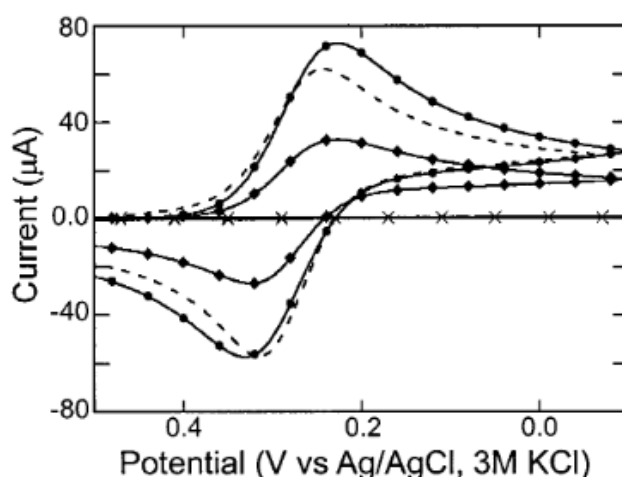


**Figure 1.16.** Cyclic voltammograms ( $\text{Fe}(\text{CN})_6^{3-}$  at 0.005 M, pH=6.3) at a gold electrodes coated with a (●) (PAH/PSS)<sub>20</sub> prepared with no supporting salt (thickness of 16 nm); (dotted line) (PAH/PAA)<sub>5</sub> film prepared with supporting salt (thickness of 44 nm); (◆) (PAH/PAA)<sub>9</sub> film prepared with no supporting salt (thickness of 15 nm); (×) (PAH/PSS)<sub>4</sub> film prepared with supporting salt (thickness of 15 nm). [43]

Donnan potential on the redox potential shift as a function of the membrane surface charge and the mobile charge in solution.

The Donnan potential ( $\Delta\Phi_D$ ) was determined from the apparent redox potential of a bare electrode ( $E^0$ ) and the obtained apparent redox potential of the constructed film on the electrode ( $E_{1/2}$ ) according to the equation,

$$E_{1/2} = E^0 + \Delta\Phi_D \quad (1.1)$$

Calvo and coworkers studied the Donnan potential of films constructed from PAH carrying osmium bipyridine groups (PAH – Os) and PVS by cyclic voltammetry. The evolution of the Donnan potential of the redox couple Os(II)/Os(III) was studied as a

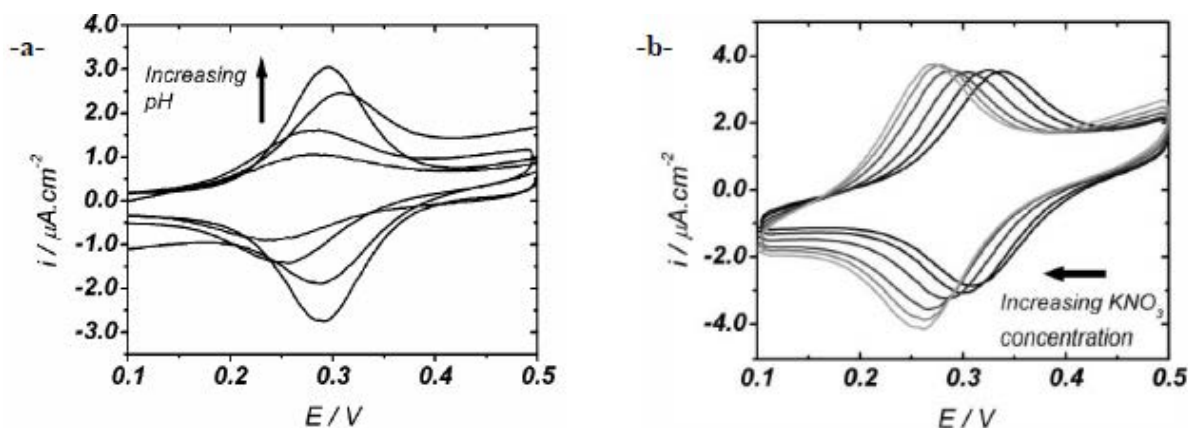


**Figure 1.17.** Cyclic voltammograms measured at a gold electrode coated with a (PAH – Os/PVS)<sub>4</sub> – PAH – Os constructed under different conditions. (a) Films constructed at different pH of polyelectrolyte solutions (3.5, 5.5, 7.3, 8.3) and measured at pH 7.3 (0.2 M of KNO<sub>3</sub>). (b) Construction of the films at neutral pH and different ionic strengths of polyelectrolyte solutions (8, 40, 137, 481, 932, and 1500 mM of KNO<sub>3</sub>). [227]

function of pH of the polyelectrolyte solutions, and as a function of ionic strength of the solution used in the film buildup [68, 69]. The studied system consisted of a strong polyelectrolyte (PVS) and a weak one (PAH – Os). The fixed charges are given by the PAH – Os (pH dependent) and PSS or PVS (pH independent) charge density in the polyion segments. When the pH of the solution increases, the charge density of PAH – Os decrease due to the protonation of the NH<sub>3</sub><sup>+</sup> groups of the polyelectrolyte chain, and the chain adopts an intertwined conformation with many loops due to the reduction of the intra-chains repulsion of NH<sub>3</sub><sup>+</sup> and thus the polyelectrolyte adsorption occurs more significantly than in

the case where the chain adopts a linear conformation. Beside this, when the ionic strength of the solution increases, the screening of the ionic charges of the two polyelectrolytes by the salt ions increase and this induces the appearance of two distinct compartments in the voltammograms provided in Figure 1.17. The redox potential dependence on electrolyte ionic strength can be described by Donnan exclusion driven by the fixed charge of polyions in the film.

#### **I.4. Applications of PEM films**

The large versatility of PEM films in terms of properties, as governed by the buildup conditions, allows them to be used in many different domains. In the biotechnology domain, PEM films are promising tools to functionalize surfaces and modify surfaces properties. Tissue reparation and recovery of biomaterial surfaces by functionalized films as in the case of prostheses and dental implants is reported [70]. Other applications include self-healing anticorrosion coatings [71] or antibacterial fibers [72]. Moreover, optic applications such as contact lens coatings, that can increase the durability of contact lenses, are also reported [73]. In drug delivery, polyelectrolyte multilayer hollow capsules showed to have potential applications in drug delivery for the controlled release of bioactive molecules that can be further transported and liberated in the body under proper conditions (pH, salt, and oxidation) [74, 75, 76]. Also, the LBL technique allows the fabrication of elastic conductor films called Metal Rubber (NanoSonic Inc, Blacksburg, Virginie) that have resistance to high temperatures (up to 160°C). Polyelectrolyte films constructed from electrochemical materials that can reversibly change color upon oxidation or reduction processes are used as electrochemical detectors [77]. Humidity detectors [78] and chemical detectors [79, 80] are reported applications as well. In solar cells, PEMs were used as luminescent materials [81]. Multilayer thin films of conjugated polymer, semiconductor nanoparticles and dyes have found applications in electronics and photonics. Future electronic components can be constructed based on conductor PEM films of polyions and with conjugated polymers for the fabrication of Light-emitting diodes (LEDs) [82] and transistors [83] or semiconductor nanoparticles (thiol-capped CdSe CdTe) [84]. Other applications include the use as biosensors [85, 86], and enzyme immobilization [87, 88]. Additional potential applications are separation membranes [89, 90, 91], chromatography columns [92], high charge density batteries [93] and antireflection surfaces [94]. Recent studies have also proven that PEM can



be used as nanofilters for biomolecules and metal nanoparticles from aqueous solutions [95, 96] which is promising in terms of environmental applications of PEM films.

### **I.5. Incorporation of Nanoparticles and Biomolecules into PEM Films**

Earlier attempts to incorporate molecules and particles into PEM films were based on the incorporation during the film buildup itself. We hereby mention the loading of particles and molecules by postdiffusion into already prepared multilayer films. Results showed that factors affecting the incorporation of nanoparticles and biomolecules in PEM films includes internal structure of the film and its ability to swell upon incorporation of charged or uncharged species, size and shape of the colloidal particles to be incorporated in the film, charge density and charge distribution within the film, and the influence of external parameters like the ionic strength, pH and temperature of the solution containing the nanoparticles and the concentration of the nanoparticles in the solution plays a role as well.

#### **I.5.1. Incorporation of bioactive molecules and ions**

Several studies showed that PEMs of weak polyelectrolytes are viable systems for the controlled loading and release of small hydrophilic molecules. (PAH/HA)<sub>10</sub> multilayer films were loaded by two water-soluble dyes; the cationic dye Indoline Blue and the anionic dye Chromotrope 2R [97]. The incorporation of the two molecules into (PAH/HA)<sub>10</sub> multilayer films and their release from the films showed a strong dependence on solution pH. The maximum loading was achieved under pH conditions that resulted in the largest electrostatic attraction between the dye molecules and the film, while the release of the molecules from the films was achieved when repulsive forces between the dye molecules and the films were dominant. It was shown also that the swelling of the film helped to facilitate the release of the dye molecules by transporting counterions into the film to screen the electrostatic interactions and also by creating pores through which the molecules can travel. One of the most interesting findings in this study is that it is possible to trap the small molecules in the film at a certain solution pH and to release the trapped molecules simply by changing the pH. So the reversible loading is controlled by a complex interplay between the physico-chemical properties of the films and of the loaded molecules.

Another study highlighted the ability to use films constructed with amphiphilic polysaccharides as hydrophobic nanoreservoirs to trap small hydrophobic molecules [98].

The loading and release behavior of polyelectrolyte multilayers based on hydrophobically modified carboxymethylpullulan derivatives ( $\text{CMP} - x\text{C}_{10}$ ) and poly(ethyleneimine) (PEI) denoted by  $(\text{PEI}/\text{CMP} - x\text{C}_{10})_n$  toward a hydrophobic dye (Nile Red) was studied. Two layer films  $(\text{PEI}/\text{CMP} - 14\text{C}_{10})_2$  of 85 Å thicknesses used for the loading experiments did not show a significant variation in thickness after being dipped in the dye solution. UV results showed that the amount of dye loaded into the film increases with the immersion time till reaching a plateau which corresponds to the maximal amount of the dye which can be loaded into the film. Loading experiments performed with thicker films  $(\text{PEI}/\text{CMP} - 14\text{C}_{10})_3$  of 206 Å showed a slower diffusion of the dye into the film revealing that the higher the film thickness, the longer is the time to reach the saturation level. Moreover, the loading and the release behavior of the films was analysed as a function of the amount of hydrophobic decyl chains grafted on the polysaccharide *i.e.* using  $(\text{PEI}/\text{CMP} - x\text{C}_{10})_n$  multilayers with  $x$  varying from 2% to 18%. The tunable hydrophobicity of the polysaccharides making up the film proved to be a convenient way to control the number of hydrophobic dye molecules trapped in the films and consequently their loading capacity. No detectable absorption of the dye was registered for film with  $\text{CMP} - 2\text{C}_{10}$  even after an immersion time of several days while the higher the grafting degrees ( $x$ ) was, the more efficient was the loading. The study also focused on the release behavior of the trapped molecules as a function of pH and nature of the salts present in the buffer. The maximum release occurred at a pH close to the  $\text{pK}_a$  of the CMP derivative. The accelerated release of the dye molecules was attributed to the formation of pores within the films due to the weakened electrostatic bonds between polyelectrolytes resulting from the change in the number of effective (pH-dependent) charges on the weak polyelectrolyte chains. The addition of two different salts, potassium thiocyanate (KSCN) and NaCl, in the dipping solution also affected the release behavior of the loaded films. Much larger dye release was obtained with KSCN which is due to the chaotropic nature of this salt that promotes a significant disruption of hydrophobic domains of the film. Thus, the addition of a chaotropic salt could be used to release efficiently an active hydrophobic component from such films.

Further studies demonstrated the use of PEM films as reservoirs for the irreversible loading of bioactive molecules or drugs. Vodouhê and coworkers proved that polylysine/hyaluronic acid multilayer films  $(\text{PLL}/\text{HA})_n$  can act as a reservoir for an antiproliferative drug, paclitaxel (commercially known as Taxol) which is one of the most

potent chemotherapeutic molecules in the treatment of breast and ovarian cancers [99]. The drug was adsorbed overnight at adequate concentration on  $(\text{PLL}/\text{HA})_n$  films with  $n=30$  and  $n=60$  followed by the deposition of  $(\text{PSS}/\text{PAH})$  multilayers capping on the top of  $(\text{PLL}/\text{HA})$  films. Confocal laser scanning microscopy (CLSM) images (Figure 1.18.A) revealed that the fluorescently labeled drug is homogeneously distributed over the whole film thickness ( $\approx 12\ \mu\text{m}$  for 60 bilayers). The fluorescence intensity remained constant after storing the film for four days at ambient temperature in  $\text{NaCl}$   $0.15\ \text{M}$  at  $\text{pH}=6.5$  which indicates that no or very low passive release occurs in a short time span. When human colonic adenocarcinoma cells HT29 were seeded on the films, paclitaxel embedded in the capped multilayer films induced a 45% decrease in cell activity at 24 h and thus strongly affects cell viability (Figure 1.18.C).

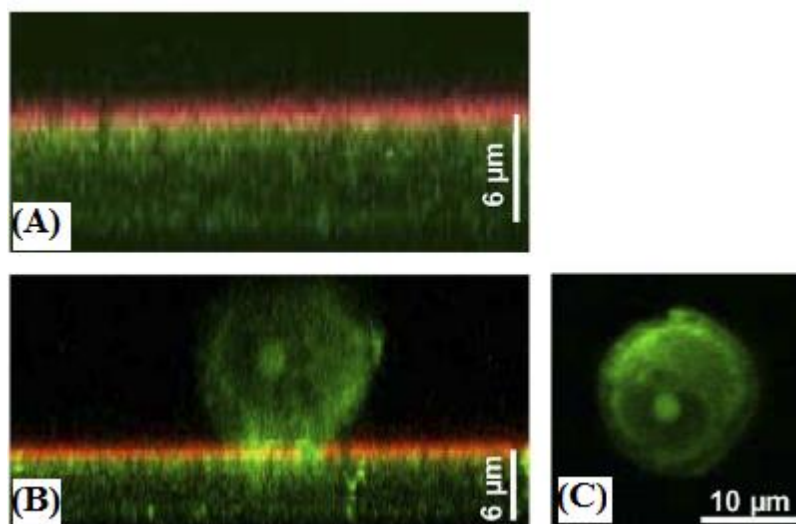


**Figure 1.18.** Confocal laser scanning (CLSM) images (A)  $(\text{PLL}/\text{HA})_{30}/\text{paclitaxel}^{\text{Green 488}}/\text{PSS}^{\text{MRho}}/\text{PAH}^{\text{MRho}}/\text{PSS}^{\text{MRho}}$  film section, (B), HT29 cell section 24 h after seeding on a  $(\text{PLL}/\text{HA})_{30}/\text{paclitaxel}^{\text{Green 488}}/\text{PSS}^{\text{MRho}}/\text{PAH}^{\text{MRho}}/\text{PSS}^{\text{MRho}}$  film and (C), top view (x,y) of the same cell. [99]

Along the same lines, Kittitheeranun and coworkers tested the reversible loading of PEM films with a lipophilic drug. Poly(diallyldimethyl-ammonium chloride) and poly(4-styrene sulfonate, sodium salt) multilayer films  $(\text{PSS}/\text{PDADMAC})$  deposited onto a quartz slide were used as a host matrix for the loading of 1,7-bis-(4-hydroxy-3-methoxyphenyl)-1,6-heptadiene-2,5-dione or curcumin, a lipophilic model drug [100]. Curcumin was loaded by dipping the PEM film into a dilute solution of curcumin dispersed in an 80/20% v/v water/ethanol solution. Results showed that the loading of curcumin occurs through a bulk

process where the amount and dose of curcumin loaded into the film could be controlled by changing the number of deposited layers (10, 20, 30, 40, 50, and 60) (Figure 1.19). More significant amounts of curcumin could be loaded into the multilayer film with increasing the number of layers, and up to  $8\mu\text{g}/\text{cm}^2$  of curcumin could be loaded into a 20-layer film. These results demonstrate that the loading of lipophilic curcumin in PEM thin films is done through a partitioning mechanism and that the PSS – PDADMAC film can be used as a loading matrix for lipophilic drugs. The loading was independent of the top layer, and the solvent quality was found to control the loading mechanism. Overall, this study has shown that PDADMAC – PSS thin films are a promising matrix for incorporating curcumin and other hydrophobic drugs, which could be of interest in drug-delivery applications.

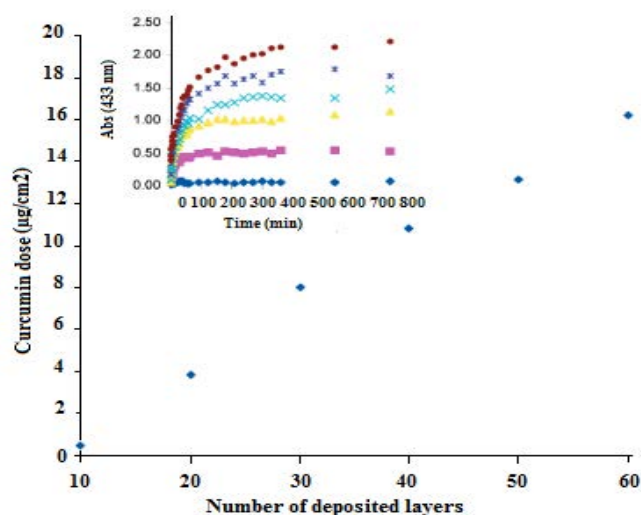


**Figure 1.19.** UV-vis absorbance of curcumin loaded into PEM thin films with an increasing number of deposited layers as a function of time. [100]

Other researchers focused on the incorporation kinetics of small molecules like polyoxometalates (POMs), polyatomic ions consisting of three or more transition metaloxyanions, into PEM films [101]. The exponentially growing  $(\text{PLL} - \text{HA})_n$  PEM films were loaded by  $\text{Na}_{33}\text{H}_7[\text{P}_8\text{W}_{48}\text{O}_{184}] \cdot 92\text{H}_2\text{O}$  denoted by  $\text{P}_8\text{W}_{48}$ . The PEM film was brought in contact with the  $\text{P}_8\text{W}_{48}$  solution at different concentrations allowing its passive diffusion into the film. Results showed that the diffusion kinetics were extremely slow (Figure 1.20), however, the  $\text{P}_8\text{W}_{48}$  loaded into the films do not desorb when the films are in contact with buffer solution. UV visible spectroscopy (UV-vis) and cyclic voltammetry (CV) results suggested that the films were homogeneously filled with  $\text{P}_8\text{W}_{48}$  after loading. It was shown also that the  $\text{P}_8\text{W}_{48}$  concentration loaded in the  $(\text{PLL} - \text{HA})_n$  film is a non-monotonous

function of the bulk  $P_8W_{48}$  concentration used to load the film *i.e.* a maximum in the amount of  $P_8W_{48}$  loaded into the film was found upon varying its concentration in solution (Figure 1.20). Beside the possible applications of POM-loaded PEM films as electrochromic and photochromic materials, findings of this study suggested that exponentially growing PEM are very promising due to their permeability to ions and colloidal nanoparticles [95].

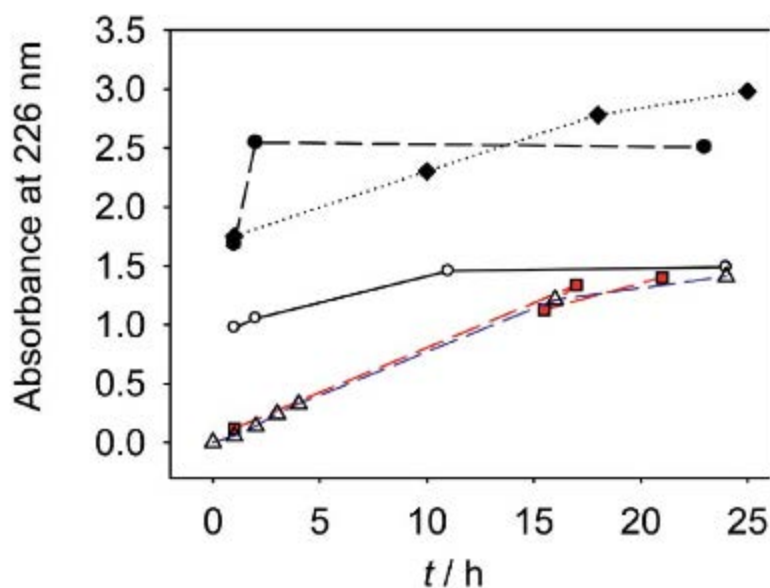


**Figure 1.20.** Permeation kinetics of  $P_8W_{48}$  in PEI – (PLL/HA)<sub>9</sub>/HA films followed by UV/Vis spectroscopy as a function of the concentration in the solution:  $\Delta$   $1.2 \times 10^{-6}$ ,  $\blacksquare$   $2.4 \times 10^{-6}$ ,  $\bullet$   $1.2 \times 10^{-5}$ ,  $\blacklozenge$   $2.4 \times 10^{-5}$ ,  $\circ$   $1.2 \times 10^{-4}$ . The lines are only aimed to guide the eye. [101]

### 1.5.2. Incorporation of Nanocolloids

Srivastava and coworkers focused on the loading of exponentially growing LBL films with rod-like nanocolloids such as single walled carbon nanotubes (SWNTs) and nanowires (NWs) [102]. Findings showed that loading of SWNTs in the already prepared (PDADMAC/PAA)<sub>n</sub> films is possible (Figure 1.22), and moreover, SWNTs display a high internal mobility resulting in deep spontaneous penetration into the matrix of the films. The study also revealed that SWNT properties remain stable even after infusion in the films. Scanning electron microscopy images (SEM) for (P A MA C/PAA)<sub>2</sub> films cross-sections revealed a clear morphological change before and after loading with negatively charged SWNT at pH=4.8

with a sequential increase in the penetration of SWNT in the films with increasing the loading time (from 1-2  $\mu\text{m}$  after 6 h, to 20-25  $\mu\text{m}$  after 7 days). In contrast, loading experiments with positively charged SWNTs showed no evidence of incorporation within the films. For more rigid CdTe and Te NW, no deep penetration occurred and hedgehog morphology of the film can be seen in the film surface with NW sticking out from the polyelectrolyte matrix (Figure 1.22). As a conclusion of this study, molecular rigidity and surface charge of nanocolloids appear to be key parameters controlling their loading into the exponential PEM films. The study also suggested that the findings will accelerate preparation of LBL films of nanotubes and that the dynamic nature of the films combined with unique SWNTs properties will lead to new type of smart materials. Moreover, the ability of exponentially growing (PDADMAC/PAA) films to host nanocolloids, due to the increased mobility of the polymer chains in the film mentioned elsewhere, opens the possibility for loading such films with other types of colloids and nanoparticles.

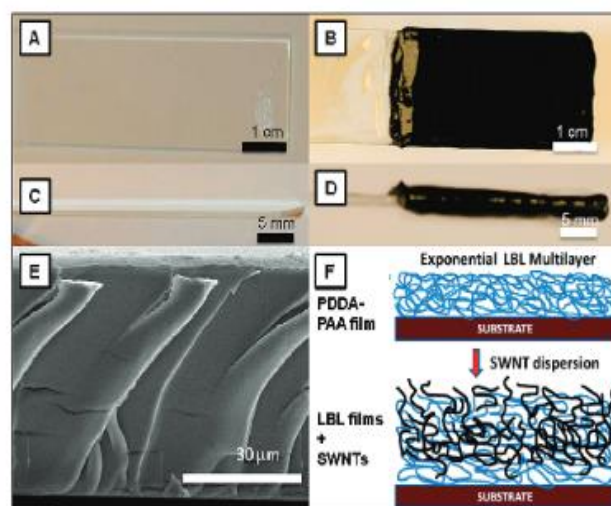


**Figure 1.21.** (A) *PDDA – PAA* film on a glass substrate (B) Film loaded with negatively charged SWNTs for 1 day. (C) Side view of *PDDA – PAA* coated glass slide. (D) Side-view of swollen *PDDA – PAA* film loaded with negatively charged SWNTs. (E) Cross-section of the *(PDDA – PAA)*<sub>200</sub> film (F) Schematics of incorporation of SWNTs in the films. [103]

Sorrenti et al. investigated the influence of the nature of the top layer (or outermost layer) of PEMs, the ionic strength of the solution, and the nature of the polyanion present in the film (PGA vs. HA) on the ability of a molecule (differing in its charge) to incorporate in and to be released from PEMs [103]. Two different copper (II) phtalocyanines differing in their charged groups (sulfonato versus pyridino) were incorporated in exponentially growing

PEM films made of poly-L-lysine (PLL) as the polycation and from poly-L-glutamic acid (PGA) as the polyanion or from PLL and sodium hyaluronate as a polyanion (HA). Results showed a marked preferential incorporation of the anionic CuPc – SO<sub>4</sub> over the cationic CuPc – Py.

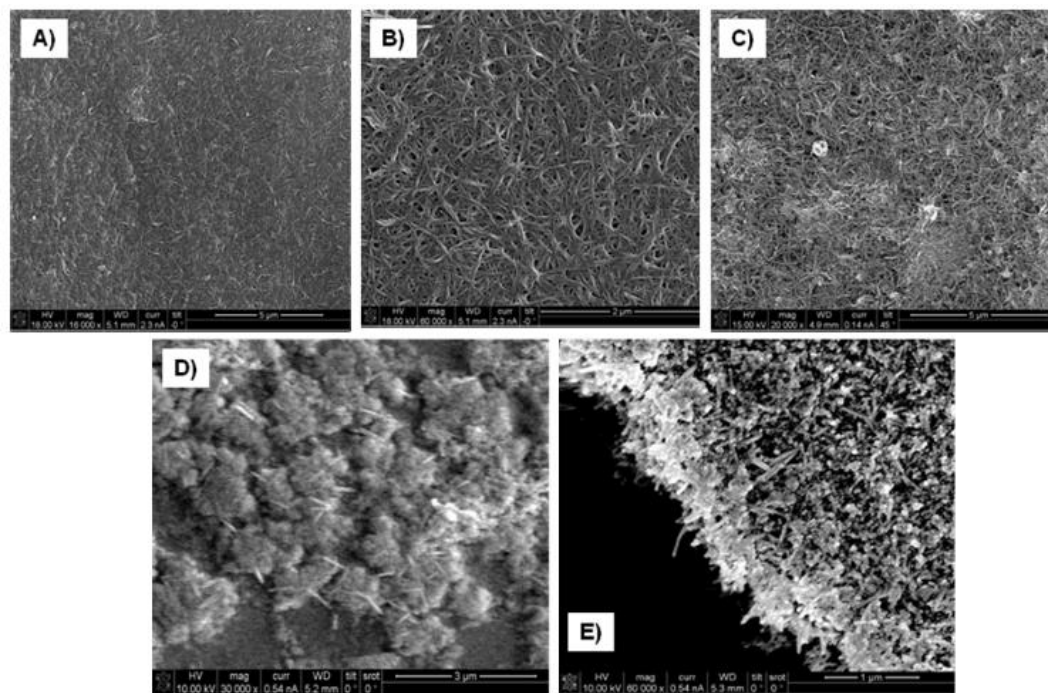


**Figure 1.22.** (A) Top view of (PDADMAC/PAA)<sub>200</sub> film infused with negatively charged SWNT (B) Zoom-in image for negatively charged SWNT (C) Top view of LBL film infused with multi-walled carbon nanotubes. (D), (E) Top view of LBL film infused with CdTe and Te NWs. The NW samples did not show any swelling and incorporation inside the films. [103]

In addition, ATR-IR data (Figure 1.23) revealed that the incorporation of CuPc – SO<sub>4</sub> particles affected the structure of the films deposited in water. ATR-IR spectra showed a decrease in the intensity of the COO stretching band which can be attributed to a small desorption of PGA, whereas for films deposited in Tris-NaCl buffer no such decrease in the COO stretching band was found. Overall results showed that exponentially growing PEMs having a positive Donnan potential can be used to incorporate negatively charged copper phthalocyanines at very high concentrations, whereas the positively charged counterparts were totally excluded. In addition, results showed that the negatively charged phthalocyanines are not homogeneously incorporated through the whole thickness of the PEMs. These results are in line with those obtained for negatively and positively capped CdTe nanocrystals. This



finding illustrates the possibility to use such films as a means to depollute water from waste dyes in the textile industry.

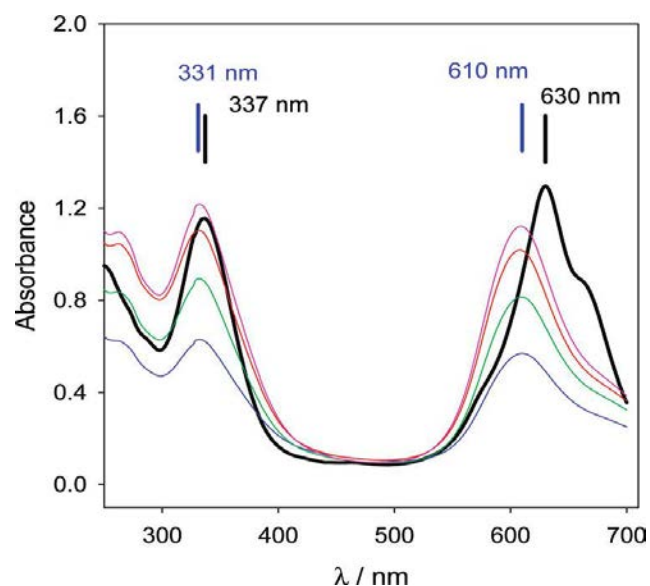


**Figure 1.23.** Absorption spectra of  $\text{CuPc} - \text{SO}_4$  at  $5 \times 10^{-4} \text{ M}$  in the Tris-NaCl buffer (black line) and of a PEI-(PGA/PLL)<sub>10</sub> films put in contact with a  $10^{-3} \text{ M}$   $\text{CuPc} - \text{SO}_4$  containing buffer after 15 (blue line), 60 (green line), 120 (red line), and 180 (pink line) min of contact with the film. The vertical lines indicate the positions of the peak maxima for the Soret and Q bands in the solution state (black vertical lines) and in the film state (blue vertical lines). The PEI-(PGA/PLL)<sub>10</sub> films were deposited from polyelectrolyte solutions in the presence of Tris-NaCl buffer. [103]

### I.5.3. Incorporation of proteins and peptides

Salloum and Schlenoff [104] showed that proteins such as Bovine serum albumin (BSA), fibrinogen, and lysozyme, are able not only to adsorb on the surface of PEM films but also to diffuse in their bulk. FTIR, Uv-vis spectroscopy, and AFM results showed that BSA dissolved in a solution in contact with (PDADMAC/PSS)<sub>n</sub> film, was able to diffuse down to the substrate/film interface. It was also found that a protein bearing a particular charge diffuses through films bearing an opposite surface charge. In like- charged films and proteins systems, AFM revealed islands of aggregates appearing on film surface. In addition, film thickness was shown to play an important role in the adsorption process of oppositely charged surfaces because the films can act as a “sponge” to load proteins, an alternative to protein/polyelectrolyte layer-by-layer assembly. It was possible also to control the release of the protein from the polymeric matrix by changing the ionic strength of the solution.

Ladhari et al. studied the loading and release kinetics of insulin, a peptide hormone indispensable for the treatment of Type 2 diabetes, into (PDADMAC/PAA)<sub>n</sub> multilayer films



[96]. The loading kinetics was studied by immersing PEM films in insulin solutions for different periods of time (2, 14 and 24 h). CLSM revealed that insulin-FITC could diffuse gradually inside the film with a larger concentration in the upper part of the film (after 2 and 14 h in contact with the polypeptide solution), and then in the whole film (after 24 h) from a solution at pH 4.3 (below insulin's isoelectric point, insulin is positively charged at this pH). Environmental scanning electron microscopy (ESEM) and AFM results showed that the loading is accompanied by a swelling of the film from  $4.2 \pm .5 \mu\text{m}$  for native films to  $5.7 \pm .5 \mu\text{m}$  after 24 h loading). In contrast, at pH=8.3 where insulin is negatively charged, CLSM observations showed little incorporation of insulin in the film with more intense fluorescence signal at film/solution interfaces. Thus, the effect of the surface charge of the film mainly determined by the outermost layer (top layer) confirms findings by Salloum *et al.* [104]. Little incorporation occurs when insulin carries the same charge as the outermost negatively charged layer of PAA. The release kinetics was investigated by ATR-FTIR spectroscopy. Results revealed that no insulin release occurred for (PDADMAC/PAA)<sub>15</sub> in distilled water while a slow unloading occurred in a NaCl 0.15 M solution (salinity close to physiological serum). This study could open the route for a new way of insulin delivery.

#### **I.5.4. Loading with Multivalent ions**

The work of Hübsch *et al.* proposed that the interactions between multivalent ions and exponentially growing multilayer films is a more complex process than expected at first sight [105]. Results showed that for exponentially growing (PGA/PAH)<sub>n</sub> multilayer films, the multivalent ferrocyanide anions can diffuse through the whole film regardless of the nature of the last deposited layer. However, the ions were only released when the films were in contact with a PAH or a PGA solution and not in an aqueous solution devoid of ions. The diffusion of the two polyelectrolytes into the multilayer liberates the ferrocyanide ions from the film into the solution. When the films were brought into contact with PGA solution, the PGA chains diffused into the films replacing the ferrocyanide ions leading to their liberation. When the films were in contact with the PAH solution, the PAH chains did not diffuse into the films to replace the ions, it rather stayed at the film/solution interface strongly interacting with the ferrocyanide ions and thus inducing their release out of the films playing the role of a sink for these ions. This shows that polyelectrolyte multilayers must be seen as dynamic entities where diffusion and exchange processes can take place.

### 1.5.5. Loading of nanoparticles in PEM films

The first work introducing the reliability of the concept of loading PEM films with nanoparticles was performed with the exponentially growing (PDDA/PAA) films by Srivastava and coworkers [95]. This study showed the possibility of loading and unloading exponentially growing PEM films with NPs by simple diffusion and thus introducing the use of PEM films as carriers of nanoparticles for biological, optoelectronic, and environmental applications. The (PDDA/PAA) films were constructed from poly-(diallyldimethylammonium chloride) (PDDA) and from poly-(acrylic acid) (PAA) and were loaded with Cadmium telluride (CdTe) nanoparticles capped either with thioglycolic acid (NP1) or 2-(dimethylamino) ethanethiol (NP2) (Figure 1.24). The reversible loading of NPs was investigated with UV-vis studies and then confirmed by confocal microscopy (Figure 1.25). Results showed a homogeneous loading of the NPs throughout the films thickness.

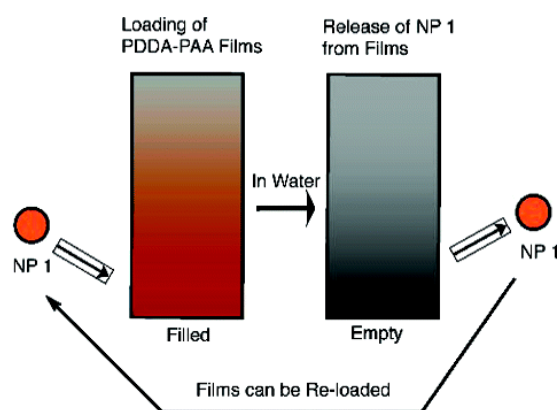


**Figure 1.24.** Schematic representation of the reversible loading of  $(\text{PDDA/PAA})_n$  PEM films with NPs. [95]

For the negatively charged nanoparticles NP1, the concentration of the entrapped particles was much higher (20-22% by weight) than that for NP2 (7-8% by weight). The release kinetics was studied at pH 9 and 7 and for films capped with linearly growing  $(\text{PDDA/PSS})_{10}$  layers. At pH 9 the amount of released NP1 was at least 2 orders of magnitude (60-70% by weight) higher than at pH 7 and a total particle retention in the film was reached by capping the film with impermeable  $(\text{PDDA/PSS})_{10}$  layers. The overall obtained results marked that the reversible loading of NPs in exponentially growing thick PEM films is governed by the variations of the structure of the multilayers (top layer or

capping), the nature of the incorporated NPs (mainly the NPs charge), and the pH of the medium.

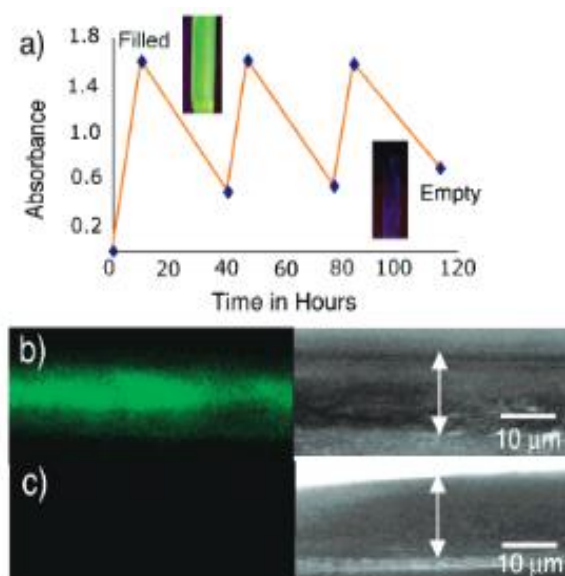


**Figure 1.25.** (a) Loading and unloading of (PDDA/PAA)<sub>45</sub> films (pH 9) with green fluorescence-emitting NP<sub>I</sub> as followed by UV-vis absorbance at 530 nm. The insets are fluorescence photographs of the filled (top) and empty (bottom) films. (b) Confocal microscopy images of (PDDA/PAA)<sub>100</sub> films loaded by 6h of exposure to NP<sub>I</sub> solution and (c) empty films after 24h exposure at pH 9. The right panels show white light images. [95]

Another study focused on the loading of the exponentially growing (PDDA – PAA)<sub>30</sub> LBL films with silver NPs (AgNPs) of diameter  $\approx 5\text{nm}$  [106]. The aim of this study was to fabricate a universal Surface-enhanced Raman scattering (SERS) sensor, which would combine a high density of NPs inside a polymeric matrix, based on PEM films loaded with AgNPs. The PEM films were first pretreated by immersing in an aqueous solution of sodium citrate (1%) for 12h in order to stabilize the PDDA inside the film and to prevent its free diffusion and thus to allow the correct organization of NPs and their successful packing along PDDA chains. The pretreated films were then immersed in an aqueous dispersion of AgNPs. NPs incorporation within the film was monitored by UV/Vis spectroscopy. Figure 1.26 shows the increase in the intensity of the silver localized surface plasmon resonance (LSPR) band with the increase of the loading time during which more silver particles diffuse into the films. The LSPR, centered at 434 nm, continuously grows until saturation of the spectrometer detector with the increase of contact time. The color change of the films from white to dark

yellow-orange after 24h of contact assures the incorporation of the NPs within the films (Figure 1.26). Other films with larger thickness (54 and 100 bilayers) were also successfully loaded with AgNPs, but the best results so far were consistently obtained with (PDDA/PAA)<sub>30</sub>.

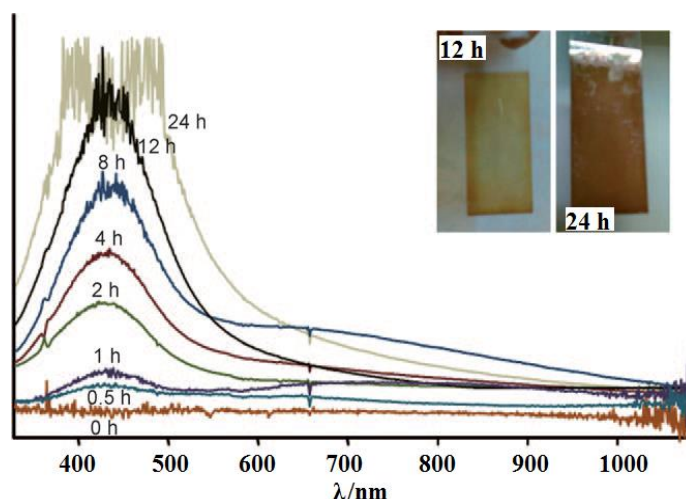


**Figure 1.26.** UV-vis spectra of e-LBL AgNP films as a function of immersion time of the e-LBL film in a silver colloid dispersion. Inset: digital photographs of films after 12 and 24h immersion. [106]

## II. Electrokinetic Investigations of Nanodendrimers

### *Basics of electric double Layer*

When an object is suspended in an electrolyte, the surface groups ionize, leading to the surface becoming charged and surrounded by a cloud of counterions from the bulk called the electric double layer (EDL).

Helmholtz first introduced the concept of the existence of the double layer [107] at the surface of a metal in contact with an electrolyte appeared in 1879. That first theoretical model assumed the presence of a compact layer of ions in contact with the charged metal surface. Gouy and Chapman [108] developed a model involving a diffuse double layer in which the accumulated ions, due to the Boltzmann distribution, extend to some distance from the solid surface. Later, Stern suggested that the electrified solid-liquid interface includes both the rigid

Helmholtz layer and the diffuse layer of Gouy and Chapman [108]. Specific adsorption of ions at the metal surface was pointed out by Graham in 1947 [109].

EDL is composed of two distinct layers: a fixed layer called Stern layer, composed of counterions strongly adsorbed on to the surface, and another slightly mobile layer called Diffuse layer composed of mixture of coions and counterions. The ions in Diffuse layer can move under tangential stress since they are not strongly adsorbed to the Stern layer. The double layer is formed in order to neutralize the charged surface and, in turn, causes an electrokinetic potential between the surface and any point in the bulk fluid. This voltage difference is on the order of millivolts and is referred to as the Surface potential. The magnitude of the surface potential is related to the surface charge and the thickness of the double layer [110].

As we leave the surface, the potential drops off roughly linearly in the Stern layer and then exponentially through the diffuse layer, approaching zero at the imaginary boundary of the double layer. The potential curve is useful because it indicates the strength of the electrical force between particles and the distance at which this force comes into play (Figure 1.27).

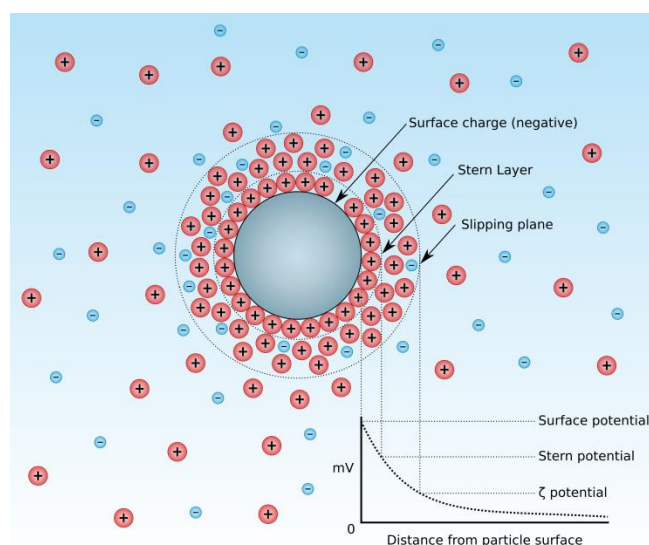


**Figure 1.27.** Schematic representation of the EDL around a solid particle

The plane separating the diffuse layer and the Stern layer is called Slipping plane and electric potential at this plane is called Zeta Potential  $\zeta$ . This potential relates to the mobility of the particle. Although zeta potential is an intermediate value, it is sometimes considered to

be more significant than surface potential as far as electrostatic repulsion is concerned. The characteristic thickness of EDL is called Debye length,

Determining the value of the charge is, however, of great importance for understanding and predicting the behavior of such particles, and systems consisting of them. Electrophoresis is a powerful tool to indirectly measure this quantity. The technique is based on the application of an electric field to an immersed charged object which results in a steady-state drift velocity. The ratio of the drift speed to the electric field strength is defined as the electrophoretic mobility  $\mu$  of the particle and is, in general, constant for small applied electric fields. The counterpart of the electrophoretic velocity is the electroosmotic flow (EOF), which is the tangential fluid flow produced by the movement of the ions in the EDL about a stationary object under the influence of an applied field. The magnitude of the EOF far from the interface is called the electroosmotic velocity, the ratio of which to the field strength defines the electroosmotic mobility

The larger the partial charges in the material, the more ions are adsorbed to the surface and larger the cloud of counterions. A solution with a higher concentration of electrolytes also decreases the size of the counter-ion cloud. This ion/counterion layer is known as the electric double layer (EDL), presence of which screens the surface charge [Kirby, 2009]. Figure 5 below shows a sketch of the EDL.

## **II.1. Concept of soft particles**

Soft particles are defined as particles covered with soft matters, or to be more specific, hard particles covered with ion-penetrable surface layer of polyelectrolytes (Figure 1.28) [111, 112, 113]. They are often encountered in biological and artificial systems. Examples of soft particles include biological cells (in which they exist in many vascular boundaries and tissues) [114], bacterial cells [115, 116], and humic acids [117]. They have also proven to be useful also as drugs and gene delivery vehicles [118]. Soft particles have various applications in catalysis [119], sensing [120], nanocomposites [121], and biotechnology [122], in addition to many other applications in industry.

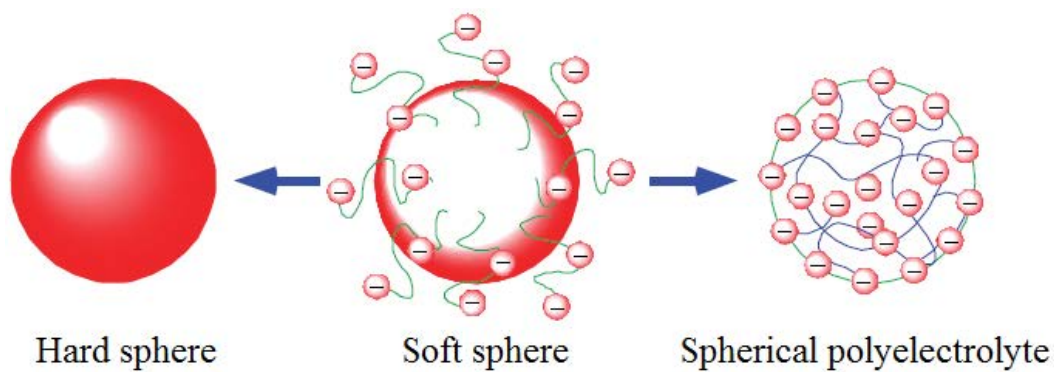


**Figure 1.28.** A soft particle becomes a hard particle in the absence of the surface charge layer, while it tends to form a spherical polyelectrolyte in the absence of the particle core.

A spherical soft colloidal particle is made of an uncharged hard impermeable core with radius  $a$ , covered by a charged ion permeable layer of polyelectrolytes of thickness  $\delta$  according to the model proposed by Ohshima [111, 112] (Figure 1.29). The polymer-coated particle has thus an inner radius  $a$  and an outer radius  $b = a + \delta$ . The permeable polyelectrolytic shell is characterized by three-dimensional spatial distribution of hydrodynamically stagnant ionogenic groups. In the absence of the surface charge layer ( $\delta = 0$ ), a soft particle becomes a hard particle, while it tends to form a spherical polyelectrolyte (or a porous sphere) in the absence of the particle core ( $a = 0$ ). Soft particles serve as a model for biocolloids, such as cells. In such cases, the electrical double layer is formed not only outside but also inside the surface charge layer (Figure 1.28) [123].

The permeability of the polyelectrolyte layer is characterized by the hydrodynamic softness parameter  $\lambda$  of the permeable polymeric shell for a uniform distribution of the segments. The quantity  $1/\lambda$  has a length dimension and represents the length of hydrodynamic flow penetration within the soft layer. In the limit of  $1/\lambda \rightarrow 0$ , the surface layer is impermeable to flow, whereas at  $1/\lambda \rightarrow \infty$  denotes a surface layer that exerts no significant frictional forces on the flow.

The polymer layer being permeable, the counterions, and to a lesser extent, the counterions are distributed inside of this same layer. Thus, in contrast to the hard surface interfaces - solution, the electrical double layer does not extend only to the core solution, but also within the polymer layer. Also the typical thickness of the permeable layer is of the same order of magnitude, if not greater, than the distance Debye altering the potential distribution in soft interphase. The potential deep inside of the surface layer is practically equal to the Donnan potential  $\psi$  since the thickness of the polymeric layer is much greater than the Debye length, i.e. for  $1 > k_d$ . The interphase can no longer be described by the Stern model. Similarly, it is impossible to place a shear plane making the notion of potential wrong-z and physically inapplicable.

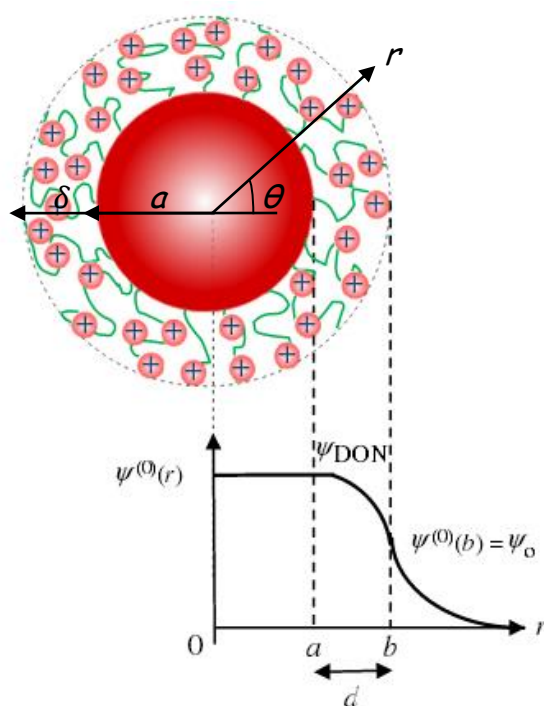


**Figure 1.29.** Schematic representation of a soft particle

Thus, the electric properties of soft particles in an electrolyte solution are essentially determined by the Donnan potential in the surface layer. The potential at the boundary between the polyelectrolyte layer and the surrounding electrolyte solution is the surface potential  $\psi_o$  of a soft particle. The following two potentials play an essential role in electrokinetics of soft particles.



## II.2. Electrokinetic Model of a soft particle

Electrokinetics of soft particles is much more complex than that of hard particles due non-uniform surface properties, the nonhomogeneous surface charge density, and the charged polyelectrolytes layer that complicates ions transport. It is therefore of great importance to study their electrical and surface properties.

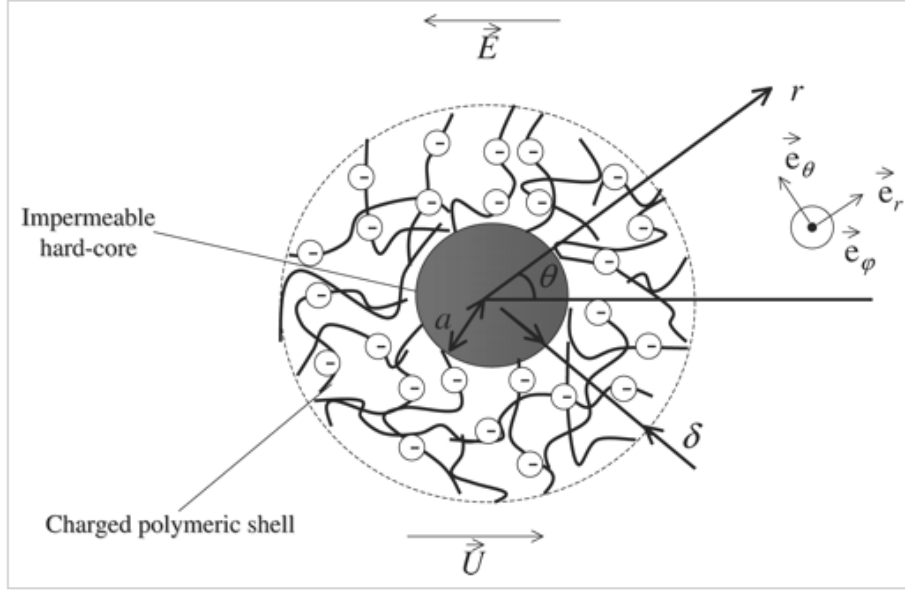


**Figure 1.30.** Schematic representation of a soft particle, composed of a rigid hard core and a permeable charged polymeric layer, moving with a velocity  $\vec{U}$  in a nonbound electrolyte subjected to a dc electric field  $\vec{E}$ . The spherical coordinate system and corresponding unit vectors are also given. In the absence of a hard core ( $a = 0$ ), the model corresponds to that of a spherical polyelectrolyte.

Ohshima brought a great contribution for the evaluation of electrophoretic properties of soft particles based on various theoretical work developed in the 1980s [111, 112, 113]. In fact, sophisticated theoretical models have been developed to study the electrophoretic mobility of soft particles over a broad range of charge densities, coatings, and double layer thicknesses [111, 112, 113, 124, 125, 126, 127, 115].

There are essential differences in electrokinetic behaviors between soft particles and hard particles. The electrophoretic mobility of a hard particle is determined by the particle surface charge  $\sigma$  and thus the particle zeta potential ( $\zeta$ ), while the mobility of a soft particle does not depend on the surface charge density  $\sigma$  ( $\text{C.m}^{-2}$ ) but on the volume charge density

$zen$  ( $\text{C.m}^{-3}$ ) (where  $e$  is the elementary electric charge) distributed in the surface layer thus on the Donnan potential  $\Psi$  in the surface layer. For dissociated groups of valence  $z$  distributed with a constant density (number density)  $n$  within the polyelectrolyte layer, the density distribution of fixed charged groups is given by:

$$\rho_{\text{fix}} = zen \quad (1.2)$$

The concept of zeta potential loses its meaning for a soft particle, provided that the surface layer is much thicker than the Debye length  $1/\kappa$ . Moreover, the electrophoretic mobility of a soft particle depends on the potential and liquid flow distributions in both regions outside and inside the surface layer and thus on the electrophoretic softness  $1/\lambda$ , with  $\eta$  being the viscosity of the electrolyte solution of the surface layer and  $\gamma$  being the frictional coefficient.

$$1/\lambda = \left(\frac{\eta}{\gamma}\right)^{1/2} \quad (1.)$$

Here, it is always assumed that the ionized groups of valence  $z$  are distributed within the polyelectrolyte layer at a uniform density  $n$  so that the layer is uniformly charged at a constant density, and the Debye-Bueche-Brinkman model for theory of hydrodynamics of polymer solution is usually adopted [128, 129]. In this model the polymer segments are regarded as resistance centers exerting frictional forces on the liquid flowing into the polymeric layer with a frictional coefficient  $\gamma$ .

The mobility assessment is based on solving the Poisson equation through the polymer layer and the Navier-Stokes equation accounting for the flow of fluid inside and outside of the permeable layer. For a symmetrical electrolyte  $z : z$ , the expression of the electrophoretic mobility obtained by Ohshima, valid in the limit where  $\lambda_a \gg 1$ ,  $\kappa_a \gg 1$ ,  $\lambda_d \gg 1$ , and  $\kappa_d \gg 1$ , is given by:

$$\mu_e = -\frac{2 \varepsilon \varepsilon_r \Psi}{\eta} \frac{1/\kappa_m + \Psi}{1/\kappa_m + 1/\lambda} \left(1 + \frac{a^3}{2b^3}\right) + \frac{\rho_{\text{fix}}}{\eta \lambda^2} \quad (1.4)$$

Where  $\kappa_m$  presents the effective Debye-Hückel parameter in the surface charge layer that involves the contribution of the fixed-charges  $zen$ ,

$$\kappa_m = \kappa \left[ 1 + \left( \frac{\rho_{fix}^0}{2zeN} \right) \right]^{1/4} \quad (1.5)$$

The Donnan potential in the surface charge layer  $\Psi$  ( $a < r < b$ ), and the potential at the front edge of the surface charge layer at ( $r = b$ ), which is termed the surface potential of the soft particle  $\Psi$ , are given by:

$$\Psi_{DON} = \frac{k_B T}{ze} \ln \left[ \frac{\rho_{fix}^0}{2zeN} + \left\{ \left( \frac{\rho_{fix}^0}{2zeN} \right)^2 + 1 \right\}^{1/2} \right] \quad (1.6)$$

$$\Psi = \Psi_{DON} + \frac{k_B T N}{\rho_{fix}} \ln \left[ 1 - \left\{ \left( \frac{\rho_{fix}}{2zeN} \right)^2 + 1 \right\}^{1/2} \right] \quad (1.7)$$

The above mobility formula (Eq. 1.5) has been derived by neglecting the relaxation effect. Ohshima recently derived an approximate mobility expression taking into account the relaxation effect can be derived from:

$$\phi_+(r) \approx \phi_+(b) = b + \frac{a^3}{b^2} \quad (1.8)$$

$$\phi_-(r) \approx \phi_-(b) = \left( b + \frac{a^3}{b^2} \right) \cdot \frac{1}{1+F} \quad (1.9)$$

$$F = \frac{2}{\kappa b} (1 + 3m_-)(e^{|y_0|/2} - 1) \quad (1.10)$$

Where  $\phi_+(r)$  and  $\phi_-(r)$  refer to coions and counter ions, respectively,  $m_-$  is the scaled drag coefficient of counter ions, and  $F$  corresponds to Dukhin's number  $Du$ , which expresses the relaxation effect with respect to counter ions. The electrophoretic mobility of a soft particle taking that the relaxation effect into account (only in the region outside the surface charge layer) is presented by:

$$\mu = -\frac{2\varepsilon\varepsilon_r}{\eta} \left(1 + \frac{a^3}{2b^3}\right) + \frac{ZeN}{\eta\lambda^2} \left(1 - \frac{F}{1+F} \cdot \frac{1}{1+e^{|y_0|}}\right) - \frac{F}{1+F} \cdot \frac{2\varepsilon\varepsilon_r}{\eta} \left(1 + \frac{a^3}{2b^3}\right) \frac{kT}{ze} \left[2 \ln 2 \left(\frac{1+e^{|y_0|/2}}{2}\right) + \frac{k}{\lambda} (e^{|y_0|/2} - 1) - \frac{\kappa^2}{2\lambda(\lambda + \kappa_m)} \cdot \frac{e^{|y_0|} - 1}{1+e^{-|y_0|}}\right] \quad (1.11)$$

Where  $y_{DON} = ze\phi_{DON}/\kappa T$  is the scaled Donnan potential.

In the limit of very high Donnan potentials (where the relaxation effect becomes very large),  $F \rightarrow \infty$  so that  $\phi_-(r) \approx 0$ . In this limit the mobility is expressed by:

$$\mu^\infty = -\frac{2\varepsilon\varepsilon_r}{\eta} \left(1 + \frac{a^3}{2b^3}\right) + \left(\frac{ZeN}{\eta\lambda^2}\right) 2 \ln 2 \quad (1.12)$$

## II.3. Polyamidoamine (PAMAM) carboxylated nanodendrimers

### II.3.1. Synthesis and structure

As their name indicate, starburst dendrimers are star-shaped, three-dimensional, highly branched and ordered macromolecules (typically 5000 to 500,000 g.mol<sup>-1</sup>) with nanometer-

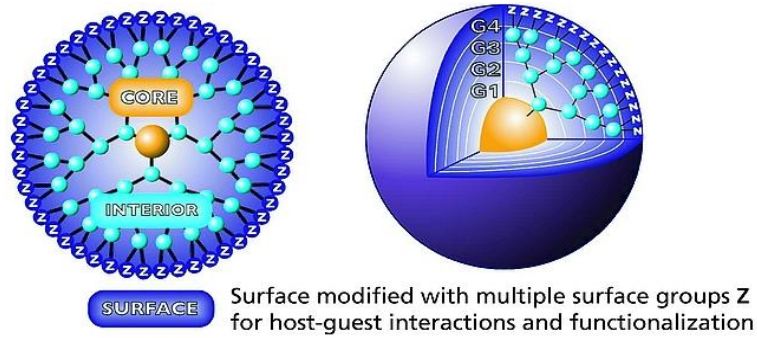


**Figure 1.31.** A schematic representation of a starburst dendrimer viewed as a spherical particle with an internal core surrounded by a shell

scale dimensions [130]. They are defined by three main components: a central core, an interior layer composed of repeating units (generations) radially attached to the initiator core and an exterior multivalent surface with functional surface groups (Figure 1.31).

Two main dendrimers synthesis methods had been developed since 1979; the divergent method, and the convergent growth process. In the divergent method, developed by Tomalia [131], the growth of the dendrimer starts from a central initiator core followed by a reaction

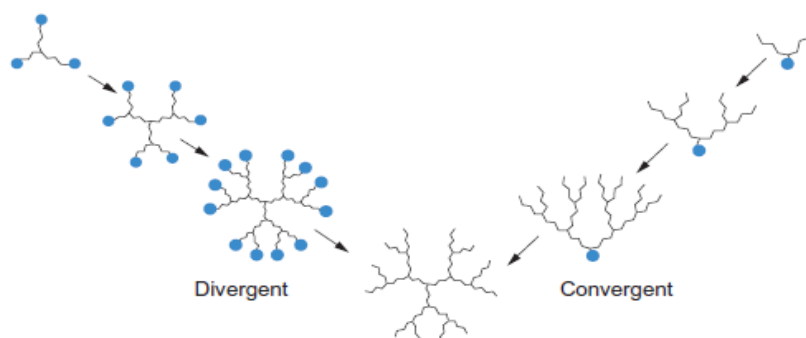


**Figure 1.32.** *The Two principle synthetic methods for constructing dendrimers*

sequence that produces concentric shells of branch cells (generations) around the core. The convergent growth process, introduced by Hawker and Fréchet [132], starts from what will become the dendrimer surface inward to a reactive focal point, leading to the formation of a single reactive Dendron, and then several dendrons are reacted with a multi-functional core to obtain a dendrimer structure (Figure 1.32. *The Two principle synthetic methods for constructing dendrimers*

Poly(amidoamine) (PAMAM) dendrimers are considered the first complete dendrimer

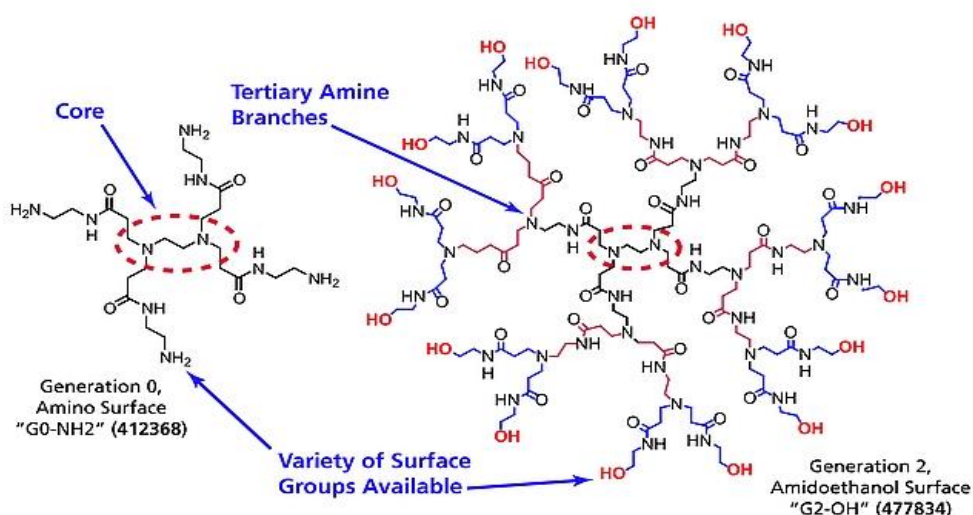


**Figure 1.33.** *PAMAM dendrimers Structure*

family to be synthesized in 1984 [133], characterized and then fully commercialized in 1990 [134]. Most PAMAM dendrimers are supplied as solutions in methanol for improved long-term storage stability. They can be dried and reconstituted in other application-specific solvents. They are synthesized by the divergent method and are considered the most common class of dendrimers suitable for many materials science and biotechnology applications.

PAMAM dendrimers consist of an ethylenediamine core (EDA) and tertiary amine branches. They ethylenediamine core is denoted as generation G0 (Figure 1.33). The PAMAM core-shell architecture grows linearly in diameter as a function of added generations. Intermediates during the dendrimer synthesis are denoted half-generations. In brief, half generation (G1.5, G2.5, G3.5, etc.) have carboxylic acid terminal groups and full generations (G1, G2, G3, etc.) have amine or hydroxyl groups. Addition of successive layers (generations) gradually increases molecular size and amplifies the number of surface groups present. As PAMAM dendrimers grow through generations 1–10 their size increases from 1.1–12.4 nm [135]. Dendrimers allow the precise control of size, shape and placement of functional groups that is desirable for many applications.

### II.3.2. Advances in nanodendrimers research and applications

Several of studies have been carried out to investigate the physicochemical and structural properties of dendrimers in solution either theoretically by applying computer simulations and or experimentally by analytical techniques. For the aim of the optimization of the computer models to give a realistic picture, a large amount of comparative studies have

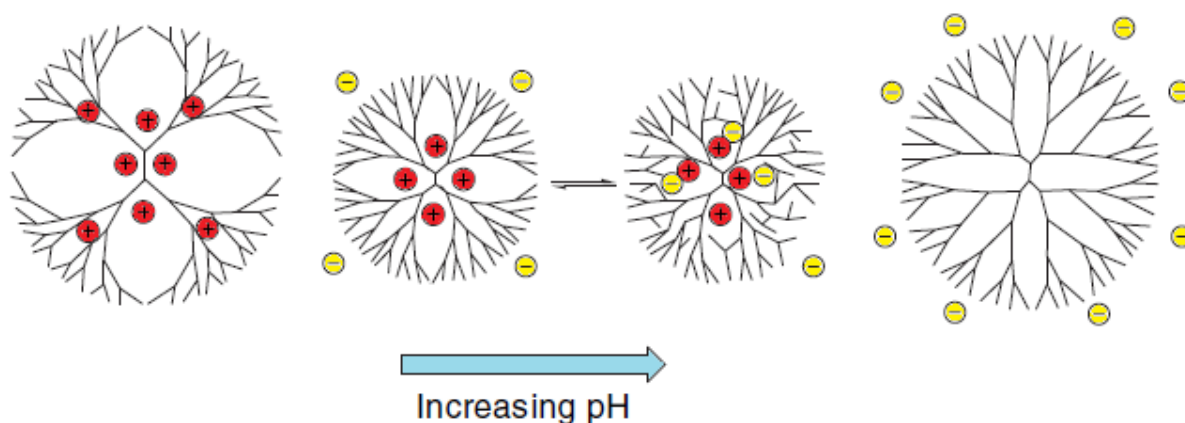


**Figure 1.34.** *Effect of pH on dendrimers conformation*

been carried out between prediction based theoretical calculations and experimental results [136].

In general, the physicochemical properties of dendrimers mainly depend on the generation number, surface functionalities and core structure. For carboxylated dendrimers with acidic end groups, SANS (small angle neutron scattering) and NMR (nuclear magnetic resonance) measurements of self-diffusion coefficients at different pH values were carried. Results showed that at pH 2, due to the electrostatic repulsion between the positively charged protonated tertiary amines of the core, the most extended conformation of the core is observed which leads to a larger core radius [137]. At pH 6, the amount of positively charged amines is equal to the amount of negatively charged carboxylic groups (isoelectric point) which gives rise to a dense core conformation more prone to shrinking as a result of electrostatic interactions between the negatively charged surface  $\text{COO}^-$  groups and the

in the inner shells of the dendrimer. This shows that shrinking is not only a result of weak forces leading to a uniform molecular density of the dendrimer (entropy), but may also be mediated by attractive forces (enthalpy) between inner parts of the dendrons and surface groups. This conformation minimizes the repulsion between the negatively charged surface carboxylates and the positively charged inner shell amines leading to a lower repulsive energy of the system. At basic pH (close to 11), the electrostatic repulsion between the negative charged forces of the surface groups again results in more extended conformation with a highly expanded surface area (swelling) (Figure 1.34).

The behavior of carboxylated nanodendrimers in solvents of various ionic strengths has been examined by Monte Carlo simulations [138]. The intramolecular density profile is observed to be heavily dependent on the Debye screening length. The high ionic strength

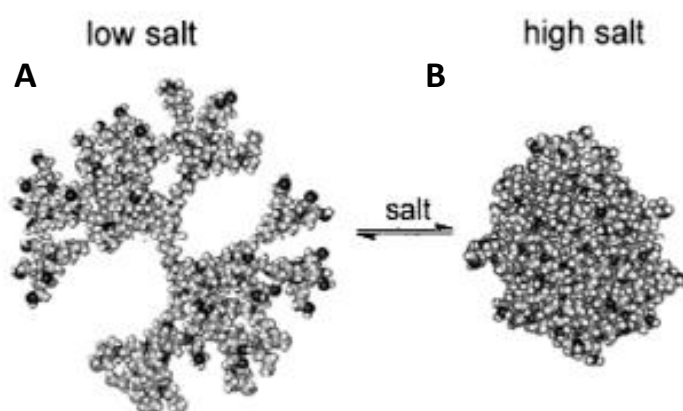


**Figure 1.35.** Effect of ionic strength on dendrimers conformation. (A) Hollow core, dense shell picture. (B) Dense core picture.

appears to have a similar effect of the pH increase. Molecular simulations generally conclude that a high salt concentration favors a contracted conformation of the carboxylated dendrimers with a high degree of shrinking leading to the formation of a dense core. At low ionic strengths, the repulsive forces between the charged dendrimer segments derive dendrimers to adopt an extended conformation favoring swelling in order to minimize charge repulsion within the structure. The effect is somewhat similar to that observed at different pH conditions (Figure 1.35). As a conclusion, the density profiles of the PAMAM-COO<sup>-</sup> nanodendrimers are tunable from a dense core to a dense shell and vice versa by simple manipulation of the ionic strength and/or the pH of the aqueous solution.

As an advanced class of polymer materials with unique architectures, PAMAM dendrimers are of interest in a wide range of applications. Their monodispersity, structural precision, as well as their functionalization possibilities makes from them a potential tool in several research areas. Different strategies have been proposed to enclose within the dendrimer structure drug molecules, genetic materials, targeting agents, and dyes either by encapsulation, complexation, or conjugation. They are used as therapeutic agents, as vectors for targeted gene, peptides and oligonucleotides delivery, and as permeability enhancers able to promote oral and transdermal drug delivery.

The most promising potential of dendrimers is in their possibility to perform controlled and specified drug delivery [139, 140]. Drugs conjugated with polymers are characterized by lengthened half-life, higher stability, water solubility, decreased immunogenicity, and antigenicity. Acetylated PAMAM dendrimers have also been used both as nanocarriers for cytostatic drugs (methotrexate) and for simultaneous monitoring of drug uptake in the tumor cell. The anti-tumor properties of the drug were greatly enhanced [141]. Thus, beside their effective role as drug delivery vehicles, dendrimer nanocarriers also offer the potential of enhancing the bioavailability of drugs that are poorly soluble due to their hydrophilic exteriors and interiors [142, 143]. They have been used to improve the solubility of sparingly soluble drugs such as piroxicam [144]. In addition, PAMAM dendrimers have shown potential as oligonucleotide [145] and gene therapy [146, 147, 148] and gene delivery systems [149, 150, 151]. Moreover, PAMAM dendrimers functionalized with glucosamine groups can provide protection against HIV infection by binding to the glycoprotein receptor on the virus and thus acting as immunomodulators [152, 153]. PAMAM dendrimers had also proved to be effective agents in wound healing leading to better healing, less scar tissue



formation and less inflammation [154, 155]. Other studies reported possible applications in the treatment of bone fractures [156].

Studies revealed that PAMAM dendrimers are also efficient in environmental remediation [157, 158]. G3 and G6 dendrimers coupled to graphene oxide (GrO) were investigated as tools for remediation of naphthalene [159]. Add to this, PAMAM dendrimers with different surface functionalities possess different metal ion (e.g.  $\text{Cu}^{2+}$ ) and proton binding capacity, providing unique opportunities to remove toxic metal ions from wastewater [158]. Other applications include catalysis [160, 161], biosensing [162, 163, 164], photonics [165, 166, 167] and contrast agents in imaging systems (MRI) [168, 169], and electronics [170]. In addition, different functionalized PAMAM dendrimers can be used for interfacial self-assembly to form monolayers at the air–water interface [171] or multilayers [172] onto solid substrates including planar substrates [173, 174, 175] and colloidal particles [176].

### **II.3.3. Investigations of dendrimer toxicity**

The recent explosion of interest in dendrimers research accompanied with their growing range of applications makes it so critical to investigate their biocompatibility and toxicity [177]. However, currently little information exists regarding the risks such materials pose to human health and the environment. To date, the cytotoxicity of dendrimers has been primarily studied *in vitro*; however, a few *in vivo* studies have been recorded [178].

Several studies showed the significant generation-dependent cytotoxicity of amino-terminated PAMAM dendrimers on human intestinal adenocarcinoma Caco-2 cells [179, 180], with higher generation dendrimers being the most toxic [179, 181]. In the same context, Fisher et al. showed that the degree of substitution as well as the type of amine functionality affects the degree of toxicity, with primary amines being more toxic than secondary or tertiary amines [181].

Malik et al. observed a generation-dependent haemolytic effect of PAMAM-NH<sub>2</sub> dendrimers on a solution of rat blood cells [182]. However, the biocompatibility of dendrimers was also dependent on the chemistry of the core, but is most strongly influenced by the nature of the dendrimers surface. Dendrimers containing an aromatic polyether core and anionic carboxylate surface groups have shown to be haemolytic on a solution of rat blood cells after 24 h. Comparative toxicity studies on anionic (carboxylate-terminated) and

cationic (amino-terminated) PAMAM dendrimers using Caco-2 cells have shown a significantly lower cytotoxicity of the anionic ones [179]. The cationic dendrimers are prone to destabilize cell membranes and cause cell lysis. Lee et al. observed down-regulation of mitochondrial DNA-encoded genes involved in the maintenance of mitochondrial membrane for human lung cells after exposure to G4-NH<sub>2</sub> PAMAM dendrimers. Results showed damage in the mitochondria and a decrease of cell viability resulting in apoptosis [183].

However, only few *in vivo* studies have reported the toxicity of dendrimers. Concerning animal models, Roberts et al. showed that upon injection into mice, doses of 10 mg/kg of PAMAM dendrimers (up to G5), with amino-terminated surfaces, did not appear to be toxic, while at very high concentrations, they induced some inhibition of cell growth *in vitro* but upon injection into mice, no acute or long-term toxicity problems were observed [184]. Li et al. studied the molecular link between exposure to cationic PAMAM dendrimers and lung damage in mice. The authors observed *in vivo* toxicity due to acute lung injury because PAMAM triggers cell death by deregulating a signaling pathway [185]. Chauhan et al. studied the toxicity of G4-NH<sub>2</sub> and G4-OH PAMAM dendrimers in Swiss albino mice. They suggested a probable interference of the dendrimers with glucose metabolism as well as toxic effects on kidney and liver [186].

Concerning aquatic organisms, Petit et al. investigated the toxicity of G2, G4 and G5 PAMAM dendrimers to the green alga *Chlamydomonas reinhardtii*. The results indicated a toxicity increase with generation number [187]. Moreover, Heiden et al. [188] studied the toxicity of G3.5 and G4 PAMAM dendrimers towards zebrafish embryos. While G4 dendrimers were toxic towards growth and development of zebrafish embryos, G3.5 carboxylated dendrimers did not exhibit toxicity. Suarez et al. followed the toxicity of G1-NH<sub>2</sub>, G4-NH<sub>2</sub>, and G4-OH PAMAM dendrimers to the microalga *Pseudokirchneriella subcapitata* [189]. Findings showed a high toxicity particularly for G4-NH<sub>2</sub> which support previous results indicating increased toxicity for higher dendrimer generation probably as a consequence of a larger surface area for interaction with living organisms [190].

The toxicity and biocompatibility of dendrimers remains a matter of discussion and much research is still to be conducted to elucidate the underlying mechanism of toxicity and its relationship with their molecular structure. Nevertheless, it remains crucial to assess not only the toxicity of dendrimers but also their environmental fate and to investigate methods and techniques to decrease their availability in the environment.

### III. References

- [1] Perico, A. (2012) Polyelectrolyte Fundamentals, in *Ionic Interactions in Natural and Synthetic Macromolecules*, (eds A. Ciferri and A. Perico), John Wiley & Sons, Inc., Hoboken, NJ, USA, pp. 49–91.
- [2] Rmaile, . . , Schlenoff, J. ., 2 2). “Internal pKa’s” in Polyelectrolyte Multilayers: Coupling Protons and Salt. *Langmuir*, 18, 8263–8265.
- [3] Blodgett, K.B. (1934). Monomolecular films of fatty acids on glass. *J. Am. Chem. Soc.*, 56, 495.
- [4] Blodgett, K.B. Langmuir, I. (1937). Built-up films of barium stearate and their optical properties. *Physical Review*, 51, 964.
- [5] Maoz, R., Netzer, L., Gun, J., Sagiv, J., (1988). Self-assembling monolayers in the construction of planned supramolecular structures and as modifiers of surface properties. *The Journal of Chemical Physics*, 85, 1059–1065.
- [6] Guang, C., Hong, H.G., Mallouk, T.E. (1992). Layered Metal Phosphates and Phosphonates - from Crystals to Monolayers. *Accounts of Chemical Research*, 25, 420–427.
- [7] Netzer, L., Sagiv, J. (1983). A new approach to construction of artificial monolayer assemblies. *Journal of American Chemical Society*, 105, 674–676.
- [8] Fromherz, P., (1980). Electron Microscopy at molecular dimensions. *Springer-Verlag, Berlin*, pp. 338–349.
- [9] Gölander, C.-G., Arwin, H., Ericksson, J.C., Lundstrom, I., Larsson, R. (1982). Heparin surface film formation through adsorption of colloidal particles studied by ellipsometry and scanning electron microscopy. *Colloids and Surfaces*, 5, 1–16.
- [10] Gaines Jr, G., (1983). Deposition of colloidal particles in monolayers and multilayers. *Thin Solid Films*, 99, 243–248.
- [11] Iler, R.K. (1966). Multilayers of colloidal particles. *Journal of Colloid and Interface Science*, 51, 569–594.
- [12] Decher, G., Hong, J.D., Schmitt, J., (1992). Buildup of ultrathin multilayer films by a self-assembly process. Consecutively alternating adsorption of anionic and cationic polyelectrolytes on charges surface. *Thin Solid Films*, 210, 831–835.
- [13] Decher, G., (1997). Fuzzy Nanoassemblies: Toward Layered Polymeric Multicomposites. *Science*, 277, 1232.
- [14] Caruso, F., Furlong, D. N., Ariga, K., Ichinose, I., and Kunitake, T., (1998). Characterization of polyelectrolyte-protein multilayer films by atomic force microscopy, scanning electron microscopy, and Fourier transform infrared reflection-absorption spectroscopy. *Langmuir*, 14, 4559–4565. Caruso, F., Donath, E., and Möhwald, H., (1998a). Influence of polyelectrolyte multilayer coatings on Forster resonance energy transfer between 6-carboxyfluorescein and rhodamine B-labeled particles in aqueous solution. *The Journal of Physical Chemistry B*, 102, 2011–2016.
- [15] Soltwedel, O., Nestler, P., Neumann, H.-G., Paßvogel, M., Köhler, R., Helm, C.A., (2012). Influence of Polycation (PDADMAC) Weight on Vertical Diffusion within Polyelectrolyte Multilayers during Film Formation and Postpreparation Treatment. *Macromolecules*, 45, 7995–8004.
- [16] Izquierdo, A., Ono, S.S., Voegel, J.-C., Schaaf, P., Decher, G., (2005). Dipping versus Spraying: Exploring the Deposition Conditions for Speeding up Layer-by-Layer Assembly. *Langmuir*, 21, 7558–7567.
- [17] Clark, S. L., Hammond, P. T., (1998). Engineering the Microfabrication of Layer-by-Layer Thin Films. *Advanced Matertilas*, 10, 1515–1519.
- [18] Lvov, Y., Decher, G., Mohwald, H., (1993). Assembly, Structural Characterization, and Thermal Behavior of Layer-by-Layer Deposited Ultrathin Films of Poly(vinyl sulfate) and Poly(allylamine). *Langmuir*, 9, 481–486.

- 
- [19] Caruso, F., Schüler, C., Kurth, J. G., (1999). Core-Shell Particles and Hollow Shells Containing Metallo-Supramolecular Components. *Chemistry of Materials*, 11, 3394–3399.
- [20] Ladam, G., Schaad, P., Voegel, J.C., Schaaf, P., Decher, G., Cuisinier, F., (2000). In Situ Determination of the Structural Properties of Initially Deposited Polyelectrolyte Multilayers. *Langmuir*, 16, 1249–1255.
- [21] Schoeler, B., Kumaraswamy, G., Caruso, F., (2002). Investigation of the Influence of Polyelectrolyte Charge Density on the Growth of Multilayer Thin Films Prepared by the Layer-by-Layer Technique. *Macromolecules*, 35, 889–897.
- [22] Steitz, R., Jaeger, W., Klitzing, R. v., (2001). Influence of Charge Density and Ionic Strength on the Multilayer Formation of Strong Polyelectrolytes. *Langmuir*, 17, 4471–4474.
- [23] Schlenoff, J.B., Ly, H., Li, M., (1998). Charge and Mass Balance in Polyelectrolyte Multilayers. *The Journal of American Chemical Society*, 120, 726–7634.
- [24] Yarwood, Stuart, C., Kim, Fleer, Tirrell, Cosgrove, Klein, Leger, Krausch, Lineton, Richards, Russell, Gast, Higgins, Penfold, Everett, Brown, McLeish, Ottewill, Jones, Shull, Kramer, Gibbon, Bates, Fernandez, Zachmann, Ryan, (1994). *General discussion. Faraday Discuss.* 98, 231–244.
- [25] von Klitzing, R., (2006). Internal structure of polyelectrolyte multilayer assemblies. *Physical Chemistry Chemical Physics*, 8, 5012–5033.
- [26] Farhat, T.E., Schlenoff, J.B., (2001). Ion Transport and Equilibria in Polyelectrolyte Multilayers. *Langmuir*, 17, 1184–1192.
- [27] Schlenoff, J.B., (2002). Charge Balance and Transport in Polyelectrolyte Multilayers, in: *Multilayer Thin Films*. pp. 99–133.
- [28] Laugel, N., Betscha, C., Winterhalter, M., Voegel, J.-C., Schaaf, P., Ball, V., (2006). Relationship between the Growth Regime of Polyelectrolyte Multilayers and the Polyanion/Polycation Complexation Enthalpy. *The Journal of Physical Chemistry B*, 110, 19443–19449.
- [29] Decher, G., Lvov, Y., and Schmitt, J. (1994). Proof of multilayer structural organization in selfassembled polycation-polyanion molecular films. *Thin Solid Films*, 244, 772–777.
- [30] Schmitt, J., Torsten, G., Decher, G., Pershan, P. S., Kjaer, K., Loesche, M., (1993). Internal structure of layer-by-layer adsorbed polyelectrolyte films: a neutron and x-ray reflectivity study. *Macromolecules*, 26, 7058–7063.
- [31] Korneeva, D., Lvov, Y., Decher, G., Schmitt, J., and Yaradaikin, S., (1995). Neutron reflectivity analysis of self-assembled film superlattices with alternate layers of deuterated and hydrogenated polystyrenesulfonate and polyallylamine. *Physica B: Condensed matter*, 213–214, 954–956.
- [32] Lavalle, P., Gergely, C., Cuisinier, F.J.G., Decher, G., Schaaf, P., Voegel, J.C., Picart, C., (2002). Comparison of the Structure of Polyelectrolyte Multilayer Films Exhibiting a Linear and an Exponential Growth Regime: An in Situ Atomic Force Microscopy Study. *Macromolecules*, 35, 4458–4465.
- [33] Picart, C., Lavalle, P., Hubert, P., Cuisinier, F.J.G., Decher, G., Schaaf, P., Voegel, J.-C., (2001). Buildup Mechanism for Poly(L-lysine)/Hyaluronic Acid Films onto a Solid Surface. *Langmuir*, 17, 7414–7424.
- [34] Collin, D., Lavalle, P., Garza, J. M., Voegel, J. C., Schaaf, P., and Martinoty, P., (2004). Mechanical properties of cross-linked hyaluronic acid/poly-(L-lysine) multilayer films. *Macromolecules*, 37, 10195–10198.
- [35] Richert, L., Lavalle, P., Payan, E., Shu, X. Z., Prestwich, G. D., Stoltz, J.-F., Schaaf, P., Voegel, J.-C., Picart, C (2004). Layer by layer buildup of polysaccharide films: Physical chemistry and cellular adhesion aspects. *Langmuir*, 20, 448–458.
- [36] Lavalle, P., Picart, C., Mutterer, J., Gergely, C., Reiss, H., Voegel, J.-C., Senger, B., and Schaaf, P., (2004). Modeling the buildup of polyelectrolyte multilayer films having exponential growth. *The Journal of Physical Chemistry B*, 108, 635–648.
- [37] Hubsch, E., Ball, V., Senger, B., Decher, G., Voegel, J.-C., and Schaaf, P., (2004). Controlling the growth regime of polyelectrolyte multilayer films: Changing from exponential to linear growth by adjusting the
-

- composition of polyelectrolyte mixtures. *Langmuir*, 20, 1980–1985.
- [38] Lulevich, V.V., Vinogradova, O.I., (2004). Effect of pH and salt on the stiffness of polyelectrolyte multilayer microcapsules. *Langmuir*, 20, 2874–2878.
- [39] Kim, B.-S., Vinogradova, O.I., (2004). pH-Controlled Swelling of Polyelectrolyte Multilayer Microcapsules. *The Journal of Physical Chemistry*, 108, 8161–8165.
- [40] Rubner, M.F., (2002). pH-Controlled Fabrication of Polyelectrolyte Multilayers: Assembly and Applications, in: *Multilayer Thin Films*, pp. 133–155.
- [41] Shiratori, S. S., Rubner, M.F., (2000). pH-Dependent Thickness Behavior of Sequentially Adsorbed Layers of Weak Polyelectrolytes. *Macromolecules*, 33, 4213.
- [42] Choi, J., Rubner, M.F., (2005). Influence of the Degree of Ionization on Weak Polyelectrolyte Multilayer Assembly. *Macromolecules*, 38, 116–124.
- [43] Harris, J.J., Stair, J.L., Bruening, M.L., (2000). Layered Polyelectrolyte Films as Selective, Ultrathin Barriers for Anion Transport. *Chemistry of Materials*, 12, 1941–1946.
- [44] Dubas, S.T., Schlenoff, J.B., (2001). Swelling and Smoothing of Polyelectrolyte Multilayers by Salt. *Langmuir*, 17, 7725–7727.
- [45] Nazaran, P., Bosio, V., Jaeger, W., Anghel, D.F., Klitzing, R. v., (2007). Lateral Mobility of Polyelectrolyte Chains in Multilayers. *The Journal of Physical Chemistry. B*, 111, 8572–8581.
- [46] McAloney, R. A., Dudnik, V., Goh, M. C., (2003). Anisotropic Diffusion of Polyelectrolyte Chains within Multilayer Films. *Langmuir*, 2003, 19, 3947.
- [47] Jaber, J.A., Schlenoff, J.B., (2006). Dynamic Viscoelasticity in Polyelectrolyte Multilayers: Nanodamping. *Chemistry of Materials*, 18, 5768–5773.
- [48] Heuvingh, J., Zappa, M., Fery, A., (2005). Salt softening of polyelectrolyte multilayer capsules. *Langmuir*, 21, 3165.
- [49] Buscher, K., Graf, K., Ahrens, H., Helm, C. A., (2002). Influence of adsorption conditions on the structure of polyelectrolyte multilayers. *Langmuir*, 18, 3585–3591.
- [50] Tan, H. L., McMurdo, M. J., Pan, G. Q., Van Patten, P. G., (2003). Temperature dependence of polyelectrolyte multilayer assembly. *Langmuir*, 19, 9311–9314.
- [51] Salomaki, M., Vinokurov, I. A., Kankare, J., (2005). Effect of temperature on the buildup of polyelectrolyte multilayers. *Langmuir*, 21, 11232–11240.
- [52] Porcel, C., Lavalle, P., Ball, V., Decher, G., Senger, B., Voegel, J.-C., Schaaf, P., (2006). From exponential to linear growth in polyelectrolyte multilayers. *Langmuir*, 22, 4376–4383.
- [53] Hofmeister, F (1888). Zur Lehre von der Wirkung der Salze. *Naunyn-Schmiedeberg's Archives of Pharmacology*, 24, 247–260.
- [54] Leontidis, E., Aroti, A., Belloni, L. (2009). "Liquid expanded monolayers of lipids as model systems to understand the anionic Hofmeister series: 1. A tale of models. *The Journal of Physical Chemistry B*, 113, 1447–1459.
- [55] Salomaki, M., Laiho, T., and Kankare, J. (2004). Counteranion-controlled properties of polyelectrolyte multilayers. *Macromolecules*, 37, 9585–9590.
- [56] Salomaki, M., Tervasmaki, P., Areva, S., Kankare, J. (2004). The Hofmeister anion effect and the growth of polyelectrolyte multilayers. *Langmuir*, 20, 3679–3683.
- [57] El Haitami, A.E., Thomann, J.-S., Jierry, L., Parat, A., Voegel, J.-C., Schaaf, P., Senger, B., Boulmedais, F., Frisch, B., (2010). Covalent Layer-by-Layer Assemblies of Polyelectrolytes and Homobifunctional Spacers. *Langmuir*, 26, 12351–12357.
- [58] Nolte, A. J., Takane, N., Hindman, E., Gaynor, W., Rubner, M. F., Cohen, R. E., (2007). Thin film thickness gradients and spatial patterning via salt etching of polyelectrolyte multilayers. *Macromolecules*, 40, 5479–5486.

- 
- [59] Lösche, M., Schmitt, J., Decher, G., Bouwman, W. G., and Kjaer, K., (1998). Detailed Structure of Molecularly Thin Polyelectrolyte Multilayer Films on Solid Substrates as Revealed by Neutron Reflectometry. *Macromolecules*, 31, 8893–8906.
- [60] Stockton, W. B., Rubner, M. F., (1997). Molecular-Level Processing of Conjugated Polymers. 4. Layer-by-Layer Manipulation of Polyaniline via Hydrogen-Bonding Interactions. *Macromolecules*, 30, 2717–2725.
- [61] Wang, L. Y., Wang, Z. Q., Zhang, X., Shen, J.-C., Chi, L. F., Fuchs, H., (1997). A new approach for the fabrication of an alternating film of poly(4-vinylpyridine) and poly(acrylic acid) based on hydrogen bonding. *Macromolecular Rapid Communications*, 18, 509–514.
- [62] Sukhishvili, S. A., Granick, S., (2002). Layered erasable polymer multilayers formed by hydrogen bonded sequential self assembly
- [63] Kharlampieva, E., Sukhishvili, S. A., (2003). Polyelectrolyte Multilayers of weak polyacid and cationic copolymer: Competition of hydrogen-bonding and electrostatic interactions. *Macromolecules*, 36, 9950–9956.
- [64] Kharlampieva, E., Sukhishvili, S. A., (2006). Hydrogen-bonded layer-by-layer polymer films. *Journal of Macromolecular Science, Part C*, 46, 377–395.
- [65] Shubin, V., Linse, P., (1995). Effect of Electrolytes on Adsorption of Cationic Polyacrylamide on Silica: Ellipsometric Study and Theoretical Modeling. *The Journal of Physical Chemistry*, 99, 1285–1291.
- [66] Van de Steeg, H.G.M., Cohen Stuart, M.A., De Keizer, A., Bijsterbosch, B.H., (1992). Polyelectrolyte adsorption: a subtle balance of forces. *Langmuir*, 8, 2538–2546.
- [67] Peeters, J.M.M., Boom, J. P., Mulder, M.H.V., Strathmann, H., (1998). Retention measurements of nanofiltration membranes with electrolyte solutions. *Journal of Membrane Science*, 145, 199–209.
- [68] Sukhorukov, G.B., Schmitt, J., Decher, G., (1996). Reversible swelling of polyanion/polycation multilayers films in solutions of different ionic strength. *Berichte der Bunsengesellschaft für physikalische Chemie*, 100, 948–953.
- [69] Naegeli, R., Redepenning, J., Anson, F.C., (1986). Influence of supporting electrolyte concentration and composition on formal potentials and entropies of redox couples incorporated in Nafion coatings on electrodes. *The Journal of Physical Chemistry*, 90, 6227–6232.
- [70] Ugo, P., Anson, F.C., (1989). Poly(2-vinylpyrazine) as a soluble polymeric ligand and as an electrode coating. Reactions with pentacyanoferrate(II). *Analytical Chemistry*, 61, 1799–1805.
- [71] Doblhofer, K., Zhong, C., (1991). The mechanism of electrochemical charge-transfer reactions on conducting polymer films. *Synthetic Metals*, 43, 2865–2870.
- [72] Hodak, J., Etchenique, R., Calvo, E.J., Singhal, K., Bartlett, P.N., (1997). Layer-by-Layer Self-Assembly of Glucose Oxidase with a Poly(allylamine)ferrocene Redox Mediator. *Langmuir*, 13, 2708–2716.
- [73] Calvo, E.J., Wolosiuk, A., (2002). Donnan Permselectivity in Layer-by-Layer Self-Assembled Redox Polyelectrolyte Thin Films. *The Journal of the American Chemical Society*, 124, 8490–8497.
- [74] Voegel, J.-C., Decher, G., Schaaf, P., (2003). Multicouches de polyélectrolytes dans le domaine des biotechnologies. *L'actualité chimique*, 30–38.
- [75] Andreeva, D.V., Fix, D., Möhwald, H., Shchukin, D. G., (2008). Self-Healing Anticorrosion Coatings Based on pH-Sensitive Polyelectrolyte/Inhibitor Sandwichlike Nanostructures. *Advanced Materials*, 20, 2789–2794.
- [76] Westman, E.H., Ek, M., and Wagberg, L., (2008). Antimicrobial Activity of Polyelectrolyte Multilayer-Treated Cellulose Films. *Holzforschung*, 63, 33–39.
- [77] Decher, G., Schlenoff, J. B., (2003). Multilayer Thin Films: Sequential Assembly of Nanocomposite Materials, Wiley-VCH, Weinheim.
- [78] Sukhorukov, G. B., Antipov, A. A., Voigt, A., Donath, E., and Möhwald, H., (2001). pH-Controlled Macromolecule Encapsulation in and Release from Polyelectrolyte Multilayer Nanocapsules. *Macromolecular Rapid Communications*, 22, 44–46.
-

- 
- [79] Antipov, A.A., Sukhorukov, G. ., Leporatii, S., Radtchenko, I.L., o nath, E., and Möhwald, . 2 2). Polyelectrolyte multilayer capsule permeability control. *Colloids and Surfaces A*, 198, 535–541.
- [80] Gao, C., o nath, E., Moya, S., u dnik, V., and Möhwald, . , 2 1). Elasticity of hollow polyelectrolyte capsules prepared by the layer-by-layer technique. *The European Physical Journal E*, 5, 21–27.
- [81] Laurent, D., Schlenoff, J.B., (1997). Multilayer assemblies of redox polyelectrolytes. *Langmuir* 13, 1552–1557.
- [82] Kleinfel, E.R., Ferguson, G.S. **(1995)**. Rapid, Reversible Sorption of Water from the Vapor by a Multilayered Composite Film: A Nanostructured Humidity Sensor. *Chemistry of Materials*, 7, 2327–2331.
- [83] Yang, X., Johnson, S., Shi, J., Holesinger, T., Swanson, B., (1997). "Polyelectrolyte and molecular host ion self-assembly to multilayer thin films: An approach to thin film chemical sensors. *Sensors and Actuators B: Chemical*, 45, 87–92.
- [84] Pearson, C., Nagel, J., Petty, M. C., (2001). "Metal ion sensing using ultrathin organic films prepared by the layer-by-layer adsorption technique. *Journal of Physics D: Applied Physics*, 34, 285–291.
- [85] Sun, Y., Zhang, X., Sun, C., Wang, B., and Shen, J., (1996). Fabrication of Ultrathin Film Containing Bienzyme of Glucose Oxidase and Glucoamylase Based on Electrostatic Interaction and Its Potential Application as a Maltose Sensor. *Macromolecular Chemistry and Physics*, 197, 147–153.
- [86] Moriguchi, I., Fendler, J. H., **(1998)**. Characterization and Electrochromic Properties of Ultrathin Films Self-Assembled from Poly(diallyldimethylammonium) Chloride and Sodium Decatungstate. *Chemistry of Materials*, 10, 2205–2211.
- [87] Salloum, D. S., Schlenoff, J. B., (2004). Rectifiedion currents through ultrathin polyelectrolyte complex: Toward chemical transistors. *Electrochemical Solid-State Letters*, 7, E45–E47.
- [88] Woo, W.-K., Shimizu, K.T., Jarosz, M.V., Neuhauser, R.G., Leatherdale,C.A., Rubner, M.A., and Bawendi,M.G., (2002). Reversible Charging of CdSe Nanocrystals in a Simple Solid-State Device. *Advanced Materials*, 14, 1068–1071.
- [89] Galeska, I., Hickey, T., Moussy, F., Kreutzer, D., Papadimitrakopoulos, F., (2001). Characterization and Biocompatibility Studies of Novel Humic Acids Based Films as Membrane Material for an Implantable Glucose Sensor. *Biomacromolecules*, 2, 1249–1255.
- [90] Sukhorukov, G.B., Montrel, M.M.,Petrov, A.I., Shabarchina, L.I., Sukhorukov, B.I., (1996). Multilayer films containing immobilized nucleic acids. Their structure and possibilities in biosensor applications. *Biosensors and Bioelectronics*., 11, 913– 922.
- [91] Onda, M., Lvov, Y., Ariga, K., Kunitake, T., (1996). Sequential reaction and product-separation on molecular films of glucoamylose and glucose oxidase assembled on an ultrafilter. *Journal of Fermentation and Bioengineering*, 82, 502–506.
- [92] Caruso, F., Rodda,E., Furlong, D.F., Niikura, K., Okahata, Y., (1997). Quartz Crystal Microbalance Study of DNA Immobilization and Hybridization for Nucleic Acid Sensor Development. *Analytical Chemistry*, 69, 2043–2049.
- [93] Kotov, N.A., Magonov, S., andTropsha, E., (1998). Layer-by-layer self-assembly of aluminosilicate-polyelectrolyte composites: Mechanism of deposition, crack resistance, and perspectives for novel membrane materials. *Chemistry of Materials*, 10,886–895.
- [94] Meier-Haack, J., Lenk, W.,Lehmann, D., and Lunkwitz, K., (2001). Pervaporation separation of water/alcohol mixtures using composite membranes based on polyelectrolyte multilayer assemblies. *Journal of Membrane Science*, 184, 233–243.
- [95] Stanton,B.W., Harris, J.J., Miller, M.D., andBruening, M.L., (2003). Ultrathin, Multilayered Polyelectrolyte Films as Nanofiltration Membranes. *Langmuir*, 19, 7038–7042.
- [96] Kapnissi, C.P., Akbay, C., Schlenoff, J.B., and Warner, I.M., (2002). Analytical Separations Using Molecular Micelles in Open-Tubular Capillary Electrochromatography. *Analytical Chemistry*, 74, 2328–2335.
- [97] Cassagneau, T. and Fendler, J.H., (1998). High Density Rechargeable Lithium-Ion Batteries Self-Assembled
-

- from Graphite Oxide Nanoplatelets and Polyelectrolytes. *Advanced Materials*, 10, 877–881.
- [98] Hattori, H., (2001). Anti-Reflection Surface with Particle Coating Deposited by Electrostatic Attraction. *Advanced Materials*, 13, 51–54.
- [99] Srivastava, S., Ball, V., Podsiadlo, P., Lee, J., Ho, P., Kotov, N.A., (2008). Reversible Loading and Unloading of nanoparticles in “Exponentially” Growing Polyelectrolyte Multilayers. *Journal of the American Chemical Society*, 130, 3748–3749.
- [100] Ladhari, N., Hemmerle, J., Haikel, Y., Voegel, J.C., Ball, V., (2010). Polyelectrolyte multilayer films: A sponge for insulin? *Bio-Medical Materials and Engineering*, 20, 217–225.
- [101] Burke, S.E., Barrett, C.J., (2004). pH-Dependent Loading and Release Behavior of Small Hydrophilic Molecules in Weak Polyelectrolyte Multilayer Films. *Macromolecules*, 37, 5375–5384.
- [102] Guyomard, A., Nysten, B., Muller, G., Glinel, K., (2006). Loading and Release of Small Hydrophobic Molecules in Multilayer Films Based on Amphiphilic Polysaccharides. *Langmuir*, 22, 2281–2287.
- [103] Vodouhê, C., Guen, E.L., Garza, J.M., Francius, G., Déjugnat, C., Ogier, J., Schaaf, P., Voegel, J.-C., Lavalle, P., (2006). Control of drug accessibility on functional polyelectrolyte multilayer films. *Biomaterial*, 27, 4149–4156.
- [104] Kittitheeranun, P., Sanchavanakit, N., Sajomsang, W., Dubas, S.T., (2010). Loading of Curcumin in Polyelectrolyte Multilayers. *Langmuir*, 26, 6869–6873.
- [105] Ball, V., Bernsmann, F., Werner, S., Voegel, J.-C., Piedra-Garza, L.F., Kortz, U., (2009). Polyoxometalates in Polyelectrolyte Multilayer Films: Direct Loading of  $[\text{H}_7\text{P}_8\text{W}_{48}\text{O}_{184}]_{33-}$  vs. Diffusion into the Film. *European Journal of Inorganic Chemistry*, 5115–5124.
- [106] Srivastava, S., Podsiadlo, P., Critchley, K., Zhu, J., Qin, M., Shim, B.S., Kotov, N.A., (2009). Single-Walled Carbon Nanotubes Spontaneous Loading into Exponentially Grown LBL Films. *Chemistry of Materials*, 21, 4397–4400.
- [107] Sorrenti, E., Ball, V., Del Frari, D., Arnoult, C., Toniazio, V., Ruch, D., (2011). Incorporation of Copper (II) Phtalocyanines as Model Dyes in Exponentially Growing Polyelectrolyte Multilayer Films: A Multiparametric Investigation. *The Journal of Physical Chemistry C*, 115, 8248–8259.
- [108] Salloum, D.S., Schlenoff, J.B., (2004). Protein Adsorption Modalities on Polyelectrolyte Multilayers. *Biomacromolecules*, 5, 1089–1096.
- [109] Hübsch, E., Fleith, G., Fatisson, J., Labbé, P., Voegel, J.C., Schaaf, P., Ball, V., (2005). Multivalent Ion/Polyelectrolyte Exchange Processes in Exponentially Growing Multilayers. *Langmuir*, 21, 3664–3669.
- [110] Abalde-Cela, S., Ho, S., Rodríguez-González, B., Correa-Duarte, M.A., Álvarez-Puebla, R.A., Liz-Marzán, L.M., Kotov, N.A., (2009). Loading of Exponentially Grown LBL Films with Silver Nanoparticles and Their Application to Generalized SERS Detection. *Angewandte Chemie International Edition*, 48, 5326–5329.
- [111] Helmholtz, H., (1853), "Ueber einige Gesetze der Vertheilung elektrischer Ströme in körperlichen Leitern mit Anwendung auf die thierisch-elektrischen Versuche", *Annalen der Physik und Chemie* (in German), 165 (6), pp. 211–233.
- [112] Gouy, G., (1913). Sur la constitution de la charge électrique à la surface d'un électrolyte. *Journal de Physique Archives*, 9, 457–468.
- [113] Chapman, D. L., (1913). A contribution to the theory of electrocapillarity. *Philosophical Magazine*, 25, 475–481.
- [114] Stern, O., (1924). Zur Theorie der elektrischen Doppelschicht. *Z. Elektrochemie*, 30, 508–516.
- [115] Graham, R. C., (1947). The estimation of vertical motion in the atmosphere. *Quarterly Journal of the Royal Meteorological Society*, 73, 407–417.
- [116] Bruus, H., 2008. Theoretical Microfluidics, Oxford Master Series in Physics. OUP Oxford.
- [117] Ohshima, H., (1994). Electrophoretic Mobility of Soft Particles. *The Journal of Colloid and Interface Science*, 163, 474–483.



- 
- [118] Ohshima, H., (1995). Electrophoresis of soft particles. *Advances in Colloid and Interface Science*, 62, 189–235.
- [119] Ohshima, H., (1995). Electrophoretic mobility of soft particles. *Colloids and Surfaces A: Physicochemical and Engineering Aspects*, 103, 249–255.
- [120] Ohshima, H., (2013). Electrokinetic phenomena of soft particles. *Current Opinion in Colloid & Interface Science*, 18, 73–82.
- [121] Swartz, M.A., Fleury, M.E., (2007). Interstitial flow and its effects in soft tissues. *Annual Review of Biomedical Engineering*, 9, 229–256.
- [122] Duval, J. F.L., Gaboriaud, F., (2010). Progress in electrohydrodynamics of soft microbial particle interphases. *Current Opinion in Colloid & Interface Science*, 15, 184–195.
- [123] Gaboriaud, F., Gee, M. L., Strugnell, R., Duval, J. F.L., (2008). Coupled Electrostatic, Hydrodynamic, and Mechanical Properties of Bacterial Interfaces in Aqueous Media. *Langmuir*, 24, 10988–10995.
- [124] Duval, J. F. L., Wilkinson, K. J., van Leeuwen, H. P., Buffle, J., (2005). Humic Substances Are Soft and Permeable: Evidence from Their Electrophoretic Mobilities. *Environmental Science & Technology*, 39, 6435–6445.
- [125] Torchilin, V. P., (2007). Targeted pharmaceutical nanocarriers for cancer therapy and imaging. *The AAPS Journal*, 9, E128–E147.
- [126] Jiang, X., Wang, B., Li, C. Y., Zhao, B., (2009). Thermosensitive polymer brush-supported 4-N, N-dialkylaminopyridine on silica particles as catalyst for hydrolysis of an activated ester in aqueous buffers: Comparison of activity with linear polymer-supported version and effect of LCST transition. *Journal of Polymer Science Part A: Polymer Chemistry*, 47, 2853–2870.
- [127] Wu, T., Zou, G., Hu, J., Liu, S., (2009). Fabrication of photo switchable and thermotunable multicolor fluorescent hybrid silica nanoparticles coated with dye-labeled poly (N-isopropylacrylamide) brushes. *Chemistry of Materials*, 2, 3788–3798.
- [128] Pyun, J., Matyjaszewski, K., (2001). Synthesis of nanocomposite organic/inorganic hybrid materials using controlled/“living” radical polymerization. *Chemistry of Materials*, 13, 3436–3448.
- [129] Chanana, M., ahn, S., Georgieva, R., Lutz, F., Bumler, H., Wang, D., (2009). Fabrication of colloidal stable, thermosensitive, and biocompatible magnetite nanoparticles and study of their reversible agglomeration in aqueous milieu. *Chemistry of Materials*, 21, 1906–1914.
- [130] Ohshima, H., (2009). Theory of electrostatics and electrokinetics of soft particles. *Science and Technology of advanced Materials*, 10, 063001.
- [131] Duval, J. F. L., (2005). Electrokinetics of Diffuse Soft Interfaces. 2. Analysis Based on the Nonlinear Poisson– Boltzmann Equation. *Langmuir*, 21, 3247–3258.
- [132] Duval, J. F. L., Ohshima H., (2005). Electrophoresis of Diffuse Soft Particles. *Langmuir*, 22, 3533–3546.
- [133] Hill, R. J., Saville, D. A., Russel, W. B., (2003). Electrophoresis of spherical polymer coated particles. *Journal of Colloid and Interface Science*, 258, 56–74.
- [134] Zimmermann, R.; Kuckling, D.; Werner, C.; Duval, J. F. L., (2010). Electrokinetics of poly(N-isopropylacrylamide)-co-carboxyacrylamide soft thin-film. Evidence of diffuse segment distribution in the swollen state. *Langmuir*, 26, 18169–18181.
- [135] Zimmermann, R., Dukhin, S. S., Werner, C., Duval, J. F. L., (2013). On the use of electrokinetics for unraveling charging and structure of soft planar polymer films. *Current Opinion in Colloid and Interface Science*, 18, 83–92.
- [136] Debye, P., Bueche, A.J., (1948). Intrinsic viscosity, diffusion and sedimentation rate of polymers in solution. *Chemical Physics*, 16, 573–579.
- [137] Brinkman, H.C., (1955). A calculation of the viscous force exerted by a flowing fluid on a dense swarm of
-

- particles. *Applied Scientific Research A*, 1, 27–34.
- [138] Duval, J. F. L.; Ohshima, H., (2006). Electrophoresis of Diffuse Soft Particles. *Langmuir*, 22, 3533–3546.
- [139] Zimmermann, R.; Kuckling, D.; Kaufmann, M.; Werner, C.; Duval, J. F. L., (2010). Electrokinetics of a Poly(N-isopropylacrylamid-co-carboxyacrylamid) Soft Thin Film: Evidence of Diffuse Segment Distribution in the Swollen State. *Langmuir*, 26, 18169–18181.
- [140] Duval, J. F. L.; Küttner, D.; Nitschke, M.; Werner, C.; Zimmermann, R., (2011). Interrelations between charging, structure and electrokinetics of nanometric polyelectrolyte films. *Journal of Colloid and Interface Science*, 362, 439–449.
- [141] Duval, J. F. L.; Küttner, D.; Werner, C.; Zimmermann, R., (2011). Electrohydrodynamics of Soft Polyelectrolyte Multilayers: Point of Zero-Streaming Current. *Langmuir*, 27, 10739–10752.
- [142] Langlet, J.; Gaboriaud, F.; Gantzer, C.; Duval, J. F. L., (2008). Impact of chemical and structural Anisotropy on electrophoretic mobility of spherical soft multilayer particles/ The case of bacteriophage MS2. *Biophysical Journal*, 94, 3293–3312.
- [143] Duval, J. F. L.; Busscher, H. J.; van de Belt-Gritter, B.; van der Mei, H. C.; Norde, W., (2005). Analysis of the Interfacial Properties of Fibrillated and Nonfibrillated Oral Streptococcal Strains from Electrophoretic Mobility and Titration Measurements: Evidence for the Shortcomings of the 'Classical Soft-Particle Approach'. *Langmuir*, 21, 11268–11282.
- [144] Jiménez, M. L.; Delgado, A. V.; Ahualli, S.; Hoffmann, M.; Witteman, A.; Ballauff, M., (2011). Giant permittivity and dynamic mobility observed for spherical polyelectrolyte brushes. *Soft Matter*, 7, 3758–3762.
- [145] López-García, J. J.; Grosse, C.; Horno, J., (2003). Numerical study of colloidal suspensions of soft spherical particles using the network method: 2. AC electrokinetic and dielectric properties. *Journal of Colloid and Interface Science*, 265, 341–350.
- [146] Ohshima, H., (2001). Dynamic Electrophoretic Mobility of a Soft Particle. *Journal of Colloid and Interface Science*, 233, 142–152.
- [147] Ahualli, S.; Jiménez, M. L.; Carrique, F.; Delgado, A. V., AC Electrokinetics of Concentrated Suspensions of Soft Particles. *Langmuir* 2009, 25 (4), 1986–1997.
- [148] Tomalia, D. A.; Baker, H.; Dewald, J.; Hall, M.; Kallos, G.; Martin, S.; Roeck, J.; Ryder J.; Smith, P., (1985). A new class of polymers: starburst-dendritic macromolecules. *Polymer Journal*, 17, 117–132.
- [149] Tomalia, D. A., (1996). Starburst dendrimers-nanoscopic supermolecules according to dendritic rules and principles, *Macromolecular Symposia*, 101, 243–255.
- [150] Hawker, C.J.; Fréchet, J.M.J., (1990). Preparation of polymers with controlled molecular architecture. A new convergent approach to dendritic macromolecules, *The Journal of the American Chemical Society*, 112, 7638–7647.
- [151] Tomalia, D. A., (2004). Birth of a new macromolecular architecture: dendrimers as quantized building blocks for nanoscale synthetic organic chemistry, *Aldrichimica Acta*, 37, 39–57.
- [152] Tomalia, D. A.; Esfand, R., (1997). Dendrons, dendrimers and dendrigrafts. *Chemistry and Industry*, 11, 416–420.
- [153] Tomalia, D. A.; Naylor, A. M.; Goddard III, W. A., (1990). Starburst dendrimers: Molecular-level control of size, shape, surface chemistry, topology, and flexibility from atoms to macroscopic matter. *Angewandte Chemie International Edition in English*, 29, 138–175.
- [154] Ballauf, C.; Likos, L., (2004). Dendrimers in Solution: Insight from Theory and Simulation, *Angewandte Chemie International Edition*, 43, 2998.
- [155] Rietveld, I.B.; Bouwman, W.G.; Baars, M.W.P.L.; Heenan, R.K., (2001). Location of the Outer Shell and Influence of pH on Carboxylic Acid-Functionalized Poly(propyleneimine) Dendrimers. *Macromolecules*, 34, 8380.
- [156] Welch, P.; Muthukumar, M., (1998). Tuning the Density Profile of Dendritic Polyelectrolytes. *Macromolecules*, 31, 5892.
- [157] Esfand, R.; Tomalia, D. A., (2001). Poly(amidoamine) (PAMAM) dendrimers: from biomimicry to drug

- delivery and biomedical applications. *Drug Discovery Today*, 6, 427–436.
- [158] Patri, A.K., Majoros, I., Baker Jr, J.R., (2002). Dendritic polymer macromolecular carriers for drug delivery. *Current Opinion in Chemical Biology*, 6, 466–471.
- [159] Kukowska-Latallo, J. F., Candido, K. A., Cao, Z., Nigavekar, S. S., Majoros, I. J., Thomas, T. P., Balogh, L. P., Khan, M.K., Baker Jr, J. R., (2005). Nanoparticle targeting of anticancer drug improves therapeutic response in animal model of human epithelial cancer. *Cancer Research*, 65, 5317–5324.
- [160] Tomalia, D. A., Baker, H., Dewald, J.R., Hall M., Kallos G., Martin S., Roeck J., Ryder J., Smith P., (1986). Dendrimers II: architecture, nanostructure and supramolecular chemistry. *Macromolecules*, 9, 2466.
- [161] Froehling, PE. (2001). Dendrimers and dyes – a review. *Dyes Pigments*, 9, 187–195.
- [162] Wiwattanapatapee, R., Jee, R. D., Duncan. R., (1999). PAMAM dendrimers as a potential oral drug delivery system: Dendrimer complexes with piroxicam. *In Controlled Release of Bioactive Materials, Boston, MA*, 145–146.
- [163] Delong, R., Stephenson, K., Fisher, T. L. M., Alahari, S., Nolting, A., Juliano, R. L., (1997). Characterization of complexes of oligonucleotides with polyamidoamine starburst dendrimers and effects on intracellular delivery. *Journal of pharmaceutical sciences*, 86, 762–764.
- [164] Kukowska-Latallo, J.F., Bielinska, A.U., Johnson, J., Spindler, R., Tomalia, D. A., Baker Jr., J.R., (1996). Efficient transfer of genetic material into mammalian cells using Starburst polyamidoamine dendrimers. *Proceedings of the National Academy of Sciences of the U.S.A.* 93, 4897–4902.
- [165] Eichman, J.D., Bielinska, A.U., Kukowska-Latallo, J.F., Baker Jr., J.R., (2000). The use of PAMAM dendrimers in the efficient transfer of genetic material into cells. *Pharmaceutical Science & Technology Today*, 3, 232–245.
- [166] Luo, D., Haverstick, K., Belcheva, N., Han, E., Saltzman W.M., (2002). Poly(ethylene glycol)-Conjugated PAMAM Dendrimer for Biocompatible, High-Efficiency DNA Delivery. *Macromolecules*, 35, 3456–3462.
- [167] Haensler, J., Szoka, F. C., (1993). Polyamidoamine cascade polymers mediate efficient transfection of cells in culture. *Bioconjugate Chemistry*, 4, 372–379.
- [168] Tang, M. X., Redemann, C. T., Szoka, F. C., (1996). In vitro gene delivery by degraded polyamidoamine dendrimers. *Bioconjugate Chemistry*, 7, 703–714.
- [169] Tang, M. X., Szoka, F. C., (1997). The influence of polymer structure on the interactions of cationic polymers with DNA and morphology of the resulting complexes. *Gene Therapy*, 4, 823–832.
- [170] Halford, B., (2005). *Chemical & Engineering News*, 13, 30–36
- [171] Bernejo, J. F., Ortega, P., Chonco, L., Eritja, R., Samaniego, R., Müllner, M., de Jesus, E., de la Mata, F. J., Flores, J. C., Gomes, R., Muñoz-Fernández, A., (2007). Water-soluble carbosilane dendrimers: synthesis biocompatibility and complexation with oligonucleotides; evaluation for medical applications. *Chemistry A European Journal*, 13, 483–495.
- [172] Shaunak, S., Thoas, S., Gianasi, E., Godwin, A., Jones, E., Teo, I., Mireskandari, K., Luthert, P., Duncan, R., Patterson, S., Khaw, P., Brocchini, S., (2004). Polyvalent dendrimer glucosamine conjugates prevent scar tissue formation. *Nature Biotechnology*, 22, 977–984.
- [173] Wathier, M., Johnson, S.M., Kim, T., Grinstaff, M.W., (2006). Hydrogels formed by multiple peptide ligation reactions to fasten corneal transplants. *Bioconjugate Chemistry*, 17, 873–876.
- [174] Stupp, S. I., lecture at EURESC Symposium “Supramolecular Chemistry” in Bern, October 2–5.
- [175] Diallo, M. S., Balogh, L., Shafagati, A., Johnson Jr., J. H., Goddard III, W. A., Tomalia, D. A., (1999). Poly(amidoamine) dendrimers: A new Class of High Capacity Chelating Agents for Cu(II) Ions. *Environmental Science and Technology*, 33, 820–824.
- [176] Diallo, M.S., Christie, S., Swaminathan, P., Balogh, L., Shi, X., Um, W., Papelis, C., Goddard III, W.A., Johnson Jr, J.H., (2004). Dendritic chelating agents. 1. Cu(II) binding to ethylene diamine core

- poly(amidoamine) dendrimers in aqueous solutions.. *Langmuir*, 20, 2640–2651.
- [177] DeFever, R. S., Geitner, N. K., Bhattacharya, P., Ding, F., Ke, P. C., Sarupria, S., (2015). PAMAM Dendrimers and Graphene: Materials for Removing Aromatic Contaminants from Water. *Environmental Science & Technology*, 49, 4490–4497.
  - [178] Wiesler, U.-M., Müllen, K., (1999), Polyphenylene dendrimers via Diels–Alder reactions: the convergent approach. *Chemical Communications*, 22, 2293–2294.
  - [179] Cheng, L., Pacey, G.E., Cox, J.A., (2001). Preparation and electrocatalytic applications of a multilayer nanocomposite consisting of phosphomolybdate and poly(amidoamine). *Electrochimica Acta*, 46, 4223–4228.
  - [180] Nevins Buchanan, S.A., Balogh, L.P., Meyerhoff, M.E., (2004). Potentiometric Response Characteristics of Polycation-Sensitive Membrane Electrodes toward Poly(amidoamine) and Poly(propylenimine) Dendrimers. *Analytical Chemistry*, 76, 1474–1482.
  - [181] Snejdarkova, M., Svobodova, L., Evtugyn, G., Budnikov, H., Karyakin, A., Nikolelis, D.P., Hianik, T., (2004). Acetylcholinesterase sensors based on gold electrodes modified with dendrimer and polyaniline, A comparative research. *Analytica Chimica Acta*, 514, 79–88.
  - [182] Shen, L., Hu, N., (2004). Heme protein films with polyamidoamine dendrimer: direct electrochemistry and electrocatalysis. *Biochimica et Biophysica Acta (BBA) - Bioenergetics*, 1608, 23–33.
  - [183] Grabchev, I., Bojinov, V., Chovelon, J.M., (2003). Synthesis, photophysical and photochemical properties of fluorescent poly(amidoamine) dendrimers. *Polymer*, 44, 4421–4428.
  - [184] Ispasoiu, R. G., Balogh, L., Varnavski, O. P., Tomalia, D. A., Goodson III., T. G., (2000). Large Optical Limiting from a novel Metal–dendrimer nanocomposite Materials. *Journal of the American Chemical Society*, 122, 11005–11006.
  - [185] Senarath-Yapa, M.D., Saavedra, S.S., (2001). Dye leaching from a doped sol–gel is eliminated by conjugation to a dendrimer. *Analytica Chimica Acta*, 432, 89–94.
  - [186] Kobayashi, H., Kawamoto, S., Jo, S.-K., Bryant, H. L., Brechbiel, M. W., Star, R. A., (2003). Macromolecular MRI Contrast Agents with Small dendrimers: Pharmacokinetic differences between Sizes and Cores. *Bioconjugate Chemistry*, 14, 388–394.
  - [187] Andolina, C. M., Klemm, P. J., Floyd III, W. C., Fréchet J. M. J., Raymond, K. N., (2012). Analysis of Lanthanide Complex Dendrimer Conjugates for Bimodal NIR and MRI Imaging. *Macromolecules*, 45, 8982–8990.
  - [188] Grabchev, X., Qian, V., Bojinov, Y., Xiao, W., Zhang., (2002). Synthesis and photophysical properties of 1,8-naphthalimide-labelled PAMAM as PET sensors of protons and of transition metal ions. *Polymer*, 43, 5731–5736.
  - [189] Sayed-Sweet, Y., Hedstrand, D. M., Spinder, R., Tomalia, D. A., (1997). Hydrophobically modified poly(amidoamine) (PAMAM) dendrimers: their properties at the air–water interface and use as nanoscopic container molecules. *Journal of Materials Chemistry*, 7, 1199–1205.
  - [190] Sui, G., Micic, M., Huo, Q., Leblanc, R. M., Synthesis and Surface Chemistry Study of a New Amphiphilic PAMAM Dendrimer. (2000). *Langmuir*, 16, 7847–7851.
  - [191] Khopade, A. J., Caruso, F., (2002). Investigation of the factors influencing the formation of dendrimer/polyanion multilayer films. *Langmuir*, 18, 7669–7676.
  - [192] Tsukruk, V. V., (1998). Dendritic Macromolecules at Interfaces. *Advanced Materials*, 10, 253–257.
  - [193] Kim, B., Bruening, M. L., (2003). pH-Dependent growth and morphology of multilayer dendrimer/poly(acrylic acid) films. *Langmuir*, 19, 94–99.
  - [194] Khopade, A. J., Caruso, F., (2002). Electrostatically assembled polyelectrolyte/dendrimer multilayer films as ultrathin nanoreservoirs. *Nano Letters*, 2, 415–418.
  - [195] Duncan, R., Izzo, L., (2005). Dendrimer biocompatibility and toxicity, *Advanced Drug Delivery Reviews*, 57,

- 2215–2237.
- [196] Boas, U., Heegaard, P.M.H., (2004). Dendrimers in drug research. *Chemical Society Reviews*, 33, 43–63.
- [197] Jevprasesphant, R., Penny, J., Jalal, R., Attwood, . , McKeown, . . , Emanuele, A., 2 ). The influence of surface modification on the cytotoxicity of PAMAM dendrimers, *International Journal of Pharmaceutics*, 252, 263–266.
- [198] El-Sayed, M., Ginski, M., Rhodes, C., Ghandehari, H., (2002). Transepithelial transport of poly(amidoamine) dendrimers across Caco-2 cell monolayers. *Journal of Controlled Release*, 81, 355–365.
- [199] Fischer, D., Li, Y., Ahlemeyer, B., Krieglstein, J., Kissel, T., (2003). In vitro cytotoxicity testing of polycations: influence of polymer structure on cell viability and hemolysis. *Biomaterials*, 24, 1121–1131.
- [200] Malik, N., Wiwattanapatapee, R., Klopsch, R., Lorenz, K., Frey, H., Weener, J.W., Meijer, E.W., Paulus, W., Duncan, R., (2000). Dendrimers: relationship between structure and biocompatibility in vitro, and preliminary studies on the biodistribution of I-125-labelled poly(amidoamine) dendrimers in vivo. *Journal of Controlled Release*, 65, 133–148.
- [201] Roberts, C., Bhalgat, M.K., Zera, R.T., (1996). Preliminary biological evaluation of poly(amidoamine) (PAMAM) starburst dendrimers, *Journal of Biomedical Materials Research*, 30, 53–65.
- [202] Lee, J-H, Cha, K. E., Kim, M. S., Hong, H. W., Chung, D. J., Ryu, G., Myung, H., (2009). Nanosized polyamidoamine (PAMAM) dendrimer-induced apoptosis mediated by mitochondrial dysfunction. *Toxicology Letters*, 190, 202–207.
- [203] Li, C., Liu, H., Sun, T., Wang, H., Guo, F., Rao, S., Deng, J., Zhang, Y., Miao, Y., Guo, C., Meng, J., Chen, X., Li, L., Li, D., Xu, H., Wang, H., Li, B., Jiang, C., (2009). PAMAM nanoparticles promote acute lung injury by inducing autophagic cell death through the Akt-TSC2-mTOR signaling pathway. *Journal of Molecular Cell Biology*, 1, 37–45.
- [204] Chauhan, A. S., Jain, N. K., Diwan, P. V., (2010). Pre-clinical and behavioural toxicity profile of PAMAM dendrimers in mice. *Proceedings of the Royal Society A*, 466, 1535–1550.
- [205] Petit, A-N., Eullaffroy, P., Debenest, T., Gagné, F., (2010). Toxicity of PAMAM dendrimers to *Chlamydomonas reinhardtii*. *Aquatic Toxicology*, 100, 187–193.
- [206] Heiden, T.C., Dengler, E., Kao, W.J., Heideman, W., Peterson, R.E., (2007). Developmental toxicity of low generation PAMAM dendrimers in zebrafish. *Toxicology and Applied Pharmacology*, 225, 70–79.
- [207] Suarez, I. J., Ucles, A., Rosal, R., Rodriguez, A., er nando, M. . , Garcia-Calvo, E., Fernandez-Alba, A. R., (2011). Chemical and ecotoxicological assessment of poly(amidoamine) dendrimers in the aquatic environment. *TrAC Trends in Analytical Chemistry*, 30, 492–506.
- [208] Naha, P. C, Davoren M., Casey, A., Byrne, H. J., (2009). An ecotoxicological study of poly(amidoamine) dendrimers-toward quantitative structure activity relationships. *Environmental Science & Technology*, 43, 6864–6869.

## **Chapter II**

# **Materials and Methods**

## II.1. Materials and samples preparation

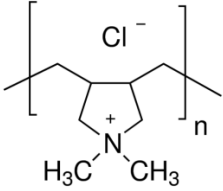
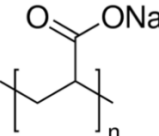
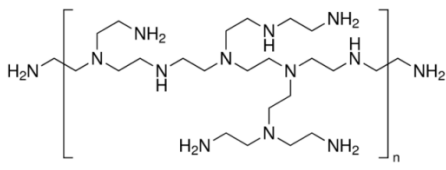
### II.1.1. The polyelectrolyte solutions

To construct the films used in this work, PDADMAC was selected as a polycation and PAA as a polyanion. All polyelectrolytes involved in the building of the multilayer films are mentioned in table 2.1. PDADMAC, a strong polyelectrolyte with a charge density that is independent of solution pH, was dissolved at a concentration of 5 mg/mL. PAA was dissolved at a concentration of 3 mg/mL. Unlike PDADMAC, PAA is a weak polyelectrolyte with a pH-dependent charge density. The pH of the PAA solution was adjusted to 3 (with use of HCl) or 6 with use of Tris buffer, depending on the desired film properties (in particular with regard to surface roughness). In all cases, the pH of the PDADMAC solution was set to 6 (natural pH of 10 mM NaNO<sub>3</sub>) with or without the use of Tris buffer (Tris buffer was used for experiments where PAA solution at pH=6 were considered).

Similarly, the choice of the polyelectrolyte solution concentrations was adopted after several trials that helped in choosing the polycation/polyanion concentrations ratio leading to the searched film properties. Both polyelectrolytes were dissolved in a        at 10 mM. Higher ionic strengths were also tested to modulate film thickness and stiffness.        was dissolved in ultra-pure water 18.2 MΩ/cm, Mili-Q-plus, Milipore) buffered by Tris buffer. The PEI, a polycation, (1 mg.mL<sup>-1</sup> in water) was used as an initiator layer in order to enhance the fixation of the film on the substrate. All solutions were filtered with PSS membrane filters (0.2 μm, Millipore).

The choice of the ionic strength and pH was motivated by data mentioned in literature [1, 2]. The goal was to obtain films of ~1 μm in thickness, which we considered thick enough to be loaded with nanodendrimers. Such thickness was achieved with PAA dissolved at pH 3 in 10 mM        . Yet, under such conditions the films showed high rigidity and atypical structural instability that we investigated in details (see related results in Chapter 3). Therefore, for the films to be loaded with nanodendrimers, solution ionic strength was maintained at 10 mM and all polyelectrolyte solutions were dissolved in 10 mM        in Tris buffer (1M) at pH 6. The resulting films displayed the searched properties in terms of thickness and stiffness in order to be loaded successfully with nanodendrimers. It is worth mentioning that films prepared under various ionic strength conditions were tested (50 mM,

100 mM, and 150 mM) at pH 3, but we did not observe any significant changes in film thickness, and we systematically identified solution pH as the major parameter that impacted film structure and elasticity. An explanation for this pH effect is proposed in Chapters 3 and 5.

Polyelectrolyte	Structural Formula	Molecular mass $M_w$ (g/mol)	pK <sub>a</sub>	Supplier
Poly(diallyldiméthyl Ammonium chloride) (PDADMAC)		400 000-500 000	-	Sigma-Aldrich
Poly(acrylic acid sodium salt) (PAA)		50 000	4.5	Polysciences
Poly(ethyleneimine) (PEI)		750 000	6-10	Sigma-Aldrich

**Table 2.1.** Polyelectrolytes used for construction of PEM films

### II.1.2. Construction of the — ( D D - ) films

For AFM experiments, multilayer films were deposited on bare borosilicate glass slides of 1-1.2 cm in thickness (preciver, France). The glass slides were cleaned using a detergent (Sodium dodecyl sulfate, or SDS 1%) for 30 minutes at 60°C, followed by a rinsing step with Milli-Q water, then with HCl (0.1 M) for 30 minutes at 60°C, followed again by water rinsing, ethanol rinsing then drying under nitrogen flux. The final step was a UV ozone cleaning treatment (UV ozone cleaner, Novascan) for 30 minutes at 40°C.



Germanium crystals (12 mm in diameter, 1 cm in thickness) were used as supporting substrates for the construction of the films investigated by Raman confocal microscopy (RCM). Quartz crystals were employed for *in situ* construction of films analyzed by Quartz Crystal Microbalance with Dissipation Monitoring (QCMD). Both types of substrates were cleaned according to the procedure mentioned above for glass slides.

PEI – (PDADMAC – PAA) films were then constructed by automatic dip coating, i.e. the alternative dipping of the substrates in the proper polyelectrolyte solutions [3], which was realized with use of an automatic dipping robot (Riegler & Kirsten GmbH, Germany) (Figure 2.1. *Automated dip coating (Dipping robot, Riegler and Kirstien, GmbH, Berlin, Germany)*). Each dipping cycle corresponds to the buildup of one bilayer, i.e. one layer of polycation and one layer of polyanion. The dipping robot was programmed so that each cycle consisted in immersing the substrate in a first polyelectrolyte solution for 5 minutes, followed by two rinsing steps in  $\text{NaNO}_3$  solution (5 minutes each), then immersing the substrate in the second polyelectrolyte solution, followed again by two rinsing steps of 5 minutes each. For all experiments performed, 30 bilayer films were constructed and are subsequently denoted as  $\text{PEI}-(\text{PDADMAC}/\text{PAA})_{30}$ . It is stressed that the substrates are fixed on adequate sample



**Figure 2.36.** *Automated dip coating (Dipping robot, Riegler and Kirstien, GmbH, Berlin, Germany)*

holders that could be easily removed and attached to the dipping robot. The sample holders were also cleaned before and after each deposition experiment upon immersion for few hours in a concentrated nitric acid solution, followed by rinsing with water then cleaning with the

same protocol adopted for the glass slides. Once constructed, the films were stored in  $\text{NaNO}_3$  solution in sterile wells, used directly or kept at  $4^\circ\text{C}$  prior to experiments.

### **II.1.3. Heating and aging of the films**

Films were heated in  $\text{NaNO}_3$  solution (10mM) at  $60^\circ\text{C}$ . A thermometer was used to monitor the temperature and ensure its stability. The beaker in which the films were heated was kept closed to avoid any variation in solution ionic strength as a result of evaporation. Films were heated for 1, 2 and 6 hours successively in order to investigate the effect of heating time on film structure and mechanical properties. All experiments making use of heated films were carried on directly immediately after the heating stage. In addition, the natural-aging films were stored in sterile wells filled with  $\text{NaNO}_3$  solution (10mM) at room temperature.

### **II.1.4. Electrokinetics of the nanodendrimers**

Commercial carboxylated poly(amido)-amine (PAMAM) dendrimers of half generations G4.5 and G6.5 (Sigma Aldrich, USA) were diluted to 0.1%v for all electrophoretic mobility and size measurements. The pH of the dispersions was adjusted by the addition  $\text{NaOH}$  (0.1 M) and  $\text{HNO}_3$  (0.1 M). The ionic strength of the dispersions was adjusted with addition of  $\text{NaNO}_3$  (0.5, 1, and 2 M). The size measurements were carried out in disposable polystyrene cuvettes (Malvern Instruments Ltd, UK) filled with 1 mL of the dendrimers suspension. The salt was added to the measurement cell with the aid of a micropipette followed by rigorous shaking in order to homogenize the cell content. For the electrophoretic mobility measurements, disposable folded capillary cells (or zeta cells) (Malvern Instruments Ltd, UK) were filled with dendrimers suspension after the adjustment of their ionic strength to desired value. All electrokinetic and size measurements were performed at room temperature. Commercially available G6.5 PAMAM dendrimers were employed less than three months after their purchase. The here-reported mobility and size results are an average of at least three measurements collected on different fresh dendrimer suspensions.

### **II.1.5. Loading the films with nanodendrimers**

For (PDADMAC – PAA)<sub>30</sub> multilayer films to be loaded with nanodendrimers, the polyelectrolyte solutions were dissolved in NaNO<sub>3</sub> solution (10mM) buffered by Tris-buffer at pH 6 were constructed. The films were used without further heating treatment and/or aging delay. G6.5 PAMAM carboxylated dendrimers dispersions at different concentrations (0.2, 0.5, 0.8, and 2 g/L) were prepared in NaNO<sub>3</sub> solution (10mM), Tris buffer (1M) at pH 6. The G6.5 dendrimers were brought into contact with the films at room temperature for 24 hours in sterile wells (4 mL) prior to AFM experiments. AFM Peak force images and elasticity evaluations were carried out for (PDADMAC – PAA)<sub>30</sub> films loaded with G6.5 at 0.2, 0.5, 8, and g/L and for control films (i.e. not loaded by dendrimers).

## **II.2. Characterization methods**

### **II.2.1. Atomic force microscopy (AFM)**

The atomic force microscopy (AFM) was developed by Binnig et al. in 1986 based on the principle of the scanning tunneling microscopy (STM) which allowed the imaging of surfaces of conducting and semiconducting materials [4, 5, 6]. The STM allowed the imaging of single atoms on flat surfaces. In the same context, the scanning near-field optical microscope (SNOM) was invented which allowed microscopy with light below the optical resolution limit. AFM was the last one in the series of techniques belonging to the family of scanning-probe microscopes (SPM) which includes new microscopic techniques all based on the generation of images of surfaces by measuring the physical interaction between a sharp nanometric tip and a sample of interest rather than by using an incident beam (light or electrons) as in classical microscopy. AFM allows the imaging of both conducting and insulating surfaces, in vacuum, air, liquids with an atomic scale resolution [7, 8].

### II.2.1.1. AFM technique and principles

An atomic force microscope consists mainly of an AFM probe, a sample stage with a ceramic piezoelectric, and an optical detection system, which comprises a laser diode and a photodetector. An AFM probe consists of a support chip to which a spring cantilever is attached (Figure 2.4. *Schematic representation of an AFM probe*). A ceramic piezoelectric translator controls the three dimensional movement of the sample relative to the probe.

The AFM technique is based on the movement of the spring cantilever onto which an AFM tip is mounted. The cantilever, while scanning the sample of interest, is deflected. This deflection or bending is used to measure the force between the tip and the sample. The deflection of the cantilever is detected by the photodetector. For that purpose, a laser beam is focused on the cantilever and the variations in position of the reflected beam are detected by a photodetector with four quadrants (Figure 2.2. *Schematic diagram of atomic force microscopy*). When the reflected beam is deviated, the intensity of the signal received by each of the quadrants of the detector changes. The light intensity is then converted into an electrical signal and the voltage applied to the piezoelectric translator is recorded by an acquisition card and transmitted via a computer to data processing software. The conversion of the electrical signals from volts into nm is formed directly by the software.

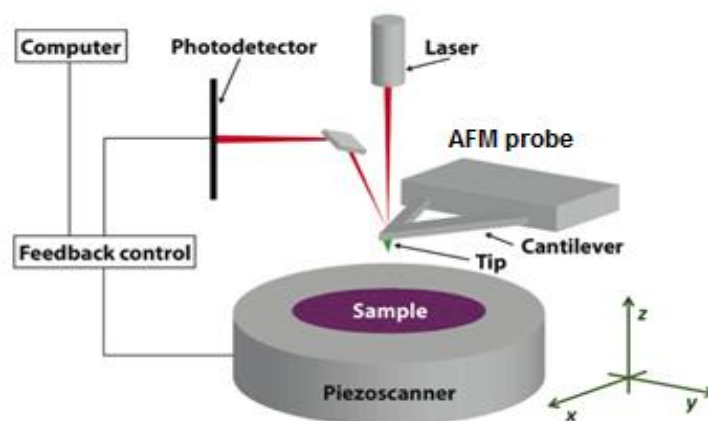


**Figure 2.37.** *Schematic diagram of atomic force microscopy* [74]

Since its invention and within only two and half decades, AFM had quickly become a powerful multifunctional research tool due to its various potentialities ranging from topographical applications as a high-resolution surface imaging technique at the nanometer

scale to measuring the forces between two elements and thus offering new surface characterization opportunities. The non-topographical applications include the quantification of the mechanical properties of a viscoelastic material as well as its electrical, chemical, adhesive and capacitive features [9], surface roughness, friction or rigidity. Moreover, AFM tips can be functionalized with molecules, proteins, or cells so that the interactions between a functionalized tip and a surface of interest can be studied by so-called molecular recognition measurements [10, 11]. Force measurements using a functionalized AFM tip can be used to map the spatial distribution of functional groups on a sample surface [12, 13], and to measure the forces between the interacting molecules [14, 15]. In biological sciences, AFM allows samples (cells, biomolecules, cell compartments, *etc.*) to be imaged *in situ* under physiological conditions. Besides imaging, the AFM technique can provide information about single cell mechanics, cell stiffness and the binding force of individual molecular complexes [16, 17, 18]. Cell stiffness was investigated as a powerful tool for cancer detection on a single cell level [19, 20, 21]. In addition, AFM measurements allowed the conformational analysis of the DNA double-helix [22, 23, 24, 25] and direct measurement of DNA mechanical properties [26]. Quantification of bacterial adhesion forces was also achieved using AFM [27]. Applications in biochemistry include imaging of the structure of different molecules like proteins [28, 29, 30], lipids [31], carbohydrates [32], identification of individual polysaccharide molecules in solution [33], detection and localization of individual antibody-antigen recognition events [34], measuring the mechanical properties of proteins and the strength of intermolecular and intramolecular bonds [35, 36], and the conformational alteration of polysaccharides [37]. Applications of AFM in chemistry, materials science and nanotechnology include the visualization of polymer nanostructure, morphology and properties [38, 39]. Atomic force microscopy has also allowed the visualization of microsurfaces and polymeric matrices that have been inaccessible with other imaging techniques [40]. It made possible the measuring of the structural and mechanical properties of thin polymer films [41, 42, 43, 44]. Researchers also were able to achieve a real-space visualization of the formation of hydrogen bonding via AFM imaging [45]. Biophysical applications include probing of double-layer forces [46]. Recent developments of AFM combine the traditional AFM setup with other techniques for more detailed investigation of materials. Examples include combined AFM-optical microscope, AFM-Raman, and AFM-confocal fluorescence microscopy.

---



**Figure 2.38.** Dimension FastScan AFM setup. (1) Acoustic and Vibration Isolation Enclosure; (2) Scanners (includes 2, see right); (3) Ultra-Stable High-Resonance Microscope Base; (4) 30" Monitor and FastScan Nanoscope Software; (5) Computer; (6) Nanoscope voltage stage controller and HV amplifier. [75]

### II.2.1.2. AFM cantilevers and probes

As mentioned before, an AFM probe consists of a support chip to which a spring cantilever is attached (Figure 2.4. *Schematic representation of an AFM probe*). The cantilever acts as a spring nanoindenter. The micro-fabricated cantilevers used nowadays were invented in the early 90's by Quate [47, 48] and Wolter [49]. Cantilevers differ in terms of geometry, coating, and spring constant (typically  $\sim 0.1$ -1 N/m). Mainly rectangular and triangular cantilevers are commonly used. Typically, most cantilevers are made of silicon or silicon nitride. AFM tips are mounted on the cantilevers and are generally characterized by a specific tip radius and a tip half angle. Most of the tips have a pyramidal shape with three or four side walls with an angle (usually) 35 degrees and a length of about  $4\mu\text{m}$  between the tip end and the cantilever. The tip is made out of the same material as the cantilever with a radius ranging from 20 to 50

nm. The choice of the cantilever depends mainly on the stiffness of the sample and the type of measurement intended. Often the backside of the cantilever is covered with a thin gold layer to enhance its reflectivity.

Prior to all AFM experiments, two main parameters related to the cantilever are calibrated: deflection sensitivity, and cantilever's spring constant. The deflection sensitivity factor is the conversion factor of the detector signal in volts to cantilever deflection in nanometers. It is calculated from force curves measured on a rigid surface (usually a bare glass slide). The spring constant of the cantilever is calibrated generally according to thermal

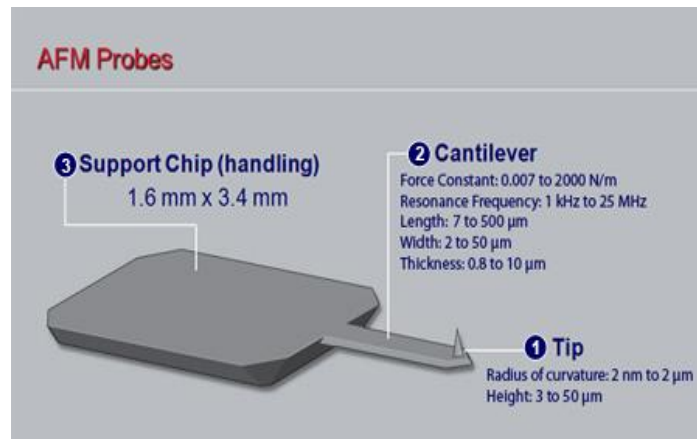


**Figure 2.39.** Schematic representation of an AFM probe [76]

tune method [50]. This method is based on modeling the cantilever as a simple harmonic oscillator [51, 52]. It mainly measures the cantilever's mechanical response to thermal noise.

The thermal (Brownian) motion of the cantilever's fundamental oscillation mode is related to its thermal energy ( $k_B T$ ) by the energy equipartition theorem:

$$= c \overline{\left\{ \frac{z_c^2}{c} \right\}} \quad (2.1)$$

where  $k_B$  is the Boltzmann constant ( $1.8 \times 10^{-23}$  J/K),  $c$  is a constant related to the geometry of the cantilever [52],  $T$  is the temperature, and  $z_c^2$  is the mean square displacement of the cantilever with respect to its reference position at  $z_c^2 = 0$ .

The manipulation is simple, after acquiring a force curve on a hard substrate for the calculation of the deflection sensitivity, the thermal motion of the cantilever is measured. The computation of the corrected spring constant is automated. In general, all AFM softwares

have algorithms that make use of the thermal noise data in order to calibrate the spring constant in air or in fluid medium.

In the AFM experiments we carried, the NanoScope Software, based on the aforementioned technique, allowed the real-time calibration of the probe spring constant with very short measurement and computation times (less than a minute per cycle of real-time measurement and spring constant calibration).

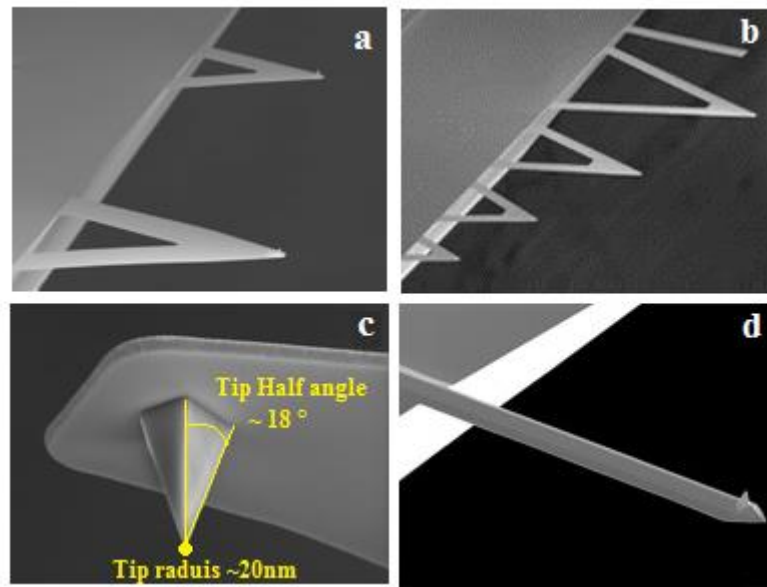


**Figure 2.40.** Scanning Electron Microscopy of AFM cantilevers. (a) NPG-10 probe with triangular cantilevers; (b) MLCT probe with triangular and rectangular cantilevers; (c) AFM tip with a rotated (symmetrical) geometry; (d) Rectangular cantilever. [78]

### II.2.1.3. Different AFM modes

In general, AFM imaging operates using three modes, the contact mode, the tapping intermittent mode, and the non-contact mode (Figure 2.6). These modes correspond to different types of interactions between the tip and the surface (Figure 2.10. *The sketch of forces of interaction ( $F_{int}$ ) as a function of tip-sample separation distance ( $z_d$ ).*

The contact mode was the first established AFM imaging mode. It is based on the use of repulsive forces. The probe remains in contact with the sample all the time. The cantilever



deflects periodically with the applied force (i.e. imaging force) maintained constant by the feedback system while the tip scans the surface by moving the sample using the Z-piezoelectric translator. This Z-piezo movement at each pixel location generates a height profile image of the surface. This method of operation is suitable for wet or dry imaging and can reach atomic resolution. AFM Contact mode provides information about the surface topography as well as friction forces exerted between tip and surface. A limitation is that constant contact with the surface can cause damage to both the sample (especially soft biological samples and LBL films) and the probe as lateral forces develop with scanning.

The non-contact mode, first introduced in 1987 by Martin *et al.* [53], uses attractive inter-atomic forces between the tip and the sample surface. The attractive forces are often too small for traditional direct current (DC) methods to resolve a surface topography so a piezoelectric modulator is used so that the cantilever oscillates close to its resonance

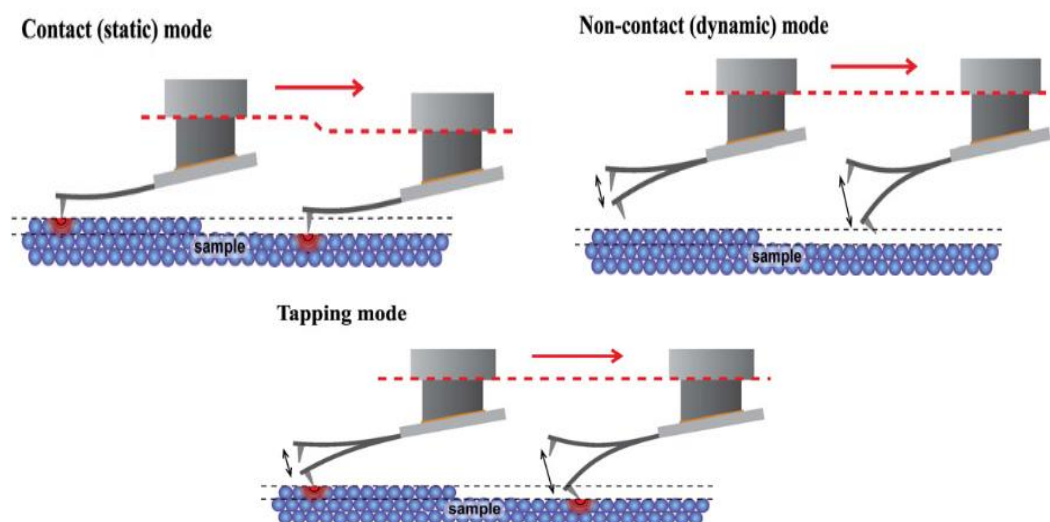


**Figure 2.41.** Different modes of AFM operation [79]

frequency at a small distance (1-10 nm) above the surface. As the tip approaches a sample, the van der Waals attractive forces between the tip and the sample induce changes in the amplitude, frequency and phase of the cantilever oscillation. Maintaining a constant tip-sample distance during scanning is necessary in this mode to prevent any contact between the tip and the sample surface, since if the tip accidentally contacts the sample, the tip can stick to the sample surface and stop its vibration due to the force of the liquid layer on the sample surface. The non-contact mode is rarely used, because the attractive forces are weak and

require a low noise environment. Furthermore, the sample surface is always covered with a thin layer (of the order of a nanometer), consisting mainly of water vapor and other pollutants. This layer necessarily affects the measurements.

The intermittent contact or Tapping Mode was first introduced in 1993 [54, 55]. In this mode the cantilever is oscillated near its resonance frequency (in the order of 10 to 100 kHz), but unlike non-contact mode, the cantilever gently taps the surface during scanning, greatly reducing damaging lateral forces. During scanning an electronic feedback loop ensures that the oscillation amplitude remains constant. The amplitude of the oscillation is set between 10 and 100 nm, and the probe "taps" the surface at the end of its bounce (downward movement) which reduces the contact time and the friction forces compared to contact-mode. When the tip is brought close to the sample the forces between the tip and the sample will cause a shift of the resonance frequency of the cantilever. If the cantilever is excited at a fixed frequency, the amplitude of the oscillation changes. This change is detected by the photodiode and a controller changes the distance between tip and sample so that the preset amplitude remains constant. Tapping mode in fluids was first introduced in 1994.

Besides its imaging mode, non-imaging AFM modes had been developed. An AFM can be used as a spectroscopy tool, probing the tip-sample interactions, and thus providing information about the adhesive and mechanical properties of the surface. Force spectroscopy was developed in the early nineties [56] and is being widely used nowadays.

PeakForce Tapping<sup>®</sup> by Bruker [57] is a recently patented mode in which the probe oscillates at a set frequency of 1 kHz. Unlike in tapping mode where the cantilever vibration amplitude is kept constant by the feedback loop, in PeakForce Tapping the maximum force (Peak Force) on the tip is directly controlled, it can be fixed down to 10 pN. This allows the minimization of the force and thus the tip-sample contact area which protects the tip and reduces the sample damage. With each tap of the tip on the sample surface a force curve is captured and the maximum peak force of the tap is used as the feedback signal. Peak Force Tapping offers a quantitative mapping of the electrical, mechanical, biological, and chemical properties of a sample besides the high resolution imaging of the surface topography. It's the first technique that provides direct nanoquantification of the AFM signals at high resolution.

Peakforce Quantitative Nanomechanical Mapping<sup>™</sup> (QNM) [58] is a PeakForce Tapping based image optimization technique. PeakForce QNM<sup>™</sup> maps and provides

information about nanomechanical properties simultaneously with imaging the sample topography at a high resolution. It is non-destructive to both tip and sample since it directly controls the peak normal force and minimizes the lateral force on the probe. A force curve is captured and saved at every pixel in the image. The sample properties including elastic modulus, adhesion, dissipation, and deformation are obtained from the analyzed curves and the information is sent directly to one of the image data channels while imaging continues at usual imaging speeds (Figure 2.7). The result is images that contain maps of material properties of the sample. Mechanical properties can be extracted from the calibrated force curves. PeakForce mapping employs a sinusoidal modulation of the base of the cantilever relative to the sample surface allowing the acquisition of more detailed material property

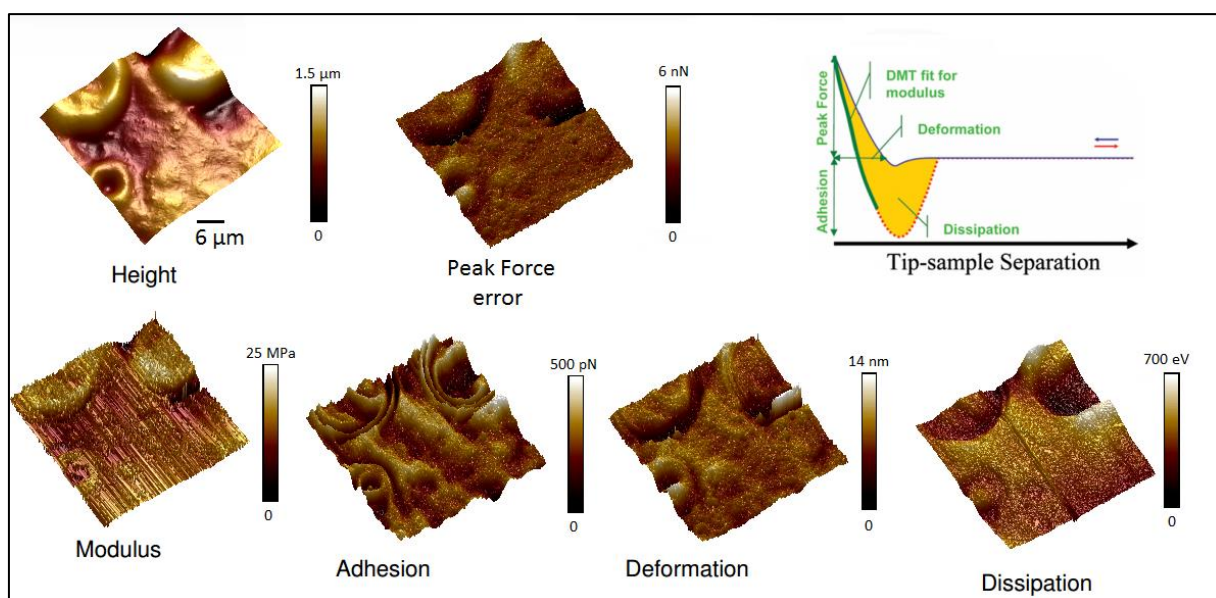


**Figure 2.42.** Real time QNM data obtained from different measurement channels for a (PDADMAC – PAA)<sub>30</sub> film at pH 3 in 10mM NaNO<sub>3</sub>, and details on the parts of the approach/retract curves from which each parameter can be obtained (upper right).

maps in a short time (thousands of ramps per second, 4 minutes per measurement).

The height channel usually displays a topographical image of the sample (Figure 2.7). PeakForce QNM channels include Peak Force, DMT Modulus, logDMT Modulus, Adhesion, Deformation, and Dissipation channels (Figure 2.7). The peak force channel produces a map of the peak force measured during the scan and because the PeakForce QNM mode uses peak force as the feedback signal, this channel is essentially the Peak Force Set point plus the error. DMT Modulus is the reduced Young Modulus which is obtained by fitting the retract

curve using the Derjaguin-Muller-Toropov (DMT) model. Adhesion represents the peak force below the baseline (in pN). Deformation is defined as the distance (in nm) from the base of the Deformation Fit Region position to the peak interaction force position. It has a close correlation with sample indentation in which softer samples has higher deformation. The maximum deformation of the sample is caused by the probe. Energy Dissipation (W) is given by the force times the velocity integrated over one period of the vibration, and is defined as the hysteresis between the approach and withdrawal curves. Pure elastic deformation has no hysteresis which corresponds to very low dissipation. Energy dissipated is displayed in electron volts as the mechanical energy lost per tapping cycle. The Dissipation channel plots the dissipated energy in each cycle by integrating the area between the approach and withdrawal curves.

Peak orce Capture™ feature allows force curves from the Peak orce Q M images to be saved alongside the standard image file. PeakForce Capture™ enables a force-distance curve to be collected at each pixel in the image for additional offline analysis in which it acquires the entire force distance curve used to create the interaction maps. This feature also allows the simple export to other systems or programs for additional analysis. When paired with PeakForce QNM, it provides the highest resolution mechanical mapping capabilities and data export features for easy analysis.

Force Volume mapping is another AFM mode in which the force between the AFM tip and the sample varies as the tip scans the sample. The principle is based on the change in the approach curve of the force measurements at every point in the scan area of the sample. For

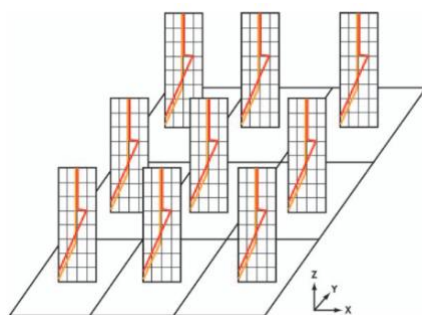


**Figure 2.43.** Force volume mapping: Force volume data set can be seen as a stack of horizontal slices, each representing the array of force data at a given height  $Z$ . A single force volume image represents one of these slices, showing the  $X,Y$  distribution of the force data over the scan area at that height. The value at a point  $(X,Y,Z)$  in the volume is the deflection (force) of the cantilever at that position in space. [80]

each point of the scan area, a force curve is obtained, and as the topographic data is collected, an array of force-distance curves is also collected. The array of force curves is combined into a 3D array, or volume, of force data (Figure 2.8). This type of data is then called force volume. In force volume mode the AFM is driven in contact or tapping imaging mode combined with recording the approach force curves for every point in the sample. Force Volume mapping allows the study of materials mechanical, adhesive, electrical, magnetic, and chemical properties, but unlike PeakForce mapping, it uses linear ramping, the lateral resolution is typically lower and image acquisition is slower.

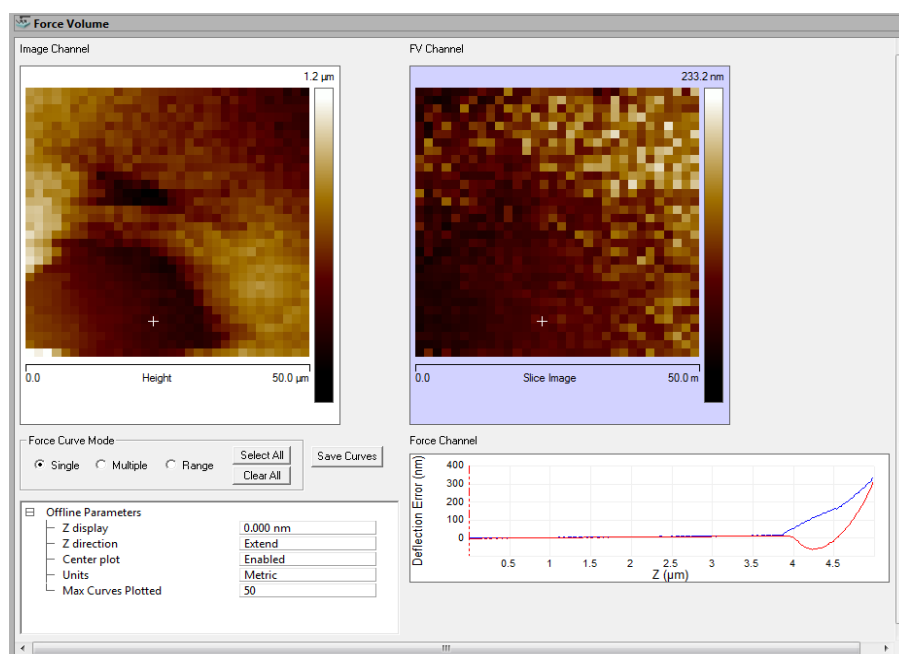


**Figure 2.44.** Force volume data for (PDADMAC/PAA) multilayer films at pH 6 acquired from NanoScope Analysis software, the surface topography appears in the image to the left, the image to the right corresponds to the force volume channel, and the curve below corresponds to the deflection of the cantilever versus piezo  $z$  position at a selected pixel (white cross).

### Forces of interaction

The different AFM modes operate with different types of interactions between the tip and the surface. The positive deflection of the cantilever is linked to repulsive forces pushing the tip away from the surface which stands for a positive interaction force. On the contrary, attractive forces pull the tip toward the surface causing a negative downward deflection of the

cantilever. The attractive force zone starts at infinite distance  $z_i$  from the sample where the interaction force approaches zero and is negligible (Figure 2.10). The *sketch of forces of interaction*

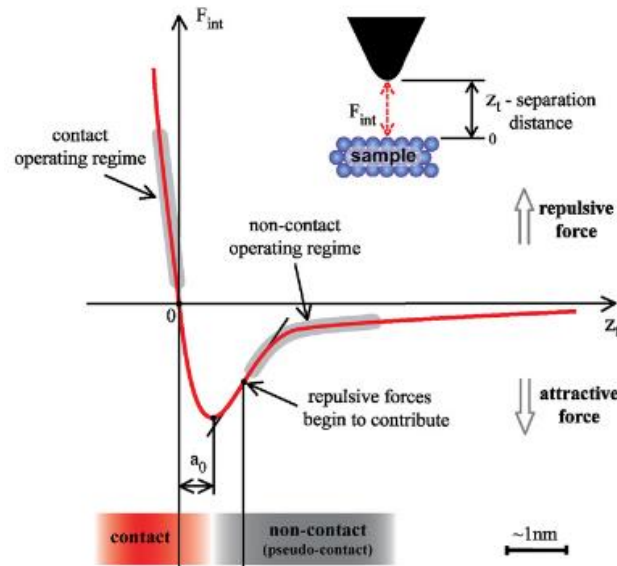


**Figure 2.45.** The sketch of forces of interaction ( $F_{int}$ ) as a function of tip-sample separation distance ( $z_t$ ). [79]

( $F_{int}$ ) as a function of tip-sample separation distance ( $z_t$ ). These forces are used in non-contact (dynamic) mode. The zone of attractive forces ends when the repulsive interaction starts to contribute. In this second zone, both kinds of forces contribute to the interaction and the attractive force reaches its maximum. When the gradients of attractive and repulsive forces are equal (the minimal force of interaction), the most significant distance is reached, and the distance from this point to the full contact (point "zero") is equal to the intermolecular distance  $a_0$ . It depends on material properties of the tip and the sample and is usually is in order of few Angstroms. The third zone is the repulsive forces zone. These forces are used in contact (static) mode. When the interaction point is equal to zero (at the "zero" point), there is a full contact between the tip and the sample and the cantilever is not deflected. As the tip continues to approach the sample, the interaction force increases very fast and the tip starts to deform the surface and the cantilever deflects.

#### II.2.1.4. Force measurements

##### *The force spectroscopy*



In a force measurement the probe to which the cantilever is attached is moved up and down by the piezoelectric translator, while measuring the cantilever deflection. The data obtained from AFM measurements is the cantilever deflection, measured in volts by the photodiode, versus piezo extension measured in nanometers. The cantilever deflection is converted into distance based on a constant compliance region where the cantilever deflection varies linearly with the displacement of the piezo. The slope of the constant compliance region is used to convert the deflection unit from voltage to nanometers [59].

Force curves measure the amount of force detected by the cantilever as the tip approaches or indents into the sample surface and then is pulled away. In a force curve analysis the probe is repeatedly brought towards the surface and then retracted (Figure 2.12). Force curve analyses can be used to determine chemical and mechanical properties such as adhesion, elasticity, hardness and rupture bond lengths. The deflection is plotted according to the displacement of the piezoelectric translator. The approach phase (red) followed by the withdrawal or retract phase (blue) constitute a complete cycle approach/withdrawal of the probe (Figure 2.12. .

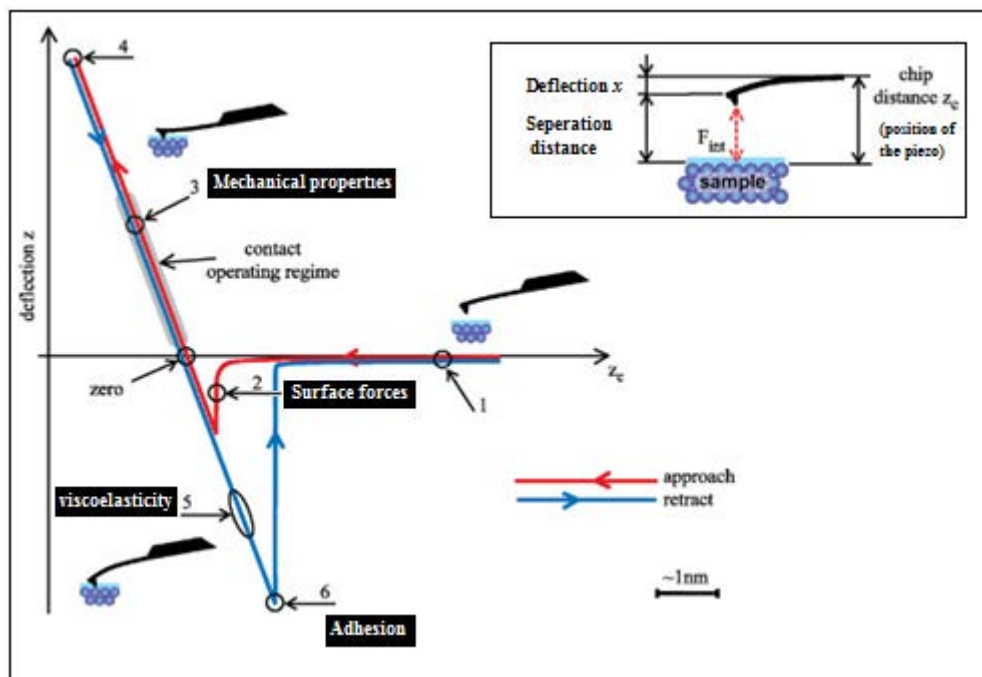
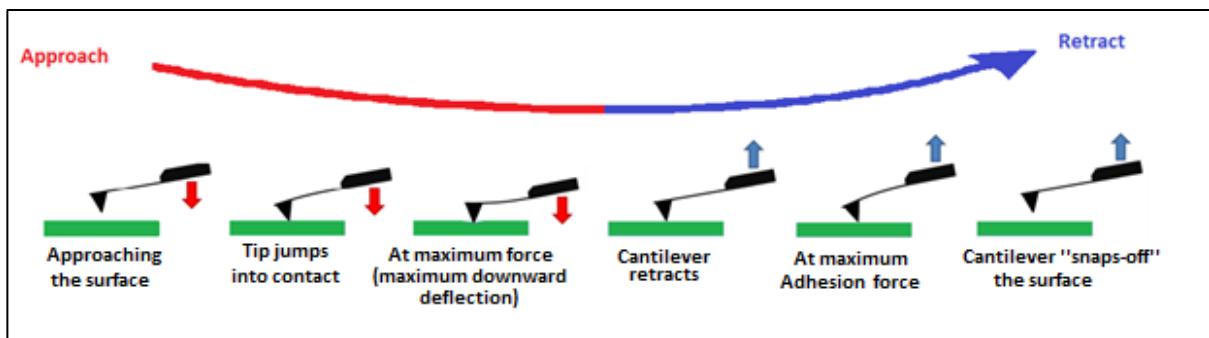


Figure 2.46. Typical AFM force curve [79]

During the approach phase, there are two common parts of the curve, when the tip is far from the surface there is little or no force and thus no deflection is recorded (Figure 2.12. .

This field defines the base line ( $F = 0$ ), there is no tip-sample contact and the microlever is at its equilibrium state (point 1). In the second part, as the tip approaches the surface, the cantilever deflects downward towards the sample but its stiffness keeps the tip away from the surface. The tip jumps into contact with the sample surface when it is near enough to feel attractive forces (Van der Waals, electrostatic and electromagnetic attractive forces); the cantilever deflects downward in this process. This full tip-sample contact occurs at point 2. At this point the attractive forces have a bigger gradient than the restoring force from the cantilever spring i.e. they overcome the cantilever spring constant. The deflection of the cantilever depends greatly on the viscoelasticity of the sample. The treatment of this part of the curve with an elastic or viscoelastic model is used to determine elasticity of the sample.

After the tip is in contact with the sample, the distance  $z_c$  between the cantilever chip and the surface continues to decrease causing the downward negative deflection towards the surface and the increase in the repulsive contact force. The tip then stays on the surface and the force increases until the  $z$  position of the deflection reaches its bottom-most position. This is where the peak force occurs. At point "zero", the attractive and repulsive interaction forces are equal. Then the cantilever is pushed up to the surface, it deflects upwards, which is seen as a sharp increase in the measured force (point 3). The operation of the AFM in contact mode occurs usually at this point. The upward deflection continues to increase until reaching its maximum at point 4. The scanner then begins to retract and the cantilever deflection retraces the same curve in the reverse direction.



**Figure 2.47.** Deflection of the cantilever during force measurement [80]

During the withdrawal phase of the probe, the upward deflection starts decreasing and passes through its equilibrium position (point zero). As we start moving away from the surface the tip "snaps in" due to interaction with the surface, and the cantilever is deflected



downwards (point 5). Point 6 is the distance where the cantilever's downward deflection is large enough to overcome the adhesion, the tip will break free and return to zero position (no deflection). The force needed to "snap off" the sample is used to measure the adhesion properties of the studied materials [60]. The force curves give access to several parameters specific to the sample. The approach curve is used to determine the mechanical properties (elasticity) while the retraction curve to determine dissipative (viscosity) and adhesion forces.

Plotting the deflection of the cantilever versus its position on the sample yields a topographic image of the sample. Alternatively, it is possible to plot the height position of the translation stage. The result of a force measurement is a measure of the cantilever deflection ( $x$ ) versus position of the piezo ( $z$ ) normal to the surface.

To obtain a force-versus-distance curve,  $x$  and  $z$  have to be converted into force and distance (Figure 2.13). The indentation ( $\delta$ ) is thus defined by the difference between the displacement of the piezo and the deflection of the cantilever (Figure 2.13. *Left: Sketch of an indentation experiment. Right: The correction of the height for the cantilever deflection ( $x$ ) to derive the tip sample separation.* :

$$\delta = \Delta z - x = (z - z_0) - (d - d_0) \quad 2.2)$$

The amount of force between the probe and the sample is dependent on the spring constant ( $k_c$ ) (stiffness of the cantilever) and the distance between the probe and the sample surface ( $x$ ). This force can be described using Hooke's Law:

$$F = k_c \cdot x \quad 2.3)$$

If the spring constant of cantilever is less than that of the surface, the cantilever bends and the deflection is monitored. This typically results in forces ranging from nN ( $10^{-9}$ ) to  $\mu\text{N}$  ( $10^{-6}$ ).

We can also represent the force as a function of the indentation:

$$F = k_c [(z - z_0) - \delta] \quad 2.4)$$

The shape of the force versus indentation curve gives a hint of the rigidity or softness of the analyzed sample (Figure 2.14).

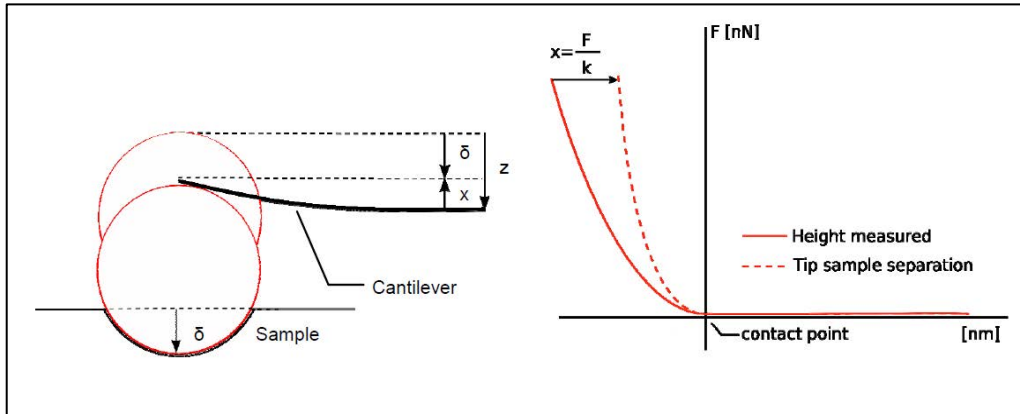


**Figure 2.48.** Left: Sketch of an indentation experiment. Right: The correction of the height for the cantilever deflection ( $x$ ) to derive the tip sample separation. [81]

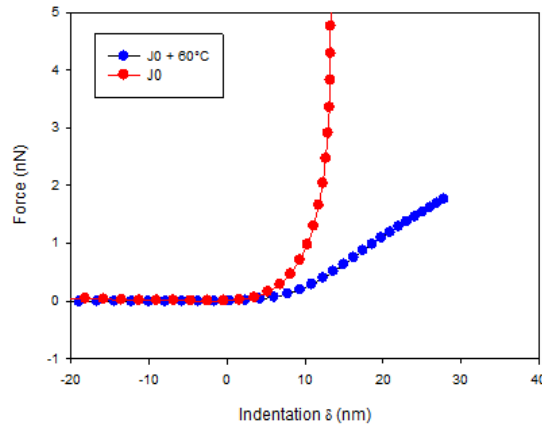


**Figure 2.49.** Force versus indentation curves: comparison between the shape of the curve of a rigid (PDADMAC – PAA)<sub>30</sub> film denoted by  $J_0$  and a soft film after thermal treatment denoted by ( $J_0 + 60^\circ\text{C}$ ).

### II.2.1.5. Determining the elastic modulus using AFM

Since the cantilever is a sensitive force transducer, the cantilever/probe combination can be used to push on a sample to extract elastic mechanical properties. The probe is indented to a known load or displacement, and a force-displacement curve is collected and analyzed. Maximum (peak) force, deformation, adhesion force and energy dissipation can be found directly from proper analysis of raw data.

The Hertz model [61] describes the indentation of an infinitely hard spherical indenter (the probe tip) on an elastic flat surface (the sample). The Hertz model is valid for

indentations significantly less than the sphere radius of the probe ( $\delta \ll R$ ). The Hertz model does not take adhesion into account and is often modified using the DMT model [62]. When the indentation depth is close to or exceeds the radius of curvature of the probe, the Sneddon model of contact between an infinitely hard conical indenter and an elastic flat surface is used. For the Sneddon model the indentation has to be so large that the cone apex can be considered infinitely sharp (Figure 2.15).

### **Hertz model**

For a spherical indenter of radius  $R$ , the loading force  $F$  is defined by:

$$F = \frac{4E}{3(1-\nu^2)} \sqrt{R} \delta^{3/2} \quad (2.5)$$

### **Sneddon model**

For a conical indenter with half angle  $\alpha$ ,  $F$  is defined by:

$$F = \frac{2E}{\pi(1-\nu^2)} \tan(\alpha) \delta^2 \quad (2.)$$

where  $E$  is the (searched) young modulus of the sample,  $\nu$  is Poisson's ratio which depends on the material's properties ( $\nu$  is classically set to 1/2),  $\delta$  is the indentation in nm,  $R$  is the tip radius in case of a spherical tip, and  $\alpha$  is the tip half angle in case of a conical indenter. As a

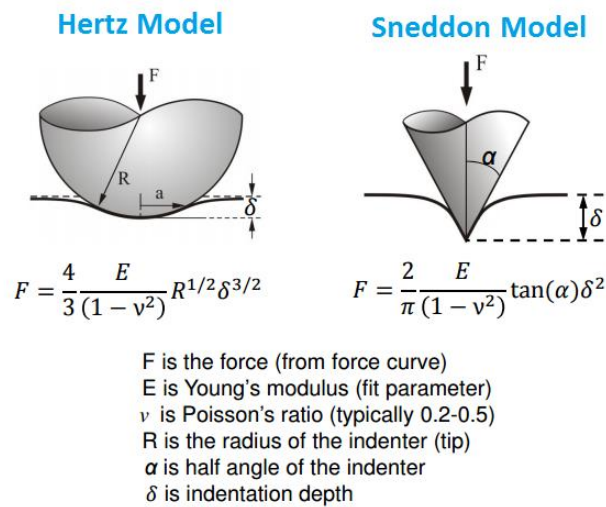


**Figure 2.50.** Sneddon model versus Hertz model [82]

result, by acquiring the experimental data of  $F$  and  $\delta$ ,  $E$  can be simply extracted based on one of the two models.

### ***Correction of the finite thickness of the sample***

For thin samples of thickness  $h$  deposited on hard substrates, the young modulus of the sample can be overestimated due to the effect of the stiffness of the supporting hard substrate [63]. Dimitriadis proposed a correction factor  $f_D$  for the Hertzian Model for a spherical indenter:

$$F = \frac{4E}{3(1-\nu^2)} \sqrt{R} \delta^{3/2} \cdot f_D \quad (2.7)$$

where  $f_D$  is defined by:

$$f_D = [1 + 1.133\chi + 1.283\chi^2 + 0.769\chi^3 - 0.0975\chi^4] \quad (2.8)$$

$$\text{with } \chi = \frac{\sqrt{R\delta}}{h}$$

Similarly, in case of conical tips, the Bottom Effect Cone Correction (BECC) corrects the Sneddon model [64];

$$F = \frac{2E}{\pi(1-\nu^2)} \tan(\alpha) \delta^2 \cdot f_{BECC} \quad (2.9)$$

$$f_{BECC} = 1 + 1.7795 \frac{2 \tan(\alpha)}{\pi^2} \frac{\delta}{h} + 16 (1.7795)^2 \tan^2(\alpha) \frac{\delta^2}{h^2} + O\left(\frac{\delta^3}{h^3}\right) \quad (2.1)$$

### ***Instrumentation and data analysis***

All the AFM experiments were conducted using a Dimension FastScan AFM setup from Bruker, Germany (Figure 2.3. *Dimension FastScan AFM setup. (1) Acoustic and Vibration Isolation Enclosure; (2) Scanners (includes 2, see right); (3) Ultra-Stable High-Resonance Microscope Base; (4) 30" Monitor and FastScan Nanoscope Software; (5) Computer; (6) Nanoscope voltage stage controller and HV amplifier.*). The Dimension Icon scanner was used to obtain larger scan range (up to 8  $\mu\text{m}$  x 8  $\mu\text{m}$ ) that cannot be achieved by the FastScan scanner (5  $\mu\text{m}$  x 5  $\mu\text{m}$ ). The two scanners allow the nanomechanical mapping of the surface with a preference of Dimension Icon for Force Volume measurements and also for thicker samples (loading experiments) due to its typical 1  $\mu\text{m}$  z range in imaging and force curve modes.

Silicon nitride MLCT and NPG-10 probes with rotated (symmetric) tips (Bruker AXS, Palaiseau, France) were used to conduct the force measurements. MLCT probes have 6 gold coated cantilevers of both rectangular and triangular geometry with spring constants ( $k_C$ ) of 0.07-0.6 N/m, 20 nm tip radius, and  $\sim 18^\circ$  tip half angle. NPG-10 probes have 4 triangular gold coated cantilevers with spring constants of 0.06-0.35 N/m, tip of 30 nm radius and  $\sim 18^\circ$  tip half angle (Figure 2.5. *Scanning Electron Microscopy of AFM cantilevers. (a) NPG-10 probe with triangular cantilevers; (b) MLCT probe with triangular and rectangular cantilevers; (c) AFM tip with a rotated* . Prior to all AFM measurements the deflection sensitivity and the tip spring constant were calibrated by the methods previously described. (II.2.1.1. and II.2.1.2.).

Measurements were always performed in liquid (10 mM a filtered with 0.2  $\mu\text{m}$  PES filters) at room temperature. The mechanical properties and the topography of the polyelectrolyte films were achieved by PeakForce Quantitative Nanomechanical Mapping™ measurements. Force curves were extracted from the height images consisting of a grid of 256×256 pixels in which each pixel accounts for a force curve (Figure 2.16). For each measurement, a total of 65536 force curves were exported and analyzed offline (Figure 2.17). Force Volume Imaging was also done for the polyelectrolyte films (Figure 2.9). A total of 32×32 force curves were collected. The approach speed was set to 1  $\mu\text{m/s}$ .

PeakForce capture files, saved as pfc files, were analyzed offline by NanoScope Analysis Software (NanoScope Analysis v.1.5, Bruker, France). Each force curve is saved as its own standard force curve file (spm file) that can be opened separately in NanoScope Analysis. Raw data files (force curves or .spm files) were then exported from NanoScope Analysis and converted into ASCII format (text files) so that the data files could be loaded into a Matlab editor (Figure 2.18). The data was then analyzed by an automated Matlab

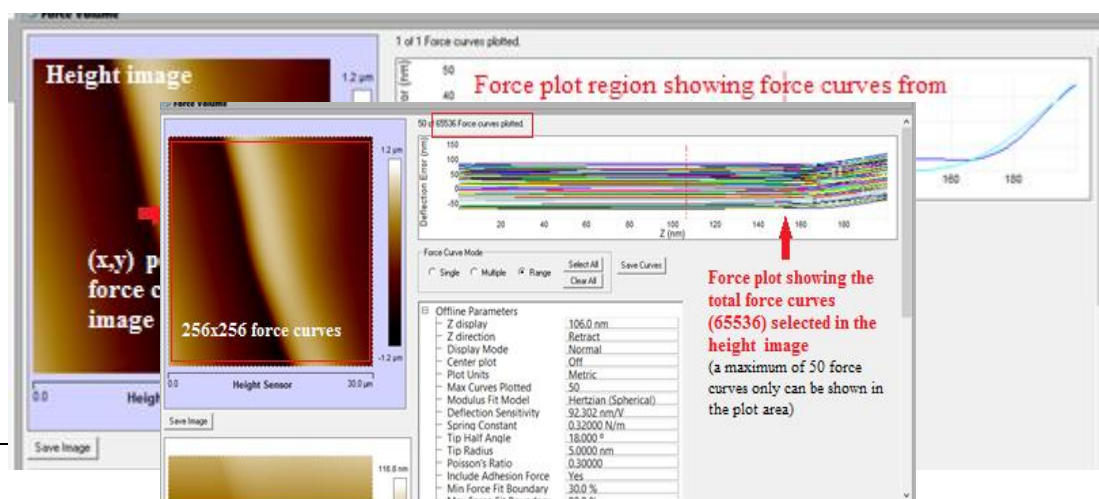


**Figure 2.51.** Data presented in NanoScope Analysis software: Height image of a (Figure 2.52. Data presented in NanoScope Analysis software: Height image of a  $c(\text{PDADMAC} - \text{PAA})_{30}$  polyelectrolyte film (right), and force plot region (deflection error (versus Z piezo position) displaying 50 of all the force curves (256x256) corresponding to all the selected pixels in the height image (left)

algorithm which takes into account all the parameters needed (film thickness, tip radius, tip half angle, etc.) to obtain the young modulus data based on the two models previously described (Figure 2.19). The analyzed results appear .res file extension which are exported to SigmaPlot and data analysis softwareS. The analysis of the obtained data sheet provides the force versus distance and force versus indentation data (**Error! Reference source not found.**). The young modulus is then evaluated from the quantitative interpretation of force versus indentation curves according to the Sneddon model for a conical indenter mentioned previously. For Poisson's ratio we used  $\nu = .5$  as for perfect rubber. Origin software was used to obtain the distribution of Young modulus of the samples.

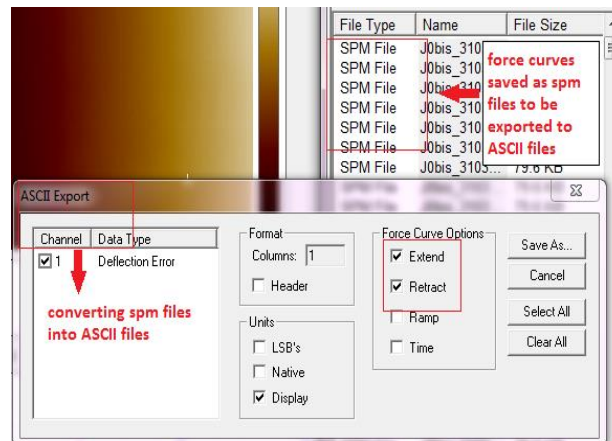


**Figure 2.53.** Raw force curves (spm files) exported as ASCII files (text files) to be loaded into Matlab editor.

```

1 function y=hertz(kC,alpha,R,h,nsnd,niter,epsilon,corp,cors)
2 %marlabpool open
3 %kC = spring constant of the cantilever
4 %alpha = tip half-angle (only for contact cone/plan)
5 %R = tip radius
6 %h = film thickness (only for contact sphere/plan)
7 %nsnd = nombre of probings per point
8 %niter = nombre of tests per point
9 %epsilon = precision of the solution
10 %corp = correction piezo
11 %cors = correction sensitivity
12
13 %hertz(kC,alpha,R,h,nsnd,niter,epsilon,corp,cors)
14
15 typ=input('use sphere-plane contact (y/n) : ','s');
16 isize=input('Image size [um]: ');
17 monteCarlo = [980629335, 889272121, 422278310,1042669295, 531256381, 335028099, 47160432, 788808135, 660624592,
18 kmonte=55;
19 lmonte=31;
20 Etemp=10000;
21 Poisson=0.5;
22 R=2e-8;
23 corp=1e-9;
24 cors=1e-9;
25 epsilon=1e-11;
26 nsnd=100;
27 niter=1;
28 h=1e-6;% thickness of the sample in m
29 kC=0.35;% adjust the spring constant of the cantilever
30 pi=3.14159265359;
31 C = (16/9)*sqrt(R); % constante of dimitriadis (correction of the finite thickness)
32 alpha=17.5;
33
34 [filenamef, pathname] = uigetfile( '*.txt','Text Files (*.txt)', 'Pick the first file');
35 [filenamel, pathname] = uigetfile( '*.txt','Text Files (*.txt)', 'Pick the last file');
36 i=length(filenamef);
37 while (isempty(str2num(filenamef(i))))
38 i=i-1;

```

**Figure 2.54.** Matlab editor with the main parameters used for the derivation of Young modulus data

The Thickness of the polyelectrolyte multilayers under different experimental conditions was obtained by “scratching” the film with a syringe and then imaging the “scratch” site by A M and measuring the difference of the height between the support and the “scratch” Figure 2.).

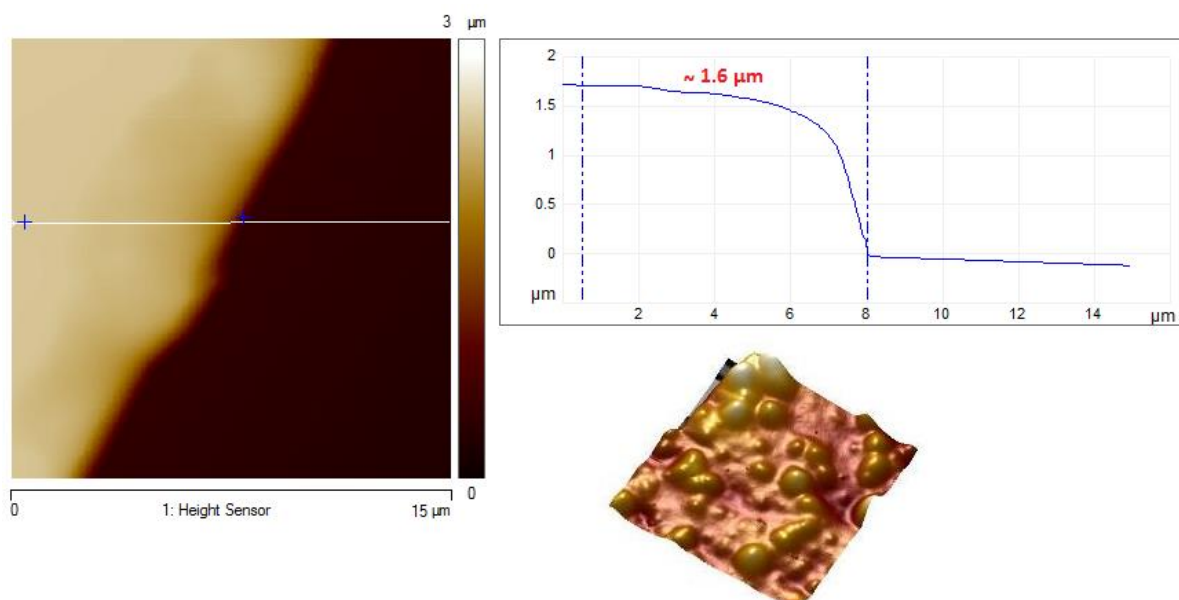


**Figure 2.21.** Thickness ( $\sim 1.6\mu\text{m}$ ) of (PDADMAC – PAA)<sub>30</sub> films prepared with  $\text{NaNO}_3$  at 100 mM and pH 3.

### II.2.2. Quartz Crystal Microbalance-dissipation (QCMD)

The quartz crystal microbalance was developed in the late 50s by Sauerbrey to measure the mass of a rigid deposit on a quartz crystal [65]. The QCM is based on the piezoelectric properties of quartz, characterized by two complementary phenomena: (i) When force is applied to a quartz crystal changing its dimensions, a potential difference is generated across it. (ii) When a potential is applied across it its dimensions are changed [66].

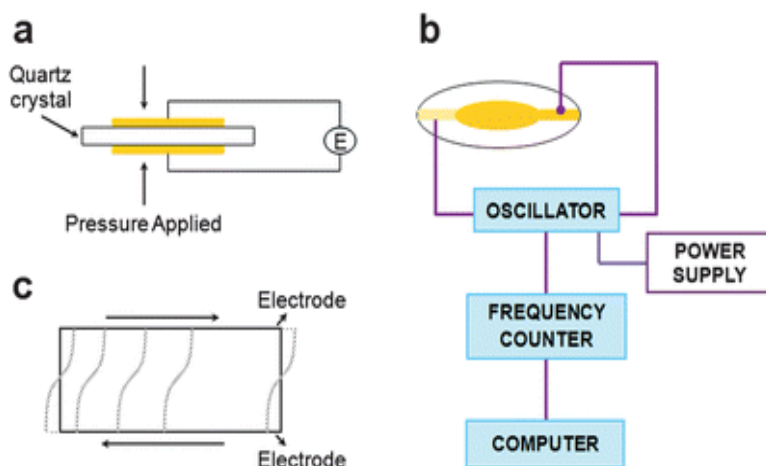


Figure 2.55. QCM-D setup [83]

The QCM comprises a measuring chamber and an electronic control unit interfaced with a computer (Figure 2.22). The quartz plate is located between two thin gold layers which serve as electrodes. By applying a potential difference between the two faces, a shearing movement is induced without vertical deformation. If the underside of the blade is fixed on a support, the upper face undergoes a translational movement. The entire system is equivalent to a harmonic oscillator. An important property of the quartz crystal is that its resonance frequency changes when its mass is changed, either by adding or removing weight or by interaction with the medium in which the crystal is immersed i.e. after the deposition of a polyelectrolyte layer. Sauerbrey derived the following equation linking the mass of an adsorbed layer to the frequency change of the resonating crystal. Typically, the relation between the frequency shift and the added mass per unit area is linear obeying the Sauerbrey equation:

$$\Delta f = \left[ \frac{-2f_0^2}{A \sqrt{\rho_q \mu_q}} \right] \Delta m \quad (2.11)$$



where  $\Delta f$  is the change in the resonance frequency due to the added mass,  $f_0$  is the resonance frequency of the resonator (the crystal),  $\rho_q$  and  $\mu_q$  are the density and shear modulus of the quartz,  $A$  is the surface area of the resonator, and  $\Delta m$  is the change in mass per unit surface area.  $C_m$  is the characteristic constant of quartz (or mass conversion factor-mass sensitivity parameter) given by:

$$C_m = 2f_0^2 / \sqrt{\rho_q \mu_q} \quad (2.12)$$

Then, 
$$\Delta f = -C_m \Delta m / A \quad (2.1)$$

$$\Delta m = -A \Delta f / C_m \quad (2.14)$$

Where  $\mu_q = 2.947 \times 10^{11} \text{ g.cm}^{-1}.\text{s}^{-2}$  is the shear modulus and  $\rho_q = 2.648 \text{ g.cm}^{-3}$  is the density of quartz. Quartz crystals most commonly used for QCM have resonance frequencies in the range of about (5-10 MHz). For  $f = 5 \text{ MHz}$ ,  $C_m = 8.13 \times 10^7 \text{ Hz.g}^{-1}.\text{cm}^2$ .

From the 1980s, the technique was extended to the measurement of the viscoelastic properties and the thickness of a film in a liquid environment [67]. Therefore, it was named "quartz crystal microbalance with dissipation measurement" or QCM-D.

The viscoelastic properties of the adsorbed layer, softness or rigidity, are evaluated by measuring the energy dissipation of the crystal oscillation. Typically, a soft layer is able to dampen out the crystal oscillation more effectively, while a rigid layer may not contribute significantly to dissipation of vibrational energy of the crystal. The energy dissipation, or dampening, is defined by:

$$D = \frac{E_{\text{dissipated}}}{2\pi E_{\text{stored}}} \quad (2.15)$$

where  $D$  is the dissipation factor of the crystal oscillation;  $E_{\text{dissipated}}$  is the lost energy, or dissipation during one oscillation cycle, and  $E_{\text{stored}}$  is the total energy in the oscillator.

The energy dissipation  $D$ , related to the damping of the sensor oscillation, is used to study the viscoelastic properties of the adsorbed layer. The changes in QCM frequencies were assumed to be proportional to the adsorbed mass only in the case of rigid layers, as reported by Sauerbrey [65]. Hence, the Sauerbrey equation is based on the assumptions that the added mass is uniform and evenly distributed over the electrode, rigid and integral to the quartz

crystal with no deformation from oscillatory motion of the crystal, and that the added mass must be much less than the mass of the quartz crystal itself. The change in the resonance frequency of the crystal due to the presence of the liquid is given

$$\Delta f = \frac{-\sqrt{f} \rho_l \eta_l}{\rho_q h \sqrt{2\pi}} \sin[\pi/4 - \phi_l/2] \quad (2.1)$$

where  $h$  is the thickness of the quartz crystal,  $\rho_l$  is the density of the liquid,  $\eta_l$  and  $\phi_l$  are the magnitude of the complex viscosity and relative phase angle of the liquid medium respectively.

For viscoelastic films not obeying Sauerbrey approximation, the experimental data ( $\Delta f$  and  $\Delta D$ ) can be analyzed by using a model developed by Voinova and coworkers under the assumption that the film is a homogeneous and isotropic viscoelastic layer [68, 69]. The model consider the case of two viscoelastic layers covering the surface of a piezo-electric plate oscillating in a pure shear mode in a bulk liquid. The geometry of the model system is shown in (Figure 2.23). The frequency and energy dissipation changes can be fitted assuming that the film behaves as a Voight element (Figure 2.24. *Schematic depiction of the Voight viscoelastic element consisting of a spring and a dashpot* [84]). The Voight element is a mechanical element analogy for a viscoelastic system that consists of a spring and dashpot. In this model,

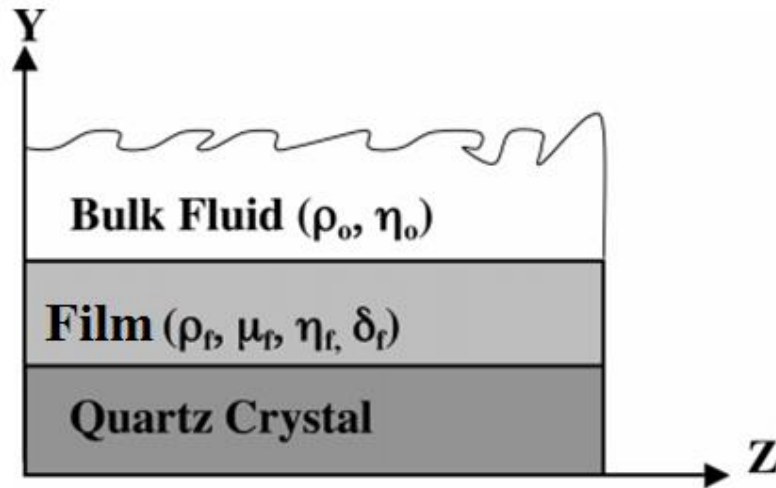


**Figure 2.56.** Geometry of a quartz crystal microbalance (QCM) covered by a double-layer viscoelastic film. The QCM system oscillates in a bulk liquid. [68]

the spring corresponds to the shear rigidity and the dashpot to the viscosity ( $\eta_i$ ).

Deviations from the Sauerbrey equation should be observed when  $\beta_1 D > 0.28$ , where  $\beta_1 = 2\pi/\lambda_s$ ,  $\lambda_s$  is the shear wavelength and  $D$  is the film thickness [260]. The frequency and energy dissipation changes can be related to the film density, viscoelastic properties, and thickness using the derivation of Voinova and coworkers,

$$\Delta f \approx \frac{1}{2\pi\rho_q h_q} h\rho_f \left(1 + \frac{2h^2\chi}{\delta^2(1+\chi^2)}\right) \quad (2.18)$$

$$\Delta D \approx \frac{2h^3\rho_f}{\pi f \rho_q h_q} \frac{1}{\delta^2(1+\chi^2)} \quad (2.19)$$

$$\chi = \frac{\mu}{\eta f} \quad (2.2)$$

$$\delta = \sqrt{\frac{2\eta}{\rho f}} \quad (2.21)$$

where  $\rho_q$  and  $\rho_f$  are the density of the quartz and film respectively,  $h_q$  and  $h$  are the thickness of the quartz and film respectively,  $f$  is the measured frequency,  $\chi$  is the ratio of the storage modulus ( $\mu$ ) and the loss modulus ( $\eta$ ),  $f_0$  is the resonance frequency of the crystal, and  $\delta$  is the viscous penetration depth. The frequency and dissipation of the crystal could be measured

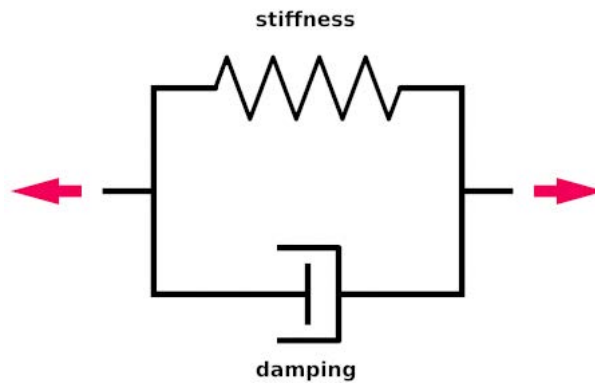


**Figure 2.57.** Schematic depiction of the Voight viscoelastic element consisting of a spring and a dashpot [84]

from the relationship  $f = nf_0$  at the resonance frequency ( $n=1$ ), and at several overtones ( $n=3, 5, 7$ ).

### Experimental protocol

A quartz crystal microbalance with dissipation (QCM-D, from Q-sense, Gothenburg, Sweden) was used to monitor the deposition steps and the multilayers build-up on a pre-cleaned (*in situ*) silica coated quartz crystal (5 MHz, 50 nm) (Figure 2.25). The deposition was done *in situ* in the QCM-D chamber by alternative injection of the

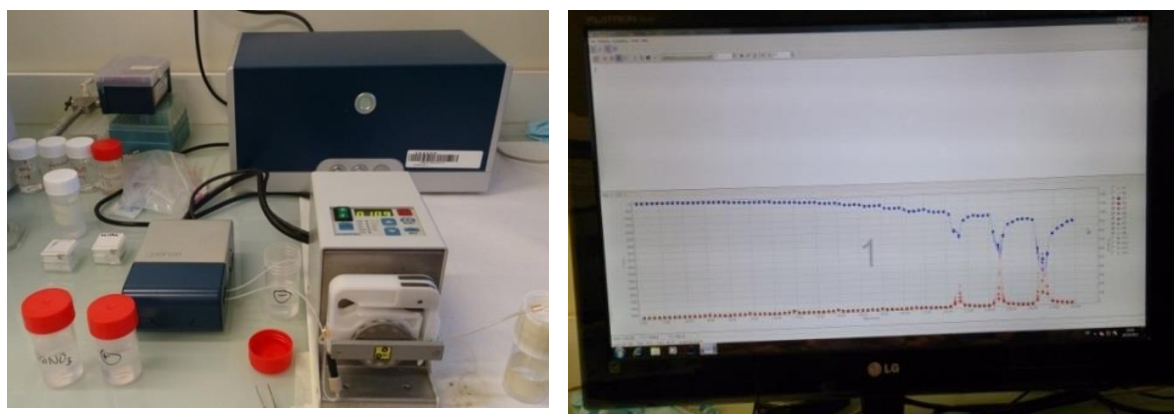


**Figure 2.58.** Right: QCM-D3 setup (Qsense, Göteborg, Sweden); Left: real-time data of the variation in frequency (blue) and in dissipation (red) as function of time during the *in situ* deposition of a (PDADMAC-PAA) film

polyelectrolytes/rinsing solutions ( $\text{NaNO}_3$  at 10 mM) by the QCM pump at a flow rate of  $14 \mu\text{ l/min}$ . The temperature was fixed at  $25^\circ\text{C}$ . A time lap of 5 minutes was set between 2 successive injections. At the end of the deposition, the change in the frequency and dissipation,  $\Delta f$  and  $\Delta D$  respectively, versus time data were collected for the 3<sup>rd</sup>, 5<sup>th</sup> and 7<sup>th</sup> overtones using the Q-tools software (from Q-sense, Gothenburg, Sweden) (Figure 2.). These

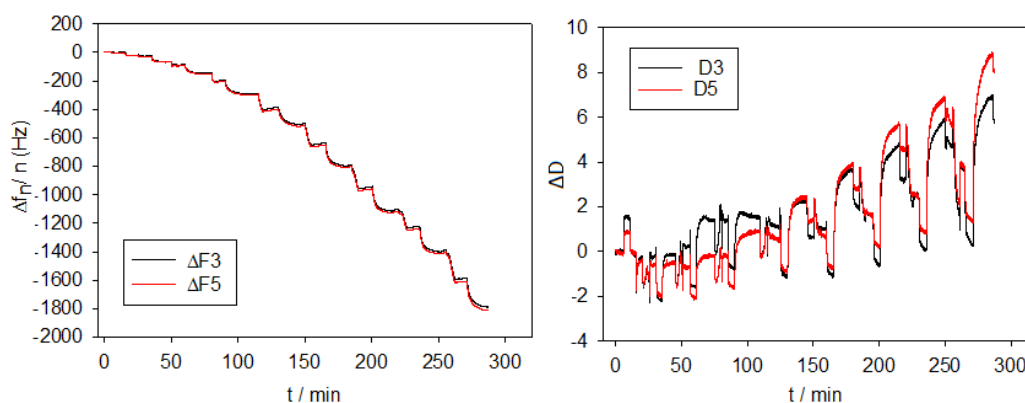


**Figure 2.26.**  $\Delta f$  and  $\Delta D$  data collected from the 3<sup>rd</sup> and the 5<sup>th</sup> overtone during the buildup of a (PDADMAC-PAA) multilayer film.

curves were analyzed manually to obtain the variation of the film properties as a function of number of deposited layers. The related data were saved as datasheets. The viscoelastic properties of the films were estimated based on Voinova's model by a program developed at INSERM U.1121 (Figure 2.27), it is stressed that the density of the film used in the

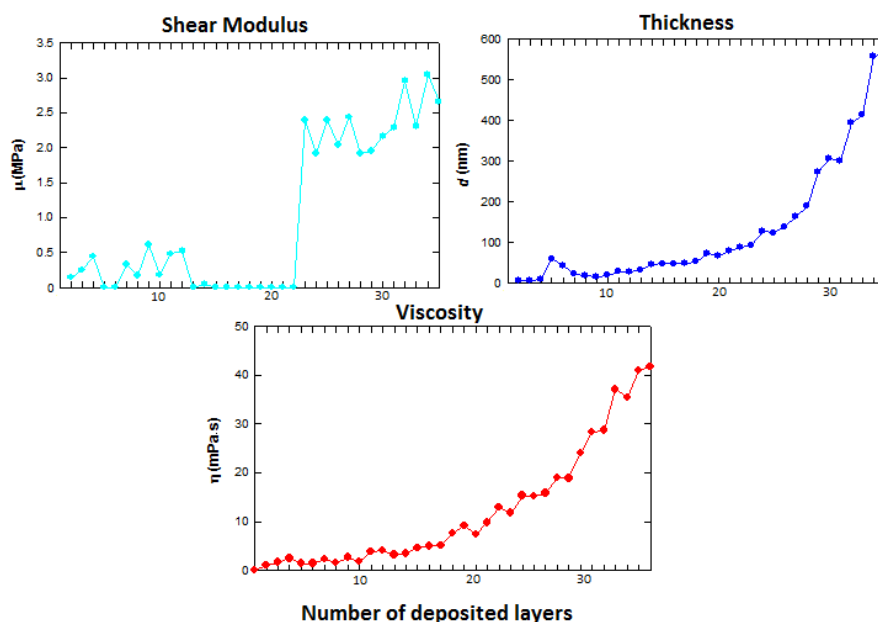


**Figure 2.59.** Results obtained from QCMD data analysis: graphs showing the properties of the constructed film (shear modulus, viscosity, and thickness) versus the number of deposited layers.

calculations is the average of the densities of the polyelectrolytes used in the film buildup.

### II.2.3. Confocal Raman Spectroscopy (CRS)

Raman spectrometer, developed by Raman [71], was first combined with an optical microscope in the 1990s to obtain the so-called Confocal Raman microspectroscopy. The microscope was used to focus the excitation light to a small spot a few micrometers in diameter to obtain a Raman spectrum from a microscopic area. For the first time, Raman spectra could be obtained from samples of only a few micrometers in diameter. Confocal Raman microspectroscopy proved to be a high-resolution imaging technique that is widely used for the characterization of materials and specimens in terms of their chemical composition. With Raman images, information regarding the chemical compounds and their distribution within the sample can be illustrated clearly. The CRS allows investigating both

the Raman spectrum and a 3D- Raman image with a relatively low concentration of the chemical components in a sample.

A Raman confocal microscope consists of an excitation source (usually a temperature-stabilized laser diode), a microscope, and a spectrometer with CCD (charge-coupled device) detector. The advantage of using a microscope objective instead of a simple lens is the high collection efficiency for the Raman signals due to the high numerical aperture of the microscope objective. On the other hand, as one focuses the light to a microscopic spot, care must be taken to not heat the sample and thermally destroy it with an overly intense laser

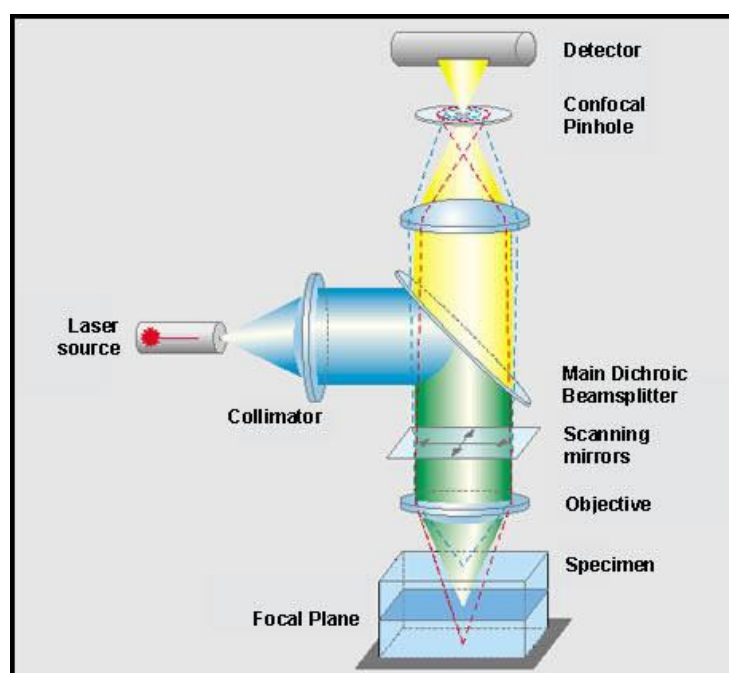


**Figure 2.60.** Schematic representation of a confocal Raman microspectrometer [85]

beam. Different wavelengths of excitation can be used depending on the aim of the study. The Raman scattering intensity is proportional to  $\nu^4$ , where  $\nu$  is the frequency of the exciting laser radiation. Excitation at 400 nm therefore leads to 16 times higher Raman signal than excitation at 800 nm. The Raman signal is proportional to the excitation power, but the excitation laser power should be chosen well below the point where absorption leads to thermal decomposition of the sample. The acceptable laser power depends on laser wavelength, sample properties (absorption, thermal conductivity), and other imaging conditions (laser focus diameter, etc.).

A laser is focused into the sample by the objective of a microscope (Figure 2.28. *Schematic representation of a confocal Raman microspectrometer*). The laser beam is coupled into the microscope with a dichroic beam splitter. The reflectivity of this beam splitter should be as high as possible for the laser excitation wavelength, while its transmission for the Raman light should be high as well. Excitation and collection of Raman scattering are performed by the high numerical aperture objective of the microscope. The Raman backscattered light is collected by the objective and passed through the confocal aperture (pinhole) into the detection system. This confocal set-up leads to a 3-D confinement of the measuring volume down to  $1\text{ }\mu\text{m}^3$  depending on the width of the aperture and the magnification of the objective. The weak Raman signal is first separated from the laser Rayleigh background by an edge or notch filter and afterwards spectrally analyzed by a single grating stage. The grating in a spectrometer disperses the signal onto a cooled CCD detector by deflecting each wavelength at a slightly different angle. The number of grooves per millimeter of the grating determines the dispersion characteristics. A high number of grooves/mm (lines/mm) results in a high dispersion and a high resolution, but also distributes the signal over a large number of CCD pixels. The scanning movement of the sample is ensured with a piezo-scanner. In confocal Raman microscopy experiments, tens of thousands of spectra are commonly acquired in each measurement by the spectroscopic CCD camera. These spectra are further processed and exported by adhoc softwares.

### ***Experimental protocol***

In this work, we used a Raman spectrometer (Witec alpha 300S) with a frequency doubled Nd:YAG laser (wavelength 532 nm) as an excitation source with an output power of  $15\text{ kW.cm}^{-2}$  to avoid the thermal destruction of the samples. An output power of  $250\text{ kW.cm}^{-2}$  was used for the experiments involving laser heating of the samples, and Raman analysis was done at  $15\text{ kW.cm}^{-2}$  otherwise. The spectrometer is equipped with an optical fibered microscope with a fiber core diameter of  $150\text{ }\mu\text{m}$ . The laser was focused at the sample surface through a  $\times 60$  water immersion objective. The scattered light was collected by the same objective in backward mode; the numerical aperture of the microscope was fixed at 0.95 by a calibration grid to obtain a spatial resolution of *ca.* 500 nm, while the spectral resolution was  $6\text{ cm}^{-1}$ . A notch-filter allowed the elimination of the Rayleigh scattering. The Raman signal is then directed in the spectrometer by a 600 grooves/mm grating and finally towards the CCD detector cooled by liquid nitrogen. An acquisition time of 2 seconds and spatial steps of 300

nm were used to generate the Raman film mapping. The software from Witec allowed the acquisition and the integration of the peaks and a subtraction of the baseline was carried out manually before integration. The analyzed PEI – (PAA/PDADMAC)<sub>30</sub> films were constructed on germanium crystals, native films and films subjected to further heating and aging were kept in 10 mM NaNO<sub>3</sub> in a small petri dish (40 mm in diameter) during the Raman scattering experiments.

## II.2.4. Dynamic light scattering (DLS) and Phase Analysis light Scattering (PALS)

### II.2.4.1. Size measurements by DLS

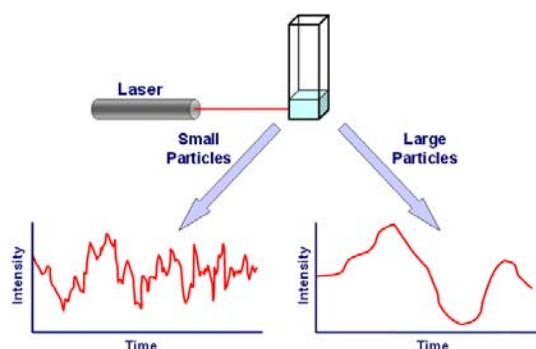


**Figure 2.61.** Typical intensity fluctuations of large and small particles [86]

Dynamic light scattering, also called photon correlation spectroscopy (PCS), is one of the most powerful light scattering techniques for studying the properties of suspensions and solutions of colloids, bioparticles, macromolecules or polymers. The first name given to the technique was quasi-elastic light scattering (QELS) because, when photons are scattered by mobile particles, the process is quasi-elastic. QELS measurements yield information on the dynamics of the scattering objects, which gave rise to the acronym DLS (dynamic light scattering). In particle size analysis, DLS has been established over several years for the characterization of sub-micron particles and macromolecules. This technique is also useful for measuring the speed of e.g. microorganisms floating in solution, or to analyze fluids flow.

When a small particle is illuminated by a light source such as a laser, particles scatter the light in all directions. Small particles in suspension undergo random thermal motion known as Brownian motion. Brownian motion is the movement of the particles due to their random collision with surrounding solvent molecules. An important feature of Brownian



motion for DLS is that small particles move quickly and large particles move more slowly (Figure 2.29. *Typical intensity fluctuations of large and small particles*). Velocity of the Brownian motion may be defined from their translational diffusion coefficient. The relationship between the size of a particle and its speed due to Brownian motion is defined by the Stokes-Einstein equation (valid for hard particles),

$$d_H = \frac{k_B T}{3\pi\eta D} \quad (2.2)$$

where  $d_H$  is the hydrodynamic diameter,  $D$  is the translational diffusion coefficient,  $k_B$  is the Boltzmann's constant,  $\eta$  is the viscosity of the solvent, and  $T$  is the absolute temperature. The hydrodynamic diameter obtained by DLS technique is the diameter of a sphere that has the same translational diffusion coefficient as the particle. The translational diffusion coefficient depends not only on the size of the hard particle core (i.e. impermeable to ions and solvent), but also on any particle polymeric surface structure, the thickness of which is often modulated by concentration and type of ions present in the medium (swelling/shrinking processes).

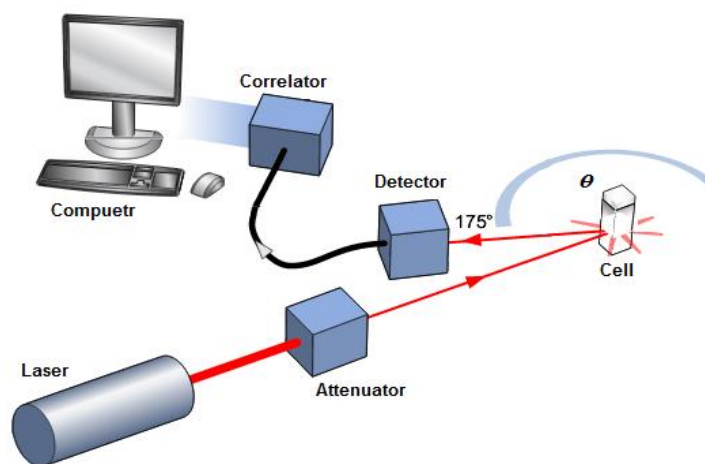


**Figure 2.62.** Setup of DLS system of Zetasizer Nano ZS [86]

In a typical DLS set up (Figure 2.30. *Setup of DLS system of Zetasizer Nano ZS*), the laser first goes through an attenuator (a collimator lens) that enables focusing the beam into the cell in order to reduce the intensity of the laser and thus reducing the intensity of the scattering. When the sample is illuminated by a laser beam, the particle will scatter the light in all directions. A photon detector is used to measure the intensity of the scattered light. The

fluctuations of the scattered light are detected at a known scattering angle  $\theta$  by the fast photon detector that transform the variation of intensity into a variation of voltage. The scattering intensity signal for the detector is passed to a digital signal processing board called a correlator. The correlator compares the scattering intensity at successive time intervals to derive the rate at which the intensity is varying. This correlator information is then transferred to a computer where data are analyzed. Analysis of the fluctuations of the scattered light intensity yields information about the particles diffusion coefficient and, pending proper conversion, about their size.

In this study, a Zetasizer Nano ZS (Malvern instruments, UK) was used to carry out the DLS experiments on nanodendrimers. The Zetasizer Nano ZS (He-Ne red laser.633 nm) measures the scattering information at an angle close to  $175^\circ$  (Figure 2.30. *Setup of DLS system of Zetasizer Nano ZS* ) which is known as backscatter detection. One of the advantages of measuring the backscattering is the reduction of the effect of dust and large contaminants that usually scatter in the forward direction.

The correlator compares the signal intensity collected at time  $t$  to the intensity at  $t+\delta t$  with  $t \gg \delta t$ . It basically measures the degree of similarity between two successive signals or one signal with itself at varying time intervals. The correlator will then construct the time autocorrelation function  $G(\tau)$  of the scattered intensity according to:

$$G(\tau) = \langle I(t).I(t + \tau) \rangle \quad 2.24)$$

where  $I$  is the intensity and  $\tau$  is the delay time (the sampling time) of the correlator. For monodisperse particles in Brownian motion, the correlation function  $G(\tau)$  can be modeled with an exponential decaying function of the correlator time delay  $\tau$ ,

$$G(\tau) = A[1 + \beta e^{(-2\Gamma\tau)}] \quad 2.25)$$

where  $A$  is the baseline of the correlation function,  $\beta$  is the intercept of the correlation function (Figure 2.31.) which represents the degree of spatial coherence of the scattered light over the detector, and  $\Gamma$  is the decay rate (the inverse of the correlation time) and is defined by:

$$\Gamma = Dq^2 \quad 2.2 )$$

where  $D$  is the translational diffusion coefficient, and  $q$  is the scattering vector defined by:

$$q = (4\pi n / \lambda_o) \sin (\theta/2) \quad 2.27)$$

where  $n$  is the refractive index of dispersant,  $\lambda_o$  is the wavelength of the laser, and  $\theta$  is the scattering angle. For polydisperse samples, the equation can be rewritten in the form:

$$G(\tau) = A[1 + B g^1(\tau)^2] \quad 2.28)$$

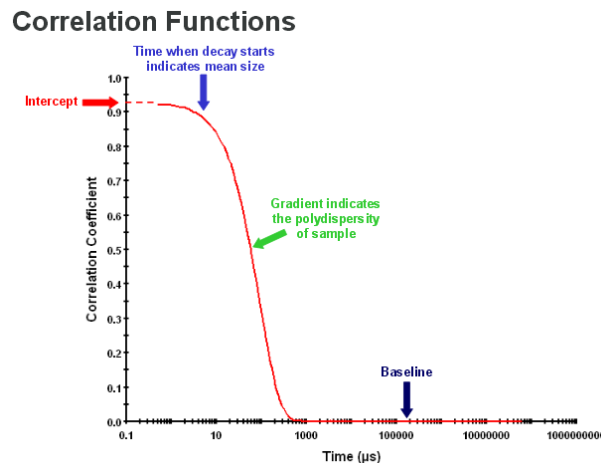


**Figure 2.63.** The correlation function [86]

where  $g^1(\tau)$  is the sum of all the exponential decays involved in the correlation function.

The correlation function contains the diffusion coefficient present in the Stokes-Einstein equation. These diffusion coefficients are obtained by fitting the correlation function with a suitable algorithm.

Two methods of analysis are classically used: cumulants analysis and distribution analysis. The cumulant analysis gives a mean particle size (z-average) that is very sensitive to the presence of aggregates or large contaminants (such as dust), and provides an estimate of the polydispersity index (PdI) or the width of the distribution. The polydispersity index is a dimensionless scalar for the broadness of the size distribution calculated from the cumulants analysis. The distribution analysis fit a multiple exponential to the correlation function to obtain the distribution of particle sizes.

The primary size distribution obtained from a DLS measurement is the intensity-weighted distribution obtained from the chosen analysis. This size distribution is displayed as a plot of the relative intensity of light scattered by particles (on the Y axis) versus various size classes (on the X axis) which are logarithmically spaced. The Zetasizer software uses

various algorithms to obtain a size distribution. The size distribution obtained is known as intensity size distribution since it is a plot of the relative intensity of light scattered by particles of various size classes. The intensity distribution can be converted into a volume distribution using Mie theory, and the volume distribution can also be further converted to a number distribution. However, distribution by number is of limited use since simple errors in the correlation function data leads to huge errors in the number distribution (Figure 2.32).

#### II.2.4.2. Electrophoretic mobility measurements by PALS

Phase analysis light scattering (PALS) technique is used to determine the electrophoretic mobility of charged colloidal suspensions. PALS is an improvement of the classical Laser Doppler Velocimetry (LDV) technique (also called Laser Doppler Electrophoresis (LDE)) for the measurement of extremely low particles mobility. Unlike LDV, the PALS does not require the application of large fields which may give rise to thermal problems. The same optical setup as conventional LDV is used in PALS. However, a different signal processing method is employed. Instead of measuring the frequency shift as in LDV, the measurement in PALS -as its name indicates- analyzes the phase shift. The phase is defined as frequency  $\times$  time. For charged particles placed between electrodes of opposite

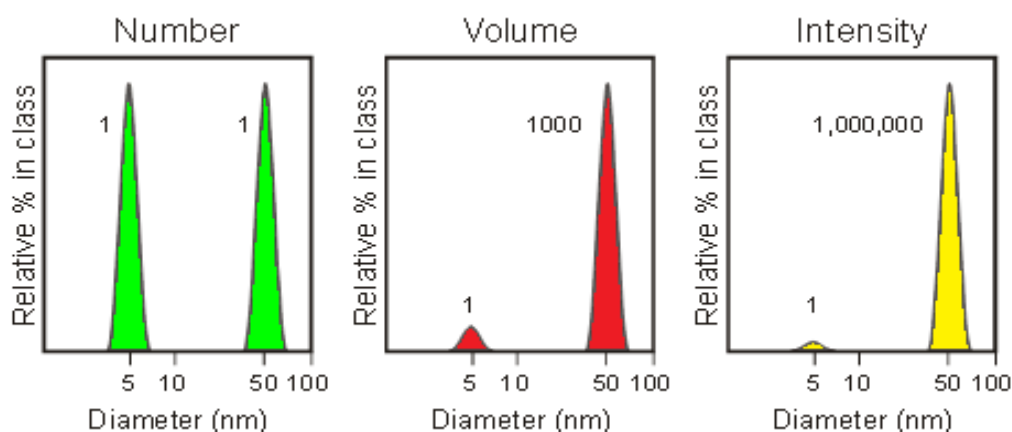


**Figure 2.64.** Number, volume and intensity distributions of a bimodal mixture of 5 and 50nm particles present in equal number. For a number distribution a plot consisting of 2 peaks of a 1 to 1 ratio would be obtained. If this number distribution was converted into volume, then 2 peaks of 1:1000 ratio would be obtained (because the volume of a sphere is equal to  $\frac{4}{3}\pi(d/2)^3$ ). For an intensity distribution 1:1000000 ratio would be obtained (the intensity of scattering is proportional to  $d^6$ ). From the DLS, the distribution obtained from a measurement is based on intensity. [86]

sign, there develops an electrophoretic velocity in addition to diffusion. Scattered light is affected in a way that there is a shift in the phase of the scattered light (PALS). This phase shift is measured by comparing the phase of the light scattered by the particles under application of the constant direct-current electric field with the phase of a reference beam. A beam splitter is used to extract a small proportion of the original laser beam to use as the reference. PALS measures the rate of change of the phase difference between the two signals. The measured phase change is proportional to the change in the position of the particles. The frequency or phase shift yields an electrophoretic velocity from which an electrophoretic mobility  $\mu_e$  is calculated.

The time derivative of the phase is equivalent to the frequency [72]

$$\frac{d\Phi_s(t)}{dt} = \omega_s = q \cdot (v_e \pm v_c) \quad 2.29)$$

with  $v_c$  a field-independent collective velocity,  $v_e$  particle electrophoretic velocity,  $q$  is the momentum transfer vector and  $\omega_s$  is the shifted frequency. With averaging  $v_e$  over all particle velocities in the scattering volume, the time derivative of the phase can be rewritten as:

$$\frac{d\Phi_s(t)}{dt} = q \cdot [\langle \mu_e \rangle E(t) \pm v_c] \quad 2. )$$

where  $\langle \mu_e \rangle$  is the first moment of the mobility distribution,  $\Phi_s$  is the Doppler-shifted phase of the scattered light and  $E(t)$  the time-dependent magnitude of the applied electric field.

Thus, by measuring time series of the phase rather than the frequency, particle electrophoretic mobility can be derived [73]. The sensitivity is 1000 times higher than that achieved in conventional LDV measurements, thereby enabling the determination of very low velocities of the scatters. Phase modulation is applied so that the Doppler frequency of a zero mobility particle is equal to the reference modulator frequency  $\omega_0$ . The deviation of the actual frequency of the detected scattered light signal,  $S(t)$ , can be measured by performing a phase comparison of  $S(t)$  with the imposed modulator frequency  $\omega_0$ .

The phase differences  $\Phi_s$  as a function of time is extracted from the measured time series  $S(t)$  by multiplying it with the sine and cosine of the time series of the reference modulator frequency  $\omega_0$  as follows [Eqs. (2.31)-(2.35)]:

$$S(t) = A \exp[-j(\omega_0 t + \Phi_s)] \quad 2.1)$$

$$S_{\text{ref}}(t) = \exp(j\omega_0 t) = \cos(\omega_0 t) + j \sin(\omega_0 t) \quad 2.2)$$

$$A \exp[-j(\omega_0 t + \Phi_s)] \exp(j\omega_0 t) = A \exp(j\Phi_s) = A \cos(\Phi_s) + jA \sin(\Phi_s) \quad 2.3)$$

Then  $\Phi_s$  and amplitude  $A$  can be extracted by the trigonometric relations,

$$\Phi_s = \arctan[\sin(\Phi_s)/\cos(\Phi_s)] \quad 2.4)$$

$$|A| = \text{ampl} = ([A \cos(\Phi_s)]^2 + A \sin(\Phi_s)^2)^{1/2} \quad 2.5)$$

From Eq. (2.30) the average phase change as a function of time in integral form is

$$\Delta\Phi_s = \Phi_{te} - \Phi_0 = \langle A \rangle q \left\{ \left[ \int_0^{te} \langle \mu_e \rangle E(t) \pm v_c \right] dt \right\} \quad 2.6)$$

and for a sinusoidal electric field with frequency  $\omega_e/2\pi$  (Hz),

$$\Delta\Phi_s = \langle A \rangle q \{ [\langle \mu_e \rangle E_0 \cos(\omega_e t_e)/\omega_e] \pm v t_e \} \quad 2.7)$$

The extracted mobility  $\mu_e$  is a mean particle mobility. The magnitude of the scattering vector is defined as  $q = (4\pi n/\lambda_0) \sin(\theta/2)$ , where  $\lambda_0$  is the wavelength in vacuum,  $\theta$  is the scattering angle and  $n$  is the refractive index of the suspending liquid.  $\Phi(t)$  is the amplitude weighted phase at time  $t$ ,  $\langle A \rangle$  is the mean signal amplitude,  $\langle \mu_e \rangle$  is the mean electrophoretic mobility,  $E(t)$  is the electric field applied from  $t = 0$  to  $t = t_e$ , and  $v_c$  is some collective motion that is due to temperature gradients, for example, assumed to be constant over the time interval of the field application. The expression of  $\Delta\Phi_s$  represents the total distance that the scatterer travels during time  $t_e$ .

The Zetasizer Nano ZS uses patented M3-PALS to measure particle electrophoretic mobility. PALS on its own provides only mean values, M3-PALS multi-frequency measurement determines rather mobility mean and distribution during the same measurement. M3-PALS is a combination of Malvern's improved  $L \propto V$  method, termed M measurement technique, and PALS technique. The M3 method performs the measurement in the middle of the cell, rather than at the stationary layer to avoid the effect of electroosmosis. The measurement cell has two electrodes between which an electric field is applied (Figure

2.33), and particles or molecules that have a net charge will migrate towards the oppositely charged electrode.

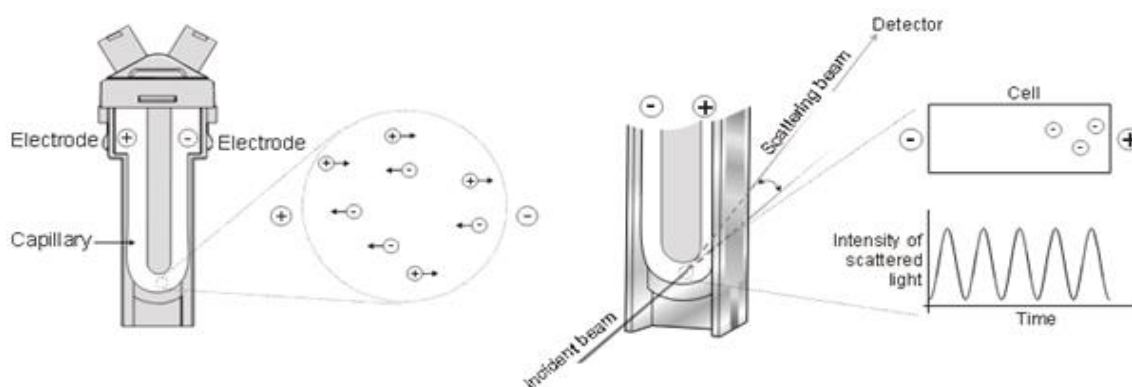


**Figure 2.66.** Zetasizer Nano ZS electrophoretic mobility measurement set up [86].

In a similar way to the typical DLS system, a zeta potential measurement system comprises six main components (Figure 2.34). The laser illuminates the particles within the sample. For zeta potential measurements this light source is split to provide an incident and a reference beam. The reference beam is also ‘modulated’ to provide the Doppler Effect

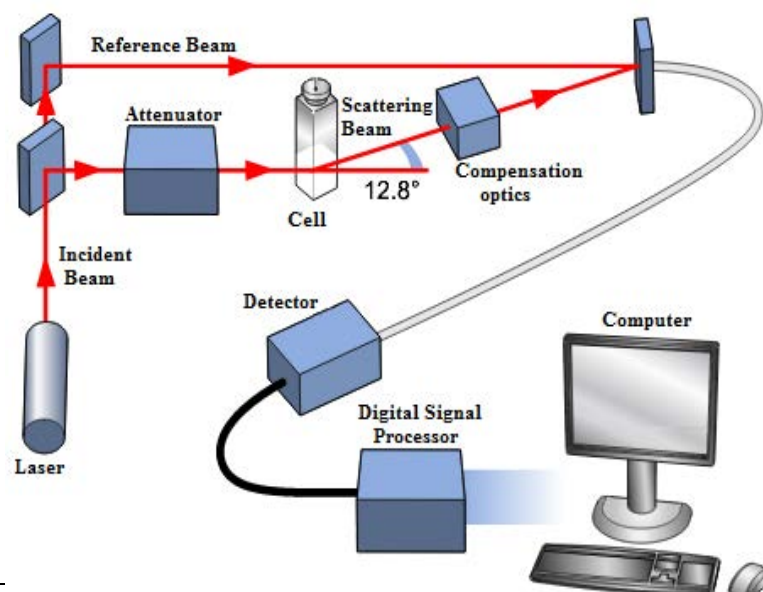


**Figure 2.65.** The measurement principle of electrophoretic mobility of charged particles in a capillary cell or zeta cell (Malvern Instruments Ltd, UK) [86]

necessary. The laser beam passes first through an attenuator that focuses the light on the sample and adjusts the intensity of the scattering and then through the center of the sample cell. The scattering beam is detected at an angle of  $\sim 12.8^\circ$  and is combined with the reference beam. When an electric field is applied to the cell, the moving particles in the cell will cause the intensity of the light to fluctuate with a fluctuating signal frequency proportional to the particle speed. The collected information passes through a digital signal processor which extracts the characteristic frequencies in the scattered light and then passes the information to a computer.



### II.3. References

- [1] Srivastava, S., Ball, V., Podsiadlo, P., Lee, J., Ho, P., Kotov, N.A., (2008). Reversible Loading and Unloading of nanoparticles in “Exponentially” Growing Polyelectrolyte L L il ms. *Journal of the American Chemical Society*, 130, 3748–3749.
- [2] Ladhari, N., (2009). *Nanostructurations de films multicouches de polyélectrolytes*. Université de Strasbourg, UMR INSERM 977.
- [3] Decher, G., (1997). Fuzzy Nanoassemblies: Toward Layered Polymeric Multicomposites. *Science*, 277, 1232.
- [4] Binnig, G., Rohrer, H., Gerber, Ch., Weibel, E., (1982) Surface studies by scanning tunneling microscopy. *Physical Review Letters*, 49, 57–61.
- [5] Binnig, G., Rohrer, H., Gerber, C., Weibel, E., (1983).  $7 \times 7$  Reconstruction on Si (111) Resolved in Real Space. *Physical Review Letters*, 50, 120.
- [6] Binnig, G., Quate, C. F., Gerber, Ch., (1986). Atomic Force Microscope. *Physical Review Letters*, 56, 930–933.
- [7] Young, RD., (1966). Field Emission Ultramicrometer. *Review of Scientific Instruments*, 37, 275–278.
- [8] Hansma, P.K., Cleveland, J.P., Radmacher, M., (1994). Tapping mode atomic-force microscopy in liquids. *Applied Physics Letters*, 64, 1738–1740.
- [9] Muller, D.J., Dufrene, Y.F., (2008). Atomic force microscopy as a multifunctional molecular toolbox in nanobiotechnology. *Nature Nanotechnology*, 3, 261–269.
- [10] Noy, A., Vezenov, D.V., Lieber, C.M., (1997). Chemical force microscopy. *Annual Review of Materials Research*, 27, 381–421.
- [11] Muller, D.J., Helenius, J., Alsteens, D., Dufrene Y.F., (2009). Force probing surfaces of living cells to molecular resolution. *Nature Chemical Biology*, 5, 383–390.
- [12] Frisbie, D., Rozsnyai, L., Noy, A., Wrighton, M., Lieber, C., (1994). Functional Group Imaging by Chemical Force Microscopy. *Science*, 265, 2071–2074.
- [13] Alessandrini, A., Facci, P., (2005). AFM: a versatile tool in biophysics. *Measurement Science and Technology*, 16, R65–R92.
- [14] Dammer, U., Popescu, O., Wagner, P., Anselmetti, D., Güntherodt, H.-J., Misevic, G.N., (1995). Binding strength between cell adhesion proteoglycans measured by atomic force microscopy. *Science*, 267, 1173–1175.
- [15] Chilkoti, A., Boland, T., Ratner, B., Stayton, P.S., (1995). The relationship between ligand-binding thermodynamics and protein-ligand interaction forces measured by atomic force microscopy.

- Biophysical Journal*, 69, 2125–2130.
- [16] Discher, D.E., Mohandas, N., Evans, E.A., (1994). Molecular maps of red cell deformation: hidden elasticity and in situ connectivity. *Science*, 266, 1032–1035.
- [17] A- assan, E., einz, W. ., Antonik, M. ., 'Costa, .P., ageswaran, S., Schoenenberger, C., Hoh, J.H., (1998). Relative microelastic mapping of living cells by atomic force microscopy. *Biophysical Journal*, 74, 1564–1578.
- [18] Goldmann, W. H., Ezzell, R. M., (1996). Viscoelasticity in wild-type and vinculin-deficient (5.51) mouse F9 embryonic carcinoma cells examined by atomic force microscopy and rheology. *Experimental Cell Research*, 226, 234–237.
- [19] Goldmann, W.H., Galneder, R., Ludwig, M., Xu, W.M., Adamson, E.D., Wang, N., Ezzell, R.M., (1998). Differences in elasticity of vinculin-deficient F9 cells measured by magnetometry and atomic force microscopy. *Experimental Cell Research*, 239, 235–242.
- [20] Lekka, M., (2012). Atomic force microscopy: A tip for diagnosing cancer. *Nature Nanotechnology*, 7, 691–692.
- [21] Lekka, M., Gil, D., Pogoda, K., ulińska-Litewka, J., Jach, R., Gostek, J., Klymenko, O., Prauzner-Bechcicki, S., Stachura, Z., Wiltowska-Zuber, J., koń, K., Laidler, P., (2012). Cancer cell detection in tissue sections using AFM. *Archives of Biochemistry and Biophysics*, 518, 151–156.
- [22] Fritzsche, W., Takac, L., Henderson, E. (1997). Application of atomic force microscopy to visualization of DNA, chromatin, and chromosomes. *ritical Reviews™ in Eu aryotic Gene Expression*, 7, 231–240.
- [23] Rivetti, C., Walker, C., Bustamante, C., (1998). Polymer chain statistics and conformational analysis of DNA molecules with bends or sections of different flexibility. *Journal of Molecular Biology*, 280, 41–59.
- [24] Hansma, H. G. (2001). Surface biology of DNA by atomic force microscopy. *Annual Review of Physical Chemistry*, 52, 71–92.
- [25] Hansma, H. G., Kasuya, K., Oroudjev, E. (2004). Atomic force microscopy imaging and pulling of nucleic acids. *Current Opinion in Structural Biology*, 14, 380–385.
- [26] Krautbauer, R., Pope, L.H., Schrader, T.E., Allen, S., Gaub, H.E., (2002). Discriminating small molecule DNA binding modes by single molecule force spectroscopy. *FEBS Letters*, 510, 154–158.
- [27] Fang, H.H., Chan, K.Y., Xu, L.C., (2000). Quantification of bacterial adhesion forces using atomic force microscopy (AFM). *Journal of Microbiological Methods*, 40, 89–97.
- [28] Muller, D. J., Fotiadis, D., Scheuring, S., Muller, S. A., Engel, A., (1999). Electrostatically balanced subnanometer imaging of biological specimens by atomic force microscope. *Biophysical Journal*, 76, 1101–1111.
- [29] Stahlberg, H., Fotiadis, D., Scheuring, S., Remigy, H., Braun, T., Mitsuoka, K., Fujiyoshi, Y., Engel, A., (2001). Two-dimensional crystals: a powerful approach to assess structure, function and dynamics of membrane proteins. *FEBS Letters*, 504, 166–172.

- 
- [30] Fotiadis, D. and Engel, A. (2004). High-resolution imaging of bacteriorhodopsin by atomic force microscopy. *Methods in Molecular Biology*, 242, 291–303.
- [31] Ikai A, Afrin, R., (2003). Toward mechanical manipulations of cell membranes and membrane proteins using an atomic force microscope: an invited review. *Cell Biochemistry and Biophysics*, 39, 257–77.
- [32] Bucior, I., Scheuring, S., Engel, A., Burger, M. M. (2004). Carbohydrate–carbohydrate interaction provides adhesion force and specificity for cellular recognition. *The Journal of Cell Biology*, 165, 529–537.
- [33] Marszalek, P.E., Li, H., Fernandez, J.M., (2001). Fingerprinting polysaccharides with single-molecule atomic force microscopy. *Nature Biotechnology*, 19, 258–262.
- [34] Hinterdorfer, P., Baumgartner, W., Gruber, H. J., Schilcher, K., Schindler, H., (1996). Detection and localization of individual antibody-antigen recognition events by atomic force microscopy. *PNAS*, 93, 3477–3481.
- [35] Lee, G. U., Kidwell, D. A., Colton, R. J., (1994). Sensing discrete streptavidin-biotin interaction with the atomic force microscope. *Langmuir*, 10, 354–357.
- [36] Rief, M., Gautel, M., Oesterhelt, F., Fernandez, J. M., Gaub, H. E., (1997). Reversible unfolding of individual titin immunoglobulin domains by AFM. *Science*, 276, 1109–1112.
- [37] Grandbois, M., Clausen-Schaumann, H., Gaub, H.E., (1998). Atomic force microscope imaging of phospholipid bilayer degradation by phospholipase A2. *Biophysical Journal*, 74, 2398–2404.
- [38] Magonov, S., Reneker, D., (1997). Characterization of polymer surfaces with atomic force microscopy. *Annual Review of Materials Research*, 27, 175–222.
- [39] Magonov, S., (2006). Atomic Force Microscopy in Analysis of Polymers. *Encyclopedia of Analytical Chemistry*.
- [40] Phillips, R.W., (1994). Atomic force microscopy for thin film analysis. *Surface and Coatings Technology*, 69, 770–775.
- [41] Ogilvy, J.A., (1993). Parametric elastic model for indentation testing of thin films. *Journal of Physics D: Applied Physics*, 26, 2123–2131.
- [42] Domke, J., Radmacher, M., (1998). Measuring the Elastic Properties of Thin Polymer Films with the Atomic Force Microscope. *Langmuir*, 14, 3320–3325.
- [43] Dimitriadis, E.K., Horkay, F., Maresca, J., Kachar, B., Chadwick, R.S., (2002). Determination of elastic moduli of thin layers of soft material using the atomic force microscope. *Biophysical Journal*, 82, 2798–2810.
- [44] Mermut, O., Lefebvre, J., Gray, D. G., Barrett, C. J., (2003). Structural and Mechanical Properties of Polyelectrolyte Multilayer Films Studied by AFM. *Macromolecules*, 36, 8819–8824.
- [45] Zhan, J., Chen, P., Yuan, B., Ji, W., Cheng, Z., Qiu, X., (2013). Real-Space Identification of Intermolecular Bonding with Atomic Force Microscopy. *Science*, 342, 611–614.
-

- 
- [46] Israelachvili, J.N, Adams, G.E., (1978). Measurement of forces between two mica surfaces in aqueous electrolyte solutions in the range 0–100 nm. *Journal of the Chemical Society, Faraday Transactions 1*, 74, 975–001.
- [47] Tortonesse, M., Barrett, R. C., Quate, C. F., (1993). Atomic resolution with an atomic force microscope using piezoresistive detection. *Applied Physics Letters*, 62, 834–836.
- [48] Akamine, S., Barrett, R. C., Quate, C. F., (1990). Improved atomic force microscope images using microcantilevers with sharp tips. *Applied Physics Letters*, 57, 316–318.
- [49] Wolter, O., Bayer, T., Greschner, J., (1991). Micromachined silicon sensors for scanning force microscopy. *Journal of Vacuum Science & Technology B*, 9, 1353–1357.
- [50] Hutter, J.L., Bechhoefer, J., (1993). Calibration of atomic-force microscope tips. *Review of Scientific Instruments*. 64, 1868–1873.
- [51] Proksch, R., Schäffer, T. E., leveland, J PC., Callahan, R C., Viani, M.B., (2004). Finite optical spot size and position corrections in thermal spring constant calibration. *Nanotechnology*, 15, 1344–1350.
- [52] Butt, H.-J., Jaschke, M., (1995). Calculation of thermal noise in atomic force microscopy. *Nanotechnology*, 6, 1–7.
- [53] Martin, Y., Williams, C.C., Wickramasinghe, H.K., (1987). Atomic force microscope: force mapping and profiling on a sub 100 angstrom scale. *Journal of Applied Physics*, 61, 4723–429.
- [54] Zhong, Q., Inniss, D., Kjoller, K., Elings, V.B., (1993). Fractured polymer/silica fiber surface studied by tapping mode atomic force microscopy. *Surface Science Letters*, 290, L688–L692.
- [55] Putman, C.A.J., Vanderwerf, K.O., Degrooth, B.G., Vanhulst, N.F., Greve J., (1994). Tapping mode atomic force microscopy in liquid. *Applied Physics Letters*, 64, 2454–2456.
- [56] Florin, E. L., Moy, V. T., Gaub, H. E., (1994). Adhesion forces between individual ligand receptor pairs. *Science*, 264, 415–417.
- [57] PeakForce Tapping brochure, Bruker: [https://www.bruker.com/fileadmin/user\\_upload/8-PDF-Docs/SurfaceAnalysis/AFM/Brochures/PeakForceTapping-Brochure.pdf](https://www.bruker.com/fileadmin/user_upload/8-PDF-Docs/SurfaceAnalysis/AFM/Brochures/PeakForceTapping-Brochure.pdf).
- [58] <https://www.bruker.com/AFM/ApplicationNotes/QuantitativeMechanicalPropertyMappingattheNanoscalewithPeakForceQNM-AppNote.pdf>
- [59] Assemi, S., Nguyen, A.V., Miller, J.D., (2008). Direct measurement of particle–bubble interaction forces using atomic force microscopy. *International Journal of Mineral Processing*, 89, 65–70.
- [60] Gaboriaud, F., Dufrene, Y.F., (2007). Atomic force microscopy of microbial cells: application to nanomechanical properties, surface forces and molecular recognition forces. *Colloids and Surfaces*, 54, 10–19.
- [61] Hertz, H., (1881). Ueber die Berührung fester elastischer Körper. *Journal für die reine und angewandte Mathematik*, 92, 156–171.
- [62] Derjaguin, B. V., Muller, V. M., Toporov, Yu. P., (1975). Effect of contact deformations on the
-

- adhesion of particles. *Journal of Colloid and Interface Science*, 53, 314-326.
- [63] Sneddon, I. N., (1965). The relation between load and penetration in the axisymmetric Boussinesq problem for a punch of arbitrary profile. *International Journal of Engineering Science*, 3, 47-57.
- [64] Dimitriadis, E.K., Horkay, F., Maresca, J., Kachar, B., Chadwick, R.S., (2002). Determination of elastic moduli of thin layers of soft material using the atomic force microscope. *Biophysical Journal*, 82, 2798-2810.
- [65] Gavara, N., Chadwick, R. S., (2012). Determination of the elastic moduli of thin samples and adherent cells using conical AFM tips. *Nature Nanotechnology*, 7, 733-736.
- [66] Sauerbrey, G., (1959). Verwendung von Schwingquartzen zur Wägung dünner Schichten und zur Mikrowägung. *Zeitschrift für Physik*, 155, 206-222.
- [67] Gileadi, E., (2011). Physical Electrochemistry. Fundamentals, Techniques and Applications, Wiley-WCH, New York.
- [68] Nomura, T., Okuhara, M., (1982). Frequency shifts of piezoelectric quartz crystals immersed in organic liquids. *Analytica Chimica Acta*, 142, 281-284.
- [69] Voinova, M. V., Rodahl, M., Jonson, M., Kasemo, B., (1999). Viscoelastic acoustic response of layered polymer films at fluid-solid interfaces : continuum mechanics approach. *Physica Scripta*, 59, 391-396.
- [70] Vogt, B. D., Lin, E. K., Wu, W-l, White, C. C., (2004). Effect of Film Thickness on the Validity of the Sauerbrey Equation for Hydrated Polyelectrolyte Films. *J. Phys. Chem. B*, 108, 12685-12690.
- [71] Voinova, M.V., Jonson, M., Kasemo, B., (2002). Missing mass' effect in biosensor's QCM applications. *Biosensors and Bioelectronics*, 17, 835841
- [72] Ferry, J.D., (1980). Viscoelastic Properties of Polymers, John Wiley and Sons: New York.
- [73] Raman, C., (1928). A new radiation. *Indian Journal of Physics*, 2, 387-398.
- [74] Tscharnuter, W.W., (2001). Mobility measurements by phase analysis. *Applied Optics*, 40, 3995-4003.
- [75] Miller, J.F., Schatzel, K., Vincent, B., (1991). The Determination of Very Small Electrophoretic Mobilities in Polar and Nonpolar Colloidal Dispersions Using Phase Analysis Light Scattering. *Journal of Colloid and Interface Science*, 143, 532-554.
- [76] [https://www.bruker.com/fileadmin/user\\_upload/8-PDF-Docs/SurfaceAnalysis/AFM/Brochures/Dimension\\_FastScan\\_Atomic\\_Force\\_Microscope\\_brochure.pdf](https://www.bruker.com/fileadmin/user_upload/8-PDF-Docs/SurfaceAnalysis/AFM/Brochures/Dimension_FastScan_Atomic_Force_Microscope_brochure.pdf).
- [77] <http://www.nanoandmore.com/afm-probes-guide.php>.
- [78] *Malvern Zetasizer Nano ZS user manual.pdf* ([www.malvern.com](http://www.malvern.com))
- [79] <http://www.bruker.co.jp/axs/nano/imgs/pdf/AN020.pdf>
- [80] Hrouzek, M., (2007). *Atomic force microscopy, modeling, estimation, and control*. Université Joseph

Fourier, Grenoble.

- [81] [usa.jpk.com/index.download.c46f64176d66c310620d0c4bdf4be7ef](http://usa.jpk.com/index.download.c46f64176d66c310620d0c4bdf4be7ef)
- [82] [usa.jpk.com/index.download.c46f64176d66c310620d0c4bdf4be7ef](http://usa.jpk.com/index.download.c46f64176d66c310620d0c4bdf4be7ef)
- [83] [http://mmrc.caltech.edu/AFM%20Dimension%20Icon/Bruker%20Training/Peak%20Force%20QNM\\_Adv%20Apps%20Training%202014.pdf](http://mmrc.caltech.edu/AFM%20Dimension%20Icon/Bruker%20Training/Peak%20Force%20QNM_Adv%20Apps%20Training%202014.pdf)
- [84] Casero, E., Vazquez, L., Parra-Alfambra, A. M., Lorenzo, E., (2010). AFM, SECM and QCM as useful analytical tools in the characterization of enzyme-based bioanalytical platforms. *Analyst*, 135, 1878–1903.
- [85] [http://megapov.inetart.net/manual-1.2/global\\_settings.html](http://megapov.inetart.net/manual-1.2/global_settings.html)
- [86] <http://www.nishshanka.com/experiance.html>

## **Chapter III**

# **Remarkable Electrokinetic Features of Charge-Stratified Soft Nanoparticles: Mobility Reversal in Monovalent Aqueous Electrolyte.**

Moussa, M.; Caillet, C.; Town, R.M. and Duval, J.F.L. Remarkable electrokinetic features of charge-stratified soft nanoparticles: mobility reversal in monovalent aqueous electrolyte. *Langmuir*, **2015**, 31, 5656-5666.

## Remarkable Electrokinetic Features of Charge-Stratified Soft Nanoparticles: Mobility Reversal in Monovalent Aqueous Electrolyte.

Mariam Moussa,<sup>1,2</sup> Céline Caillet,<sup>1,2</sup> Raewyn M. Town,<sup>3</sup> Jérôme F.L. Duval<sup>1,2,\*</sup>

<sup>1</sup> CNRS, LIEC (Laboratoire Interdisciplinaire des Environnements Continentaux), UMR7360, Vandoeuvre-lès-Nancy, F-54501, France.

<sup>2</sup> Université de Lorraine, LIEC, UMR7360, Vandoeuvre-lès-Nancy, F-54501, France.

<sup>3</sup> Department of Physics, Chemistry and Pharmacy, University of Southern Denmark, Campusvej 55, 5230 Odense, Denmark.

\* Corresponding author. E-mail: jerome.duval@univ-lorraine.fr

### Abstract

The electrokinetic behavior of G6.5 carboxylate-terminated poly(amido)-amine (PAMAM) starburst dendrimers ( $8 \pm 1$  nm diameter) is investigated over a broad range of pH values (3-9) and  $\text{NaNO}_3$  concentrations ( $c^\infty = 2\text{-}200$  mM). The dependence of nanodendrimer electrophoretic mobility  $\mu$  on pH and  $c^\infty$  is marked by an unconventional decrease of the point of zero mobility (PZM) from 5.4-5.5 to 3.8 upon increase in salt concentration, with PZM defined as the pH value at which a reversal of the mobility sign is reached. The existence of a common intersection point is further evidenced for series of mobility *versus* pH curves measured at different  $\text{NaNO}_3$  concentrations. Using soft particle electrokinetic theory, this remarkable behavior is shown to originate from the zwitterionic functionality of the PAMAM-COOH particles. The dependence of PZM on  $c^\infty$  results from the coupling between electroosmotic flow and dendrimeric interphase defined by a nonuniform distribution of amine and carboxylic functional groups. In turn,  $\mu$  reflects the sign and distribution of particle charges located within an electrokinetically-active region, the dimension of which is determined by the Debye length, varied here in the range 0.7-6.8 nm. In agreement with theory, the electrokinetics of smaller G4.5 PAMAM-COOH nanoparticles ( $5 \pm 0.5$  nm diameter) further confirms that the PZM is shifted to higher pH with decreasing dendrimer size. Depending on pH, a mobility extremum is obtained under conditions where the Debye length and the particle radius are comparable. This results from changes in particle structure compactness following salt- and pH-mediated modulations of intraparticle Coulombic interactions. The findings solidly evidence the possible occurrence of particle



mobility reversal in monovalent salt solution suggested by recent molecular dynamic simulations and anticipated from earlier mean-field electrokinetic theory.

## 1. Introduction

Over the past decades, much attention has been devoted to the measurement and modeling of the electrokinetic response of soft particulate and planar interfaces.<sup>1-3</sup> Unlike their hard counterparts, these colloidal systems partly or exclusively consist of a water- and ion-permeable polyelectrolyte-like layer defined by a three dimensional spatial distribution of hydrodynamically stagnant functional groups.<sup>4,5</sup> Numerous studies have now evidenced the benefits of using electrokinetics for deciphering the electrostatic and hydrodynamic properties of soft colloids and interfaces on the basis of appropriate theory where the concept of zeta-potential is abandoned.<sup>1,2,4-11</sup> For example, streaming current and streaming potential have been extensively used for addressing the charging mechanism of hydrogels and thin polymer films,<sup>12,13</sup> and electrophoresis has been employed to quantify the electrohydrodynamics of polymer-coated colloids,<sup>14</sup> microbes,<sup>15</sup> and environmental nanoparticles.<sup>16</sup> A common property of soft interfaces is that the electric double layer is not confined to the solution side of the interphase, but rather extends into the permeable material.<sup>1,2,4-11</sup> For this reason, electrokinetics may be regarded as a spatially-resolved technique suitable for probing the inner structural and electrostatic features of soft colloids/interfaces, with a resolution length scale defined by, amongst others, the Debye screening length.<sup>1,2</sup> Illustrative examples include the analysis of the swelling properties of thermoresponsive polymer layers,<sup>12</sup> or the determination of segment density distribution of surface-grafted poly(ethylene oxide) brushes beyond the resolution limit of neutron reflectivity.<sup>17</sup>

More recently, several theoretical reports focused on the electrokinetics of a specific class of soft colloidal systems defined by an interphase where anionic and cationic charges are spatially separated.<sup>18-21</sup> A remarkable feature of these systems is that their electrophoretic mobility ( $\mu$ ) or streaming current ( $I_{\text{str}}$ ) may change sign upon varying the monovalent electrolyte concentration.<sup>18-21</sup> The result is a strong dependence of the point of zero mobility (PZM) and point of zero streaming current (PZSC) on monovalent salt concentration, with the

PZM and PZSC defined as the pH value at which  $\mu=0$  and  $I_{\text{str}}=0$ , respectively.<sup>18,19</sup> The physical origin of such peculiar electrokinetic behavior basically stems from the structure of the electrostatic and hydrodynamic flow fields that develop within the soft interphase. The measured electrokinetic quantity effectively reflects the physico-chemical characteristics (*e.g.* nature, density and sign of functional charges) of an electrokinetically-active region *within* the soft interphase. Depending on salt concentration, this region may extend deep inside the interphase or be in a close vicinity to the external surface in contact with the electrolyte solution, thus offering a way to probe -within the interphase- distinct zones differing in terms of electrostatic characteristics.<sup>18-21</sup> This conclusion was originally obtained by Shinagawa *et al.*<sup>22</sup> from evaluation of electrostatic potential profiles across ion-penetrable membranes with nonuniform distribution of acidic and basic groups, *albeit* with ignoring hydrodynamic flow developed under electrokinetic conditions. Later, Langlet *et al.*<sup>19</sup> detailed a formalism for the electrophoresis of soft multilayered particles defined by inhomogeneous repartition of anionic and cationic charges with proper account of electroosmosis. Duval *et al.*<sup>18</sup> further demonstrated the strong analogy existing between soft multilayered particle electrophoresis and streaming current of soft planar polyanionic/polycationic multilayers. Recent molecular dynamic simulations<sup>20,21</sup> confirmed the physical basis of the mobility reversal anticipated from the aforementioned earlier mean-field electrokinetic models:<sup>18,19</sup> the effect takes place when anionic and cationic charges within the soft colloidal structure are separated over a distance comparable to the Debye length. The situation of interest here is thus different from that where *e.g.* a shift of isoelectric point is obtained in multivalent electrolytes.<sup>23,24</sup>

On an experimental level, and contrary to the statement by Raafatnia *et al.*,<sup>20</sup> sign reversal of electrophoretic mobility and that of streaming current in monovalent electrolyte solution have already been reported for complex soft (bio)colloidal systems such as guinea-pig polymorphonuclear leukocytes,<sup>25</sup> poly(ethyleneimine) (PEI)/poly(acrylic acid) bilayers,<sup>18</sup> PEI-cushioned lipidic membrane<sup>18</sup> and natural rubber (NR) colloids.<sup>26</sup> Following the theoretical conclusions outlined above, authors mainly concluded that the observed reversal of the measured electrokinetic response was qualitatively consistent with the existence of a spatial separation (or structuration) of anionic and cationic charges within the probed permeable interphase. To the best of our knowledge, there have been no attempts so far to quantitatively interpret particle

---

mobility reversal data in monovalent salt on the basis of appropriate theory. An exception is the work by Rochette *et al.*<sup>26</sup> who succeeded in theoretically reconstructing the full dependence of NR electrophoretic mobility on pH and KNO<sub>3</sub> concentration in order to extract information on the spatial organization of lipidic moieties and proteins across the interfacial NR shell structure.

In view of the above arguments, the measurement *and* the detailed analysis of mobility reversal in monovalent salt are still lacking for model colloids defined by a well-controlled intraparticulate anionic/cationic charges distribution that satisfies *a priori* the theoretical prerequisite for the mobility reversal to occur. In this work, such a confrontation between experiments and theory is provided for carboxylate-terminated poly(amido)-amine dendrimers (*ca.* 8 nm in diameter). These soft nanoparticles are defined by an internal hyperbranched structure supporting amine charges separated from an outer carboxylated shell surface.<sup>27,28</sup> Their size allows for the desired adjustment of the critical ratio between Debye length and distance over which anionic and cationic charges are nonuniformly distributed. It is shown here that the theory by Langlet *et al.*<sup>19</sup> adequately reproduces the specific features of dendrimer electrokinetics, in particular the characteristic sigmoid-like variation of their point of zero mobility with changing monovalent salt concentration. Additional information on the modulation of the dendrimer structure compactness with varying pH and salt content may be retrieved from refined analysis of the mobility data collected at sufficiently low salt concentrations and high pH values.

## 2. Materials and Methods

All routine reagents in this work were used as received from manufacturer without further purification: HNO<sub>3</sub> 0.1 M, p.a., Riedel de Haen; NaOH 0.1 M, p.a., Reag. Ph. Eur. Fluka; NaNO<sub>3</sub>, p.a., Sigma Aldrich ACS Reagents (>99%); standard pH 4, 5, 6 and 7 buffers, Merck.

### 2.1. Carboxylated PAMAM dendrimers

Half-generations G6.5 and G4.5 carboxylate-terminated poly(amido)-amine (PAMAM) dendrimers with ethylenediamine as a core initiator, were purchased from Sigma-Aldrich (St. Louis, USA).

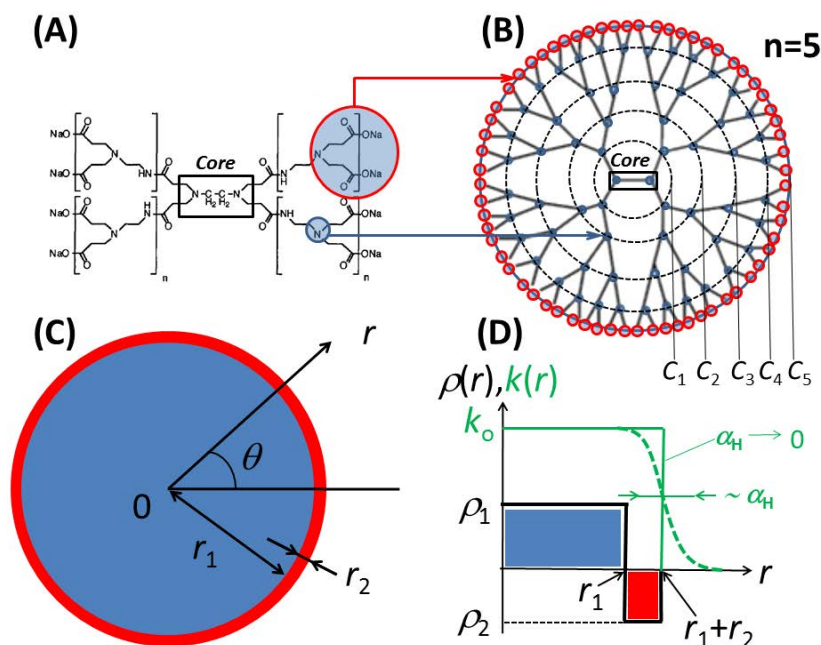


**Figure 1.** Schematic representation of carboxylate-terminated poly(amido)-amine (PAMAM) dendrimers with ethylenediamine core. (A) Chemical formula. The 4.5 and 6.5 half-generations of dendrimers used in this work correspond to  $n=5$  and  $n=7$ , respectively. (B) Hyperbranched G4.5 PAMAM-COOH dendrimer structure highlighting the spatial organization of the protonable tertiary amines (blue) along the concentric circles  $C_{i=1,\dots,n}$ . The dissociable carboxylic functional groups (red) are located at the outer surface layer of the dendrimer. (C) Representation of a PAMAM-COOH dendrimer viewed as a spherical soft polyelectrolyte consisting of an internal cationic component (radius  $r_1$ , maximum charge density  $\rho_1$ ) surrounded by a thin anionic shell layer (thickness  $r_2$ , maximum charge density  $\rho_2$ ). The polar coordinates system used for electrokinetic modeling<sup>19</sup> is indicated. (D) Radial profile for the volume charge density  $\rho(r)$  in the limits  $\alpha_{1,2} \rightarrow 0$  and  $\mu_{1,2}(y(r)) \rightarrow 1$ , and distribution of the friction coefficient  $k(r)$  across the dendrimer structure for  $\alpha_H \rightarrow 0$  and  $\alpha_H > 0$  (indicated). See text for further details.

These particles belong to a family of water-soluble polymers originally synthesized by Tomalia *et al.*<sup>27,28</sup> and defined by a unique hyperbranched architecture and a compact spherical geometry in solution. PAMAM-COOH dendrimers possess protonable tertiary amine groups located at the branching points, dissociable carboxylic groups that terminate each branch of the structure (Figures 1A,B) and secondary amines  $-(CO)-NH-$  that are not involved in protonation reaction due to the stability of the peptide nitrogens.<sup>29,30</sup> The distance between tertiary amines is approximately 0.7 nm and the last nitrogen is separated from the carbon atom of the carboxylic group by *ca.* 0.5-0.6 nm.<sup>31</sup> Intraparticle tertiary amines are distributed according to concentric circles  $C_{i=1,\dots,n}$  of diameter  $\delta_{i=1,\dots,n} = (1.5 + 0.7i)$  nm with  $n=7$  for G6.5 dendrimer generation.<sup>31</sup>

The number of functional amine groups  $N_{i=1,\dots,n}^a$  located on the  $C_{i=1,\dots,n}$  circle is given by  $N_{i=1,\dots,n}^a = 2^{i+1}$  and the outer surface layer contains  $N_n^c = 2^{n+2}$  carboxylic groups. The total amount of tertiary amines per dendrimer, including those in the core (Figure 1A), is thus  $2(2^{n+1} - 1)$ , which provides 510-512 amine-carboxylic groups for G6.5 PAMAM-COOH dendrimers.<sup>32</sup> Figure 1B illustrates the aforementioned distribution of internal cationic and peripheral anionic charges for the G4.5 generation of PAMAM-COOH dendrimers ( $n = 5$ , 126-128 amine/carboxylic groups).<sup>32,33</sup>

## 2.2. Electrophoresis

Electrophoretic mobility of G6.5 PAMAM-COOH dendrimers (0.1% volume dispersion) was measured as a function of pH and  $\text{NaNO}_3$  salt concentration at room temperature (25°C). Using a Zetasizer Nano ZS instrument (Malvern Instruments), electrophoretic mobility was determined from Phase Analysis Light Scattering (PALS) that consists in measuring particle velocity from the phase shift between light scattered by moving particles under application of a constant direct-current electric field and a reference beam. Solution pH and salinity were fixed after addition of appropriate aliquots of 0.1 M NaOH, 0.1 M  $\text{HNO}_3$ , 1 M  $\text{NaNO}_3$  solutions in ultrapure Milli-Q water and we did not measure noticeable changes in solution pH with time. It was further systematically checked that dendrimers electrophoretic mobility measured in unbuffered  $\text{NaNO}_3$  electrolytes was -within experimental error- similar to that obtained under conditions where the desired solution pH was maintained constant with proper use of acetate (experiments at pH 3.6, 4, 5.1, and 5.5, Figure 2) or phosphate buffers (experiments at pH 6.7, Figure 2) in concentrations well below that of  $\text{NaNO}_3$  electrolyte. In details, acetate buffer was prepared from acetic acid and sodium acetate (>99.8%, 0.2 M, Sigma-Aldrich) and phosphate buffer from sodium hydroxide (fisher chemicals) and potassium dihydrogen phosphate (99.5%, 0.2 M, Fluka). Experiments were carried out on at least 3 freshly prepared dendrimer suspensions and each reported data point is the average of 3 to 5 distinct mobility acquisitions.

Particle diffusion coefficients were measured by dynamic light scattering (DLS) using the above Zetasizer Nano ZS equipment (He-Ne red laser, 633 nm). As a first approximation,

---

distributions in (hydrodynamic) size of equivalent hard spheres were evaluated on the basis of the Stokes-Einstein equation. Within experimental uncertainty, we found  $d = 8 \pm 1$  nm for G6.5 dendrimer diameter with no clear pH- or salt-concentration dependence under the tested conditions. Additional electrokinetic experiments were conducted on G4.5 PAMAM-COOH dendrimers with diameter  $d = 5 \pm 0.5$  nm, also stable against aggregation under all conditions examined in this work. These particle size values are in good agreement with literature data obtained from *e.g.* size exclusion chromatography.<sup>33,34</sup>

### 3. Theory

In this section, the bases for the evaluation of electrophoretic mobility  $\mu$  of PAMAM-COOH dendrimers are briefly detailed along the lines set forth by Langlet *et al.*<sup>19</sup> in their mean-field modeling of chemically-stratified particle electrophoresis. Briefly, PAMAM-COOH dendrimers are represented as soft particles consisting of an inner shell of radius  $r_1$  defined by a density  $n_1$  of tertiary amines and a surrounding outer shell layer of thickness  $r_2$  where carboxylic groups are distributed with volume density  $n_2$  (Figures 1C,D). For the sake of demonstration and unless otherwise specified,  $n_1$  will be taken as being independent of the radial position across the dendrimer structure so that, according to this smeared-out picture,  $n_1$  is simply given by  $n_1 = 3(2^{n+1} - 1) / (2\pi r_1^3)$ . It will be shown that this simplified dendrimer representation is sufficient to capture the physical origin of dendrimer mobility reversal in monovalent salt and to interpret the full dependence of  $\mu$  on electrolyte concentration and pH without the need to include details on the discrete amine electrostatic features. The radial distribution of the density of hydrodynamically stagnant charges,  $\rho(r)$ , located at the radial position  $r$  (Figure 1 C), may then be formulated according to the generic expression<sup>18,19</sup>

$$\rho(r) = \omega \left\{ [\rho_1 \mu_1(y(r)) - \rho_2 \mu_2(y(r))] f_1(r) + \rho_2 \mu_2(y(r)) f_2(r) \right\}, \quad (1)$$

where  $f_{1,2}(r)$  are radial functions used to define the density distribution of polymer material supporting the internal and peripheral functional groups

$$f_{j=1,2}(r) = \left\{ 1 - \tanh \left[ \left( r - \sum_{p=1}^j r_p \right) / \alpha_j \right] \right\} / 2, \quad (2)$$

where the length scales  $\alpha_1$  and  $\alpha_2$  basically determine the sharpness of the transitions from internal dendrimer volume to peripheral shell layer, and from peripheral shell layer to outer electrolyte solution, respectively.<sup>19,35</sup> In eq 1,  $\omega$  is a scalar that ensures the constancy of the total number of polymer segments upon possible variation of particle size and/or interfacial segment density distribution due to pH- or salt-mediated swelling processes,  $\gamma(r)$  is the local dimensionless electrostatic potential defined by  $\gamma(r) = F\Psi(r)/RT$  with  $T$  the absolute temperature,  $R$  the gas constant,  $\Psi$  the potential and  $F$  the Faraday number. Denoting as  $e$  the elementary charge, the quantities  $\rho_1 = n_1 e$  and  $\rho_2 = -n_2 e$  denote the maximum charge densities (in  $C.m^{-3}$ ) in respectively the dendrimer volume, within which the amine groups are fully protonated, and in the outer shell layer, within which the carboxylic groups are completely dissociated. The dissociation functions  $\mu_{1,2}$  for the ionogenic groups located at the radial coordinate  $r$  in the dendrimer interior ( $j=1$ ) and in the outer shell ( $j=2$ ), respectively, depend on the local potential  $\gamma(r)$  via<sup>18</sup>

$$\mu_j(\gamma(r)) = 1 / \left\{ 1 + 10^{-\varepsilon_j(pK_j - \gamma(r))} \exp(\varepsilon_j \gamma(r)) \right\}, \quad (3)$$

with  $\varepsilon_1 = +1$ ,  $\varepsilon_2 = -1$  and  $K_j = 10^{-pK_j}$  the acidity constant associated to the reactions  $\equiv NH^+ \rightleftharpoons \equiv N + H^+$  ( $j=1$ ) and  $-COOH \rightleftharpoons -COO^- + H^+$  ( $j=2$ ). In the limit  $\alpha_{1,2} \rightarrow 0$  and  $\mu_{1,2}(\gamma(r)) \rightarrow 1$ , densities of protonated amines and carboxylate groups become independent of  $r$ , so that  $\rho(r)$  is reduced to the step-function like distribution given in Figure 1D. The electrophoretic mobility  $\mu$  follows from numerical solving of the set of coupled electrohydrodynamic equations given elsewhere,<sup>19,35</sup> which includes: (i) the non-linear Poisson-Boltzmann equation that defines the electrostatic potential distribution  $\gamma(r)$ , (ii) the Navier-Brinkman equation that involves the electroosmotic flow penetration length  $1/\lambda_o$  within the dendrimer particle, and (iii) the continuity equations for mobile electrolyte ions and for steady incompressible flow. The reader is referred to Refs. [19,35] and [36] for further details on the

theory and on the collocation method adopted for solving the above equations. It is stressed that the applicability of Brinkman theory for evaluating the friction force exerted by a soft interphase on the flow under electrokinetic conditions has been validated by Dukhin *et al.*,<sup>37</sup> and confirmed by recent comparison between molecular and mean-field simulations of soft particle electrophoresis.<sup>20,21</sup> Depending on salt concentration and pH, dendrimer particles may undergo complex volume and/or interfacial swelling/shrinking processes<sup>38</sup> that not only affect charge distributions *via* changes in  $\alpha_{1,2}$  (eq 1), but also the local friction that the particle exerts on the flowing fluid.<sup>35</sup> For this reason, and in line with previous work,<sup>19,35</sup> the following radial distribution is introduced for the friction coefficient  $k(r)$  involved in the Navier-Brinkman equation

$$k(r) = \omega k_o \left\{ 1 - \tanh \left[ (r - r_1 - r_2) / \alpha_H \right] \right\} / 2, \quad (4)$$

where  $\alpha_H$  is the length scale over which modifications of hydrodynamic drag operate (Figure 1D) as a result of changes in particle structure compactness/size. The friction term  $k_o$  corresponds to the limit reached by  $k(r)$  when  $\alpha_H \rightarrow 0$ . It is formally defined by  $k_o = \eta \lambda_o^2$ , with  $\eta$  the dynamic viscosity of water and  $1/\lambda_o^2$  the particle permeability that decreases with increasing bulk polymer segment density, as formulated within the framework of Debye-Bueche theory.<sup>39</sup> The presence of a finite polymer gradient at the interphase between dendrimer and solution, reflected here by  $\alpha_{2,H} \neq 0$ , may lead to an increase or decrease in particle mobility  $|\mu|$  depending on whether the effects are primarily mediated by the underlying modifications of the interfacial electrostatic potential profile (*via* eqs 1-2 and changes in  $\alpha_2$ ) or of the hydrodynamic flow field distribution (*via* eq 4 and changes in  $\alpha_H$ ), respectively.<sup>35</sup> These results will help us to interpret the dendrimer electrokinetic data upon adjustment -if necessary- of  $\alpha_{1,2}$  and/or  $\alpha_H$  at low electrolyte concentrations. This salt regime corresponds to that where intraparticle interactions between functional groups are expected to most significantly modify particle structure/compactness,<sup>38</sup> and thereby the interfacial distribution of the electrostatic and flow fields.



## 4. Results and discussion

### 4.1. PAMAM-COOH dendrimer electrophoresis

The dependence of G6.5 PAMAM-COOH dendrimer electrophoretic mobility  $\mu$  on  $\text{NaNO}_3$  electrolyte concentration  $c^\infty$  is shown in Figure 2 for various values of solution pH. At  $\text{pH} = 3.6$ ,  $\mu$  is positive over the entire range of  $\text{NaNO}_3$  concentrations tested, which suggests that dendrimer electrophoretic motion is here primarily driven by the internal tertiary amines which are fully protonated at such low pH.<sup>28,40-42</sup> As expected,  $\mu$  increases with decreasing  $c^\infty$  from 200 mM to 10 mM due to insufficient screening of the dendrimer charges by electrolyte ions. At  $c^\infty \sim 10$  mM,  $\mu$  reaches a maximum before slightly decreasing upon further decrease in salt concentration. At  $\text{pH} = 4$  and  $c^\infty = 200$  mM,  $\mu$  is negative; upon decreasing the salt concentration,  $\mu$  decreases in magnitude and changes sign at  $\sim 100$  mM. With further decrease in

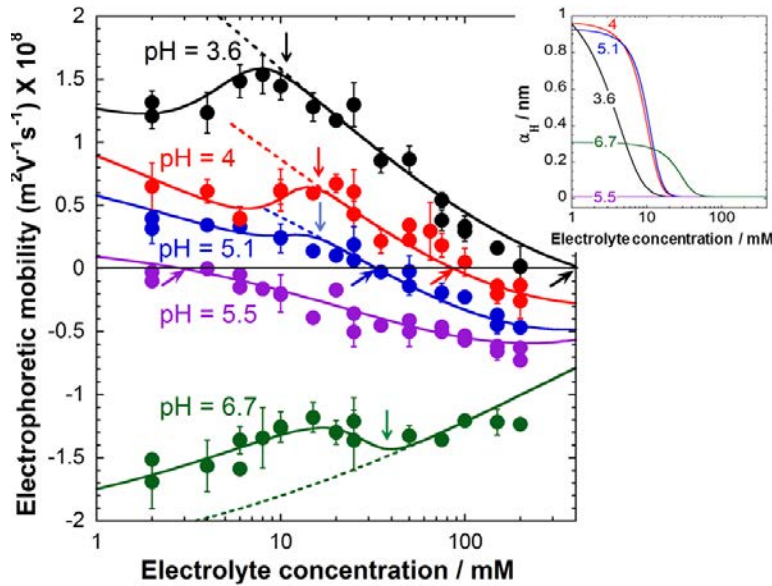


**Figure 2.** Electrophoretic mobility of G6.5 PAMAM-COOH dendrimer as a function of  $\text{NaNO}_3$  electrolyte concentration at several pH values (indicated). Symbols correspond to measurements. Curves pertain to mobility evaluation from the theory outlined in §3 in the limit  $\alpha_H \rightarrow 0$  (dashed curves) and with adopting the  $\alpha_H$  values reported in the inset (solid curves). 1, 10 and 100 mM  $\text{NaNO}_3$  concentrations correspond to  $kd/2 = 0.4, 1.3$  and  $4.2$ , respectively. Other model parameters:  $\alpha_{1,2} \rightarrow 0$ ,  $r_1 = 3.5$  nm,  $r_2 = 0.55$  nm (except  $0.6$  nm at  $\text{pH} = 4$ ),  $\rho_1 / F = 4.71 \times 10^3$  mM,  $-\rho_2 / F = 2.3 \times 10^3$  mM,  $\text{p}K_1 = 7.1$ ,  $\text{p}K_2 = 3.7$ . See text for further details on modeling. Mobility reversals are marked by oblique arrows and local mobility maxima by vertical arrows.

$c^\infty$ ,  $\mu$  increases and reaches a local maximum at  $\sim 10$ -20 mM before increasing again at salt concentrations lower than *ca.* 6 mM. A similar electrophoretic behavior is observed at pH = 5.1 and pH = 5.5 except that the critical salt concentration where mobility reversal occurs is significantly shifted to lower values with increasing pH. In addition, within experimental uncertainty, the local extremum observed at pH = 4 becomes less pronounced at pH = 5.1 and disappears at pH = 5.5. At pH = 6.7,  $\mu$  is negative regardless of NaNO<sub>3</sub> concentration, which indicates that  $\mu$  is now predominantly determined by the strongly dissociated peripheral carboxylic groups and that the overall contribution of the weakly protonated tertiary amines has become marginal. Similar to the case at pH = 4,  $|\mu|$  first increases in absolute value with decreasing  $c^\infty$ , passes through a local maximum at *ca.* 20-40 mM, and then increases again with further decrease in the solution salinity.

For the sake of completeness, Figure 3 displays G6.5 PAMAM-COOH dendrimer mobility measured as a function of pH at the selected 10 mM, 25 mM, 100 mM and 200 mM NaNO<sub>3</sub> concentrations. With increasing pH at fixed  $c^\infty$ ,  $\mu$  decreases from positive to negative values and it levels off at pH 8-9, which reflects the complete dissociation of carboxylic groups in the outer dendrimer shell layer. In agreement with Figure 2, the larger is the NaNO<sub>3</sub> concentration, the lower is the solution pH required to achieve zero electrophoretic mobility condition. At a given fixed pH value, changing salt concentration not only leads to mobility reversal but also to significant screening effects, as evidenced by the decrease in  $|\mu|$  with increasing  $c^\infty$ . An additional striking feature revealed by Figure 3 is the existence of a common intersection point (noted A in Figure 3) for the  $\mu$  *versus* pH curves at different salt concentrations. This property was already observed for natural rubber (NR) particles ( $\sim 50$  nm radius),<sup>26</sup> and an analogous situation was reported for a poly(ethyleneimine)-supported bilayer membrane from measurements of streaming current as a function of pH at different KCl concentrations.<sup>18</sup>

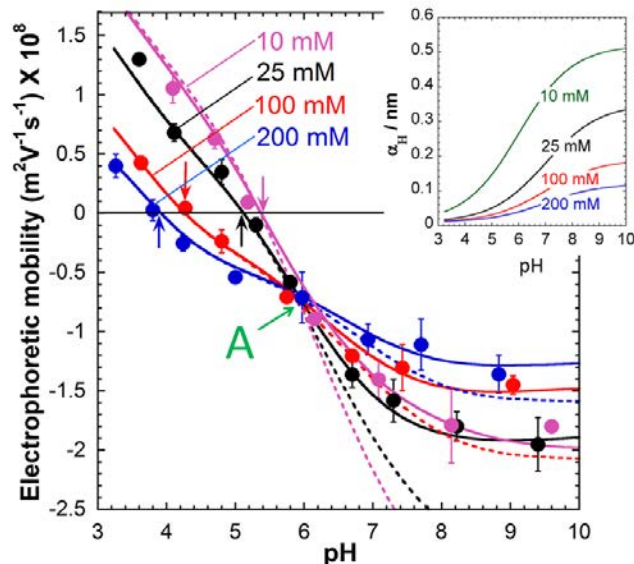


**Figure 3.** Electrophoretic mobility of G6.5 PAMAM-COOH dendrimer as a function of pH at several  $\text{NaNO}_3$  electrolyte concentrations (indicated). Symbols correspond to measurements; curves correspond to mobility evaluation from the theory outlined in §3 with  $\alpha_H \rightarrow 0$  (dashed curves) and with adopting the  $\alpha_H$  values reported in the inset (solid curves). Other model parameters: as in Figure 2. Vertical arrows indicate dendrimer mobility reversals.

Figure 4 shows the full dependence of the dendrimer point of zero mobility (PZM) on salt concentration. Data in Figure 4 were derived from a set of  $\mu$  versus pH curves of the types shown in Figure 3 and measured for  $\text{NaNO}_3$  concentrations finely tuned in the range 2 mM to 200 mM (not shown). With decreasing  $c^\infty$  from 200 mM to *ca.* 20 mM, the PZM abruptly increases from 3.8 to 5.3 and asymptotically reaches the plateau value 5.4-5.5 for salt concentrations below 20 mM. On a qualitative level, the dependence of the PZM on  $c^\infty$  observed for G6.5 dendrimers remarkably conforms to that obtained for larger NR particles.<sup>26</sup>

In the next section, the full electrokinetic behavior of G6.5 dendrimer described above in the pH range 3 to 9 and monovalent salt concentration range 2 mM-200 mM, is quantitatively discussed on the basis of the electrokinetic theory outlined in §3.

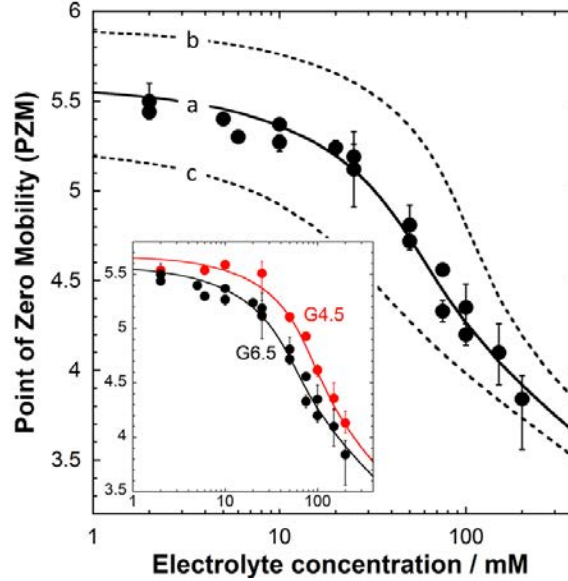


**Figure 4.** Comparison between the Point of Zero Mobility (PZM) of G6.5 PAMAM-COOH dendrimer measured at several  $\text{NaNO}_3$  concentrations (symbols) and that evaluated from theory (solid curve (a)). Model parameters: as in Figure 2 with  $\alpha_H \rightarrow 0$ . Dashed curves (b) and (c) correspond to simulations performed with  $r_2 = 0.5$  nm and  $r_2 = 0.6$  nm, respectively, with the other model parameters fixed at the values used for deriving the results displayed in curve (a). The inset shows measured and theoretical PZM for G6.5 PAMAM-COOH dendrimer together with those of the smaller G4.5 PAMAM-COOH particles (experiments: red symbols; theory: red curve). Model parameters for G4.5: as for G6.5 except  $r_1 = 2$  nm,  $\rho_1 / F = 6.25 \times 10^3$  mM and  $-\rho_2 / F = 2.1 \times 10^3$  mM.

## 4.2. Quantitative description of PAMAM-COOH dendrimer electrokinetics.

**4.2.1. Setting the stage.** The theoretical parameters required for mobility evaluation are the dendritic dimensions  $r_1$  and  $r_2$  (Figure 1C), the maximum charge densities  $\rho_1$  and  $\rho_2$  corresponding to full protonation of the tertiary amines and complete dissociation of peripheral carboxylic groups, respectively, the proton dissociation constants  $\text{p}K_1$  and  $\text{p}K_2$  for amine and carboxylic groups (eq 3), respectively, the interphasial length scales  $\alpha_{1,2,H}$  (eqs 1, 4) and the hydrodynamic penetration length  $1/\lambda_0$ . Our goal is to provide a *constrained modeling* of dendrimer electrokinetics and to demonstrate the relationship with the nonuniform distribution of amine and carboxylic groups in the dendrimer body. For these reasons, unless otherwise specified,  $r_1$  and  $r_2$  are fixed to  $r_1 = 3.5$  nm and  $r_2 = 0.55$  nm, which is in line with the measured G6.5 dendrimer radius  $d/2$  (§2) and with the 0.5-0.6 nm separation between the last outer nitrogen and the carbon of the peripheral carboxylic groups.<sup>31</sup> In addition, as a first step of the analysis, we adopt the limits  $\alpha_{1,2,H} \rightarrow 0$  that correspond to step-function profiles for the density of

amines and carboxylic groups, and for the friction coefficient  $k(r)$  (Figure 1D). Finally, the value of  $\rho_1$  is fixed to  $\rho_1 = n_1 e$  with  $n_1 = 3N_{n=7}^a / (4\pi r_1^3) = 3(2^{n+1} - 1) / (2\pi r_1^3) \Big|_{n=7}$  the volume density of tertiary amines in G6.5 PAMAM-COOH dendrimer (see §2 and §3). Consequently, the quantitative modeling of the electrokinetic data collected in Figures 2, 3 and 4 is attempted hereafter upon the sole adjustment of  $\rho_2$ ,  $1/\lambda_o$  and  $pK_{1,2}$ , with the further requirement that  $pK_1$  should be in the (narrow) 6.3-7.2 range derived from titration experiments.<sup>40-42</sup> Due to the molecular dimension of the outer carboxylate layer ( $r_2 \ll r_1$ ), there is some significant uncertainty for accurate estimation of the volume charge density  $\rho_2 = -3eN_{n=7}^c / \left\{ 4\pi \left[ (r_1 + r_2)^3 - (r_2)^3 \right] \right\}$ . This motivates our choice for not fixing  $\rho_2$  *a priori* in the electrokinetic analysis. In addition, counterion condensation on the outer dendrimer surface<sup>43-45</sup> may lead to a discrepancy between the structural amount  $N_{n=7}^c$  of carboxylic groups and that inferred from electrokinetics.<sup>46</sup> This feature is addressed later in the manuscript.

**4.2.2. Comparison between theory and experiments.** For the limits  $\alpha_{1,2,H} \rightarrow 0$ , the dashed curves in Figure 2 shows the successful modeling of dendrimer electrokinetics at pH 3.6 to 6.7 for NaNO<sub>3</sub> concentrations ( $c^\infty$ ) higher than those corresponding to the (local) electrophoretic mobility maxima marked by vertical arrows in Figure 2. The exception is pH = 5.5 where theory satisfactorily recovers the variations of  $\mu$  over the entire range of tested salt concentrations. The obtained  $pK_1 = 7.1$  and  $pK_2 = 3.7$  adequately compare with literature data<sup>40,42</sup> and the analysis further provides  $-\rho_2 / F = 2.3 \times 10^3$  mM and  $(\lambda_o d / 2)^{-1} \rightarrow 0$ , which suggests that the dendrimer structure is poorly permeable to flow. Using the aforementioned parameter values, the theory correctly predicts the dependence of  $\mu$  on pH at 10 mM, 25 mM, 100 mM and 200 mM NaNO<sub>3</sub> concentrations in the pH range 3 to ~7 and, in particular, it properly evidences the existence of the common intersection point A (Figure 3). Finally, the salt concentration-dependent PZM simulated with the model parameters adopted for fitting the data of Figures 2-3, agrees remarkably well with the pH values where mobility reversal occurs upon increasing  $c^\infty$  from 2

mM to 200 mM (Figure 4). The corresponding  $\{\text{PZM}; c^\infty\}$  data falls within the  $\text{pH}-c^\infty$  domains where theoretical mobility adequately compares with measurements (Figures 2-3). The recovery of the sigmoidal variation of the PZM in the 2 mM to 200 mM  $\text{NaNO}_3$  concentration range thus underlines the consistent and constrained adjustment of  $\rho_2$ ,  $1/\lambda_0$  and  $\text{p}K_{1,2}$  parameters that quantitatively capture the electrokinetic response of G6.5 PAMAM-COOH at  $\text{pH} < \sim 7$  and/or  $c^\infty \geq 10\text{-}40$  mM. For the reader to further appreciate the parametric sensitivity in fitting electrokinetic data, Figure 5 reports the computed dependence of the PZM on  $c^\infty$  with changing either  $\text{p}K_{1,2}$ ,  $1/\lambda_0$  or  $\rho_{1,2}$  while fixing the other parameters to values derived from theory/experiments confrontation. Figure 5 is further discussed in the following section.

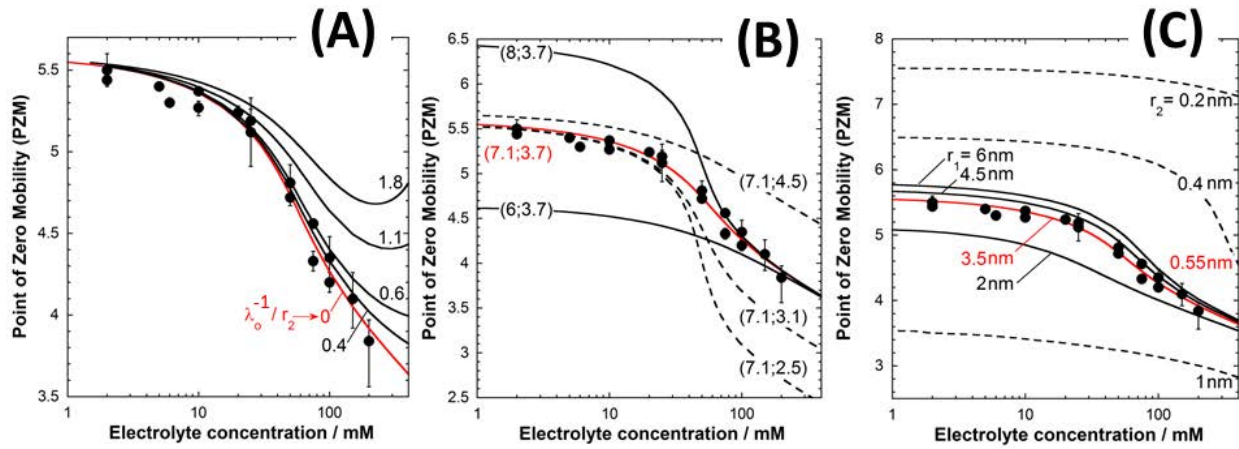


**Figure 5.** Theoretical dependence of the Point of Zero Mobility (PZM) on monovalent salt concentration for various values of  $1/\lambda_0$  (A),  $\text{p}K_{1,2}$  (B) and  $r_{1,2}$  (C) (indicated). For the sake of comparison, experimental data collected on G6.5 PAMAM-COOH dendrimers are reported, and solid red curves correspond to the theoretical results obtained with the set of parameters adjusted to capture the dendrimer electrokinetic properties displayed in Figures 2, 3 and 4. Values of the model parameters left unchanged in the simulations: as in Figure 2 with  $\alpha_H \rightarrow 0$ . In (A), results are given in terms of the dimensionless ratio  $1/(\lambda_0 r_2)$ . In (B), solid curves correspond to simulations with  $\text{p}K_2$  fixed at 3.7, and dashed curves have  $\text{p}K_1$  fixed at 7.1. In (C), solid curves correspond to simulations with  $r_2$  fixed at 0.55 nm, and dashed curves have  $r_1$  fixed at 3.5 nm.

Under conditions where  $\text{pH}$  is greater than  $\sim 7$  and/or  $c^\infty$  is lower than 10 mM to 40 mM (depending on solution  $\text{pH}$ , see Figure 2), the theory with  $\alpha_{1,2,H} \rightarrow 0$  systematically overestimates the magnitude of dendrimer electrophoretic mobility. Such a discrepancy between theory and measurements has already been reported for various (bio)colloids, including

bacteria.<sup>15</sup> It cannot be attributed here to double layer polarization/relaxation effects known to give rise to a maximum in  $\mu$  versus salt concentration curves.<sup>8,9,35</sup> Indeed, the theory accounts for such effects and is valid without approximation on either the magnitude of the interfacial electrostatic potential or on the size of the considered particles. Besides, the (local) mobility maxima are not the result here of an increased double layer compression following a significant contribution of protons or hydroxyl ions to solution ionic strength. Instead, Duval and Ohshima<sup>35</sup> showed that the introduction of a diffuse (or gradual) distribution in polymer material density at the particle interphase generates an increased friction exerted on the electroosmotic flow and a decrease in particle mobility compared to the situation where the friction coefficient abruptly decreases to zero at the very particle/solution interface (Figure 1D). Analogous effects of interfacial segment density gradient on particle mobility, have been theoretically and experimentally evidenced for thin polymer films from streaming current analysis.<sup>13</sup> This trend is confirmed here from the recovery of the dendrimer mobility data collected at low salt concentrations (Figure 2, solid curves) and high pH (Figure 3, solid curves) with adjustment of  $\alpha_H$  according to the values specified in the insets of Figures 2 and 3, respectively. It is stressed that the adopted (monotonous) increase of  $\alpha_H$  with decreasing  $c^\infty$  not only generates the observed (local) mobility maxima - in line with expectation from previous work-<sup>35</sup> but also reproduces the further increase in  $|\mu|$  measured at pH = 4, 5.1 and 6.7 with decreasing  $c^\infty$  from 6-10 mM to 2 mM.

In the next section, the rich electrokinetic response of G6.5 PAMAM-COOH dendrimers is further detailed with emphasis on the physical processes underlying dendrimer mobility reversal and modulations of  $\alpha_H$  upon changing pH and NaNO<sub>3</sub> salt concentration.

#### **4.2.3. Physical processes underlying electrokinetic behavior.**

*Dendrimer mobility reversal.* The origin of the sign reversal in dendrimer mobility is illustrated in Figure 6 where the radial distribution of the electrostatic potential  $\psi(r)$  is given for selected values of  $c^\infty$  and pH.

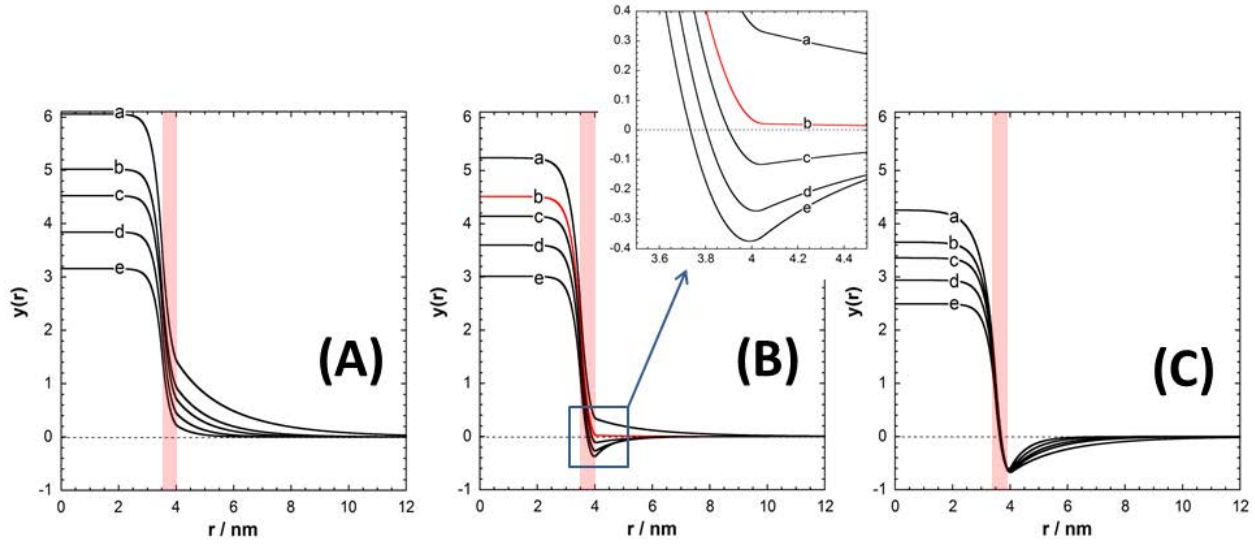


**Figure 6.** Distribution of the dimensionless electrostatic potential  $y(r)$  at pH = 3.5 (A), 5 (B) and 6 (C) for monovalent electrolyte concentration values of 10 mM (a), 30 mM (b), 50 mM (c), 100 mM (d) and 200 mM (e). The red solid curve in (B) corresponds to conditions where the PZM is reached and the vertical shaded bar indicates the location of the carboxylated peripheral dendrimer layer. Model parameters: as in Figure 2.

At pH = 3.5, 5 and 6,  $y(r)$  is positive across the entire internal dendrimer structure, in agreement with the sign of the amine charges and the magnitude of their protonation constant ( $pK_1 = 7.1$ ). Regardless of pH and salt concentration,  $y(r)$  remains constant in the bulk of the dendrimer body, but sharply decreases at the interface with the peripheral layer containing the carboxylate charges. The existence of a zero electric field in the dendrimer volume is explained by the fact that the thickness of the electric Debye layer *within* the dendrimer structure, denoted as  $1/\kappa_m$ ,<sup>4</sup> is here small as compared to the particle radius  $d/2$ . In such a situation, the bulk potential identifies with the Donnan potential  $\psi^D$  (dimensionless form  $y^D = F\psi^D / RT$ ), defined by the transcendental equation  $y^D = \sinh^{-1}[\mu_1(y^D)\rho_1 / (2Fc^\infty)]$ .<sup>11,47</sup> The latter expression reduces to the explicit form  $y^D = \sinh^{-1}[\rho_1 / (2Fc^\infty)]$  at pH 3.5 (Figure 6A) where full protonation of the amines is achieved ( $\mu_1(y^D) \rightarrow 1$ ). On a quantitative level, the intraparticulate Debye length is



given by  $\kappa_m^{-1} = \kappa^{-1} [\cosh(y^D)]^{-1/2}$ ,<sup>4,47</sup> which yields  $\kappa_m d / 2 \sim 14.7-20.3$  under the salinity conditions in Figure 6. With increasing pH at fixed salt concentration,  $y^D$  decreases due to the decreasing protonation of the amines, while the decrease in  $y^D$  with increasing  $c^\infty$  at fixed pH stems from charge screening by electrolyte ions. Let us now focus on the characteristics of the potential distribution across the carboxylic layer and in the outer electrolyte solution. At pH 3.5,  $y(r)$  is positive in the peripheral dendrimer layer of thickness  $r_2$  and it smoothly tends to zero with distance from the outer dendrimer surface located at  $r = r_1 + r_2$ . A sharp decrease of the electric field ( $\sim dy(r)/dr$ ) is further observed with increasing  $r$  from  $(r_1 + r_2)^-$  to  $(r_1 + r_2)^+$ . This is a consequence of the significant difference between the typical length scales  $1/\kappa_m$  and  $1/\kappa$  for the potential distributions inside and outside the dendrimer volume, respectively ( $\kappa_m^{-1}/\kappa^{-1} = 0.07-0.29$  in Figure 6A).

At pH 5 a different situation arises:  $y(r = r_1 + r_2)$  decreases from positive to negative values with increasing salt concentration from 10 mM to 200 mM (Figure 6B). In particular,  $y(r = r_1 + r_2)$  reaches zero value at  $c^\infty \sim 30$  mM (red curve in Figure 6B) corresponding to the salt concentration at which  $\mu = 0$  (Figure 4). The sign reversal of  $y(r = r_1 + r_2)$ , or equivalently that of  $\mu$ , results from the combination of two features. First, the anionic charge density in the peripheral layer significantly increases with increasing pH from 3.5 to 5, while the density of cationic charges in the dendrimer volume decreases ( $pK_1 = 7.1$  and  $pK_2 = 3.7$ ). Secondly, upon increase of the salt concentration, most of the counterions become confined in close vicinity of the outer dendrimer interface. The electrostatic potential distribution in the extraparticulate counterion atmosphere then increasingly reflects the density and sign of charges distributed in the outer carboxylate layer. The transition from positive to negative values of  $y(r = r_1 + r_2)$  occurs within a salt concentration regime where the Debye length  $\kappa^{-1}$  becomes comparable with the thickness of the zone where carboxylate charges are located,  $r_2$ . This transition takes place provided that the dissociation of the carboxylic groups is sufficiently strong to compete with the internal positive amine charges for fixing  $y(r)$  at the dendrimer/solution interphase.

At sufficiently high pH where carboxylic groups are fully dissociated and amines are protonated to a smaller extent, the features of the electric double layer at the outer dendrimer surface become predominantly determined by the electrostatic properties of the carboxylic layer alone. The result is a negative dendrimer surface potential  $\psi(r=r_1+r_2)$  over the whole range of tested monovalent salt concentrations (Figure 6C).

The molecularly crowded surface structure of the G6.5 dendrimer<sup>38</sup> qualitatively agrees with the reduced particle permeability derived here from electrokinetic analysis and reflected in the dimensionless ratio  $(\lambda_0 d / 2)^{-1} \rightarrow 0$ . In turn, the sign and magnitude of dendrimer mobility are essentially governed by the sign and magnitude of the surface potential  $\psi(r=r_1+r_2)$ , which explains why mobility reversal coincides here with that of  $\psi(r=r_1+r_2)$ . More generally, the crossover from positive to negative electrophoretic mobility is influenced by the finite penetration length  $\lambda_0^{-1}$  of the electroosmotic flow within the soft particle structure (Figure 5A). Upon arbitrarily increasing the ratio  $\lambda_0^{-1} / r_2$ , the electrokinetically-active region where electroosmotic flow of counterions is operative, extends deeper into the particle structure. Consequently, the contribution of the amine charges to the overall electroosmotic flow significantly grows, which leads to an increase of the PZM, especially in the high electrolyte concentration regime where the dendrimer's electrokinetic features are dominated by the electrostatic properties of the peripheral anionic layer (Figure 5A). These results indicate that mobility reversal of soft permeable particles with nonuniform distribution of positive and negative charges is generally mediated by the interplay between  $\lambda_0^{-1}$ ,  $\kappa^{-1}$  and the thickness of the layer where anionic/cationic charges are heterogeneously distributed. These conclusions agree with those recently detailed by Raafatnia *et al.* from molecular dynamic simulations<sup>20,21</sup> and with earlier work based on the standard electrokinetic model.<sup>19</sup> In light of the above arguments, the general picture is that electrophoretic mobility of PAMAM-COOH dendrimers in the high salt concentration regime mainly mirrors the electrostatic details of the outermost carboxylic layer, while mobility in the low salt domain reflects predominantly those of the internal amine volume. This is further illustrated in Figure 5B where the dependence of the PZM on  $c^\infty$  is provided for various values of  $pK_1$  and  $pK_2$ . Increasing  $pK_1$  mainly yields a significant

increase of the PZM plateau value reached at low  $c^\infty$ , whilst decreasing  $pK_2$  results in a decrease of the PZM at sufficiently large  $c^\infty$  without affecting significantly the PZM at lower salt concentrations. The magnitude and direction of the shift in PZM with varying salinity are defined by the dissymmetry in the protolytic characteristics and in the density of the chargeable groups distributed in the bulk of the particle body and in the surrounding surface layer. Replacing the electrostatic features of the peripheral dendrimer layer by those of the internal compartment and *vice-versa*, would thus lead to increasing PZM with increasing  $c^\infty$  (not shown). The reader is referred to Ref. [18] for the analogy with streaming current of thin polyelectrolyte multilayer films.

Figure 5C displays the dependence of the PZM on monovalent salt concentration with arbitrarily varying the thickness  $r_2$  of the outer peripheral dendrimer layer. Consistent with the preceding arguments, the electrolyte concentration domain where the PZM abruptly decreases is shifted to larger  $c^\infty$  with decreasing  $r_2$ . Indeed, the Debye length required for the switch from amine- to carboxyl-dominated electrokinetics necessarily decreases with decreasing the thickness of the outer dendrimer peripheral layer, recalling that the transition takes place for  $\kappa r_2 \sim 1$ . Figure 5C further highlights that the overall dependence of the PZM on  $c^\infty$  is strongly affected by changing  $r_2$ . Upon variation of  $r_2$ , one basically modifies the respective contributions of the internal and peripheral dendrimer compartments to the particle mobility, with the limit  $r_2 \ll r_1$  corresponding to that where  $\mu$  and PZM are essentially defined by only the amine charges. We attempted to reconstruct the measured dependence of the PZM on  $c^\infty$  for G6.5 PAMAM-COOH dendrimers at various values of  $\rho_2$  upon adjustment of  $r_2 \leq .55$  nm) (Figure S1 in Supporting Information, SI). None of the considered  $(\rho_2; r_2)$  couples led to a satisfactory interpretation of the PZM over the entire range of tested  $c^\infty$  (Figure S2, SI), which further supports the consistent electrokinetic data fitting achieved with  $r_2 = 0.55$  nm (Figures 2-4). In the most favorable case, the PZM plateau value measured at low salt concentration could be captured upon appropriate adjustment of  $r_2$ , and the lowest PZM value at  $c^\infty = 200$  mM recovered with slight increase of this  $r_2$  value, as shown in Figure S2. In the limit  $r_2 \rightarrow 0$ ,  $\rho_2$  is found to increase linearly with

$1/r_2$  (Figure S1), as expected from the relationship  $\sigma_2 = -\lim_{r_2 \rightarrow 0}(\rho_2 r_2)$  with  $\sigma_2$  the surface density of fully dissociated carboxylic groups. Results provide the rough estimate  $\sigma_2 = 0.21\text{-}0.28 \text{ C.m}^{-2}$  to be compared with the  $0.4 \text{ C.m}^{-2}$  value derived for 512 carboxylic groups distributed at the surface of a sphere with radius  $r_1 + r_2 = 4.05 \text{ nm}$ . A refined evaluation of  $\sigma_2$  is obtained by considering the only  $(\rho_2; r_2)$  data couple that adequately captures the electrokinetic dendrimer properties depicted in Figures 2-4. It leads to  $\sigma_2 \sim 0.11 \text{ C.m}^{-2}$ , *i.e. ca. 27%* of the structural carboxylic charges are effectively probed by electrophoresis. This large discrepancy between structural and effective carboxylic charge density is consistent with the occurrence of significant counterion condensation for dendrimers of high generations, as demonstrated for dendrigraft poly-L-lysine and positively-charged PAMAM dendrimers by diffusion and electrophoresis NMR,<sup>43</sup> atomic force microscopy,<sup>44</sup> or isotachophoresis.<sup>45</sup>

*On the origin of the common intersection point denoted A in Figure 3.* Figure 2 evidences the existence of a critical pH value, hereafter called  $\text{pH}^*$ , satisfying  $5.5 < \text{pH}^* < 6.7$ , and at which the derivative of the mobility  $\mu$  with respect to the logarithm of the electrolyte concentration is zero over a given range of  $c^\infty$  (typically  $c^\infty > 10 \text{ mM}$ ). The mobility value reached at that specific pH is denoted  $\mu^*$  in the following. By definition, the couple  $(\text{pH}^*, \mu^*)$  does not depend on  $c^\infty$  and it thus corresponds to the coordinates of the intersection point A in Figure 3. At  $\text{pH}=\text{pH}^*$ , the contribution of the positive amine charges to the overall dendrimer mobility is counterbalanced by that of the carboxylate surface groups. Recalling that the respective contributions of the spatially-separated internal and peripheral charges to  $\mu$  are strongly determined by  $c^\infty$  (see discussion above on the origin of dendrimer mobility reversal), the peculiar situation met at  $\text{pH}=\text{pH}^*$  arises when the amounts of *electrokinetically-active* amine and carboxylate charges are not too different. This requirement is achieved (i) for a pH value intermediate between  $\text{pK}_1$  and  $\text{pK}_2$ , and (ii) under salinity conditions where screening of the internal positive and peripheral negative charges by electrolyte ions is similar. While the screening of the peripheral charges is essentially a diffuse double layer effect, that of the internal charges depends on both salt concentration and Donnan potential, as evidenced by the expression

$\kappa_m^{-1} = \kappa^{-1} [\cosh(y^D)]^{-1/2}$ . Accordingly, starting from  $\text{pH} < \text{pH}^*$  at fixed  $c^\infty$  (or, equivalently, fixed  $\kappa^{-1}$ ), increasing pH leads to a reduction in  $y^D$  ( $> 0$ ) and thus to a decrease in the screening of the amine charges (*i.e.* increase in  $\kappa_m^{-1}$ ). Meanwhile, the amount of peripheral charges increases but their screening extent remains constant as it solely depends on  $c^\infty$ . Therefore, there comes a critical pH value at which the screening of amine and carboxyl charges is similar. This peculiar situation is materialized by the vanishing of the sharp change in electric field ( $\sim dy(r)/dr$ ) with increasing  $r$  from  $(r_1 + r_2)^-$  to  $(r_1 + r_2)^+$ . This critical pH value identifies with  $\text{pH}^*$  defined above and it basically refers to the case depicted in Figure 6C. It is interesting to note the resemblance between the origin of the common intersection point A of Figure 3 and that discussed by De Keizer *et al.*<sup>48</sup> for cases where adsorption of organic ions takes place on an oppositely charged colloidal surface. A separation between positive and negative charges also occurs in these cases and the role of the concentration in organic ions is somewhat similar to that played by solution pH in our study. As a final comment, it is emphasized that for charge-stratified soft interfaces where one of the charge-supporting component undergoes significant pH- and/or salt concentration-dependent swelling, the common intersection point disappears, as discussed by Duval *et al.* in their analysis of streaming current of polyelectrolyte multilayers.<sup>18</sup>

*Comparison between G6.5 and G4.5 PAMAM-COOH dendrimers PZM.* As detailed in §2, G4.5 PAMAM-COOH particles are smaller than their G6.5 analogues and contain lower structural amounts of carboxylic and tertiary amines charges (128 and 126, respectively). Using  $r_1^{n=5} = 2$  nm and  $r_2^{n=5} = r_2^{n=7} = 0.55$  nm, in agreement with the G4.5 size measured by DLS, we evaluate from G4.5 chemical composition  $\rho_1^{n=5}/F = 6.25 \times 10^3$  mM and  $\sigma_2^{n=5} = 0.25$  C.m<sup>-2</sup>, where the superscript  $n=5$  and  $n=7$  refer to quantities pertaining to G4.5 and G6.5 PAMAM-COOH dendrimers, respectively (Figure 1). Based on the preceding theoretical arguments on the origin of mobility reversal, these values of  $\rho_1^{n=5}/F$  and  $\sigma_2^{n=5}$  suggest a larger contribution of the protonated tertiary amine groups in governing the mobility of G4.5 as compared to that for G6.5 ( $\rho_1^{n=5}/\rho_1^{n=7} \sim 1.3$  and  $\sigma_2^{n=5}/\sigma_2^{n=7} \sim 0.6$ ). This prediction is confirmed by measurements of PZM for

G4.5 as a function of  $\text{NaNO}_3$  concentration (inset Figure 4). Over the whole range of  $c^\infty$ , the PZM of G4.5 dendrimer is indeed systematically shifted to higher pH values compared to that obtained for the larger G6.5 dendrimer generation. Adopting the fitting procedure outlined in §4.2.1 with  $\text{p}K_{1,2}^{n=5} = \text{p}K_{1,2}^{n=7}$  and  $1/\lambda_0^{n=5} = 1/\lambda_0^{n=7}$ , the above shift in PZM is reproduced upon adjustment of  $\rho_2^{n=5}$  according to  $-\rho_2^{n=5}/F = 2.1 \times 10^3 \text{ mM}$ , which indicates that *ca.* 36% of the structural G4.5 carboxylic groups are effectively probed. This outcome again points to the presence of counterion condensation and is qualitatively consistent with the expected increase of the effective dendrimer charge upon decreasing dendrimer generation.<sup>43,45</sup>

*On the origin of the local mobility extrema observed at low salt concentrations.* Figures 2-3 show that the electrokinetic properties of G6.5 PAMAM-COOH dendrimers collected at low  $\text{NaNO}_3$  concentrations ( $c^\infty \leq 10\text{-}40 \text{ mM}$ ) and large pH ( $> \sim 7$ ) can be explained with arguing an increase of the interfacial length scale  $\alpha_H$  where friction on the electroosmotic flow is operational (see insets Figure 2-3). If true, these modulations of  $\alpha_H$  should be connected to subtle changes of the dendrimer particle compactness/size with modifying pH and/or  $c^\infty$ . In turn, such changes should affect the density distribution of interfacial segments viewed as resistance centers within the framework of the Debye-Bueche formalism<sup>39</sup> integrated in the here-adopted electrokinetic theory. There are numerous reports in the literature that confirm the existence of conformational changes of PAMAM and PPI (poly (propylene imine)) dendrimers containing internal tertiary amines and terminated or not by carboxylic groups.<sup>49-52</sup> At low pH, the conformation of these dendrimer types is extended as a result of intraparticulate electrostatic repulsion between protonated amines. This structural extension is most pronounced at low salt concentrations to minimize charge repulsion in the particle body. With increasing pH, carboxylic end groups dissociate and the protonation of amines becomes weaker, so that the net charge of the dendrimer decreases. This leads to a collapse of the dendrimer structure at pH values of  $\sim 6$  where attractive Coulomb interactions between negatively charged surface carboxy-groups and internal positively charged amines are significant. Upon further increase in pH, electrostatic repulsive forces push the peripheral dissociated carboxyl groups apart, which generates a more

extended dendrimer structure with expanded surface area. These conclusions from the literature<sup>38</sup> are in line with (i) the increase of  $\alpha_H$  with decreasing  $c^\infty$  at fixed pH value (inset Figure 3), (ii) the decrease of  $\alpha_H$  with increasing pH from 3.6-4 to 5.5, and (iii) the increase of  $\alpha_H$  with further increase in pH from 5.5 to 6.7 (inset Figure 2). In particular, the existence of the minimum in  $\alpha_H$  at pH=5.5 and low salt content (inset Figure 2) very well reflects the minimum in dendrimer particle size reported in the literature at pH  $\sim$  6. When the salt concentration is sufficiently below the values corresponding to the (local) mobility maxima (Figure 2), the Debye length  $\kappa^{-1}$  becomes significantly larger than the corresponding  $\alpha_H$  so that electrostatics start to overwhelm the  $\alpha_H$ -mediated friction effects,<sup>35</sup> which explains the further increase of  $|\mu|$ , in agreement with experimental data (Figure 2). With increasing pH from 4-5.1 to 6.7, the mobility maxima are distinctly shifted to higher  $c^\infty$  (Figure 2), which is reflected in particular by the smoother decay of  $\alpha_H$  at pH 6.7 with increasing  $c^\infty$  from 2 mM to 200 mM (see inset Figure 2). This trend indicates that the accompanying changes in dendrimer structure take place closer to the particle periphery upon increasing pH, recalling that electrophoresis probes intra-dendrimer spatial regions of thickness  $\sim \kappa^{-1}$  (see above discussion on mobility reversal). This is again in qualitative agreement with the expected increased contribution of the carboxyl-surface layer in defining  $\mu$  with increasing  $c^\infty$  and with the modification of the dendrimer surface area at high pH due to increased repulsion between surface groups. As a final comment, it is stressed that the sub-nanometric changes of  $\alpha_H$  with changing pH and  $c^\infty$  result in dendrimer size modification that cannot be accurately addressed by dynamic light scattering.<sup>53</sup> Small angle neutron scattering (SANS) and NMR measurements of self-diffusion coefficients are more suitable for probing such dendrimer size/structure variations<sup>38,53</sup> that are further clearly manifest in the dendrimer electrokinetic response, as demonstrated here on the basis of the standard electrokinetic model.<sup>19,35</sup>

## 5. Conclusions

Combined experimental and theoretical evidence are given for the occurrence of particle electrophoretic mobility reversal in monovalent electrolyte solution and the underlying physical

---

phenomena. The analysis is performed for G6.5 and G4.5 PAMAM-COOH dendrimers with well-defined, nonuniform distribution of internal cationic and peripheral anionic charges. Full quantitative interpretation of the electrokinetic data collected over a wide range of pH and  $\text{NaNO}_3$  concentrations is provided on the basis of the standard electrokinetic formalism, with accounting for the heterogeneous charge distribution and the diffuse nature of the soft particle interphase. The theory adequately captures the peculiar shift of the point of zero mobility with increasing salt concentration and the existence of a common intersection point for the mobility *versus* pH curves plotted at various salt concentrations. It further highlights how pH- and salt-mediated modifications of the particle structure affect dendrimer electrokinetic features at large pH and/or low salt concentrations. For the first time, this detailed confrontation between experiments and theory solidly supports some previous conclusions drawn from molecular dynamic simulations<sup>20,21</sup> and earlier mean-field electrokinetic modeling<sup>19</sup> on the electrophoresis of chemically-stratified soft particles. More generally, it paves a way for refined evaluation of soft nanoparticles electrostatic features from detailed understanding of the roles played by charge density distribution in- and thickness of polymeric coatings in determining particle mobility, similarly to analyses of supported soft thin-films by streaming-current/streaming potential electrokinetic methods.<sup>2</sup>



## References.

1. Duval, J. F. L.; Gaboriaud, F. Progress in electrohydrodynamics of soft microbial particle interphases. *Curr. Opinion Colloid Interface Sci.* **2010**, *15*, 184-195.
2. Zimmermann, R.; Dukhin, S. S.; Werner, C.; Duval, J. F. L. On the use of electrokinetics for unraveling charging and structure of soft planar polymer films. *Curr. Opinion Colloid Interface Sci.* **2013**, *18*, 83-92.
3. Delgado, A. V.; González-Caballero, F.; Hunter, R. J.; Koopal, L. K.; Lyklema, J. Measurement and interpretation of electrokinetic phenomena. *J. Colloid Interface Sci.* **2007**, *309*, 194-224.
4. Ohshima, H. Electrophoresis of soft particles. *Adv. Colloid Interface Sci.* **1995**, *62*, 189-235.
5. Ohshima, H.; Kondo, T. Electrokinetic flow between two parallel plates with surface charge layers: electro-osmosis and streaming potential. *J. Colloid Interface Sci.* **1990**, *135*, 443-448.
6. Wunderlich, R. W. The effects of surface structure on the electrophoretic mobilities of large particles. *J. Colloid Interface Sci.* **1982**, *88*, 385-397.
7. Ohshima, H.; Ohki, S. Donnan potential and surface potential of a charged membrane. *Biophys. J.* **1985**, *47*, 673-678.
8. Hill, R. J.; Saville, D. A.; Russel, W. B. Electrophoresis of spherical polymer coated particles. *J. Colloid Interface Sci.* **2003**, *258*, 56-74.
9. Lopez-Garcia, J. J.; Grosse, C.; Horno, J. Numerical study of colloidal suspensions of soft spherical particles using the network method: 1. DC electrophoretic mobility. *J. Colloid Interface Sci.* **2003**, *265*, 327-340.
10. Yezek, L. P.; van Leeuwen, H. P. An electrokinetic characterization of low charge density cross-linked polyacrylamide gels. *J. Colloid Interface Sci.* **2004**, *278*, 243-50.
11. Duval, J. F. L. Electrokinetics of diffuse soft interfaces. II. Analysis based on the non-linearized Poisson-Boltzmann equation. *Langmuir* **2005**, *21*, 3247-3258.
12. Duval, J. F. L.; Zimmermann, R.; Cordeiro, A. L.; Rein, N.; Werner, C. Electrokinetics of diffuse soft interfaces. IV. Analysis of streaming current measurements at thermoresponsive thin films. *Langmuir* **2009**, *25*, 10691-10703.
13. Zimmermann, R.; Kuckling, D.; Werner, C.; Duval, J. F. L. Electrokinetics of poly(N-isopropylacrylamide)-co-carboxyacrylamide soft thin-film. Evidence of diffuse segment distribution in the swollen state. *Langmuir* **2010**, *26*, 18169-18181.
14. Louie, S. M.; Phenrat, T.; Small, M. J.; Tilton, R. D.; Lowry, G. V. Parameter identifiability in application of soft particle electrokinetic theory to determine polymer and polyelectrolyte coating thicknesses on colloids. *Langmuir* **2012**, *28*, 10334-10347.
15. Francius, G.; Polyakov, P.; Merlin, J.; Abe, Y.; Ghigo, J.-M.; Merlin, C.; Beloin, C. and Duval, J.F.L. Bacterial surface appendages strongly impact nanomechanical and electrokinetic properties of *Escherichia coli* cells subjected to osmotic stress. *PLoS ONE* **2011**, *6*(5), e20066.
16. Duval, J. F. L.; Wilkinson, K. J.; van Leeuwen, H. P.; Buffle, J. Humic substances are soft and permeable: evidence from their electrophoretic mobilities. *Environ. Sci. Technol.* **2005**, *39*, 6435-6445.
17. Zimmermann, R.; Romeis, D.; Bihannic, I.; Cohen-Stuart, M.; Sommer, J.-U.; Werner, C.; Duval, J. F. L. Electrokinetics as an alternative to neutron reflectivity for evaluation of segment density distribution in PEO brushes. *Soft Matter* **2014**, *10*, 7804-7809.
18. Duval, J. F. L.; Küttner, D.; Werner, C.; Zimmermann, R. Electrohydrodynamics of soft polyelectrolyte multilayers: point of zero-streaming current. *Langmuir* **2011**, *27*, 10739-10752.
19. Langlet, J.; Gaboriaud, F.; Gantzer, C.; Duval, J. F. L. Impact of chemical and structural anisotropy on the electrophoretic mobility of spherical soft multilayer particles: the case of bacteriophage MS2. *Biophys. J.* **2008**, *94*, 3293-3312.
20. Raafatnia, S.; Hickey, O. A.; Holm, C. Mobility Reversal of Polyelectrolyte-Grafted Colloids in Monovalent Salt Solutions. *Phys. Rev. Lett.* **2014**, *113*, 238301.

21. Raafatnia, S.; Hickey O. A.; Holm, C. Electrophoresis of a Spherical Polyelectrolyte-Grafted Colloid in Monovalent Salt Solutions: Comparison of Molecular Dynamics Simulations with Theory and Numerical Calculations. *Macromolecules* **2015**, *48*, 775-787.
  22. Shinagawa, T.; Ohshima, H.; Kondo, T. Isoelectric point of an ion-penetrable membrane. *Biophys. Chem.* **1992**, *43*, 149-56.
  23. Lyklema, J. Overcharging, charge reversal: chemistry or physics ? *Colloids Surf. A: Physicochem. Eng. Asp.* **2006**, *291*, 3-12.
  24. Semenov, I.; Raafatnia, S.; Sega, M.; Lobaskin, V.; Holm, C.; Kremer, F. Electrophoretic mobility and charge inversion of a colloidal particle studied by single-colloid electrophoresis and molecular dynamics simulations *Phys. Rev. E* **2013**, *87*, 022302.
  25. Nagahama, T.; Muramatsu, N.; Ohshima, H.; Kondo, T. Surface electric characteristics of guinea-pig polymorphonuclear leucocytes. *Colloids Surf.* **1992**, *67*, 61-65.
  26. Rochette, C. N.; Crassous, J. J.; Drechsler, M.; Gaboriaud, F.; Eloy, M.; de Gaudemaris, B.; Duval, J. F. L. Shell structure of natural rubber particles: evidence of chemical stratification by electrokinetics and cryo-TEM. *Langmuir* **2013**, *29*, 14655-14665.
  27. Tomalia, D. A.; Naylor, A. M.; Goddard III, W. A. Starburst dendrimers: Molecular-level control of size, shape, surface chemistry, topology, and flexibility from atoms to macroscopic matter. *Angew. Chem. Int. Ed. Engl.* **1990**, *29*, 138-175.
  28. Tomalia, D. A.; Baker, H.; Dewald, J.; Hall, M.; Kallos, G.; Martin, S.; Roeck, J.; Ryder J.; Smith, P. A new class of polymers: starburst-dendritic macromolecules. *Polymer Journal* **1985**, *17*, 117-132.
  29. Anderson, J. S.; Hernandez, G.; LeMaster, D. M. A billion-fold range in acidity for the solvent-exposed amides of *Pyrococcus furiosus* rubredoxin. *Biochemistry* **2008**, *47*, 6178-6188
  30. Buczkowski, A.; Urbaniak, P.; Stawowska, J.; Romanowski, S.; Palecz, B. Interaction between PAMAM-NH<sub>2</sub> G0 dendrimer and dissociated sodium chloride in aqueous solution. *J. Mol. Liquids* **2012**, *171*, 54-59.
  31. Niu, Y.; Sun, L.; Crooks, R. M. Determination of the intrinsic proton binding constants for poly(amidoamine) dendrimers via Potentiometric pH Titration. *Macromolecules* **2003**, *36*, 5725-5731.
  32. Tomalia, D. A.; Fréchet J. M. J. Discovery of dendrimers and dendritic polymers: A brief historical perspective. *Journal of Polymer Science Part A: Polymer Chemistry* **2002**, *40*, 2719-2728.
  33. Lin, Y.-L.; Khanafer, K.; El-Sayed M. E. H. Quantitative evaluation of the effect of poly(amidoamine) dendrimers on the porosity of epithelial monolayers. *Nanoscale* **2010**, *2*, 755-762.
  34. Dubin, P. L.; Edwards, S. L.; Kaplan, J. I.; Mehta, M. S.; Tomalia, D.; Xiat, J. Carboxylated Starburst Dendrimers as Calibration Standards for Aqueous Size Exclusion chromatography. *Anal. Chem.* **1992**, *84*, 2344-2347.
  35. Duval, J. F. L.; Ohshima, H. Electrophoresis of diffuse soft particles. *Langmuir* **2006**, *22*, 3533-3546.
  36. Ascher, U.; Christiansen, J.; Russell, R. . Collocation software for boundary value E's. *ACM Trans. Math. Software* **1981**, *7*, 209-222.
  37. Dukhin, S. S.; Zimmermann, R.; Duval, J. F. L.; Werner, C. On the applicability of the Brinkman equation in soft surface electrokinetics. *J. Colloid Interface Sci.* **2010**, *350*, 1-4.
  38. Boas, U.; Christensen, J. B.; Heegaard, P. M. H. Dendrimers: design, synthesis and chemical properties. *J. Mater. Chem.* **2006**, *16*, 3785-3798.
  39. Debye, P.; Bueche, A. Intrinsic viscosity, diffusion, and sedimentation rates of polymers in solutions. *J. Chem. Phys.* **1948**, *16*, 573-579.
  40. Diallo, M. S.; Christie, S.; Swaminathan, P.; Balogh, L.; Shi, X.; Um, W.; Papelis, C.; Goddard III, W. A.; Johnson Jr., J. H. Dendritic chelating agents. 1. Cu(II) binding to ethylene diamine core poly(amidoamine) dendrimers in aqueous solutions. *Langmuir* **2004**, *20*, 2640-2651.
  41. Cakara, D.; Kleiman, J.; Borkovec, M. Microscopic protonation equilibria of poly(amidoamine) dendrimers from macroscopic titrations. *Macromolecules* **2003**, *36*, 4201-4207.
-

42. Tajarobi, F.; EL-Sayed, M.; Rege, B. R.; Pollo, J. E.; Ghandehari, H. Transport of poly-amidoamine dendrimers across Madin-Darby canine kidney cells. *Int. J. Pharm.* **2001**, *215*, 263-267.
43. Böhme, U.; Klenge, A.; Hänel, B.; Scheler, U. Counterion condensation and effective charge of PAMAM dendrimers. *Polymers* **2011**, *3*, 812-819.
44. Pericet-Camara, R.; Papastavrou, G.; Borkovec, M. Effective charge of adsorbed poly(amidoamine) dendrimers from direct force measurements. *Macromolecules* **2009**, *42*, 1749-1758.
45. Ibrahim, A.; Koval, D.; Kasicka, V.; Faye, C.; Cottet, H. Effective charge determination of dendrigraft poly-L-lysine by capillary isotachopheresis. *Macromolecules* **2013**, *46*, 533-540.
46. Lyklema, J. Surface charges and electrokinetic charges: Distinctions and juxtapositionings. *Colloids Surf. A: Physicochem. Eng. Asp.* **2011**, *376*, 2-8.
47. Ohshima, H. Donnan potential and surface potential of a spherical soft particle in an electrolyte solution. *J. Colloid Interface Sci.* **2008**, *323*, 92-97.
48. de Keizer, A.; Bohmer, M. R.; Mehrian T.; Koopal, L. K. Adsorption of organic ions at the solid-electrolyte interface. Interpretation of common intersection points. *Colloids and Surfaces* **1990**, *51*, 339-357.
49. Hong, K.; Liu, Y.; Porcar, L.; Liu, D.; Gao, C. Y.; Smith, G. S.; Herwig, K. W.; Cai, S.; Li, X.; Wu, B.; Chen, W.-R.; Liu, L. Structural response of polyelectrolyte dendrimer towards molecular protonation: the inconsistency revealed by SANS and NMR. *J. Phys.: Condens. Matter* **2012**, *24*, 064116.
50. Lee, I.; Athey, B. D.; Wetzel, A. W.; Meixner, W.; Baker Jr., J. R. Structural molecular dynamics studies on polyamidoamine dendrimers for a therapeutic application: effects of p and generation. *Macromolecules* **2002**, *35*, 4510-4520.
51. An, M.; Hutchison, J. M.; Parkin, S. R.; DeRouchey, J. E. Role of pH on the compaction energies and phase behavior of low generation PAMAM–DNA complexes. *Macromolecules* **2014**, *47*, 8768-8776.
52. Bosman, A. W.; Janssen, H. M.; Meijer, E. W. About dendrimers: structure, physical properties, and applications. *Chem. Rev.* **1999**, *99*, 1665-1688.
53. Rietveld, I. B.; Bouwman, W. G.; Baars, M. W. P. L.; Heenan, R. K. Location of the outer shell and influence of pH on carboxylic acid-functionalized poly(propyleneimine) dendrimers. *Macromolecules* **2001**, *34*, 8380-8383.

## SUPPORTING INFORMATION

### Remarkable Electrokinetic Features of Charge-Stratified Soft Nanoparticles: Mobility Reversal in Monovalent Aqueous Electrolyte.

Mariam Moussa,<sup>1,2</sup> Céline Caillet,<sup>1,2</sup> Raewyn M. Town,<sup>3</sup> Jérôme F.L. Duval<sup>1,2,\*</sup>

<sup>1</sup> CNRS, LIEC (Laboratoire Interdisciplinaire des Environnements Continentaux), UMR7360, Vandoeuvre-lès-Nancy F-54501, France.

<sup>2</sup> Université de Lorraine, LIEC, UMR7360, Vandoeuvre-lès-Nancy, F-54501, France.

<sup>3</sup> Department of Physics, Chemistry and Pharmacy, University of Southern Denmark, Campusvej 55, 5230 Odense, Denmark.

\* Corresponding author. E-mail: jerome.duval@univ-lorraine.fr

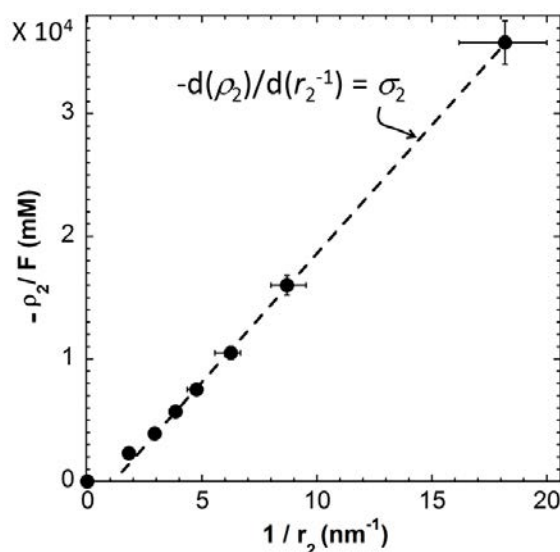


**Figure S1.** Variations of the volume charge density  $\rho_2$  with  $1/r_2$ , where  $r_2$  was adjusted to best fit the measured salt concentration dependence of the point of zero mobility for G6.5 PAMAM-COOH dendrimer (see Figure 4 and Figure S2 in Supporting Information). The dashed curves correspond to the expected linear dependence of  $\rho_2$  on  $1/r_2$  in the limit  $r_2 \rightarrow 0$ . See text for further details.

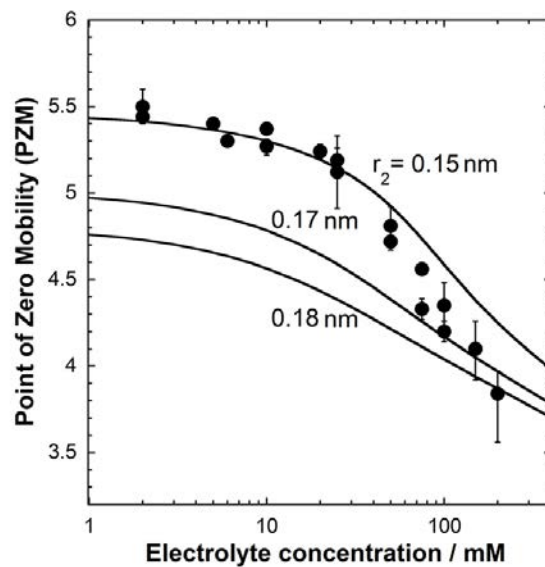


**Figure S2.** Comparison between the Point of Zero Mobility (PZM) measured for G6.5 PAMAM-COOH at various  $\text{NaNO}_3$  concentrations (symbols) and that evaluated from theory with  $-\rho_2 / F = 10.5 \times 10^3 \text{ mM}$  at  $r_2$  values (indicated) that best bracket the overall dependence of the PZM on salt concentration. Other model parameters: as in Figure 2 with  $\alpha_H \rightarrow 0$ .

## **Chapter IV**

# **Remarkable Structure and Elasticity Relaxation Dynamics of Poly(diallyldimethylammonium chloride)-Poly(acrylic acid) Multilayer Films**

Francius, G.; Razafitianamaharavo, A.; Moussa, M.; Dossot, M.; André, E.; Bacharouche, J.; Senger, B.; Ball, V. and Duval, J.F.L. Remarkable structure and elasticity relaxation dynamics of poly(diallyldimethylammonium chloride)-poly(acrylic acid) multilayer films. *The Journal of Physical Chemistry C*, **2016**, 120, 5599–5612.

## Remarkable Structure and Elasticity Relaxation Dynamics of Poly(diallyldimethylammonium chloride)-Poly(acrylic acid) Multilayer Films

Grégory Francius,<sup>1,2</sup> Angéline Razafitianamaharavo,<sup>3,4</sup> Mariam Moussa,<sup>3,4</sup> Manuel Dossot<sup>1,2</sup>, Erwan André,<sup>1,2</sup> Jalal Bacharouche,<sup>1,2</sup> Bernard Senger,<sup>5,6</sup> Vincent Ball,<sup>5,6\*</sup> Jérôme F.L. Duval<sup>3,4\*</sup>

<sup>1</sup> Université de Lorraine, Laboratoire de Chimie Physique et Microbiologie pour l'Environnement, LCPME, UMR 7564, 54600 Villers-lès-Nancy, France.

<sup>2</sup> C RS, Laboratoire de Chimie Physique et Microbiologie pour l'Environnement, LCPME, UMR 7564, 54600 Villers-lès-Nancy, France.

<sup>3</sup> Université de Lorraine, Laboratoire Interdisciplinaire des Environnements Continentaux, UMR 7 545 1 Vandœuvre-lès-Nancy, France.

<sup>4</sup> CNRS, Laboratoire Interdisciplinaire des Environnements Continentaux, UMR 7360, 54501 Vandœuvre-lès-Nancy, France.

<sup>5</sup> Institut National de la Santé et de la Recherche Médicale, INSERM Unité 1121, 11 rue Humann, 67085 Strasbourg Cedex, France.

<sup>6</sup> Université de Strasbourg, Faculté de Chirurgie Dentaire, 8 rue Sainte Elisabeth, 67000 Strasbourg, France.

\* Corresponding author. E-mail: jerome.duval@univ-lorraine.fr

### Abstract

Remarkable mechanical and structural properties of out-of-equilibrium poly(diallyldimethylammonium chloride) (PDADMAC)-poly(acrylic acid) (PAA) multilayer films are elucidated from in-situ Atomic Force Microscopy and spatially-resolved Raman spectroscopy analyses complemented by Density Functional Theory (DFT) computations. Surprisingly, fresh exponentially-grown (PDADMAC-PAA)<sub>n</sub> polyelectrolyte films behave as glassy materials with Young moduli as large as 2 MPa. Their organization is governed by a competition between PDADMAC-PAA electrostatic interactions and water-stabilization of PAA charges that limits association between polycationic and polyanionic chains. At pH 3 where PAA is weakly deprotonated, this competition leads to the formation of water-free PDADMAC-PAA polyelectrolyte complexes within well-defined donut-like structures (2-12  $\mu\text{m}$  in diameter, 100-200 nm in height) that confer upon the film a mechanical rigidity comparable to that classically achieved for linearly-growing films. The relaxation of (PDADMAC-PAA)<sub>n</sub> films to equilibrium occurs over 5 days and is marked by a gradual disappearance of all donut-like structures, resulting in a three-fold decrease of the Young modulus. This mechanical softening of the film is significantly accelerated by increasing the diffusion rate of PDADMAC and PAA chains upon heating: the morphological and mechanical features of the 5-day old, naturally aged films are recovered after two hours heating treatment at 60°C. In combination, this invokes a transition from intrinsic to extrinsic film charge compensation, i.e. the tightly compacted polyelectrolyte complexes progressively

change to coacervates that are loosely associated by electrostatics. It is shown that such atypical structure transition of exponentially-grown films can be used for reversible laser-assisted printing applications at microscales.

## 1. Introduction

Polyelectrolyte multilayer (PEM) films are constructed through the successive deposition of polyelectrolytes carrying charges of opposite signs.<sup>1-3</sup> In the past decade, PEM materials have been used in numerous applications including *e.g.* the design of energy conversion devices,<sup>4, 5</sup> the elaboration of strategies for surface protection against corrosion<sup>6, 7</sup> or for separation purposes,<sup>8</sup> and the synthesis of functionalized biomaterials.<sup>9, 10</sup> This spectrum of applications stems from the versatile character of PEM films and the numerous available options for fine tuning their physical-chemical properties, especially their structure and mechanical stiffness. In particular, the capability to systematically vary the elasticity of PEM coatings by chemical crosslinking,<sup>11</sup> the addition of inorganic nanofillers,<sup>12, 13</sup> or by controlling the composition of the physicochemical medium (namely the pH and the ionic strength<sup>14</sup>), led to the production of films with Young modulus ranging in magnitude from a few kPa only up to the MPa level. The accessibility to such a formidable range of material elasticity paved the way for understanding specific cell adhesion behavior.<sup>15</sup> In the course of successive polycation-polyanion deposition cycles, the thickness of the PEM film increases in a way that may contradict the intuitive expectation that each deposition cycle adds a constant amount of polymer material of fixed thickness. This simplistic view only holds for homogenous films whose constituent polymer chains exhibit very low mobility such that they remain essentially spatially frozen within the films after their deposition. This situation is encountered for most PEM films that have been investigated to date and it corresponds to a so-called linear growth regime. There is a second type of polyelectrolyte multilayer films for which the thickness increases with the number of deposition cycles according to an exponential-like relationship at least up to a given number of deposition cycles.<sup>16-18</sup> Comparison between the properties of these films and those of their linearly growing counterparts reveals that the exponentially grown materials are more hydrated,<sup>19</sup> resulting in a lower refractive index and apparent elasticity, together with a significantly higher mobility of the constituent chains.<sup>20, 21</sup> In addition, these exponential films display a larger permeability to ions and to molecules of given size, and they have characteristic charge permselectivity



features. This restriction of permeation of (macro)molecules across exponential PEM films according to charge, essentially stems from the existence of a Donnan potential<sup>22</sup> in the bulk PEM phase where electroneutrality is ensured by extrinsic charge compensation, contrary to linearly growing PEMs that are intrinsically charge compensated,<sup>23</sup> *i.e.* the amount of positive charges supported by polycations is exactly compensated by the amount of negative charges from polyanions.

The exponential or linear character of a PEM film is not dictated by the inherent nature of the polycation/polyanion combination that underlies its composition. Rather, it can potentially be changed upon appropriate control of the physicochemical conditions adopted during the deposition steps. For the sake of illustration, while the combination between poly(allylamine hydrochloride) (PAH) and poly(4-styrene sulfonate) (PSS) leads usually to linearly growing films over a large domain of solution ionic strengths,<sup>24</sup> increasing the deposition temperature from 55°C to 80°C generates an exponential-like PEM construction.<sup>25</sup> It was recently found that the nature of the internal PEM charge compensation shifts from intrinsic to extrinsic when the growth regime changes from linear to exponential for a given combination of polyelectrolytes.<sup>26</sup> Overall, these findings suggest that linearly growing films are out of equilibrium, in a ‘frozen state’, and their transition to an equilibrium state is extremely slow due to the reduced mobility of the polyelectrolyte chains. In contrast, exponential PEM films are thought to be closer to thermodynamic equilibrium and their constitutive polyelectrolyte chains are expected to be well inter-mixed, as confirmed by laser confocal scanning microscopy measurements.<sup>27</sup> These elements are also in agreement with the evaluation by neutron reflectivity of the diffusion coefficient of PSS in linear (poly(diallyldimethyl ammonium chloride) [hereafter denoted as PDADMAC]-PSS)<sub>n</sub> films ( $\sim 10^{-17}$  cm<sup>2</sup>.s<sup>-1</sup>)<sup>28</sup> and with measurement by fluorescence recovery after photobleaching (FRAP) of polycations diffusion coefficient in exponentially growing films where chains mobility may be equivalent to that in solution.<sup>21</sup>

In the current study, it is demonstrated that the dichotomous differentiation between non-equilibrated linearly growing films and (quasi-)equilibrated exponentially growing films is not a general rule. Our analysis is based on the molecular investigation of the structure and mechanical properties of (PDADMAC-PAA)<sub>n</sub> films (PAA denotes poly(acrylic acid)) using Raman confocal spectroscopy and Atomic Force Microscopy (AFM) in imaging and force spectroscopy modes, complemented by Density Functional Theory molecular simulations.

(PDADMAC-PAA)<sub>n</sub> films are shown to exhibit exponential growth in 10 mM NaNO<sub>3</sub> deposition solution with an elasticity and a surface morphology that relax over time scales of the order of 10<sup>5</sup>-10<sup>6</sup> s at room temperature (22°C). The results unambiguously point out that the exponentially growing (PDAMAC-PAA)<sub>n</sub> films are far from equilibrium immediately after their deposition, and that their relaxation to an equilibrium state is extremely slow. The characteristic timescale for film relaxation to equilibrium can be further decreased to a few hours by immersing the film in a 10 mM NaNO<sub>3</sub> solution at 60°C. This operation provides enough activation energy for the system to more rapidly attain the equilibrium state evidenced by a (flat) surface morphology and lower film elasticity. To the best of our knowledge, this work provides the first evidence that contradicts the commonly accepted equilibrated or quasi-equilibrated nature of exponentially growing polyelectrolyte multilayers. In the case of (PDAMAC-PAA)<sub>n</sub> grown under the conditions specified above, their relaxation can be as slow as that reported for linearly growing films. This study opens new perspectives for basic research on thermo-mechanics of out-of-equilibrium polyelectrolyte multilayer films and the design of new versatile, thermoresponsive materials for *e.g.* biosensing or reusable printing-supports.

## Experimental Section

### Polyelectrolyte film buildup and sample preparation

Poly(dimethyldiallylammonium chloride) (PDADMAC, Mw = 400000-500000 g/mol, ref. 409030) and poly(acrylic acid sodium salt) (PAA, Mw ~ 50000 g/mol, ref. 00627) were purchased from Sigma-Aldrich (France) and Polysciences (Biovalley, France), respectively. All reagents were used without further purification. PDADMAC (5 mg/mL) and PAA (3 mg/mL) polyelectrolyte solutions were prepared in 10 mM NaNO<sub>3</sub> electrolyte with pH adjusted to 6 and 3, respectively.

The automated sequential build-up of the multilayer films at room temperature (22°C) was performed on borosilicate and germanium slides to facilitate subsequent analysis by atomic force microscopy and Raman confocal spectroscopy, respectively, using a dipping robot (Riegler & Kirstein GmbH, Berlin, Germany). The first deposited layer consisted of PDADMAC, and the sample was subsequently rinsed by immersion for 5 min in 10 mM NaNO<sub>3</sub> solution (99.9 % pure NaNO<sub>3</sub> salt purchased by Sigma/Aldrich, used without further

purification). The polyanion PAA was then deposited according to the same procedure. This build up process was continued *via* alternate deposition of PDADMAC and PAA until the PEM film consisted of 30 bilayers. If not used immediately after construction, the PEM films, hereafter denoted as (PDADMAC-PAA)<sub>30</sub>, were stored at 4°C in 10 mM NaNO<sub>3</sub> solution to avoid microbial contamination. The sample adjustment from 4°C to room temperature was achieved after 10 min maximum, as judged from the time required for stabilization of the AFM and Raman measurements on such samples.

The time evolution of the elasticity, surface composition and morphology of the PEM samples were followed by AFM and Raman micro-spectroscopy at room temperature in a 10 mM NaNO<sub>3</sub> solution (conditions referred to as natural aging) or after various periods of thermal treatment. The thermal treatment of constructed PEM films comprised the following: PEM samples were first placed into a beaker containing 100 mL of 10 mM NaNO<sub>3</sub> solution and heated in a water bath at 60°C for 1 h to 6 h. After heating, samples were immediately placed in a fresh 10 mM NaNO<sub>3</sub> solution (neutral pH) at room temperature and then analyzed by AFM and Raman micro-spectroscopy. The dynamics of films relaxation under natural aging conditions was monitored for a period of 14 days after construction. The choice of NaNO<sub>3</sub> electrolyte in this work is motivated by the expected absence of significant specific interactions between NO<sub>3</sub><sup>-</sup> and the charged functional groups carried by the polycationic and polyanionic chains. These interactions are, at least, less significant than those expected between Cl<sup>-</sup> and charged polymers. In addition, NO<sub>3</sub><sup>-</sup> is more chaotropic than Cl<sup>-</sup> (see Hofmeister series) and as such, NO<sub>3</sub><sup>-</sup> is expected to show weaker interactions with water than water with itself. For that reason, NO<sub>3</sub><sup>-</sup> has supposedly less influence on the here-evidenced peculiar film donuts formation than Cl<sup>-</sup>, recalling that these donuts stem from the formation of complexes (*i.e.* soluble association of oppositely charged polyelectrolytes) between deprotonated PAA molecules and PDADMAC polycations *with water exclusion*, as extensively detailed in the Results and Discussion section.

### Film characterization by Quartz Crystal Microbalance (QCM)

The (PDADMAC-PAA)<sub>n</sub> film build up was monitored *in-situ* with a quartz crystal microbalance QCM-D301 device (Qsense, Göteborg, Sweden). Briefly, the quartz crystal was excited at its fundamental frequency (about 5 MHz), and at the third, fifth, and seventh overtones indexed by  $\nu = 3$ ,  $\nu = 5$  and  $\nu = 7$  corresponding to 15, 25, and 35 MHz, respectively). Changes in the resonance frequencies ( $\Delta f_\nu$ ) and in the relaxation of the vibration once the excitation stopped, was measured at these four frequencies. The relaxation time allowed the estimation of the dissipation ( $\Delta D_\nu$ ) of the mechanical energy stored in the resonator. As commonly done, an increase in  $-\Delta f_\nu/\nu$  was associated, as a first approximation, to an increase in deposited mass on the quartz surface. It was further possible to determine from  $\Delta f_\nu$  and  $\Delta D_\nu$  measurements, the elastic shear modulus ( $\mu$ ), the dynamic viscosity ( $\eta$ ) and the hydrodynamic thickness of the film ( $h$ ) deposited on the crystal on the basis of the viscoelastic model developed by Voinova *et al.* and previously used for successful characterization of various polyelectrolyte multilayers films.<sup>17, 29, 30</sup>

### **Raman Confocal Spectroscopy (RCS)**

Raman scattering experiments were performed on some of the PEM films using a Witec alpha 300S spectrometer equipped with a frequency-doubled Nd:YAG laser (wavelength: 532 nm), a 600 grooves/mm grating, an optical fibered microscope with a fiber core diameter of 150  $\mu\text{m}$  and a water immersion objective ( $\times 60$  magnification, numerical aperture 0.95). Samples were stored in a 10 mM NaNO<sub>3</sub> solution in a small Petri dish (40 mm diameter). The immersion objective was used to focus the laser light at the sample surface and Raman scattering light was collected by the same objective in backward mode. The laser irradiance was kept at 15 kW.cm<sup>-2</sup> for Raman analysis and the sample was not heated during measurement because of heat dissipation brought about by water. For experiments involving laser-heating of the film, the adopted irradiance was 250 kW.cm<sup>-2</sup>. The spectral resolution was 6 cm<sup>-1</sup> and the spatial resolution obtained using the water immersion objective was estimated to be *ca.* 500 nm using a calibration grid (composed by an array of gold stripes of 5  $\mu\text{m}$  width, separated by 5  $\mu\text{m}$ , and deposited on a silicon wafer). Raman maps were generated using spatial steps of 300 nm and 2 s acquisition time. Integration of the peaks of interest was carried out numerically using the software from Witec. A baseline was subtracted before integration.

### AFM imaging and evaluation of PEM films mechanical properties

AFM images of the surface topography of (PDADMAC-PAA)<sub>30</sub> films were recorded with a Dimension FastScan AFM (Bruker AXS, Palaiseau, France). Silicon nitride cantilevers of conical shape were purchased from Bruker (MLCT and NPG-10, Bruker AXS, Palaiseau, France) with spring constants of 20-50 pN/nm. AFM measurements were performed in 10 mM NaNO<sub>3</sub> at room temperature. The mechanical properties of the polyelectrolyte films were further addressed upon measurements by Peak force Mapping™ (PFM) and Force-Volume Images (FVI) consisting of a grid of 256×256 and 32×32 force curves collected upon approach of the tip (approach speed 1 μm/s) toward the samples, respectively. The Young modulus  $E$  was evaluated from the quantitative interpretation of force *versus* indentation curves according to the Sneddon model for a conical apex indenter.<sup>31</sup> Within the framework of this theory, the loading force  $F$  depends on the indentation depth  $\delta$  according to:

$$F = \frac{2E \cdot \tan(\alpha)}{\pi(1-\nu^2)} \delta^2 \cdot f_{\text{BECC}}, \quad [1]$$

where  $\delta$  is the indentation depth,  $\nu$  the Poisson coefficient ( $= 1/2$ ),  $\alpha$  is the semi-top angle ( $=18^\circ$  for MLCT tips) of the tip and  $f_{\text{BECC}}$  is the Bottom Effect Cone Correction function that takes into account the stiffness of the film-supporting substrate.<sup>32</sup> All the force curves were analyzed by means of an automated Matlab algorithm described elsewhere.<sup>62</sup> Unless otherwise stated, for each sample analyzed, three  $30 \mu\text{m} \times 30 \mu\text{m}$  PFM and FVI measured over different sample surface locations were recorded.

## Results and discussion

### QCM monitoring of film build-up

Typical results for a (PDADMAC-PAA)<sub>n</sub> film constructed under the conditions specified in the Experimental Section, are reported in **Figure 1**. The film thickness increases with the number of deposition cycles according to an exponential relationship with values of about 50, 200 and 500 nm for 9, 14 and 17 deposited bilayers, respectively. The existence of such a supra-linear growth regime has already been reported for films composed of PAA and

PDADMAC but constructed under medium conditions different from those adopted in this work.<sup>33, 34</sup> **Figure 1A** further shows that the increase in dynamic viscosity of the film with increasing number of deposited layers follows a trend similar to that obtained for the film thickness, with a value of *ca.* 40 mPa.s reached after 18 deposited bilayers, in agreement with literature data on (PDADMAC-PSS)<sub>n</sub> films.<sup>35, 36</sup> Unlike film thickness and film viscosity, the shear modulus does not increase monotonously upon increase in the number of deposited bilayers (**Figure 1B**). This parameter is rather found to fluctuate in the 0-0.5 MPa range whilst the number of deposited bilayers remains below 11, before increasing sharply and eventually levelling off to a value of 2-3 MPa for thicker films. This behavior can be rationalized by arguing that the film grows *via* a gradual coalescence of the deposited polyelectrolyte droplets and that 11 bilayers likely correspond to a fully covered microbalance crystal surface, which then allows a relevant evaluation of film shear modulus. This scenario is in line with previous work reported on the exponential growth of other polyelectrolyte systems.<sup>37, 38</sup>

An AFM image of the freshly built (PDADMAC-PAA)<sub>30</sub> film is given in **Figure S1A** (see **Supporting Information**) under conditions where polymer material covers the entire supporting glass substrate (30 bilayers). The film thickness derived from the height profile after scratching the film surface (inset in **Figure 1A**) is *ca.* 2  $\mu\text{m}$  while a surface roughness of about 50-75 nm is estimated from the distribution of the relative height profile over a 15 $\times$ 15  $\mu\text{m}^2$  surface area (**Figure S1B**). Overall, the measured film thickness agrees well with that obtained in previous studies on (PDADMAC-PAA)<sub>n</sub> films.<sup>39</sup> However, the surface roughness of our exponentially growing PEM film is significantly larger (by a factor 10) than that reported for other exponential films such as (PLL-HA)<sub>n</sub> (where PLL: poly(L-lysine); HA: hyaluronic acid).<sup>38</sup> The latter systems are known to be fluid enough for the surface to relax in order to minimize the interfacial contact area<sup>40</sup> and thereby promote polyelectrolyte interdiffusion with a simultaneous decrease in surface roughness.<sup>41, 42</sup> Consequently, at this preliminary stage of the analysis, the larger roughness obtained for our films could be indicative of a segregated structure with (partial) phase separation between polycationic and polyanionic polyelectrolytes, as confirmed later in the manuscript.

### **Dependence of PEM film physical properties on natural aging time and on heating-treatment times**

In order to address the thermodynamic stability of the film surface, the evolution of the films morphology was monitored by AFM under (i) natural aging conditions (from 0 to 5 days of relaxation) at room temperature (**Figure 2A**) in 10 mM NaNO<sub>3</sub> electrolyte solution and (ii) after heating the samples at 60°C for 1 to 6 hours (**Figure 2B**). The AFM images recorded at the end of the PEM build up process reveal the presence of ring-shaped bulges, 100-200 nm in height and 2-12 µm in diameter, supported by a wavy underlying surface. After 1 day of natural aging, these donut-like structures are still present over the film surface but they appear more flat (50-70 nm in height and 2-8 µm in diameter). Eventually, after 5 days relaxation, the AFM images reveal a film surface devoid of donut structures. Similarly, **Figure 2B** shows that the topography of the PEM films is dramatically affected by thermal treatment: the film surface obviously flattens with increasing heating-time at 60°C. These results show that a gradual disappearance of the donut structures within the film is promoted with time and/or with temperature larger than the ambient temperature at which the film was constructed.

Further analysis of the dependence of the high-frequency surface roughness on film surface area (obtained with Bruker FastScan NanoScope Software) (**Figure S1C**), facilitates elucidation of the film organization and the evolution thereof (after subtracting the contribution from the underlying surface). The results are shown in **Figure S1C** for films relaxing under natural aging conditions and in **Figure S1D** for heated films. Let us first discuss the results for the naturally aged case. As expected, surface roughness increases with increasing film surface area<sup>43</sup> and, regardless of film aging conditions, it reaches a saturation plateau value at surfaces larger than 200 µm<sup>2</sup>. More specifically, the surface roughness of a freshly built PEM film first increases from about 0.4 nm to ~1-2 nm with the surface area increasing from 0.2 µm<sup>2</sup> to ~2 µm<sup>2</sup>, followed by a plateau region before it finally increases again up to the saturation value of ~10 nm for a film surface area in the range 40 µm<sup>2</sup> to 200 µm<sup>2</sup> (inset **Figure S1C**). This two-step increase in surface roughness allows the evaluation of two correlation lengths,  $L_{c,1} = 1.6 \mu\text{m}$  and  $L_{c,2} = 14.8 \mu\text{m}$  obtained from the square root of the surface area values that delimit the two-step increase in film roughness (see inset **Figure S1C**). These length scales are indicative of the ranges over which fluctuations in one region of the film are correlated with those in another region.  $L_{c,1}$  and  $L_{c,2}$  basically correspond to the thickness of the ring structures and to the external diameter of the donut domains, respectively. With increasing aging time (**Figure S1C**) or heating-treatment time (**Figure**

**S1D**), the features discussed above for the roughness of freshly built PEM disappear and the dependence of film roughness on film area is significantly attenuated with a transition from a two-step to a one-step increase in surface roughness upon increase in film surface area. Depending on the experimental conditions, the film's roughness then reaches a saturation value of 1 to 4 nm for film areas larger than  $20\ \mu\text{m}^2$ , thus indicating a significant flattening of the surface in the course of (heating and natural aging) time, which is in line with the disappearance of the donut-structures evidenced in **Figure 2**.

**Figure 3** displays the mechanical properties (Young modulus) of (PDADMAC-PAA)<sub>30</sub> films under natural aging conditions. In details, film images are provided at different natural aging times (left column **Figure 3**) together with the corresponding spatial mapping and distribution of the Young modulus (central and right columns, respectively). The freshly built film is characterized by an average Young modulus of  $1.59 \pm 0.14$  MPa and the distribution of the Young modulus is quite broad over the whole film surface (**Figure 3A**). Higher Young moduli are measured in the direct vicinity of the donut-like structures detected by AFM. Refined analyses of the Young modulus map of the corresponding topography images highlight that the Young modulus pertaining to the zones occupied by the structural contour of the donuts is *ca.* 1.80 MPa while a lower value of approximately 1.40-1.50 MPa is obtained both inside and outside these structures (**Figure S2 in Supporting Information**). This larger stiffness of the donut-ring domains compared to that of the neighboring film region is the result of the pseudo-crystalline organization of polymer chains therein, as discussed later on the basis of Raman spectroscopy results.

Young moduli in the range of 1 to 2 MPa, measured by AFM, are in satisfactory agreement with the shear modulus evaluated from QCM-D data (**Figure 1B**). To the best of our knowledge, such film elasticity is typically obtained for linearly grown films but it has never been reported for exponentially grown, non-cross-linked PEM films.<sup>44</sup> Indeed, exponential films consisting of *e.g.* (PLL-HA), (poly(allylamine hydrochloride)-poly(L-glutamic acid))<sub>n</sub> or (poly(L-lysine)-poly(L-glutamic acid))<sub>n</sub> bilayers are generally very soft with characteristic Young moduli in the range of 0-0.10 MPa.<sup>45-47</sup> Several studies also reported very low elastic moduli of about 0.01-0.10 MPa for PDADMAC-based hydrogels, the mechanical properties of which were shown to further depend on the material's swollen state, the polyelectrolytes' ionization degree, the counterion type and the medium polarity.<sup>48</sup> Such mechanical behavior has also been recently reported for PAA-based hydrogels<sup>49</sup> with



measured Young moduli that do not exceed 0.25 MPa with or without cross-linking.<sup>50</sup> Although the (PDADMAC-PAA)<sub>30</sub> films built in 10 mM NaNO<sub>3</sub> display an exponential-like increase of their thickness with the number of deposited bilayers (**Figure 1A**), their Young modulus is 1 to 2 orders of magnitude higher than that commonly reported for exponentially grown PEM films.

After 1 day of natural aging (**Figure 3B**), the average Young modulus of the (PDADMAC-PAA)<sub>30</sub> film decreases by a factor 2.2 ( $0.71 \pm 0.19$  MPa). In addition, the spatial distribution of the Young modulus indicates a less heterogeneous film surface with the highest measured elastic modulus (about 0.75 MPa) corresponding to the donut-ring domains. Outside the latter, the film appears quite homogeneous from a mechanical point of view with modulus values in the range 0.60-0.70 MPa. For 5-day old films (**Figure 3C**), the average Young modulus is about  $0.39 \pm 0.11$  MPa and its spatial repartition over the whole film surface approaches a Dirac-like distribution, denoting a homogeneous surface. The above described evolution of both the magnitude and the spatial distribution of the elastic modulus with increasing natural aging time indicates that the donut-like structures strongly contribute to the overall film stiffness. The time-dependent disappearance of these structures and the accompanying reorganization of the polyelectrolyte chains within the (PDADMAC-PAA)<sub>30</sub> matrix give rise to the spectacular decrease in film stiffness. Previous studies have reported this softening effect upon natural relaxation of polyelectrolyte multilayer films. *E.g.*, the elastic modulus of PEM films formed by the (PLL-HA) couple decreases by a factor 2 after 14 days aging.<sup>50</sup> However, such a decrease is observed after only 1 day for the system of interest in the current work.

In order to evaluate the impact of heating on the mechanical properties and the corresponding film morphology, the Young modulus of (PDADMAC-PAA)<sub>30</sub> films was measured by AFM after 1 h, 2 h and 6 h of heating at 60°C (**Figure 4**). After 1 h of heating (**Figure 4A**), we measured an average Young modulus of  $0.52 \pm 0.08$  MPa with no dramatic sign of heterogeneity in terms of mechanical properties over the whole film surface. In addition, we did not find any correlation between film morphology and spatial distribution of the Young modulus, a situation that contrasts with that discussed above for natural aging conditions. After 2 and 6 h of heating (**Figures 4B,C**), the average Young modulus of the PEM film decreased to  $0.36 \pm 0.06$  and  $0.31 \pm 0.05$  MPa, respectively with, again, a

homogeneous distribution of the Young modulus and the absence of correlation between film morphology and Young modulus spatial mapping.

**Figure 5A** shows an exponential-like decay of the high-frequency film roughness at saturation (**Figure S1**) from  $\sim 12$  nm to  $\sim 2$  nm with heating periods increasing from 0 h to 6 h. A similar exponential-like time-dependence is obtained for the film roughness under natural aging conditions, except that the plateau value reached after 14 days relaxation is close to 3–4 nm. It is remarkable that the adopted heating protocol dramatically speeds up the morphological reorganization of the film as compared to that achieved under natural aging conditions, as revealed by the decay rates for the surface roughness of  $0.95 \pm 0.17 \text{ day}^{-1}$  and  $3.12 \pm 1.83 \text{ h}^{-1}$  under natural aging and thermal treatment conditions, respectively. The PEM surface morphology observed after 5 days of natural aging is reached after only 2 h heating at  $60^\circ\text{C}$ .

For the sake of comparison, the dependence of the average (PDADMAC-PAA)<sub>30</sub> Young modulus on aging and heating time is collected in **Figure 5B**. For both types of film treatments, the Young modulus decays with time according to an exponential-like relationship but the film elasticity achieved after complete relaxation still remains significantly larger than that classically reported for exponentially grown PEM.<sup>45, 50</sup> Heating obviously promotes film reorganization and softening in a more efficient way than does natural aging, with Young modulus decay rates of about  $1.78 \pm 0.08 \text{ h}^{-1}$  and  $1.56 \pm 0.52 \text{ day}^{-1}$  for heating and natural aging procedures, respectively. In addition, the (PDADMAC-PAA)<sub>30</sub> films after 2 h treatment at  $60^\circ\text{C}$  are mechanically and structurally equivalent to films collected after a 5-day natural aging period. This result unambiguously demonstrates that thermodynamic equilibrium conditions are achieved at a faster rate for thermally-treated films. At this stage of the analysis, it is worth mentioning that the film thickness was measured by AFM under the various aging and temperature conditions tested. For all situations, we did not measure any significant changes in thickness as compared to that of freshly built films.

### **Raman spectroscopy analysis of the donut-ring structures**

To gain further insight into the structural and chemical organizations of (PDADMAC-PAA)<sub>n</sub> films and the relationship between chemical structure and mechanical properties, Raman spectra were measured at room temperature over the surface of a 30-bilayer film

grown onto a germanium crystal. **Figure 6A** displays an optical image of such a film together with Raman spectra taken at different film surface locations marked by blue and red stars. Some 2 to 10  $\mu\text{m}$  sized and randomly distributed light-reflecting domains could be observed at the film surface, and are indicated by the red arrows in **Figure 6A**. Although the spatial resolution of the Raman micro-spectrometer was not sufficient to clearly discriminate the center and the peripheral region of these reflecting structures, they do correspond to the donut morphologies previously revealed by AFM, a conclusion that is confirmed later in the manuscript. These structures cover  $8.5 \pm 3.7\%$  of the total film surface area and, on average,  $15 \pm 6$  of them could be detected every  $1000\ \mu\text{m}^2$  and their surface distribution is patch-like. As a preliminary observation, Raman spectra indicate the absence of nitrate anions in the whole film (including the donut structures) as no Raman peak associated with this ion type could be detected even after increasing the acquisition delay to improve the sensitivity of the measurement. It seems that nitrate anions have been excluded from the film during its construction or that exchange between chloride and nitrate is not operational. The second remarkable result is that the Raman spectra typical for the light-reflecting (or donut) structures are different from those obtained in the rest of the film. The Raman spectrum obtained in the film features a mixture of PDADMAC and PAA that unambiguously contains water, as evidenced from the broad O-H stretching band between  $3100$  and  $3650\ \text{cm}^{-1}$  (**Figure 6B**, blue spectrum). In contrast, the Raman spectrum pertaining to the light-reflecting structures does not exhibit this O-H band, which therefore indicates a strong decrease of water content in the polymeric network associated with the donut structures (**Figure 6B**, red spectrum). The C-H stretching region between  $2800$ - $3100\ \text{cm}^{-1}$  is also clearly different in the two spectra displayed in **Figure 6B**. To refine the analysis of the differentiated fingerprints of the PDADMAC-PAA organization within and outside the donut-ring structures, **Figure 6** compares typical Raman spectra for solutions of pure PDADMAC and pure PAA with the spectra corresponding to the smooth parts of the film and to the donut-like structures (**Figures 6C-6D** and **Figures 6E-6F**, respectively). **Table 1** further reports the Raman positions of the most noticeable peaks, together with their assignments for the pure compounds, for the smooth film parts and for the donut-like structures. Peaks assignment was carried out on the basis of literature data on PDADMAC<sup>51</sup> and PAA<sup>52</sup> and from our own Density Functional Theory-based results (see §2.4).

The typical Raman spectrum obtained in the film outside the donut structures reveals peaks assigned to both PAA and PDADMAC compounds. The C=O stretching mode of PAA in the acidic form at  $1709\text{ cm}^{-1}$  is indeed detected in spectrum b (**Figure 6C**), while the characteristic low-frequency modes of PDADMAC at  $471\text{ cm}^{-1}$  and  $575\text{ cm}^{-1}$  are also clearly distinguished in the film spectra and their intensities are significantly larger than those obtained for pure PDADMAC solution. The C-H stretching area between  $2800$  and  $3100\text{ cm}^{-1}$  (**Figure 6D**) corresponds to a mixture of both compounds, but since the bands at  $2931\text{ cm}^{-1}$  for PAA and PDADMAC overlap, it is not straightforward to unravel their respective contributions in the film's spectrum. A refined observation of the film spectra further reveals some small but representative shifts in peak positions as compared to pure PDADMAC and PAA solutions. These shifts are probably the result of electrostatic interactions taking place between PAA and PDADMAC in the film. As an illustration, the C-H stretching mode of the methyl groups of PDADMAC at  $3020\text{ cm}^{-1}$  is shifted to  $3040\text{ cm}^{-1}$  in the film (**Figure 6D**) and the low frequency mode at  $450\text{ cm}^{-1}$  of PDADMAC is shifted to  $471\text{ cm}^{-1}$  (**Figure 6C**). While the peak at  $575\text{ cm}^{-1}$  of PDADMAC in the film is not shifted from its position when in pure solution (**Figure 6C**), its intensity is strongly enhanced in the film, and the same holds for the band at  $471\text{ cm}^{-1}$ . This basically means that the changes in polarizability associated with these two modes are more significant in the PDADMAC/PAA film mixture as compared to those in aqueous solution of pure PDADMAC. Finally, the intensity of the peak at  $1415\text{ cm}^{-1}$ , which stems from a COO<sup>-</sup> vibration band of polyacrylate anions,<sup>52</sup> is also significantly enhanced in the film (**Figure 6C**, spectrum b), which suggests that some carboxylic groups of PAA are deprotonated in the film.

The characteristic Raman spectrum obtained in the light-reflecting donut structures is compared to those of pure PDADMAC solution in **Figures 6E and 6F**. Remarkable changes can be further identified by comparing the results to those previously detailed for the film regions located outside the donut-ring structures. In detail, the low wavenumber modes at  $471$  and  $575\text{ cm}^{-1}$  in the donut structures have now a lower Raman intensity than those detected for the pure PDADMAC solution and the rest of the film surface. In addition, the three peaks detected at  $793$ ,  $847$  and  $900\text{ cm}^{-1}$  for pure PDADMAC are so weak in the donut structures that they are not detectable under the adopted experimental acquisition conditions. The peaks between  $1000$  and  $1500\text{ cm}^{-1}$  have become quite narrow in the donut structures and less numerous compared to those for the PDADMAC aqueous solution (**Figure 6E**), and the C=O

stretching mode of PAA ( $1709\text{ cm}^{-1}$ ) is further absent from the spectra in the donut structures. In addition, the C-H stretching modes of PDADMAC at  $2827\text{ cm}^{-1}$  and  $2875\text{ cm}^{-1}$  are shifted to  $2848$  and  $2883\text{ cm}^{-1}$  in the donut structures (**Figure 6F**), their intensity is significantly enhanced and the peaks are very narrow. Finally, practically no water is present in the donut structures since no O-H stretching mode could be detected above  $3200\text{ cm}^{-1}$ . The important spectral changes evidenced in **Figures 6C-6D** and **Figures 6E-6F** for the film domains outside and inside the donut-ring structures, respectively, are characteristic of a differentiated organization of the PDADMAC/PAA network in these various regions of the film. In particular, the lack of O-H stretching mode in **Figure 6F** is probably the most spectacular fingerprint of the PDADMAC/PAA assembly in the donuts: it reveals that the chains organization therein is accompanied by water exclusion. The lack of water in the donut structures is certainly thermodynamically unstable, and these structures can thus be legitimately considered as metastable. This is in agreement with the mechanical and morphological AFM results, *i.e.* freshly prepared PEM films relax towards an equilibrium state characterized by smoother and softer film surfaces (**Figure 5**). In addition, these results confirm that the light-reflecting structures of **Figure 6A** correspond to the donut structures detected by AFM. Due to the absence of water in the donut structures, these spatial domains are indeed expected to exhibit a higher Young modulus than in the rest of the film, which is in line with the spatially-resolved film mechanical properties obtained by AFM (**Figure 3A**). Since there is no obvious peak corresponding to PAA in spectrum b of **Figures 6E and 6F**, we suggest that the donut structures are significantly enriched in PDADMAC, a conclusion that is further in line with the unique water-absorption features of PAA<sup>53</sup> and the aforementioned absence of water in the donut domains. However, these film domains are probably not completely depleted in PAA as PAA-PDADMAC complex formation is known to spontaneously take place under pH conditions (met here) where PAA is poorly charged.<sup>54</sup> The water-free polyelectrolyte complexes formed in the donuts between PDADMAC and PAA as a result of electrostatic interactions between their anionic and cationic charges inevitably leads to important changes in the polarizability tensor associated with the PDADMAC vibrational modes, which can explain the important spectral modifications detected in **Figure 6**, a conclusion that is later confirmed by DFT computations.

Further supporting evidence for such a formation of polyelectrolyte complexes in the donut structures of the film is obtained by an integration of the C-H stretching mode at  $2883$

$\text{cm}^{-1}$  that is clearly enhanced in the water-free donut structures as compared to that in the neighboring film regions (**Figure 6F** and **Figure S3**). Integration of this band was performed over a large film surface area ( $\sim 46 \times 63 \mu\text{m}^2$ ) where Raman spectra were recorded (see details in Experimental Section). The results are reported in **Figure S3A** and **Figure S3B** further illustrates the adopted integration procedure. In addition, optical images of the film area probed by Raman confocal spectroscopy were recorded (**Figure S3C**). A straightforward comparison between the optical image and the Raman map fully supports our previous conclusion, *i.e.* donut-like structures are the location of polyelectrolyte complexes formation where water is excluded. Spatially resolved AFM mechanical analysis further brings to light that these complexes must be interconnected by strong ion-pair interactions resulting in tight compact structures leading to Young moduli that are one to two orders of magnitude larger than that commonly reported for exponentially-grown films. Even though the spatial resolution of the Raman map is diffraction-limited, the distribution of these donuts is quite similar to that obtained by AFM, which further supports the consistency and complementarity of the information obtained from Raman spectroscopy and AFM in imaging and force volume modes.

The fact that the Raman peaks are relatively narrow in the donuts (**Figure 6F**) is further symptomatic of a well-organized polymer network. Following the literature on alkane phases, we use here the Raman intensity of the two C-H stretching modes at  $2848 \text{ cm}^{-1}$  and  $2883 \text{ cm}^{-1}$  to estimate the degree of organization of the polymeric chains in the structure.<sup>55</sup> Indeed, like in alkane films, the higher is the intensity ratio  $r = I_{2883}/I_{2848}$ , the more organized is the phase. A low ratio is characteristic of a low range order where polymer chains are very mobile, similar to a liquid phase, whereas a high ratio indicates a higher range order as commonly found for polymer chains with reduced mobility in solid phase. For the small donut structures that optically contrast with the rest of the film, we derive a value for  $r = I_{2883}/I_{2848}$  of about 1.54. Such a ratio can be used to further estimate the order parameter  $S$ , classically defined for alkane phases but applicable to  $-\text{CH}_2$  groups involved in other types of molecules, according to the following expression:<sup>55</sup>

$$S = \frac{r - 0.7}{1.5} \quad [2]$$

A disordered or liquid phase is defined by  $S = 0$  whereas a perfect crystal corresponds to  $S = 1$ . For the system of interest here, using  $r = 1.54$ ,  $S$  has a value of 0.56, *i.e.* intermediate

between these two extreme organization modes. Basically, this suggests that the polymer chains within the reflecting structures are less mobile than the chains located in the surrounding film region, which is qualitatively in line with their stiffness and the resulting high film Young modulus. One should note that the intensity ratio  $I_{2883}/I_{2848}$  outside the donut structures is very difficult to evaluate because the corresponding  $\text{-CH}_2$  stretching modes are practically absent in the corresponding spectrum due to the fact that no polarizability enhancement is observed for these film regions.

### **Density Functional Theory computations: hint for PDADMAC-PAA organization in donut-ring structures**

As a final step toward a molecular assessment of the relationships evidenced so far between film structure, composition and stiffness, DFT-based computations were carried out to model the vibrational properties of pure PDADMAC and PAA polyelectrolytes and mixtures thereof. The quantitative interpretation of Raman intensities calls for the explicit treatment of electrons polarization. However, the latter is very demanding in terms of computational time and costs, which prevents modeling of all interactions between polymeric chains. To circumvent this difficulty, two strategies may be adopted: (i) the use of symmetry and periodic conditions to model ordered arrangements of infinite chains, or (ii) the use of cluster models to focus on a specific region of the system. It is this second approach that we adopted. This choice is motivated by the fact that the mid-infrared region ( $400\text{--}4000\text{ cm}^{-1}$ ) is dominated by vibrations of the monomeric units of the polymeric chains. Therefore, clusters built from those units should provide results that are adequate representatives of the polyelectrolyte vibrations of interest. Snapshots of PDADMAC and PAA clusters and of their complexes can be found in **Figures S4A, S4B and S4C**, respectively. While 1 monomeric unit is considered for PDADMAC, 2 were used to construct a PAA cluster in order to correctly describe the environment of the methylene bridge of PAA as well as the chelation of the dimethylamonium part of PDADMAC. For all clusters, the chemical groups corresponding to the rest of the polymeric chains have been replaced by  $\text{-CH}_3$  groups. The electronic and structural properties of all clusters were evaluated by DFT using the Gaussian09 program package.<sup>56</sup> The equilibrium geometries, the harmonic vibrational wavenumbers, and the Raman intensities were estimated under identical computational conditions, namely B3LYP/6-31+G(d,p).<sup>57, 58</sup> To correct for the systematic error due to the

neglect of anharmonicity and electron correlation, a single empirical scaling factor of 0.9648 was adopted.<sup>59</sup> The hydrogen atoms of the ‘end of chains’ methyl groups have been substituted by deuterium atoms in frequency calculations so that their vibrational signatures could be decoupled from those pertaining to the remaining CH signals.

Comparison between the experimental Raman spectra and those evaluated from DFT computations for the pure and mixed PDADMAC and PAA clusters gives an insight into the molecular organisation modes of PAA and PDADMAC. First, in order to address the issue relative to the protonation state of PAA and more specifically to identify whether the PDADMAC polycation faces the acidic or basic forms of PAA, the two PAA configurations were tested. Only the spectrum computed for the complex with the basic PAA form matches the experimental spectrum. Accordingly, the modifications of the PDADMAC Raman spectrum experimentally observed and detailed in **Figure 6** are necessarily due to electrostatic interaction of PDADMAC with the COO<sup>-</sup> groups of PAA. Testing different starting points for the construction of the complex suggested a preferred interaction of carboxylate groups with the sides of the PDADMAC cycle (CH<sub>2</sub> and CH<sub>3</sub> groups) rather than with the front of the cycle where they would then solely interact with the methyl groups. The interactions taking place between polycationic and polyanionic chains in the donut structures are likely driven by ion-pairing, in agreement with the pH conditions adopted here.<sup>54, 60</sup> DFT evaluations further suggest that ion-dipole interactions type cannot be excluded as carboxylate groups of PAA are shown to interact with electrons from the PDADMAC cycle. However, due to the necessary simplifications of the DFT computational framework adopted here, it would be speculative to draw firmer conclusions on the exact contribution of ion-pair and ion-dipole electrostatic forces leading to the PDADMAC-PAA complex assembly in the donut structures.

The proximity of the COO<sup>-</sup> groups significantly perturbs the electron density distribution along the PDADMAC cycle, particularly at the level of the H atoms involved in the -CH stretching normal modes, while leaving essentially unchanged the electron density distribution along the PDADMAC backbone. This result, obtained from DFT and natural bond orbital (NBO) investigation of PDADMAC-PAA interaction, explains the measured dramatic increase in Raman intensities of the CH stretching at 2883 cm<sup>-1</sup> and 2848 cm<sup>-1</sup> in the formed complex, as shown in **Figure S5**. In details, the latter figure compares the calculated Raman spectra of pure PDADMAC (**Figure S5A**) and PDADMAC-PAA complex (**Figure**



**S5B**) and the experimental spectra pertaining to the film (**Figure S5C**) and to the donut structures (**Figure S5D**) in the C-H stretching spectral region. The increase in polarizability of the vibrational modes at 2848 and 2883  $\text{cm}^{-1}$ , as observed in the donut-like structures (**Figure 6F** and **Figure S5D**) is well confirmed by DFT calculations which highlight the exaltation of  $\text{CH}_2$  components in PDADMAC-PAA complexes (**Figures S5A-B**). DFT also supports that water molecules strongly disturb the association of PDADMAC with PAA since no stable complex was found when explicit water molecules were added in the calculation, and the stable state corresponded to PDADMAC separated from deprotonated and hydrated PAA molecules (Supporting Information, **Table S1**). This result, that evidences a favored direct interaction between monomers upon water exclusion, very well confirms the conclusions by Alonso *et al.*<sup>54</sup> who showed that water-stabilization (through hydrogen bonding) of PAA charges prevents the association with PDADMAC, a situation met in particular at high pH values where PAA carboxylic groups are strongly dissociated. Therefore, the donut structures do result from the formation of specific polyelectrolyte complexes between deprotonated PAA molecules and PDADMAC polycations with water exclusion, a conclusion that elegantly confirms the preceding developments. This complex is not stable in the presence of water, which explains the lack of O-H stretching mode inside the donut structures, as seen in the Raman spectrum of **Figure 6F**. Based on the arguments given in the Introduction, it may then be anticipated that the reflecting structures with low chains mobility are not stable from a thermodynamic point of view and thus some material rearrangements probably take place therein over time following water diffusion inside the donut structures, and also probably salt diffusion and annealing of these structures. The dramatic consequences of the relaxation of these metastable structures in terms of overall film morphology and film stiffness are here addressed by means of AFM. This relaxation is accompanied by a progressive transition over time from stiff water-free polyelectrolyte complexes to hydrophilic polyelectrolyte coacervates loosely associated by electrostatics.<sup>61</sup> **Figure 7** summarizes the main conclusions of the results discussed so far. As a last remark, the patchy nature of the donuts distribution throughout the film surface is likely related to the existence -right from the beginning of the construction of the film- of pH gradients and of inhomogeneous distribution of water droplets at the film surface. In turn, this probably gives rise to the formation of both hydrophilic and hydrophobic domains, thus explaining the

absence of a continuous donut phase throughout the film. In that respect, a careful examination of how the film surface evolves with the number of bilayers would be decisive.

### **On the impact of heating on the structural and spectrochemical film properties.**

Raman Confocal Spectroscopy measurements were performed on a 22-day old (PDADMAC-PAA)<sub>30</sub> film before and after laser-printing of local regions of the film (**Figure 8** and **Figure S6**). In detail, the laser was used to heat locally the film and we followed optically its subsequent relaxation (**Figures 8A-E**). Before application of the laser, we measured a typical spectrum for fully relaxed (PDADMAC-PAA)<sub>30</sub> (without donut-like structures), as detailed in **Table 1**, and this spectrum was strongly modified 10 s after heating (**Figure 8F**). The spectrochemical fingerprint we found for the heated region was similar to that detailed in the preceding sections for the reflecting donut-like structures identified on a freshly built film, except that the intensities of the bands pertaining to CH<sub>2</sub> vibrations at 2848 and 2883 cm<sup>-1</sup> were significantly different (**Figure S6**). Quantitatively, the ratio  $r = I_{2883}/I_{2848}$  is about 1.87 in the heated-film domains, which corresponds to an order parameter  $S = 0.78$ , to be compared with the 0.56 value obtained for the donut-like structures observed on freshly-built PEM films. Such increase in  $S$  indicates that laser heating favors a significant reorganization of the film, certainly due to water molecules diffusing away from the laser spot due to heat deposition. The heated film thus reorganizes in a way similar to that described for the initially formed donut structures where PDADMAC/PAA polyelectrolyte complex is formed with significant exclusion of water, as evidenced by the quasi-absence of -OH Raman fingerprint (**Figure S6**, **Figure 8F**). This peculiar organization can also occur naturally (*i.e.* for non-heated films, **Figure 3A**) in small-sized domains, thereby giving rise to a local change in refractive index of the PEM film, which explains the observed contrast in optical microscopy for the donut-like structures. In addition, the fact that  $S$  remains lower than unity in the irradiated film areas suggests that the polyelectrolyte chains remain sufficiently mobile to further diffuse in the neighboring film region after turning off the laser. This is confirmed by the progression to total dissolution of the irradiated areas after 120 s relaxation of the film following laser treatment (**Figure 8E**). The observation of this relaxation indicates that the polyelectrolyte phase induced by laser irradiation is not thermodynamically stable. As discussed earlier, such unstable micro-domains naturally occur in freshly built PEM films and disappear after several days' relaxation (**Figure 3**).

---

## **Conclusions**

By combining atomic force microscopy in the imaging and force spectroscopy modes with Raman confocal spectroscopy, we have shown that exponentially growing PEM films constructed from alternate layers of PDAMAC and PAA are far from their equilibrium state after deposition. This out-of-equilibrium state is characterized by topographical heterogeneities in the form of ring-like structures, the mechanical properties and the composition (deficient in water) of which are different from those in the neighboring flat film regions. The films slowly relax to their equilibrium state with a time scale of the order of  $10^5$ - $10^6$  s. The equilibrated films are characterized by a smooth topography, by homogeneous mechanical properties and composition. Equivalent relaxation can be reached more rapidly upon heating the solution in contact with the film to 60°C. Preliminary results further indicate that increasing the pH of PAA solution to 6 leads to mechanical properties of freshly built films that are identical to those achieved by relaxed films structure obtained under the pH condition adopted in this work. These findings are new for exponential growing films. They show that slow structural relaxation is common between such films and those displaying a linear growth regime. Such a relaxation process is expected to be system-dependent and it may thus offer a huge versatility in terms of novel properties, such as a gradual but spontaneous change in mechanical properties without changes in the global chemical composition. The findings described in this article are of fundamental importance for a more general understanding of the deposition mechanism of films obtained in a layer-by-layer manner and they are also of practical interest for imprinting transient information in the films upon laser irradiation. This information can be erased again due to the natural film relaxation dynamics, thereby allowing a reuse of the film for upcoming irradiation and information storage steps. From this point of view, the current study paves the way for further investigation of film compositions that may lead to a broader range of characteristic relaxation times than those obtained here.

## Figures and table captions

**Table 1**

Assignment of the Raman bands measured for PDADMAC, PAA and PEM film outside and inside donut-ring like structures. The origins of these bands were determined from literature and from DFT computations. See Raman spectra in Figure 6.

PDADMAC		PAA		Film	Donut	Assignment
Exp.	DFT	Exp.	DFT			
450	471			471	471	PDADMAC ring+chain skeletal deformation
		511	484			PAA skeletal deformation involving neighbouring COOH groups
575	571			575	575	PDADMAC CH <sub>3</sub> -N-CH <sub>3</sub> scissoring, "umbrella mode" of the ring
		759	761			PAA C-COOH stretching + CH <sub>2</sub> rocking
793	772			793		PDADMAC CH <sub>2</sub> chain rocking + C-N stretching
847	810			847		PDADMAC CH <sub>2</sub> cycle rocking + C-C ring stretching
		853	824			PAA CH <sub>2</sub> -CH-CH <sub>2</sub> torsion mode
900	882+922			900		PDADMAC ring breathing
964	963+964					PDADMAC ring deformation + C-N stretching
1001	1000					PDADMAC skeletal C-C stretching mode
					1068	?
		1101	1129	1101		PAA CH <sub>2</sub> twisting + C-C-H bending
1107	1072/1084					PDADMAC skeletal C-C stretching mode + C-H deformation
					1136	?
		1175	1185+1255	1175	1175	PAA CH <sub>2</sub> coupled twisting modes
					1298	?
1331	1296/1328					PDADMAC CH <sub>2</sub> chain twisting
		1335	1427			PAA CH <sub>2</sub> twisting (contrary to Koda ref)
1384	1390					collective CH <sub>2</sub> chain+cycle wagging
				1415		PAA deprotonated : COO <sup>-</sup> symmetrical stretching
		1420				PAA CH <sub>2</sub> wagging (contrary to Koda ref)
1448	1488				1448	PDADMAC CH <sub>2</sub> chain scissoring
		1455	1488	1455		PAA CH <sub>2</sub> scissoring in phase
1469	1510				1469	PDADMAC CH <sub>3</sub> bending mode
		1709	1763	1709		PAA C=O stretching mode of carboxylic groups
					2725	?
2752						PDADMAC harmonic frequency of the 1384 mode
2827	2997			2827		PDADMAC CH <sub>2</sub> chain sym stretching mode
					2848	PDADMAC CH <sub>2</sub> chain sym stretching mode in complex with PAA
2875	3003			2875		PDADMAC CH <sub>2</sub> chain asym stretching mode+C-H stretch
		2876	3037			PAA CH <sub>2</sub> sym stretching mode in phase
					2883	PDADMAC CH <sub>2</sub> chain asym stretching mode+C-H stretch in complex
2904	3074					PDADMAC CH <sub>3</sub> sym stretching mode
2931	3096			2931	2931	PDADMAC CH <sub>2</sub> cycle sym stretching mode+C-H stretch
		2931	3048			PAA CH <sub>2</sub> sym stretching mode in phase opposition
		2974	3096			PAA CH <sub>2</sub> asym stretching mode + C-H stretch
2975	3137			2975		PDADMAC CH <sub>2</sub> ring asym stretching mode
3006	3161					PDADMAC CH <sub>3</sub> asym stretching mode
3020	3176			3040		PDADMAC CH <sub>3</sub> asym stretching mode
		3260		3260		H-O-H stretching modes of water bound to PAA
3395						H-O-H stretching mode of "free" water
		3420		3420		H-O-H stretching mode of "free" water

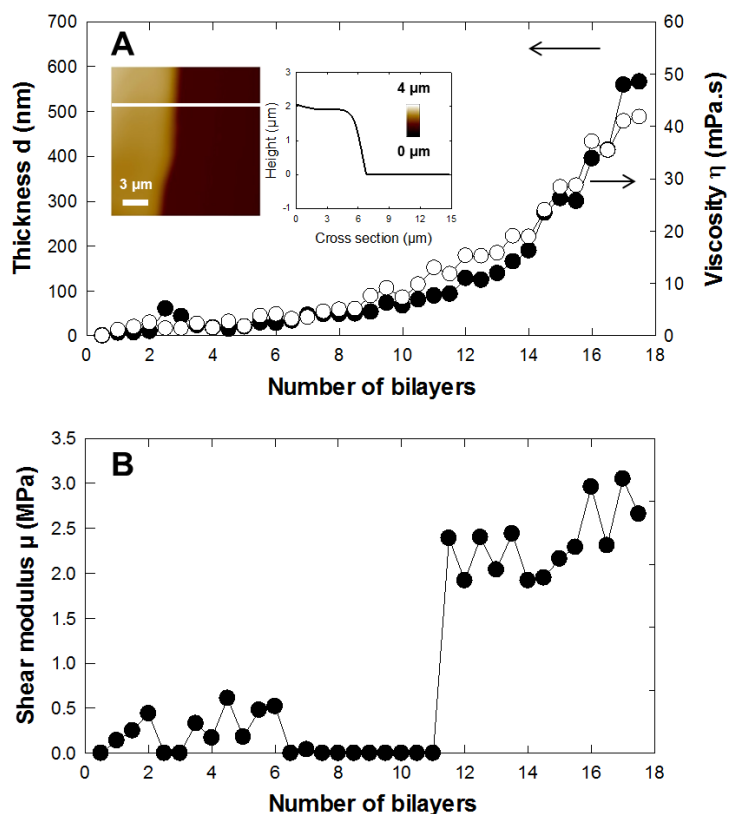


**Figure 1. Quantitative analysis of QCM-D results**

(A) Evolution of (PDADMAC-PAA) film thickness (filled circles-left axis) and dynamic viscosity (open circles-right axis) with the number of deposited (polyanion/polycation) bilayers onto the QCM-D crystal. In inset, AFM topographic image of (PDADMAC-PAA)<sub>30</sub> film over a  $15 \times 15 \mu\text{m}^2$  surface area after scratching, and height profile extracted from the cross section marked by the white line. AFM images were performed with PeakForce Mapping™ mode in 1 mM  $\text{CaCl}_2$  aqueous solution at room temperature. (B) Evolution of the (real part of the) film shear modulus with the number of (polyanion/polycation) deposited bilayers.

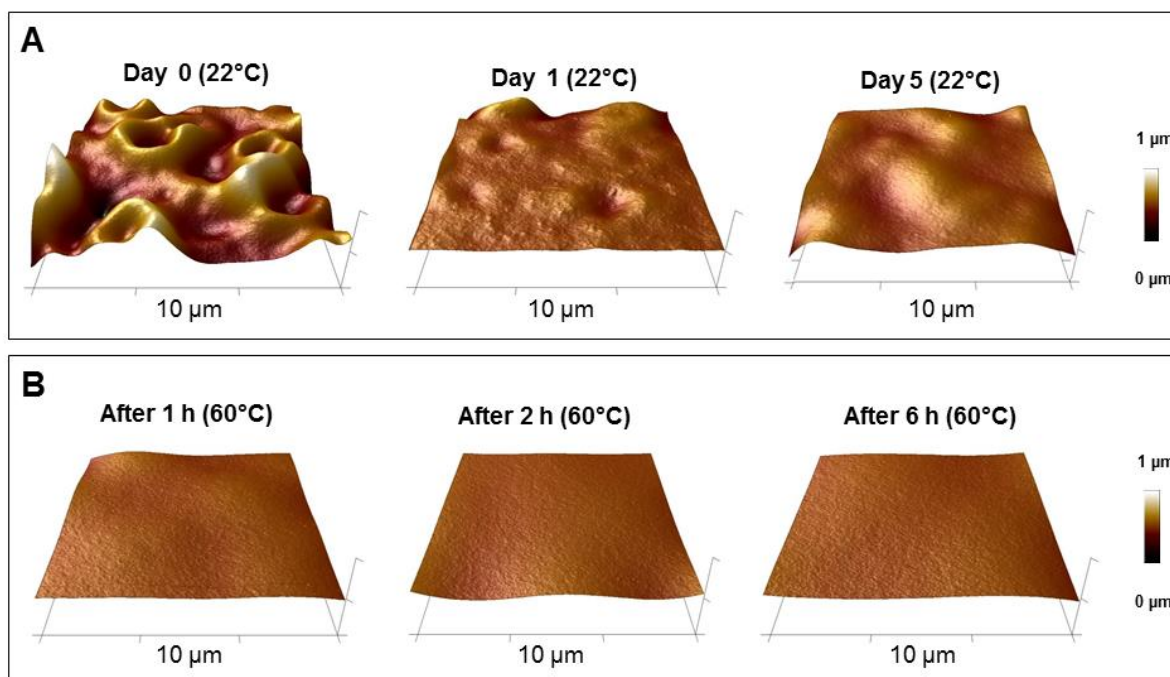


**Figure 2. Effect of aging and heating treatment on film morphology**

(A) Evolution of (PDADMAC-PAA)<sub>30</sub> film morphology during natural aging at 22°C (results obtained by AFM). 3D topographic images are given for the freshly built film, for films after 1 day and 5 days natural aging (indicated). (B) Evolution of (PDADMAC-PAA)<sub>30</sub> film morphology (3D topographic images are provided) after 1 h, 2 h and 6 h heating (indicated). A M images were performed with Peak force Mapping™ mode in 1 mM a<sub>3</sub> aqueous solution at room temperature over a 30×30 μm<sup>2</sup> surface area.

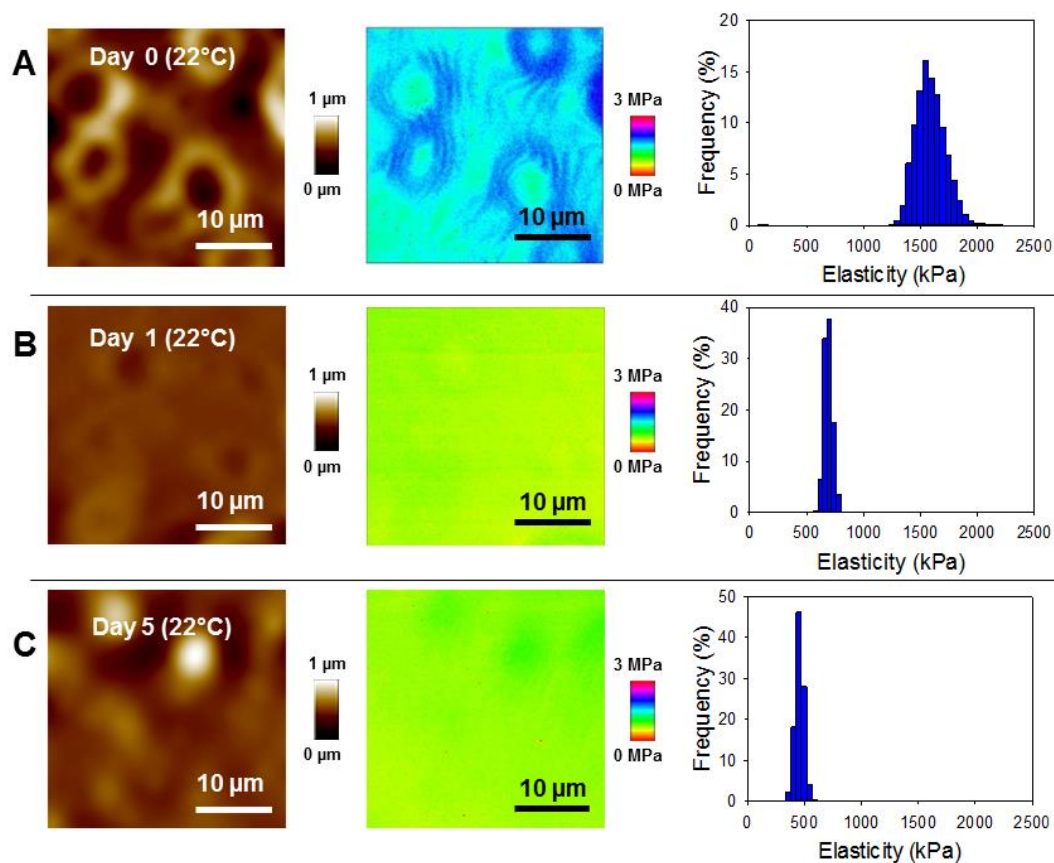


**Figure 3. Effect of natural aging on the film mechanical properties**

(A) From left to right: illustrative AFM topographic image, Young modulus map and statistical distribution of Young modulus for freshly built (PDADMAC-PAA)<sub>30</sub> films. (B) As in (A) for (PDADMAC-PAA)<sub>30</sub> films after 1 day natural aging. (C) As in (A) for (PDADMAC-PAA)<sub>30</sub> films after 5 days natural aging.

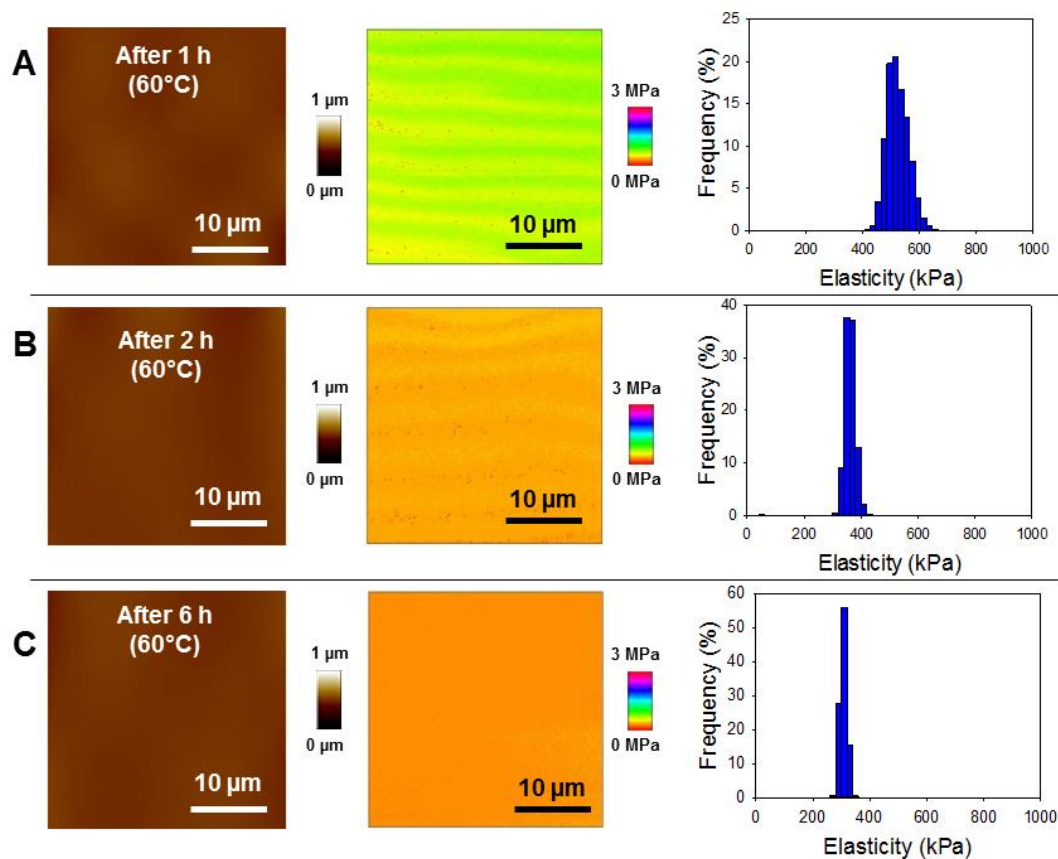


**Figure 4. Effect of heating treatment delay on the film mechanical properties**

(A) From left to right: illustrative AFM topographic image, Young modulus map and statistic distribution of Young modulus for (PDADMAC-PAA)<sub>30</sub> films after 1 h heating at 60°C. (B) As in (A) for (PDADMAC-PAA)<sub>30</sub> films after 2 h heating at 60°C. (C) As in (C) for (PDADMAC-PAA)<sub>30</sub> films after 6 h heating at 60°C.



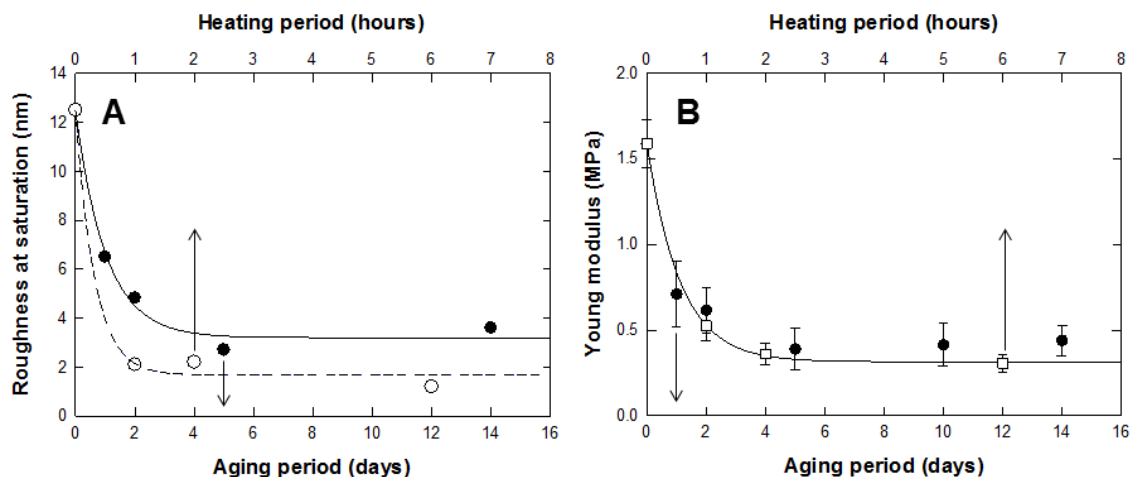


**Figure 5. Effect of natural aging and heating treatment on film surface roughness and Young modulus**

(A) Exponential decay of (PDADMAC-PAA)<sub>30</sub> film roughness at saturation (*i.e.* determined for a film surface area of 1000  $\mu\text{m}^2$ ) with increasing natural aging time (filled circles-bottom axis) and heating treatment delay (open circles-top axis). Plain and dotted lines are guides to the eye. (B) Exponential decay of the (PDADMAC-PAA)<sub>30</sub> film Young modulus with increasing natural aging time (filled circles-bottom axis) and heating treatment time (open squares-top axis). Solid line is a guide to the eye.

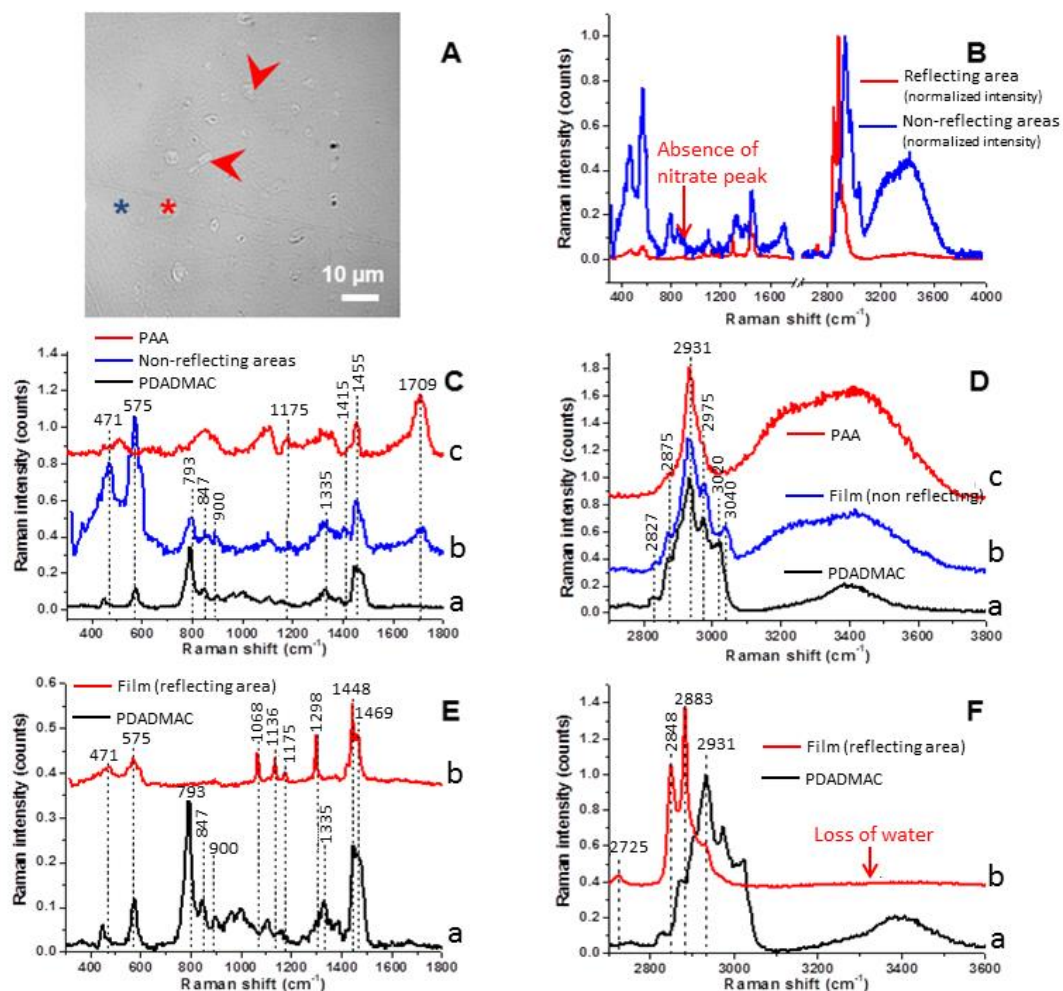


**Figure 6. Confocal Raman spectroscopy on freshly built (PDADMAC-PAA)<sub>30</sub> film**

(A) Optical microscopy image of (PDADMAC-PAA)<sub>30</sub> freshly built film and representative Raman spectra (B) recorded on the donut-like structures (red line correspond to the location marked by a red asterisk on the image in (A) and blue line to that indicated by a blue asterisk). Several reflecting structures are further marked by red arrows on the image in (A). Identification and assignments of the Raman bands in spectra measured for pure PDADMAC, pure PAA (indicated) and for the films domains outside the donut-like structures (C, D) and those corresponding to these light-reflecting structures (E, F). See text for further details. Table 1 collects the nature of the bands identified for the various systems and for the distinct probed film locations.

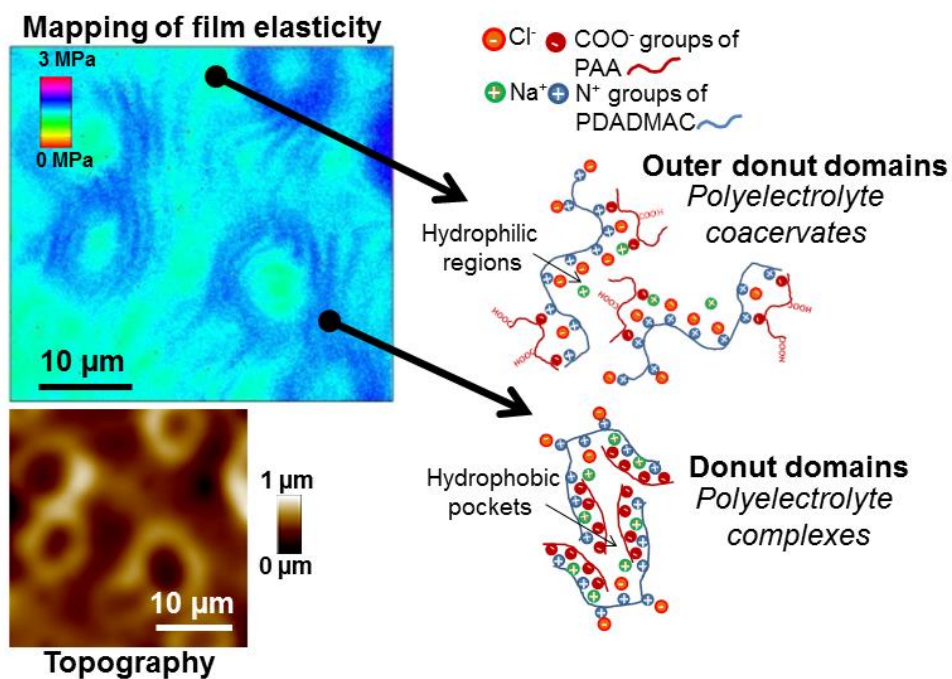
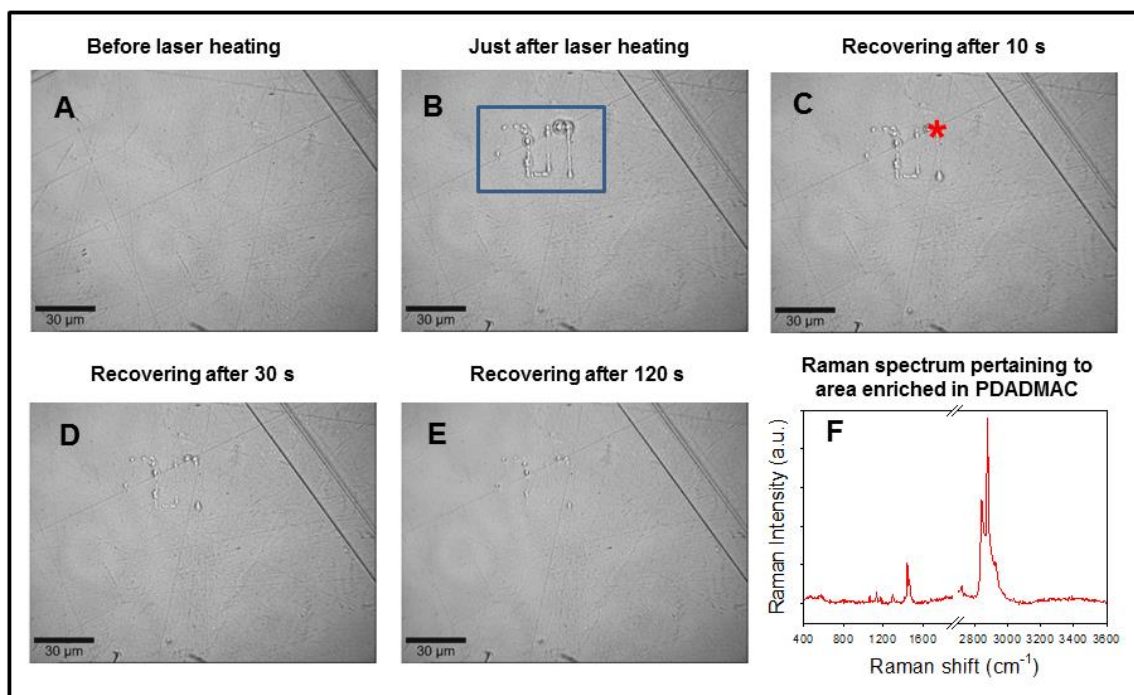


Figure 7. Schematics summarizing the structure-mechanics-molecular organization features of freshly built (PDADMAC-PAA)<sub>30</sub> film.



**Figure 8. Effect of laser printing/heating on film Raman signature**

Typical optical microscopy images obtained for a 22-days old (PDADMAC-PAA)<sub>30</sub> film before laser heating (A), just after laser heating/printing (blue rectangle in panel B), after 10s (C), 30s (D) and 120s (E) film structure relaxation following laser printing. The Raman spectrum in (F) corresponds to the spectroscopic signature of the heated film region marked by a red asterisk in panel (C), after 10s relaxation.

## References

1. Decher, G., Fuzzy nanoassemblies: Toward Layered Polymeric Multicomposites. *Science* **1997**, *277*, 1232-1237.
2. Ariga, K.; Hill, J. P.; Ji, Q., Layer-by-Layer Assembly as a Versatile Bottom-Up Nanofabrication Technique for Exploratory Research and Realistic Application. *Phys. Chem. Chem. Phys.* **2007**, *9*, 2319-2340.
3. Lavalle, P.; Voegel, J.-C.; Vautier, D.; Senger, B.; Schaaf, P.; Ball, V., Dynamic Aspects of Films Prepared by a Sequential Deposition of Species: Perspectives for Smart and Responsive Materials. *Adv. Mater.* **2011**, *23*, 1191-1221.
4. Li, L. D.; Mohwald, H., Photoinduced Vectorial Charge Transfer Across Walls of Hollow Microcapsules. *Angew. Chem. Int. Edit.* **2004**, *43*, 360-363.
5. Bricaud, Q.; Fabre, R. M.; Brookins, R. N.; Schanze, K. S.; Reynolds, J. R., Energy Transfer between Conjugated Polyelectrolytes in Layer-by-Layer Assembled Films. *Langmuir* **2011**, *27*, 5021-5028.
6. Farhat, T. R.; Schlenoff, J. B., Corrosion Control Using Polyelectrolyte Multilayers. *Electrochem. Solid St.* **2002**, *5*, B13-B15.
7. Shchukin, D. G.; Zheludkevich, M.; Moehwald, H., Feedback Active Coatings Based on Incorporated Nanocontainers. *J. Mater. Chem.* **2006**, *16*, 4561-4566.
8. Balachandra, A. M.; Dai, J. H.; Bruening, M. L., Enhancing the Anion-Transport Selectivity of Multilayer Polyelectrolyte Membranes by Templating with  $\text{Cu}^{2+}$ . *Macromolecules* **2002**, *35*, 3171-3178.
9. Tang, Z. Y.; Wang, Y.; Podsiadlo, P.; Kotov, N. A., Biomedical Applications of Layer-by-Layer Assembly: From Biomimetics to Tissue Engineering. *Adv. Mater.* **2006**, *18*, 3203-3224.
10. Gribova, V.; Auzely-Velty, R.; Picart, C., Polyelectrolyte Multilayer Assemblies on Materials Surfaces: From Cell Adhesion to Tissue Engineering. *Chem. Mater.* **2012**, *24*, 854-869.
11. Harris, J. J.; DeRose, P.; Bruening, M., Synthesis of Passivating, Nylon-Like Coatings Through Cross-Linking of Ultrathin Polyelectrolyte Films. *J. Am. Chem. Soc.* **1999**, *121*, 1978-1979.
12. Podsiadlo, P.; Shim, B. S.; Kotov, N. A., Polymer/Clay and Polymer/Carbon Nanotube Hybrid Organic-Inorganic Multilayered Composites Made by Sequential Layering of Nanometer Scale Films. *Coord. Chem. Rev.* **2009**, *253*, 2835-2851.
13. Podsiadlo, P.; Liu, Z.; Paterson, D.; Messersmith, P. B.; Kotov, N. A., Fusion of Seashell Nacre and Marine Bioadhesive Analogs: High-Strength Nanocomposite by Layer-by-Layer Assembly of Clay and L-3,4-Dihydroxyphenylalanine Polymer. *Adv. Mater.* **2007**, *19*, 949-955.
14. Heuvingh, J.; Zappa, M.; Fery, A., Salt Softening of Polyelectrolyte Multilayer Capsules. *Langmuir* **2005**, *21*, 3165-3171.
15. Discher, D. E.; Janmey, P. A.; Wang, Y.-L., Tissue Cells Feel and Respond to the Stiffness of their Substrate. *Science* **2005**, *310*, 1139-1143.

16. Picart, C.; Mutterer, J.; Richert, L.; Luo, Y.; Prestwich, G. D.; Schaaf, P.; Voegel, J.-C.; Laval, P., Molecular Basis for the Explanation of the Exponential Growth of Polyelectrolyte Multilayers. *P. Natl. Acad. Sci. USA* **2002**, *99*, 12531-12535.
17. Laval, P.; Gergely, C.; Cuisinier, F. J. G.; Decher, G.; Schaaf, P.; Voegel, J.-C.; Picart, C., Comparison of the Structure of Polyelectrolyte Multilayer Films Exhibiting a Linear and an Exponential Growth Regime : An In Situ Atomic Force Microscopy Study. *Macromolecules* **2002**, *35*, 4458-4465.
18. Boulmedais, F.; Bozonnet, M.; Schwinté, P.; Voegel, J.-C.; Schaaf, P., Multilayered Polypeptide Films: Secondary Structures and Effect of Various Stresses. *Langmuir* **2003**, *19*, 9873-9882.
19. Halthur, T. J.; Elofsson, U. M., Multilayers of Charged Polypeptides as Studied by In Situ Ellipsometry and Quartz Crystal Microbalance with Dissipation. *Langmuir* **2004**, *20*, 1739-1745.
20. Picart, C.; Mutterer, J.; Arntz, Y.; Voegel, J.-C.; Schaaf, P.; Senger, B., Application of Fluorescence Recovery after Photobleaching to Diffusion of a Polyelectrolyte in a Multilayer Film. *Microsc. Res. Techniq.* **2005**, *66*, 43-57.
21. Jourdainne, L.; Lecuyer, S.; Arntz, Y.; Picart, C.; Schaaf, P.; Senger, B.; Voegel, J. C.; Laval, P.; Charitat, T., Dynamics of Poly(L-lysine) in Hyaluronic Acid/Poly(L-lysine) Multilayer Films Studied by Fluorescence Recovery After Pattern Photobleaching. *Langmuir* **2008**, *24*, 7842-7847.
22. Hübsch, E.; Fleith, G.; Fatisson, J.; Labbé, P.; Voegel, J.-C.; Schaaf, P.; Ball, V., Multivalent Ion/Polyelectrolyte Exchange Processes in Exponentially Growing Multilayers. *Langmuir* **2005**, *21*, 3664-3669.
23. Farhat, T. R.; Schlenoff, J. B., Doping-Controlled Ion Diffusion in Polyelectrolyte Multilayers: Mass Transport in Reluctant Exchangers. *J. Am. Chem. Soc.* **2003**, *125*, 4627-4636.
24. Ladam, G.; Schaad, P.; Voegel, J.-C.; Schaaf, P.; Decher, G.; Cuisinier, F. J. G., In Situ Determination of the Structural Properties of Initially Deposited Polyelectrolyte Multilayers. *Langmuir* **2000**, *16*, 1249-1255.
25. Salomäki, M.; Vinokurov, I. A.; Kankare, J., Effect of Temperature on the Buildup of Polyelectrolyte Multilayers. *Langmuir* **2005**, *21*, 11232(11240).
26. Zan, X.; Hoagland, D. A.; Wang, T.; Su, Z., Ion Dispositions in Polyelectrolyte Multilayer Films. *Macromolecules* **2012**, *45*, 8805-8812.
27. Laval, P.; Vivet, V.; Jessel, N.; Decher, G.; Mesini, P. J.; Voegel, J.-C.; Schaaf, P., Direct Evidence for Vertical Diffusion and Exchange Processes of Polyanions and Polycations in Polyelectrolyte Multilayer Films. *Macromolecules* **2004**, *37*, 1159-1162.
28. Jomaa, H. W.; Schlenoff, J. B., Salt-Induced Polyelectrolyte Interdiffusion in Multilayered Films: A Neutron Reflectivity Study. *Macromolecules* **2005**, *38*, 8473-8480.
29. Voinova, M. V.; Rodahl, M.; Jonson, M.; Kasemo, B., Viscoelastic Acoustic Response of Layered Polymer Films at Fluid-Solid Interfaces : Continuum Mechanics Approach. *Phys. Scripta* **1999**, *59*, 391-396.

30. Lavallo, P.; Picart, C.; Mutterer, J.; Gergely, C.; Reiss, H.; Voegel, J.-C.; Senger, B.; Schaaf, P., Modeling the Build-Up of Polyelectrolyte Multilayer Films Having Exponential Growth. *J. Phys. Chem. B* **2004**, *108*, 636-648.
31. Sneddon, I. N., The relation Between Load and Penetration in the Axisymmetric Boussinesq Problem for a Punch of Arbitrary Profile. *Int. J. Eng. Sci.* **1965**, *3*, 47-57.
32. Gavara, N.; Chadwick, R. S., Determination of the Elastic Moduli of Thin Samples and Adherent Cells Using Conical AFM Tips. *Nat. Nanotechnol.* **2012**, *7*, 733-736.
33. Jiang, C.; Liu, X.; Luo, C.; Zhang, Y.; Shao, L.; Shi, F., Controlled Exponential Growth in Layer-by-Layer Multilayers Using High Gravity Fields. *J. Mat. Chem. A* **2014**, *2*, 14048-14053.
34. Srivastava, S.; Ball, V.; Podsiadlo, P.; Lee, J.; Ho, P.; Kotov, N. A., Reversible Loading and Unloading of Nanoparticles in "Exponentially" Growing Polyelectrolyte LBL Films. *J. Am. Chem. Soc.* **2008**, *130*, 3748-3749.
35. Micciulla, S.; Dodoo, S.; Chevigny, C.; Laschewsky, A.; von Klitzing, R., Short Versus Long Chain Polyelectrolyte Multilayers: a Direct Comparison of Self-Assembly and Structural Properties. *Phys. Chem. Chem. Phys.* **2014**, *16*, 21988-21998.
36. Shan, W.; Bacchin, P.; Aimar, P.; Bruening, M. L.; Tarabara, V. V., Polyelectrolyte Multilayer Films as Backflushable Nanofiltration Membranes with Tunable Hydrophilicity and Surface Charge. *J. Membrane Sci.* **2010**, *349*, 268-278.
37. Picart, C.; Lavallo, P.; Hubert, P.; Cuisinier, F. J. G.; Decher, G.; Schaaf, P.; Voegel, J.-C., Buildup Mechanism for Poly(L-lysine)/Hyaluronic Acid Films Onto a Solid Surface. *Langmuir* **2001**, *17*, 7414-7424.
38. Tezcaner, A.; Hicks, D.; Boulmedais, F.; Sahel, J.; Schaaf, P.; Voegel, J.-C.; Lavallo, P., Polyelectrolyte Multilayer Films as Substrates for Photoreceptor Cells. *Biomacromolecules* **2006**, *7*, 86-94.
39. Ladhari, N.; Hemmerle, J.; Haikel, Y.; Voegel, J.-C.; Ball, V., Polyelectrolyte Multilayer Films: A Sponge for Insulin? *Bio-Med. Mater. Eng.* **2010**, *20*, 217-225.
40. Garza, J. M.; Schaaf, P.; Muller, S.; Ball, V.; Stoltz, J.-F.; Voegel, J.-C.; Lavallo, P., Multicompartment Films Made of Alternate Polyelectrolyte Multilayers of Exponential and Linear Growth. *Langmuir* **2004**, *20*, 7298-7302.
41. Dubas, S. T.; Schlenoff, J. B., Swelling and Smoothing of Polyelectrolyte Multilayers by Salt. *Langmuir* **2001**, *17*, 7725-7727.
42. Cornelsen, M.; Helm, C. A.; Block, S., Destabilization of Polyelectrolyte Multilayers Formed at Different Temperatures and Ion Concentrations. *Macromolecules* **2010**, *43*, 4300-4309.
43. Prado, M.; Lima, L. C.; Simão, R. A., Scale Laws for AFM Image Evaluation: Potentialities and Applications In *Current Microscopy Contributions to Advances in Science and Technology*, Méndez-Vilas, A., Ed. 2012; Vol. 5, pp 923-929.
44. Lehaf, A. M.; Hariri, H. H.; Schlenoff, J. B., Homogeneity, Modulus and Viscoelasticity of Polyelectrolyte Multilayers by Nano-Indentation: Refining the Buildup Mechanism. *Langmuir* **2012**, *28*, 6348-6355.

45. Francius, G.; Hemmerle, J.; Ohayon, J.; Schaaf, P.; Voegel, J. C.; Picart, C.; Senger, B., Effect of Crosslinking on the Elasticity of Polyelectrolyte Multilayer Films Measured by Colloidal Probe AFM. *Microsc. Res. Tech.* **2006**, *69*, 84-92.
46. Trenkenschuh, K.; Erath, J.; Kuznetsov, V.; Gensel, J.; Boulmedais, F.; Schaaf, P.; Papastavrou, G.; Fery, A., Tuning of the Elastic Modulus of Polyelectrolyte Multilayer Films Built Up from Polyanions Mixture. *Macromolecules* **2011**, *44*, 8954-8961.
47. Panayotov, I. V.; Collart-Dutilleul, P. Y.; Salehi, H.; Martin, M.; Vegh, A.; Yachouh, J.; Vladimirov, B.; Sipos, P.; Szalontai, B.; Gergely, C.; Cuisinier, F. J. G., Sprayed Cells and Polyelectrolyte Films for Biomaterial Functionalization: The Influence of Physical PLL-PGA Film Treatments on Dental Pulp Cell Behavior. *Macromol.Biosci.* **2014**, *14*, 1771-1782.
48. Zaroslov, Y. D.; Philippova, O. E.; Khokhlov, A. R., Change of Elastic Modulus of Strongly Charged Hydrogels at the Collapse Transition. *Macromolecules* **1999**, *32*, 1508-1513.
49. Naficy, S.; Kawakami, S.; Sadegholvaad, S.; Wakisaka, M.; Spinks, G. M., Mechanical Properties of Interpenetrating Polymer Network Hydrogels Based on Hybrid Ionically and Covalently Crosslinked Networks. *J. Appl. Polym. Sci.* **2013**, *130*, 2504-2513.
50. Richert, L.; Engler, A. J.; Discher, D. E.; Picart, C., Elasticity of Native and Cross-Linked Polyelectrolyte Multilayer Films. *Biomacromolecules* **2004**, *5*, 1908-1916.
51. Adebahr, J.; Johansson, P.; Jacobsson, P.; MacFarlane, D. R.; Forsyth, M., Ab Initio Calculations, Raman and NMR Investigation of the Plastic Crystal Di-Methyl Pyrrolidinium Iodide. *Electrochim. Acta* **2003**, *48*, 2283-2289.
52. Koda, S.; Nomura, H.; Nagasawa, M., Raman Spectroscopic Studies on the Interaction Between Counterion and Polyion. *Biophys. Chem.* **1982**, *15*, 65-72.
53. Cranford, S. W.; Ortiz, C.; Buehler, M. J., Mechanomutable Properties of a PAA/PAH Polyelectrolyte Complex: Rate Dependence and Ionization Effects on Tunable Adhesion Strength. *Soft Matter* **2010**, *6*, 4175-4188.
54. Alonso, T.; Irigoyen, J.; Iturri, J. J.; Larena, I. L.; Moya, S. E., Study of the Multilayer Assembly and Complex Formation of Poly(Diallyldimethylammonium Chloride) (PDADMAC) and Poly(Acrylic Acid) (PAA) as a Function of pH. *Soft Matter* **2013**, *9*, 1920-1928.
55. Snyder, R. G.; Hsu, S. L.; Krimm, S., Vibrational Spectra in the C-H Stretching Region and the Structure of Polymethylene Chain. *Spectrochim. Acta A* **1978**, *34*, 395-406.
56. Frisch, M. J.; Trucks, G. W.; Schlegel, H. B.; Scuseria, G. E.; Robb, M. A.; Cheeseman, J. R.; Scalmani, G.; Barone, V.; Mennucci, B.; Petersson, G. A. *et al.* Gaussian 09, Revision B.01. In Wallingford CT, 2009.
57. Becke, A. D., Density-Functional Thermochemistry. III. The Role of Exact Exchange. *J. Chem. Phys.* **1993**, *98*, 5648-5652.
58. Lee, C.; Yang, W.; Parr, R. G., Development of the Colle-Salvetti Correlation-Energy Formula Into a Functional of the Electron Density. *Phys. Rev. B* **1988**, *37*, 785-789.
59. Merrick, J. P.; Moran, D.; Radom, L., An Evaluation of Harmonic Vibrational Frequency Scale Factors. *J. Phys. Chem. A* **2007**, *111*, 11683-11700.



60. Litmanovich, E. A.; Chernikova, E. V.; Stoychev, G. V.; Zakharchenko, S. O., Unusual Phase Behavior of the Mixture of Poly(Acrylic Acid) and Poly(Diallyldimethylammonium Chloride) in Acidic Media. *Macromolecules* **2010**, *43*, 6871-6876.
61. Wang, Q. F.; Schlenoff, J. B., The Polyelectrolyte Complex/Coacervate Continuum. *Macromolecules* **2014**, *47*, 3108-3116.

## SUPPORTING INFORMATION

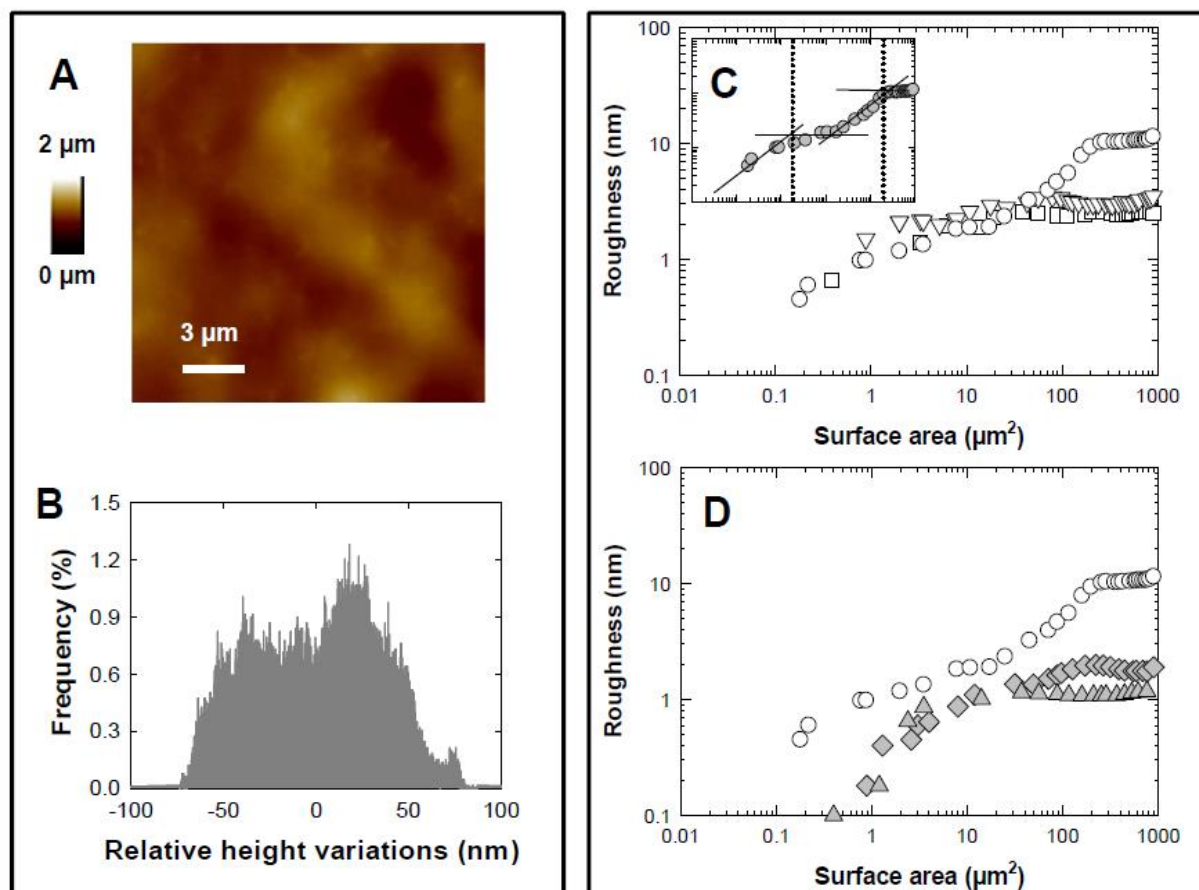


**Figure S1. Morphological analysis of the freshly built film.**

(A) AFM topographic image of (PDADMAC-PAA)<sub>30</sub> film over a  $15 \times 15 \mu\text{m}^2$  surface area before scratching. (B) Statistical distribution of the relative height variations under conditions of panel A. The reported height is relative to a mean *z*-position defined at the very film surface. (C) Evolution of the high-frequency surface roughness with surface area for the freshly built film (circles), for 1-day old (down triangles) and 5-days old films (squares). The inset highlights the two-steps increase of the surface roughness with increasing the surface area of freshly built films (see text for further details). (D) Evolution of the high-frequency surface roughness with surface area for the freshly built film (white circles), for films subjected to 1 h heating (grey diamonds) and 6 h heating (grey up triangles).

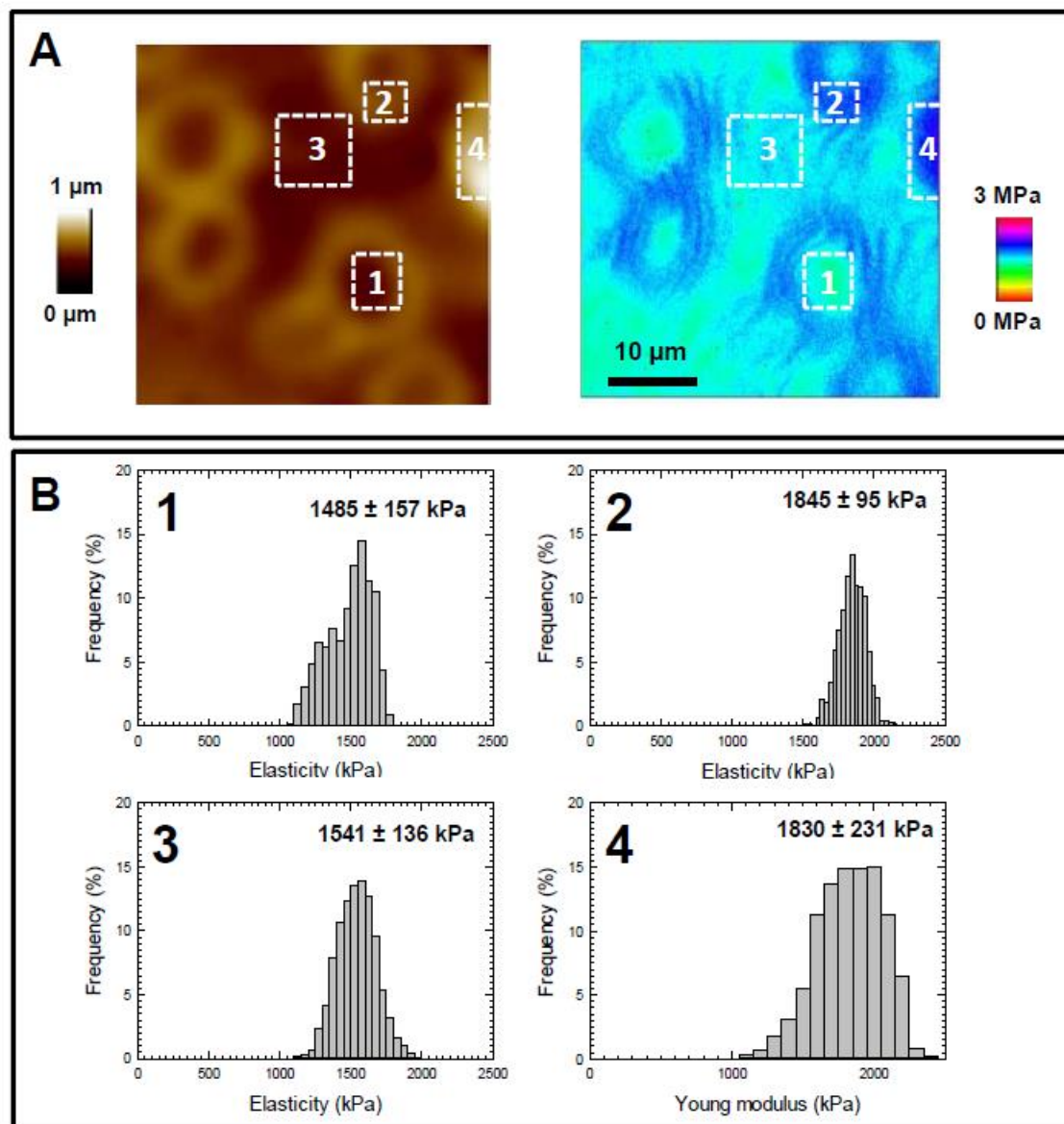


**Figure S2. Detailed analysis of mechanical heterogeneities of a freshly built (PDADMAC-PAA)<sub>30</sub> film.**

(A) Typical AFM topographic image and Young modulus map for freshly built (PDADMAC-PAA)<sub>30</sub> film, and (B) statistic distributions of Young modulus collected in regions 1, 2, 3 and 4 of panel (A) corresponding to donut-like structures and surroundings.

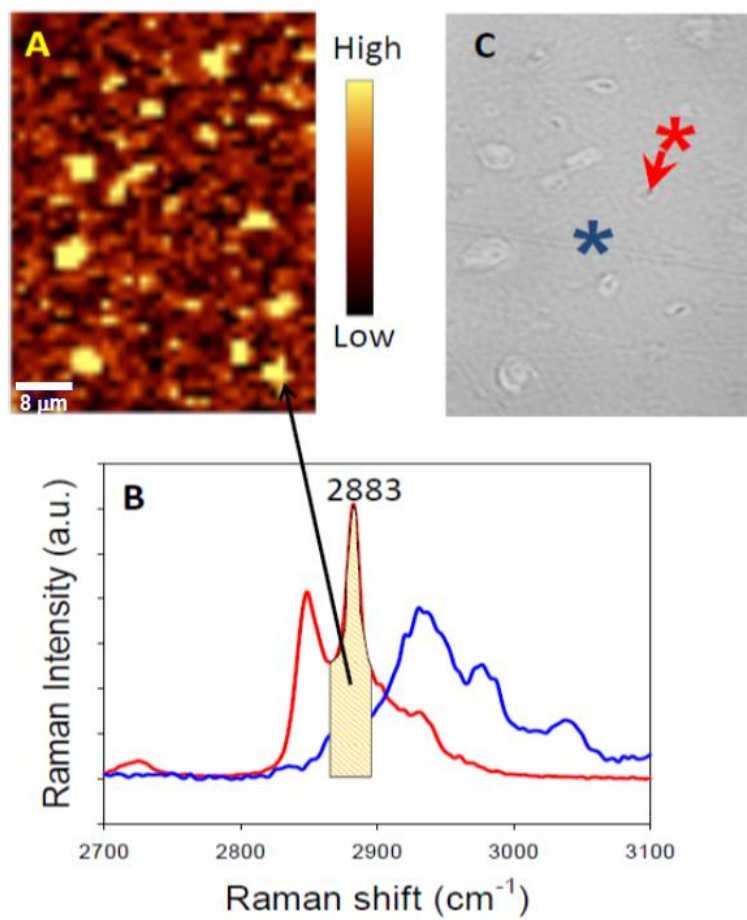


**Figure S3. Confocal Raman spectroscopic mapping of donut-like structures in freshly built (PDADMAC-PAA)<sub>30</sub> film.**

(A) Representative spatially-resolved Raman spectra recorded for a freshly built (PDADMAC-PAA)<sub>30</sub> film and constructed from (B) the spatial mapping of the integrated 2883 cm<sup>-1</sup> band intensity. (C) Corresponding optical microscopy image where the reflecting (donut) structures and surroundings are marked by red and blue asterisks, respectively. In panel (B), Raman spectra are provided in the 2700-3100 cm<sup>-1</sup> wavenumber range for the film domains outside (blue line) and inside (red line) the donut structures, and the integrated 2883 cm<sup>-1</sup> band is highlighted by the vertical yellow shaded bar.

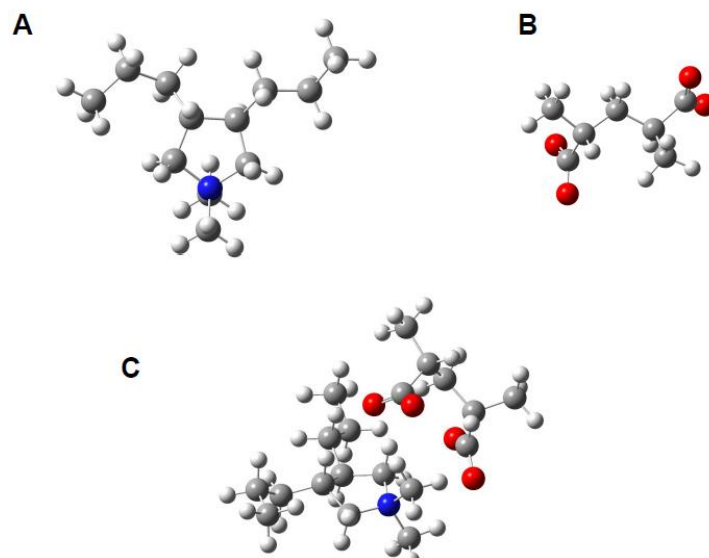


**Figure S4.** Representative snapshots of DFT-derived structures for (A) PDADMAC, (B) PAA and (C) PDADMAC-PAA complexes (see main text for further details).

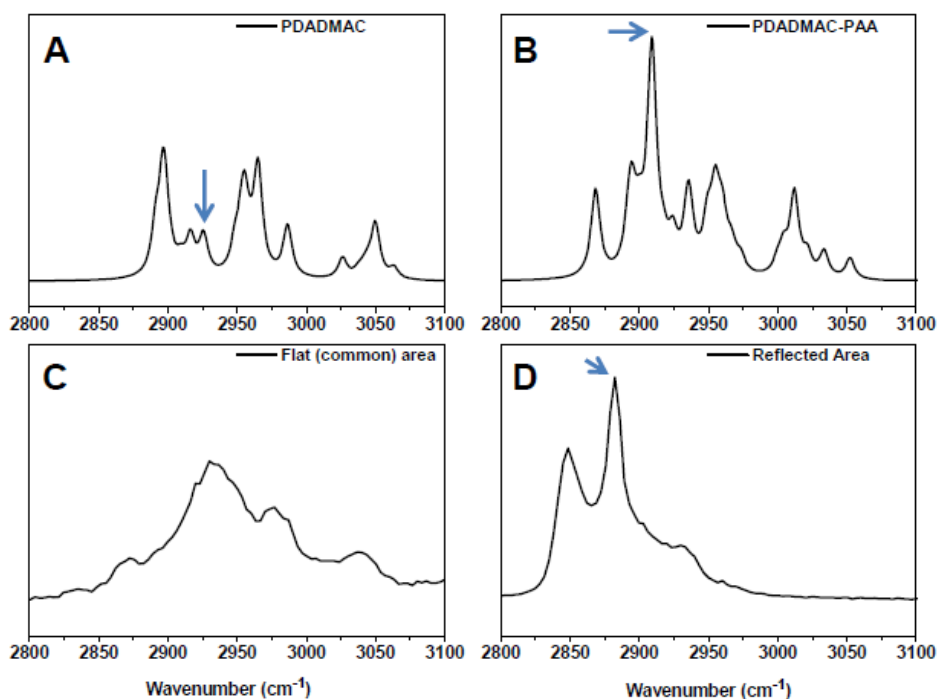


**Figure S5.** Comparison between DFT-derived and experimentally measured Raman spectra.

DFT-derived Raman spectra for pure PDADMAC (A), PDADMAC-PAA complex (B) and comparison with Raman spectra experimentally determined outside (C) and in (D) the donut-like structures. Arrows indicate increase of CH-stretching mode in PDADMAC-PAA complexes as compared to pure PDADMAC case.

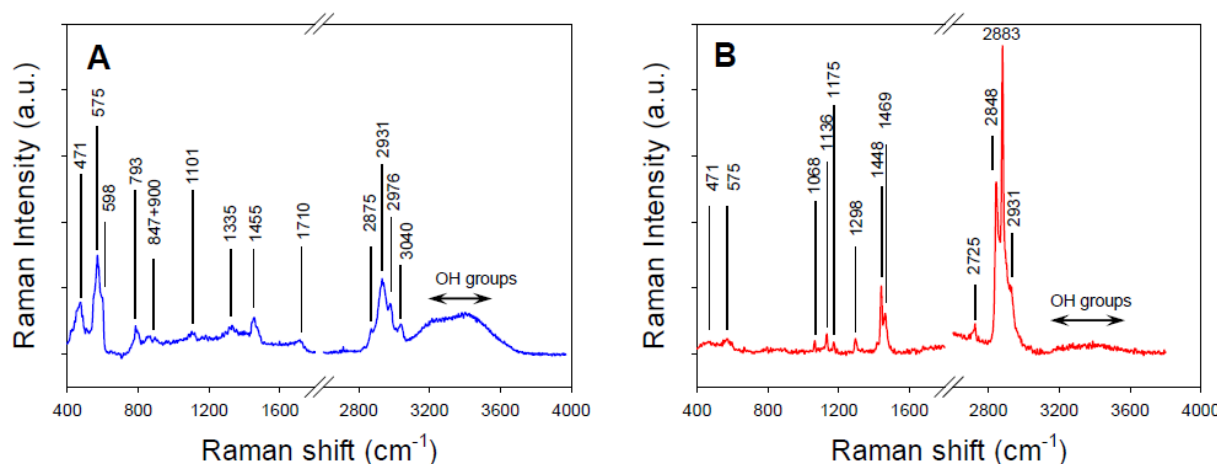


**Figure S6. Raman spectra measured for a 22-day old (PDADMAC-PAA)<sub>30</sub> film.**

(A) Typical Raman spectrum measured for fully relaxed (PDADMAC-PAA)<sub>30</sub> film (blue line) and corresponding indexation of the vibration bands (see further details in Table 1). (B) Raman spectrum measured on the laser heated/printed region of the 22-days old (PDADMAC-PAA)<sub>30</sub> film pictured in Figure 8C.

### Thermodynamic stability evaluation of PDADMAC-PAA complex.

The rigorous evaluation of the interaction energy between solvated PAA chains and PDADMAC polymer would require a computational effort that is beyond the scope of the current work. Rather, it is possible to qualitatively estimate the nature of this interaction by looking at the interaction energy between their constituent monomers. The model chosen for PAA is the acetate molecule  $\text{Me-COO}^-$ , labeled A hereafter, and we adopted for PDADMAC the 1,1-dimethylpyrrolidinium  $(\text{Me})_2\text{N}(\text{C}_4\text{H}_8)^+$  molecule, labeled B hereafter. The calculation of searched enthalpies has been performed at the DFT level (B3LYP/6-311++G(d,p)), as outlined in the main text. The basis set superposition error (BSSE) has been computed through a counterpoise correction.<sup>1,2</sup> The number of explicit water molecules taken into account to evaluate the interaction with the solvent was increased gradually until completion of the first hydration shell for each monomer. The results are collected in **Table S1**.

Species	$\Delta H$ (Ha)	kJ.mol <sup>-1</sup>
A	-228.654	
B	-291.535	
A-B + BSSE	-520.191	
$E^{\text{int}}(\text{A-B}) = [\text{A-B+BSSE}] - (\text{A} + \text{B})$	-0.003	-6.60
A(H <sub>2</sub> O) <sub>6</sub> + BSSE	-687.350	
B(H <sub>2</sub> O) <sub>3</sub> + BSSE	-520.855	
6 H <sub>2</sub> O	-458.679	
3 H <sub>2</sub> O	-229.332	
$E^{\text{int}}(\text{A(H}_2\text{O)}_6) = [\text{A(H}_2\text{O)}_6 + \text{BSSE}] - 6 \text{ H}_2\text{O}$		
A	-0.017	-45.45
$E^{\text{int}}(\text{B(H}_2\text{O)}_3) = [\text{B(H}_2\text{O)}_3 + \text{BSSE}] - 3$		
H <sub>2</sub> O - B	0.012	32.25
$E^{\text{int}}(\text{A(H}_2\text{O)}_6) + E^{\text{int}}(\text{B(H}_2\text{O)}_3)$	-0.005	-13.21

**Table S1.** DFT evaluations of PDADMAC-PAA stability with and without account of water molecules. ‘ a’ corresponds to ‘ artree’. See text for further details.

In the absence of water molecules, the interaction between monomers is thermodynamically favorable even though the stabilization of the formed complex is rather small (-6.60 kJ.mol<sup>-1</sup>). When water molecules are added, it appears that PAA monomer is strongly stabilized (-45.45 kJ.mol<sup>-1</sup>) while PDADMAC monomer is not (+32.25 kJ.mol<sup>-1</sup>). This result might seem surprising as it is clear that PDADMAC is water soluble. It must be pointed out, however, that the here-computed interaction energy does not directly correspond to a solvation energy as it does not take into account the solvation of the counter ions. After summation, it comes that the stable state corresponds to PDADMAC separated from deprotonated and hydrated PAA molecules (-13.21 kJ.mol<sup>-1</sup>).

## References.

1. Boys, S. F.; Bernardi, F. The Calculation of Small Molecular Interactions by the Differences of Separate Total Energies. Some Procedures with Reduced Errors. *Mol. Phys.* **1970**, *19*, 553-566.
2. Simon, S.; Duran, M.; Dannenberg, J. J. How Does Basis Set Superposition Error Change the Potential Surfaces for Hydrogen-Bonded Dimers? *J. Chem. Phys.* **1996**, *105*, 11024.



## **Chapter V**

### **Loading of (PDADMAC-PAA) Multilayer Films with PAMAM G6.5 Nanodendrimers**

The remarkable high diffusivity of exponentially growing multilayer thin films constructed by LBL technique [1, 2] motivated their potential use as gel-like host reservoirs for a broad variety of (bio)molecules and particles [3, 4]. In line with this idea, several studies in literature identified exponential (PDADMAC – PAA) films as suitable systems for the successful loading of nanoparticles and macromolecules [4, 5]. Interestingly, these nanostructured films can reversibly host and release charged nanoparticles from/to surrounding aqueous solution. The uptake/release kinetics was mostly addressed as a function of the medium physicochemical properties, which includes pH, solution ionic strength and particles concentration, and the impact of films structural properties were -to some extent- also analyzed (*e.g.* film thickness, nature and charge of the top layer, etc.). However, the effect of films elasticity on particle loading efficiency has received lesser attention despite the key role it plays in governing the incoming/outcoming particle flux at the very particle/solution interphase and within the bulk film. In this chapter, we present preliminary data on the dependence of Young's modulus of (PDADMAC – PAA)<sub>30</sub> films on loading with G6.5 PAMAM dendrimers (diameter below 10 nm). First, the ability of the constructed (PDADMAC – PAA)<sub>30</sub> films to host G6.5 PAMAM nanodendrimers is discussed under pH conditions corresponding to poorly and completely charged PAA polyanion component. Then, the modulation of film elasticity and surface morphology after particle loading is discussed as a function of the concentration of the dendrimer nanoparticles in bulk exposure media. These results provide insights into the film elasticity properties required for a successful loading of dendrimers nanoparticles. In addition, they will serve as guidelines for the design of more complete and systematic experiments (see Conclusion Chapter) aimed at detailing the molecular mechanisms underlying the trapping kinetics and possibly the release of nanodendrimers. In that respect, both (PDADMAC – PAA)<sub>30</sub> films and nanodendrimers exhibit highly tunable physicochemical properties, either in terms of structure dynamics (see Chapter 4) and/or electrostatics (see Chapter 3), which will be helpful for tailoring different film-dendrimer loading/interaction configurations and therewith for identifying key functional film/dendrimer characteristics compatible with proper film reservoir functioning.

### V.1. Characterization of (PDADMAC-PAA) films

A prerequisite for an efficient use of the films as reservoirs of nanodendrimers is the understanding of their basic physicochemical and structural properties (Chapter 4). Prior to any attempts for loading (PDADMAC-PAA) films with nanodendrimers, the mechanical and surface properties of the films were measured under *e.g.* different pH and ionic strength conditions adopted for their construction (the changed pH refers to that selected for dispersion of the PAA film component, see Chapter 2). The purpose, *in fine*, is to prepare a multilayer film with sufficiently large thickness to allow for the diffusion of particles inside the films matrix. Previous constructions of (PDADMAC – PAA) films showed that a thickness of  $\sim 1.5\ \mu\text{m}$  was adequate for 20 nm  $\text{TiO}_2$  nanoparticles to diffuse into the film [4,5]. After several experimental trials that consisted in constructing multilayer films with 10, 20 and 30 bilayers (PAA solution at pH 3, PDADMAC solution at pH 6, 10mM  $\text{NaNO}_3$  solution), and after referring to literature, we selected (PDADMAC – PAA)<sub>30</sub> because of its corresponding thickness *a priori* compatible with nanoparticles loading. In addition, in an attempt to construct smooth films with homogeneous surface, different ratios of polyelectrolyte solutions concentrations (1:1, 1:2, etc.) were tested. A combination of 3 mg/ml for the polyanion and 5mg/ml for the polycation leads to smooth homogeneous film surfaces (once relaxed).

However, (PDADMAC – PAA) constructed at pH = 3 (Figure 5.1) showed a remarkably high young modulus ( $\sim 1.6\ \text{MPa}$ ) as extensively detailed in Chapter 4, thus reflecting a high film rigidity, which could potentially limit their use as reservoirs for hosting nanodendrimers. For the sake of illustration, molecular film rigidity (and film surface charge) was reported to be a key parameter that determines the possibility of long axial nanocolloids to “bore into” exponential L / L films [6]. On the basis of the results reported in Chapter 4, it is worth mentioning that (PDADMAC – PAA) constructed under the above conditions undergoes structural relaxation upon heating at 60°C and a Young modulus of  $\sim 300\ \text{kPa}$  is reached after 6 hours of heating. Attempts to load (PDADMAC – PAA) film that were subjected to 6 hours heating treatment (Figure 5.2), with G6.5 at 0.5 g/L revealed no change in terms of film Young modulus after loading as compared to values for unloaded films, which suggests that a film rigidity of 300 kPa acts as a barrier for G6.5 uptake. As a result, alternative films were prepared under different pH and salt conditions in order to reach

a minimum elasticity that makes it possible for the particles to incorporate into the multilayers.

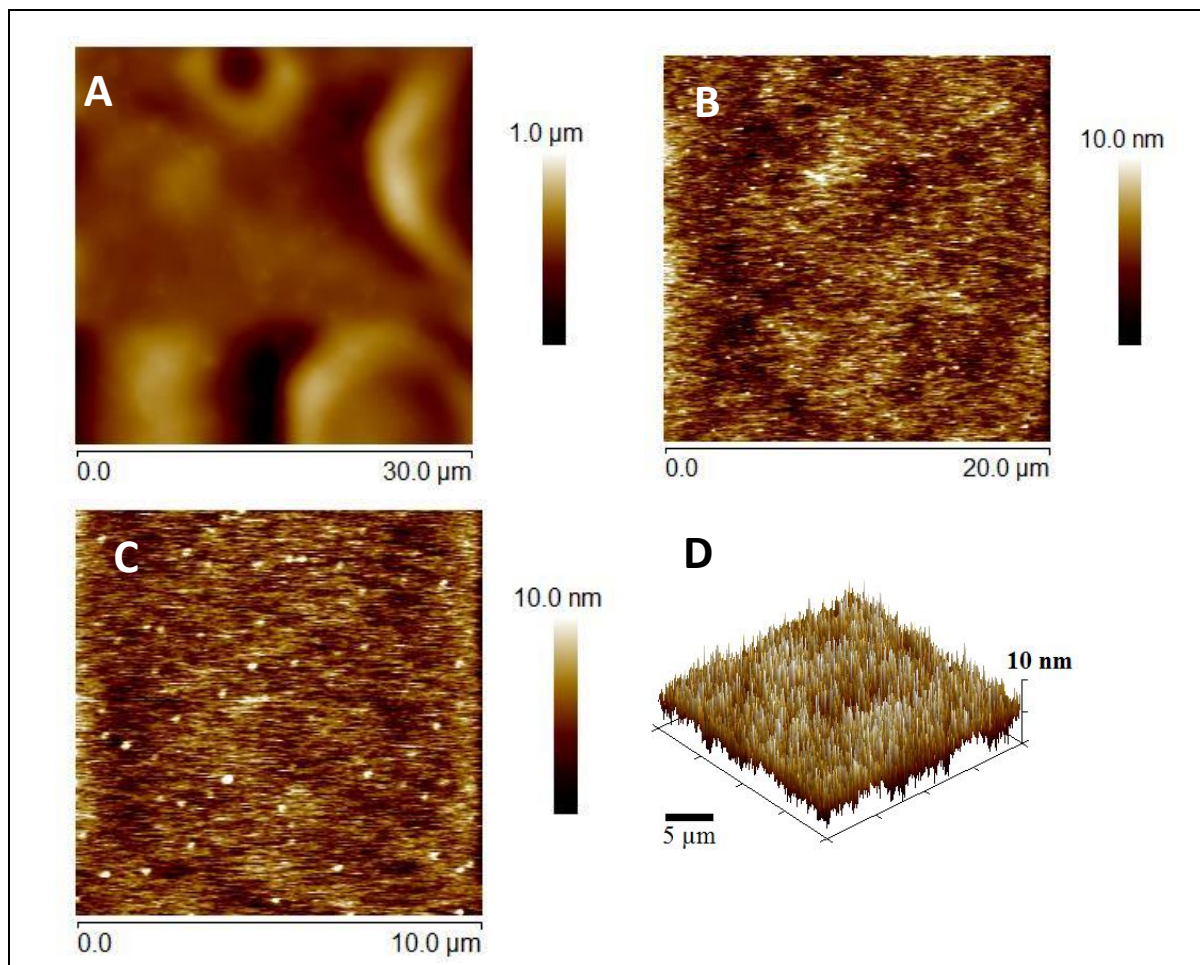


**Figure 5.67.** (PDADMAC – PAA)<sub>30</sub> at pH=3 (pH of PAA solution adjusted with HCl, see Chapter 2, and 10mM NaNO<sub>3</sub>) (A) native films; (B), (C), and (D): films after exposure to 0.5 g/l G6.5 solution for 24 hrs

Indeed, as multilayer thin films involving weak polyelectrolytes may exhibit a wide range of thickness and Young modulus values when assembled under different pH and ionic strength conditions, (PDADMAC – PAA) films were constructed at pH = 3 (that refers to PAA solution, recalling that PDADMAC is kept at pH 6 during construction) but at a solution ionic strength of 50 mM and 100 mM. Despite the exponential growth of (PDADMAC – PAA) films, this increase in ionic strength did not lead to significant change in film thickness compared to that achieved in 10 mM NaNO<sub>3</sub> solution (Figure 5.). These results thus indicate that under acidic pH conditions where PAA is poorly charged, film swelling hardly depends on solution ionic strength.

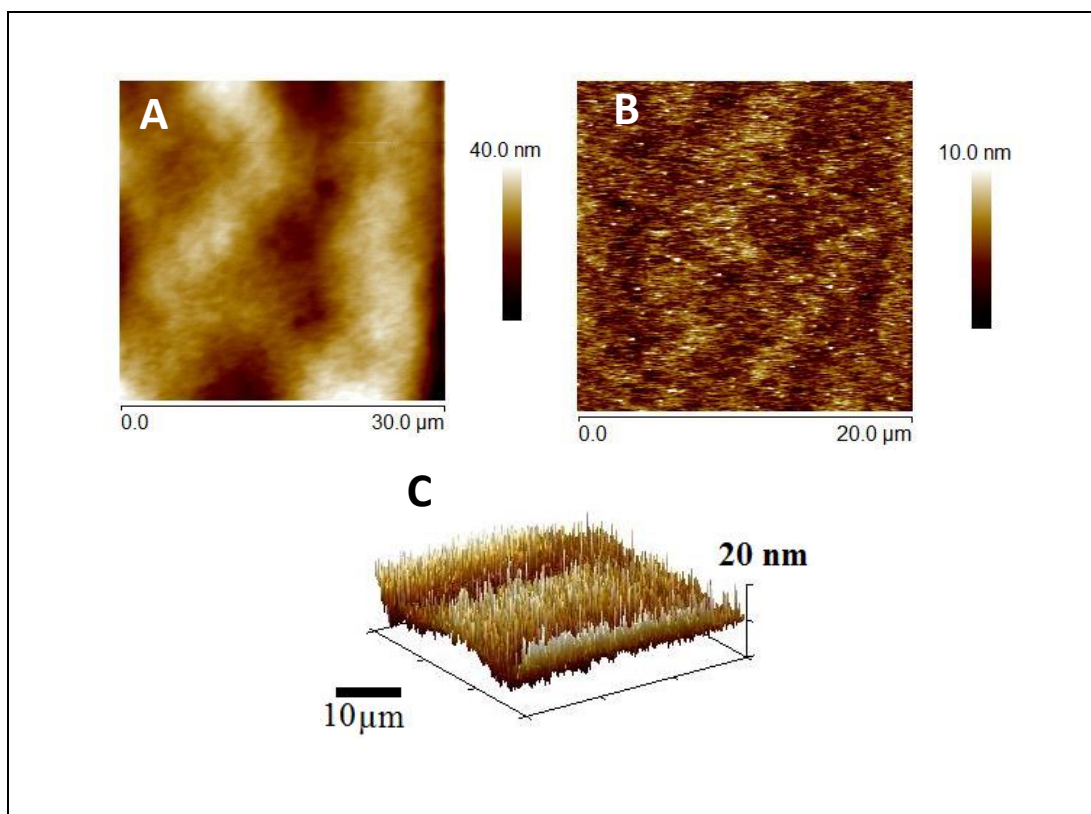


**Figure 5.68.** (PDADMA - PAA)<sub>30</sub> at pH=3 after 6 hours of heating (60°C) (A) unloaded films; (B) and (C): films loaded with G6.5 ( 0.5 g/L solution, 24 hrs exposition time).

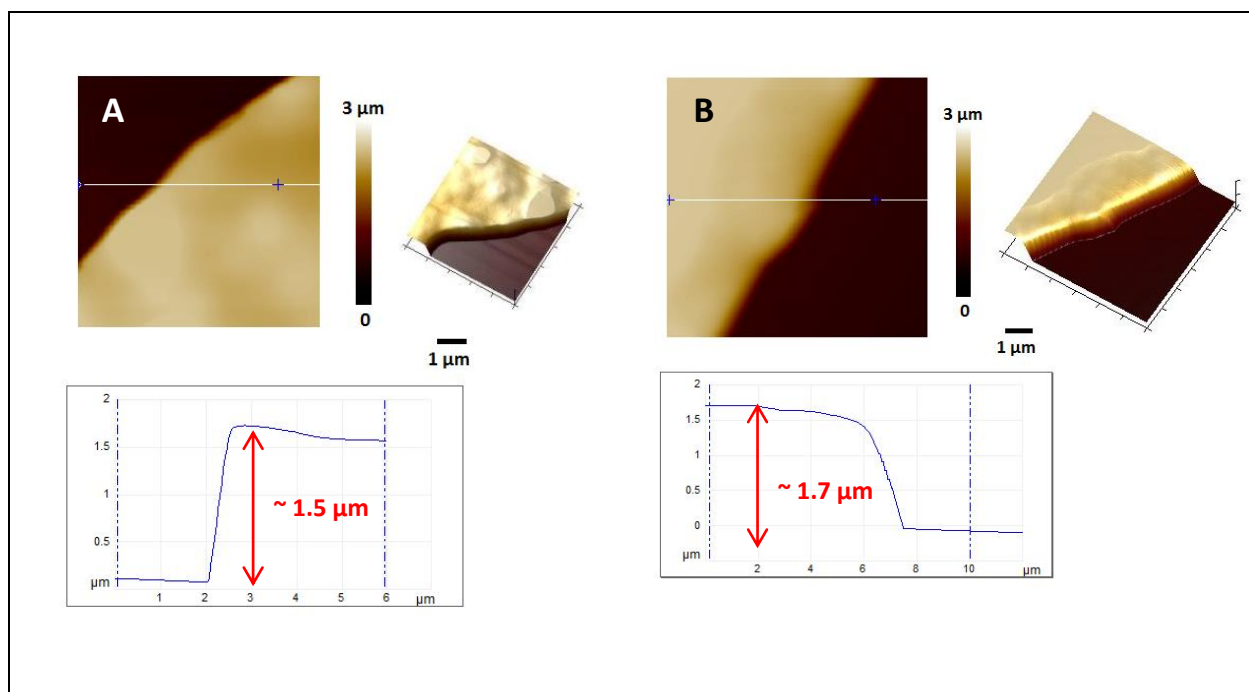


**Figure 5.3.** Thickness of (PDADMA - PAA)<sub>30</sub> films constructed with PAA solution @ pH=3 and (A) 50 mM and (B) 100 mM NaNO<sub>3</sub> concentration.

On the contrary, when assembled using PAA solution brought to  $pH = 6$  (other construction parameters: 10 mM  $NaNO_3$ , pH 6 for PDADMAC solution, 3 mg/ml PAA, 5 mg/ml PDADMAC), the film undergoes an extensive swelling with a thickness of *ca.* 4.5  $\mu m$  (Figure 5.). This increase in film thickness (compared to that achieved at pH 3) results from the increase in PAA charge, which is accompanied by an increase of the hydrophilicity of the film and a larger uptake of water from surrounding solution. In line with this, the hydrophobic pockets evidenced in Chapter 4 at pH 3 disappear, which originates the smooth aspect of the films surface and the absence of the donut-like domains identified in Chapter 4. The above conditions were then selected to test the loading of G6.5 PAMAM nanodendrimers.

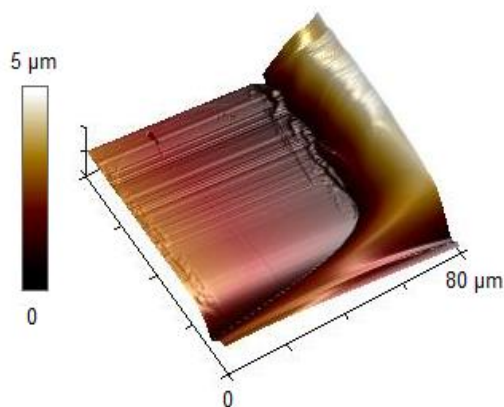


**Figure 5.4.** Thickness of  $(PDADMAC - PAA)_{30}$  at  $pH=6$  ( $pH$  of PAA solution adjusted with Tris buffer, see chapter 2) and  $NaNO_3$  10 mM

## V.2. Loading of the films with G6.5 PAMAM nanodendrimers

G6.5 PAMAM dispersions of 0.2, 0.5, 0.8 and 2 g/L concentrations were prepared in  $NaNO_3$  (10 mM) solution buffered with Tris-buffer at  $pH = 6$  (conditions that warrant particles suspensions stability against aggregation, see Chapter 3). For that purpose, required volumes of G6.5 from commercial suspensions were added to buffered  $NaNO_3$  solutions using a micropipette, and, when necessary, pH was further readjusted using HCl (0.1 M). For  $(PDADMAC - PAA)_{30}$  films to be loaded with nanodendrimers, the polyelectrolyte solutions were dissolved in  $NaNO_3$  solution (10 mM) buffered with Tris-buffer at  $pH = 6$  and concentrations of 3 g/L and 5 g/L for PAA and PDADMAC solutions were adopted,



respectively. The films were then assembled with use of an automated dipping robot and deposited on pre-cleaned borosilicate glass slides (1 × 2 × 1 mm) at room temperature. Each deposition cycle consisted of a 5 minutes step of polycation adsorption followed by two rinsing steps of 5 minutes each (using 10 mM NaNO<sub>3</sub> buffered with Tris-buffer at pH = 7.5),

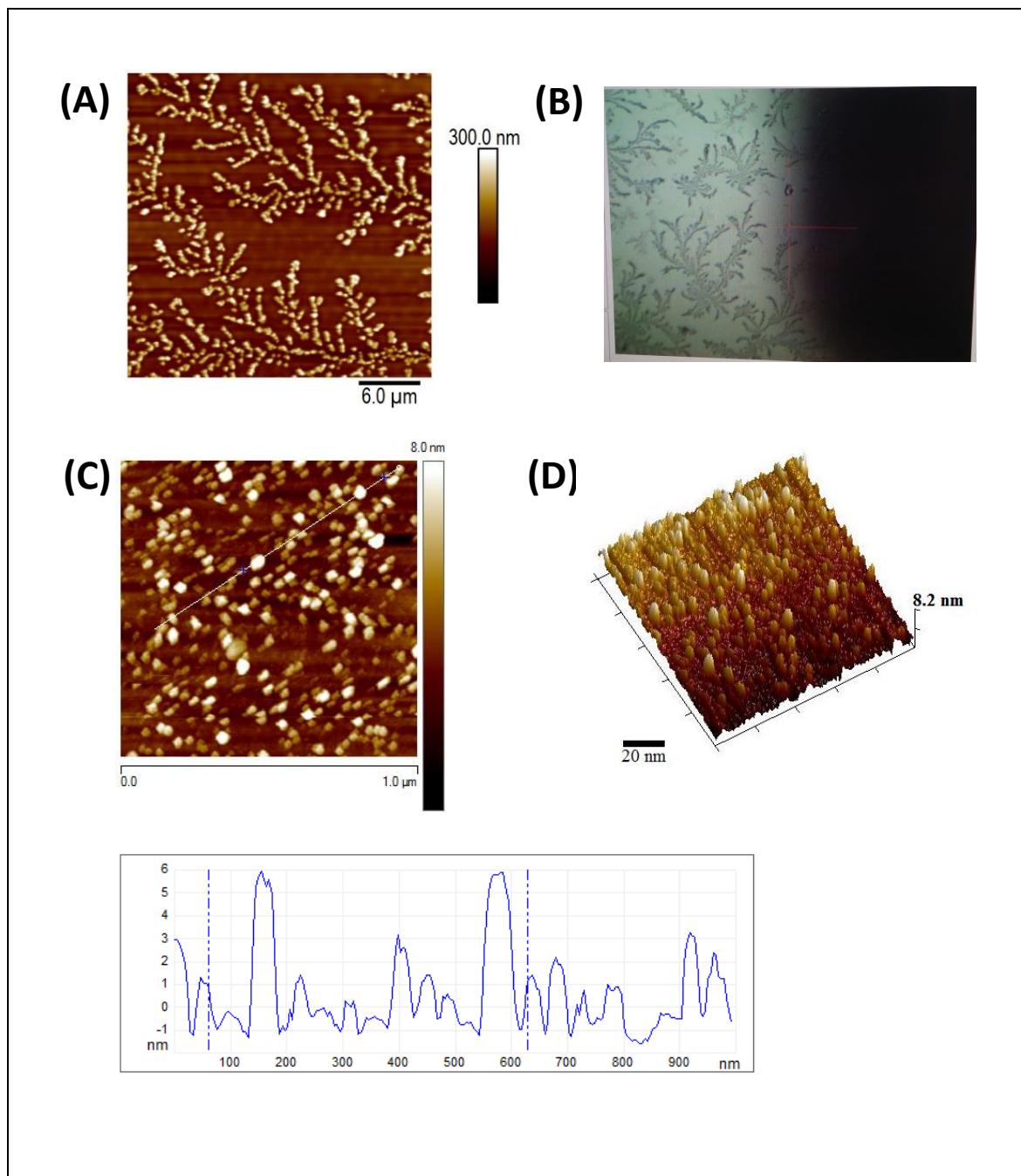


**Figure 5.5.** G6.5 immobilized on a glass substrate (image in air). (A) AFM height image (in air), (B) image captured by the AFM scanner camera, (C) Zoomed section showing G6.5 particle size (zoom of section located in between the fractal structures displayed in (A)), (D) 3-D film surface topography

then a 5 minutes step of polyanion adsorption, followed again by two rinsing steps. (PDADMAC-PAA)<sub>30</sub> films were used for loading experiments right after the end of deposition cycles without further physical and/or chemical treatments. G6.5 ( $8 \pm 1$  nm diameter) dendrimers were brought into contact with (PDADMAC – PAA)<sub>30</sub> films at room temperature for 24 hours in sterile wells (4 mL) prior to AFM experiments. Qualitative surface information was obtained by atomic force microscopy (PeakForce mode) *via* nanomechanical mapping experiments in liquid of (i) (PDADMAC – PAA)<sub>30</sub> films loaded with G6.5 at 0.2, 0.5, 0.8, and 2 g/L and (ii) control films (*i.e.* not loaded by G6.5 nanodendrimers). AFM analysis of deposits of dendrimers on glass slides (Figure 5.5) confirmed their nanometric dimensions, in line with dynamic light scattering measurements (Chapter 3). Imaging of these deposits was performed under air conditions, which explains the somewhat lower particles size compared to that measured in aqueous solution.

#### **V.2.1. Effect of G6.5 concentration on the morphology of (PDADMAC – PAA)<sub>30</sub> films**

Salloum and Schlenoff [7] suggested different modes of adsorption of nanoparticles into PEM films (Figure 5.). The adsorbed particles may form a uniform or island-like monolayer on the surface, form large aggregates above the surface, or diffuse into the film matrix with some particles remaining on the surface. AFM height images of films after loading with G6.5 0.2, 0.5, 0.8, and 2 g/L concentrations showed the absence of a G6.5 surface monolayer, but rather an island-like distribution with few large G6.5 clusters covering the multilayered surface (Figure 5.). Only few particles (or particle aggregates) resting on the P A M A C – PAA) surface can be detected. However, this is not necessarily an indication of successful incorporation of G6.5 into the films.



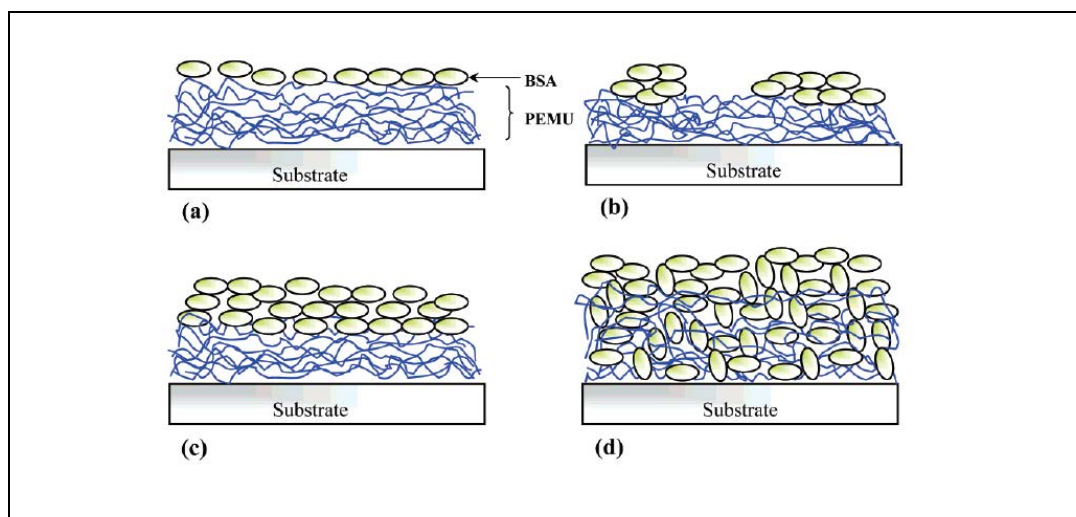


**Figure 5.6.** The different modes of adsorption of nanoparticles/molecules, as suggested by Salloum and Schlenoff [7], (a) and (b) schematically represent particles adsorbing to the surface either (a) uniformly (monolayer formation) or according to (b) island-like distribution, (c) this case represents the formation of aggregates on the surface, and (d) the sorption throughout bulk film

Furthermore, AFM topography images recorded at various scales showed that for all G6.5 concentrations tested, the film surface remained homogeneous without the presence of pores (Figure 5.), and with no changes in morphology as a whole, in roughness, and in film thickness (Figure 5.). In general, the evolution of a multilayer film thickness is an indication of the successful incorporation of particles into multilayer assemblies, but the absence of thickness variations (scenario met for our system) does not necessarily indicate the absence of incorporation. The well-dispersed and relatively small sized ( $\varnothing \sim 8$  nm) nanodendrimers incorporating into swollen, thick P A M A C – PAA) films with internal intra-molecular space to host the particles, may not cause any further film swelling or, at least, significant variations in film thickness.

At pH=6 and regardless of  $\text{NaNO}_3$  concentration (10 mM here), the electrophoretic mobility of G6.5 is predominantly determined by the strongly dissociated surface carboxylic groups (Chapter 3). The outermost layer of the P A M A C – PAA) film is a thick layer of negatively charged polyanion PAA. While the general picture suggests a major role of electrostatic interactions for nanocolloids and macromolecules incorporation in exponential PEM films with a key effect of the sign of the outermost layer, it is clear that the negatively charged G6.5 still adsorb on our like-charged PDADMAC-PAA film surface. As a result, it could be argued that non-electrostatic interactions play a major role in this adsorption step or at least in the initiation of the adsorption process.

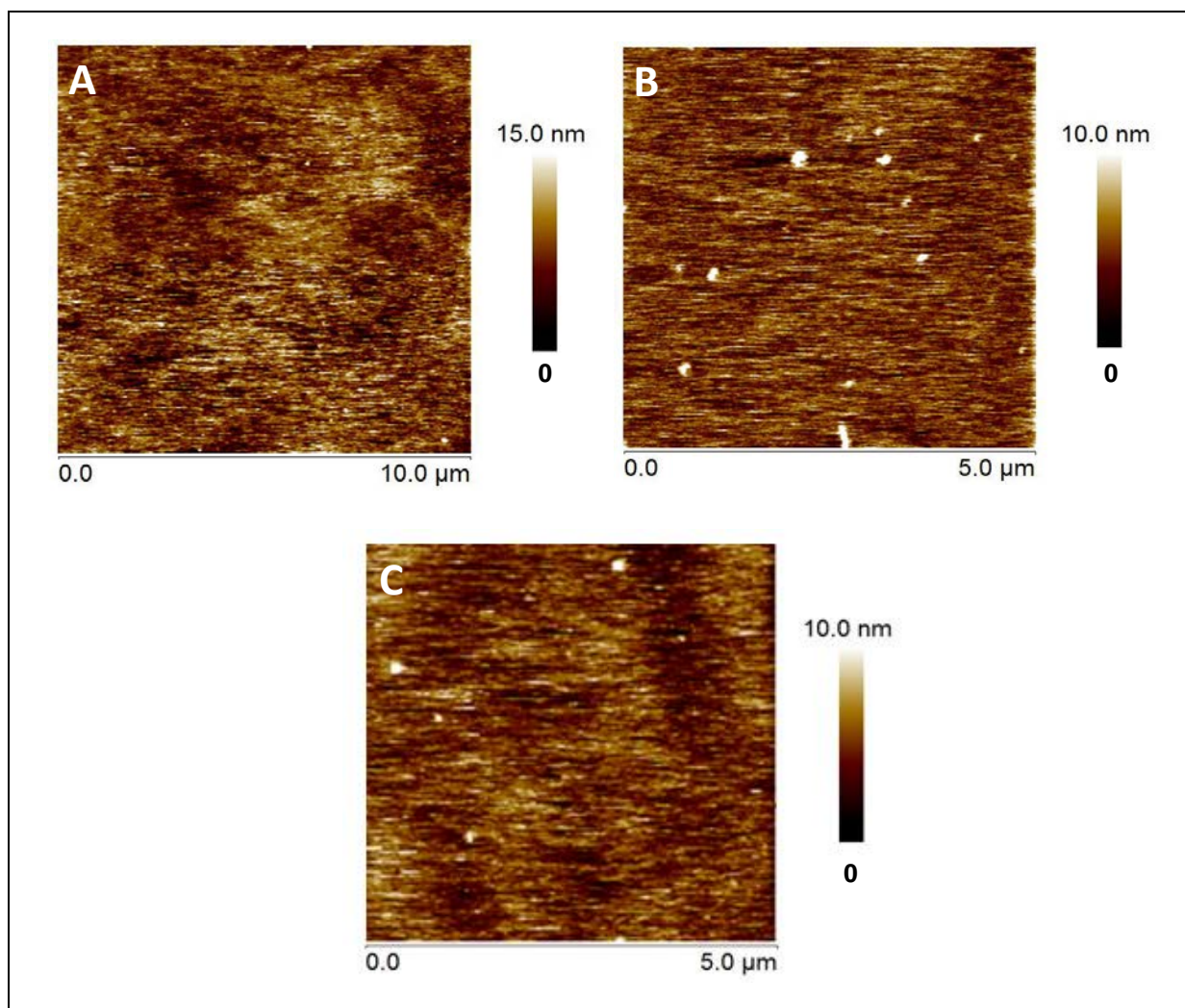


**Figure 5.7.** Effect of G6.5 concentration on the morphology of (PDADMAC-PAA)<sub>30</sub> films; (A) Control films, (B) Films loaded with 0.5 g/L G6.5, and (C) films loaded with 0.8 g/L G6.5.

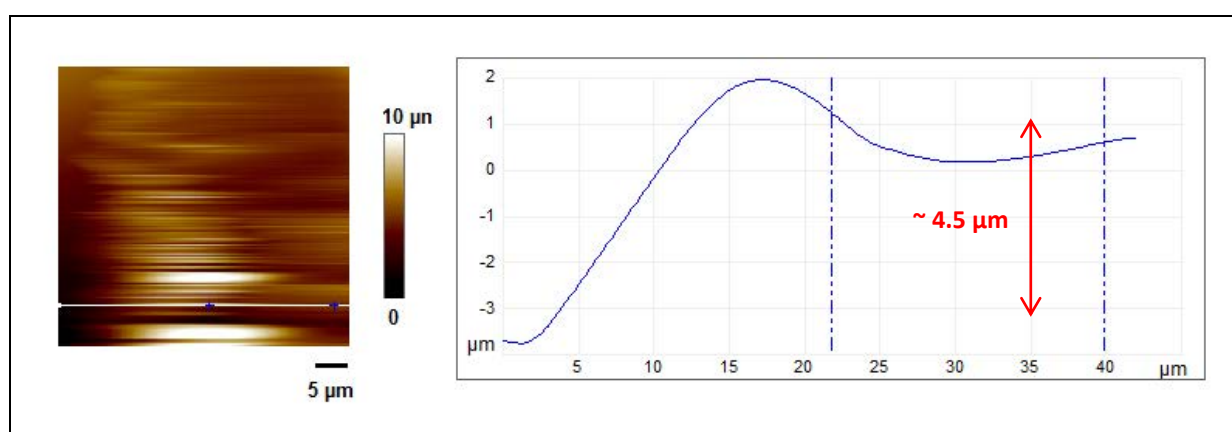


**Figure 5.8.** (Left) Surface topography in AFM contact mode for (PDADMAC – PAA)<sub>30</sub> loaded with 0.2 g/L G6.5 dendrimers; Right: section of the same film showing a thickness of 4.5 μm.

### V.2.2. Effect of G6.5 concentration on Young modulus of (PDADMAC – PAA)<sub>30</sub> films

AFM force measurements were performed on unloaded and loaded films and led to the force *versus* indentation curves displayed in Figure 5.. Young Modulus data were derived from Sneddon's model valid for a conical indenter, as mentioned in preceding Chapters. The evolution of the force *versus* indentation curves with particles concentration in exposure medium shows an apparent increase in film rigidity after loading with G6.5 dendrimers. However, the rigidity increases in a non-monotonous manner, which is transparent from the elasticity distribution (Figure 5.11).

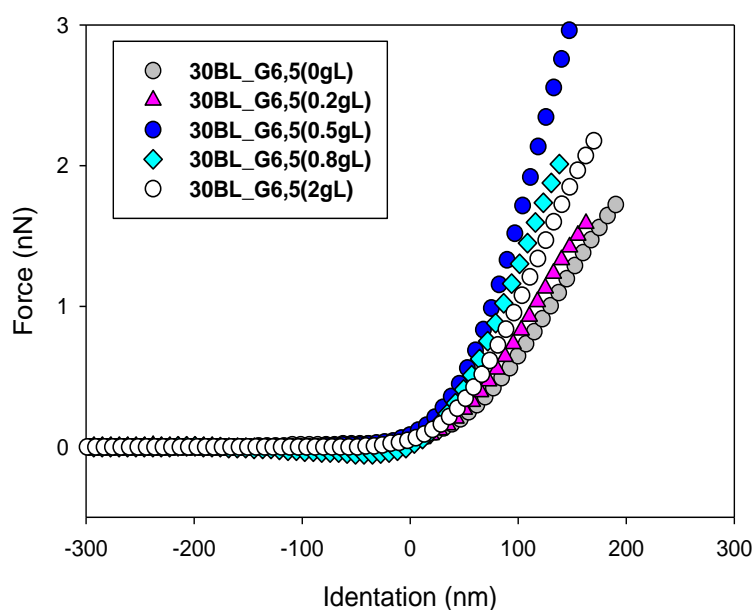


**Figure 5.9.** Force-indentation curves on (PDADMAC-PAA)<sub>30</sub> loaded with G6.5 present in different concentrations (indicated) in the exposure medium

A Young modulus of *ca.*  $80 \pm 5$  kPa is measured for unloaded films. This value is about 4 times lower than that achieved with fully relaxed films prepared from PAA solution at pH 3 (Chapter 4), thereby evidencing the crucial role played by pH in governing overall film structure. With increasing G6.5 concentration from 0 to 0.5 g/L, films modulus increases from 80 kPa to  $\sim 165$  kPa, which reflects a significant film rigidification. Upon further increase of G6.5 concentration to 0.8 g/L and 2g/L, films becomes less rigid and modulus decreases down to  $\sim 110$  kPa, which is still 1.4 times larger than the value determined for unloaded films. The maximum of film elasticity evidenced in Figure 5.11 suggests a film reorganisation upon loading with particles. Obviously, assessment of this film reorganisation requires additional experiments aimed at probing the internal structure with techniques (*e.g.*

confocal microscopy, see Conclusions Chapter) other than AFM (that is essentially a surface technique suitable for probing changes in *effective* elasticity of the film as a whole). After entering the film matrix, diffusing G6.5 nanodendrimers probably become entrapped by a variety of interactions triggered by the different chemical functionalities of both the polymeric matrix and the incorporated nanodendrimers. This likely causes changes in the balance between electrostatic and non-electrostatic (*e.g.* hydrophobic) interactions (see resulting dramatic effects for unloaded films structure in Chapter 4) between constituting polyanionic and *resulting in fine to*

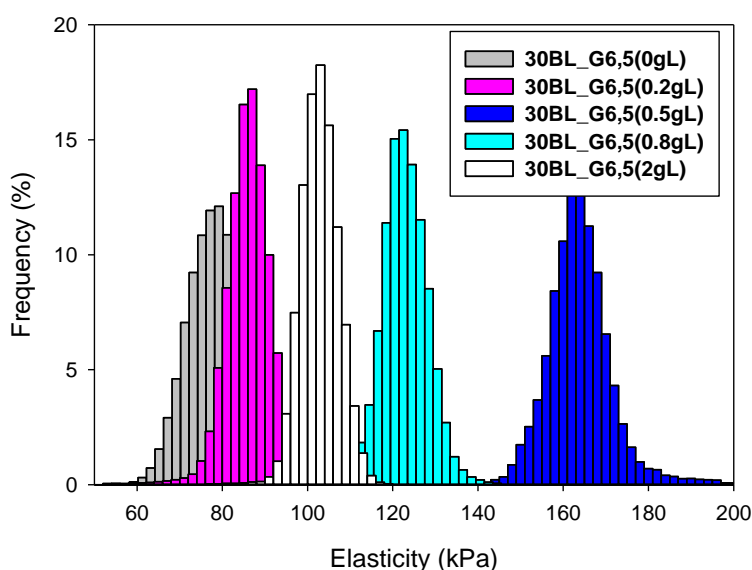


**Figure 5.10.** Distribution of Young Modulus (kPa) for (PDADMAC-PAA)<sub>30</sub> loaded with different concentrations of G6.5 nanodendrimers

an overall increase in films Young modulus for low to moderate G6.5 concentrations. The observation of an elasticity maximum with increasing G6.5 concentrations suggests that the aforementioned balance is inherently a function of the density of (negative) charges injected within the film. Solid conclusions about the origin of this maximum necessarily require, as stated above, a molecular analysis of the interaction forces operating in the polyphasic PAA/PDADMAC/dendrimers/water system. The above results essentially identify the G6.5 concentration and pH conditions where such an analysis should be conducted. In that respect, possible changes in local pH within the loaded film should be investigated, recalling that pH variations have a key impact on film structure and elasticity, as evidenced here for their unloaded counterparts from measured thickness and elasticity at pH 3 and pH 6 (pH of PAA solution). It could be that the increase in films elasticity at low G .5 c oncentrations ‘simply’

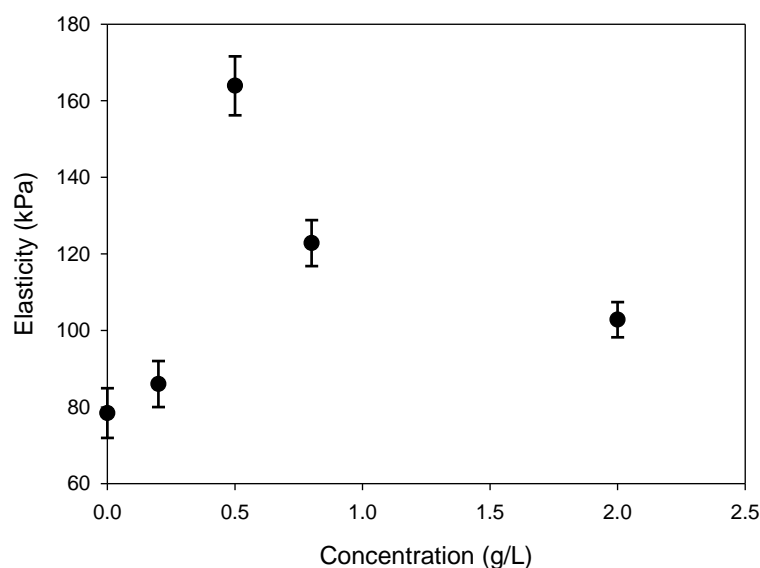


**Figure 5.11.** Variation of Young modulus as a function of G6.5 concentration

corresponds to film reinforcement with particles of rigid fractal architectures that are located in internal films pockets and that moderately modify PAA/PDADMAC interactions. At sufficiently large particle concentrations, where separation distance between PAA, PDADMAC and dendrimers necessarily gets shorter, it is likely that dendrimers significantly bind to PDADMAC and screen the interactions of the latter with PAA, thus resulting in films regions enriched with PDADMAC and in increased films elasticity (as compared to that for unloaded films), similarly to that occasioned by PDADMAC-enriched donut domains evidenced in Chapter 3. If the above scenario applies, then Figure 5.11 suggests that mechanisms operating at low and large particle concentrations increase films rigidity in a differentiated way.

### V.3. Conclusions

P A MA C – PAA) multilayer films are shown to be promising viable reservoirs for carboxylated PAMAM G6.5 nanodendrimers. The tunable film properties offer a convenient way to control the number of nanocontainers in the films and consequently their loading capacity. The loading of G6.5 nanodendrimers in exponential PEM films is effectively governed by a number of properties of the system, such as film rigidity and degree

of film swelling in a first place, as evidenced in this Chapter. The evolution of the mechanical properties of (PDADMAC – PAA)<sub>30</sub> films probed by AFM after loading with G6.5 nanodendrimers, can be used as an indicator for the ‘successful’ incorporation of the particles into the films and for the underlying polycation/polyanion chains structure modifications. Results reported here indicate that the absorption of G6.5 into the like-charged PEM surface is significantly driven by non-electrostatic interactions, and that the negatively-charged surface binding sites of G6.5 are not only directed to the cationic parts of the polyelectrolyte chains.

Further analysis is mandatory for deciphering the molecular processes governing the non-monotonous rigidification of the film upon increase of the particles concentration in solution. As an example, it could be informative to perform loading experiments with citrate pretreatment of the polycation prior to the incorporation of the particles. The polycation would then be stabilized inside the film, and the effects of nanodendrimers loading on films rigidity subsequently addressed. In addition, knowledge of the distribution of G6.5 in the 3D films matrix could be decisive for identifying processes governing the penetration of the particles inside the films. The effect of pH of the G6.5-containing exposure medium on the evolution of the structural and mechanical properties of (PDADMAC – PAA) films could be addressed as well. Analysis of the uptake and release kinetics of G6.5 together with corresponding films stability/rigidity over time are definitely routes to be explored for future investigations. Finally, evaluation of the fraction of loaded/released nanodendrimers appears to be necessary, which is possible *via* fluorescent labelling of the G6.5 nanoparticles and intra-film particles tracking with *e.g.* confocal laser scanning microscopy.

## References

- [1] Picart, C., Lavalle, P., Hubert, P., Cuisinier, F. J. G., Decher, G., Schaaf, P., Voegel, J.-C., (2001). Buildup Mechanism for Poly( L -lysine)/Hyaluronic Acid Films onto a Solid Surface. *Langmuir*, 17, 7414–7424.
- [2] Hübsch, E., Fleith, G., Fattisson, J., Labbé, P., Voegel, J. C., Schaaf, P., Ball, V., (2005). Multivalent Ion/Polyelectrolyte Exchange Processes in Exponentially Growing Multilayers. *Langmuir*, 21, 3664–3669.
- [3] Podsiadlo, P., Michel, M., Lee, J., Verploegen, E., Wong Shi Kam, N., Ball, V., Lee, J., Qi, Y., Hart, A. J., Hammond, P. T., Kotov, N. A., (2008). Exponential Growth of LBL Films with Incorporated Inorganic Sheets. *Nano Lett.*, 8, 1762–1770.
- [4] Srivastava, S., Ball, V., Podsiadlo, P., Lee, J., Ho, P., Kotov, N. A., (2008). Reversible Loading and Unloading of nanoparticles in ‘Exponentially’ Growing Polyelectrolyte LBL Films. *J. Am. Chem. Soc.*, 130, 3748–3749.
- [5] Ladhari, N., Hemmerle, J., Haikel, Y., Voegel, J.C., and Ball, V., (2010). Polyelectrolyte multilayer films: A sponge for insulin? *Biomed Mater Eng*, 20, 217–225.
- [6] Srivastava, S., Podsiadlo, P., Critchley, K., Zhu, J., Qin, M., Shim, B. S., Kotov, N. A., (2009). Single-Walled Carbon Nanotubes Spontaneous Loading into Exponentially Grown LBL Films. *Chem. Mater.*, 21, 4397–4400.
- [7] Salloum, D. S., Schlenoff, J. B., (2004). Protein Adsorption Modalities on Polyelectrolyte Multilayers. *Biomacromolecules*, 5, 1089–1096.

## Abstract

A detailed analysis of the physicochemical properties of engineered nanoparticles (NPs) is required to understand on a mechanistic level their interactions/potential toxicity with/towards biotic components of fresh water systems. Such an analysis is further mandatory to achieve a comprehensive evaluation and optimisation of the performance of (ultra)filtration methods developed to prevent NPs release into aquatic media. Within this context, the aim of this PhD thesis was to decipher the basic physico-chemical processes governing the loading of carboxylated-poly(amidoamine) (PAMAM-COOH) nanodendrimers -commonly employed in biomedical applications- into layer-by-layer assembled (poly(diallyl dimethyl ammonium) chloride-poly(acrylic acid))<sub>n</sub> ((PDADMAC-PAA)<sub>n</sub>) multilayer films. For that purpose, a systematic investigation of the electrohydrodynamic properties of PAMAM-COOH NPs was first performed as a function of pH and monovalent salt concentration in solution. On the basis of advanced electrokinetic theory for soft particles with zwitterionic functionality, it is demonstrated that the interfacial electrostatic features of the considered NPs are determined both by surface and bulk particle contributions to an extent that depends on electrolyte concentration. This leads to a remarkable NPs mobility reversal with changing monovalent salt concentration and to a marked dependence of the point of zero NPs mobility on electrolyte content. In addition, confrontation between experiments and theory further highlights how pH- and salt-mediated modifications of the NP particle structure affect dendrimer electrokinetic features at large pH and/or low salt concentrations. In a second part, the structure, morphology and mechanical properties of PDADMAC-PAA films, and their evolution over time under natural aging conditions or after thermal treatment, were addressed from atomic force microscopy (AFM) and Raman microspectroscopy analyses. Results evidence that PDADMAC-PAA multilayer films of exponential type exhibit mechanical and structural features that are typical for polyelectrolyte multilayer films with linear growth. In particular, their slow relaxation to equilibrium is accelerated after heating treatment at 60°C and, in line with density functional theory computation, this relaxation dynamics is shown to be intimately connected to instability of film domains rich in PDADMAC, depleted in water and marked by the presence of characteristic donut-like structures. In a final part, the reported dependence of PDADMAC-PAA multilayer films elasticity on concentration of nanodendrimers in bulk solution suggests that these complex multilayer films constitute a promising option to be further investigated for the loading and removal of carboxylated nanodendrimers from aqueous environments.

**Keywords:** Polyelectrolyte multilayer films, nanodendrimers, electrokinetics, nanomechanics, Atomic Force Microscopy

## Résumé

Une analyse détaillée des propriétés physico-chimiques des nanoparticules (NP) anthropogéniques est nécessaire pour comprendre à un niveau mécanistique leurs interactions/toxicité potentielle avec/envers les composants biotiques des systèmes aquatiques naturels. Une telle analyse est également requise pour réaliser une évaluation complète et une optimisation de la performance des méthodes d'ultrafiltration développées pour circonscrire le relargage des Ps dans les milieux aquatiques. Dans ce contexte, l'objectif de cette thèse de doctorat était de déchiffrer les processus physico-chimiques fondamentaux régissant la capture de nanodendrimères carboxylés (PAMAM-COOH) - utilisés fréquemment dans des applications biomédicales – par des films multicouches du type (poly(diallyldiméthylammonium)chlorure-poly(acide acrylique))<sub>n</sub> ((PDADMAC-PAA)<sub>n</sub>) assemblés par déposition séquentielle des composantes polymériques cationique et anionique. À cette fin, une étude systématique des propriétés électrohydrodynamiques des NPs PAMAM-COOH a d'abord été effectuée en fonction du pH et de la concentration en sel monovalent du milieu. Sur la base de la théorie électrocinétique de particules molles ayant une fonctionnalité zwitterionique, il est démontré que les caractéristiques électriques interfaciales des NPs considérées sont déterminées à la fois par des contributions électrostatiques de surface *et* volumique des nanoparticules, lesquelles dépendent de l'extension intraparticulaire de la double couche électrique. L'existence de ces deux types de contributions conduit à un changement remarquable de signe de la mobilité des NPs en modifiant la concentration du sel monovalent en solution et à une dépendance prononcée du point de zéro mobilité des Ps avec la concentration de l'électrolyte. En outre, une confrontation quantitative entre résultats expérimentaux et théorie souligne comment les modifications structurales des NPs induites par des changements de pH et de salinité affectent les caractéristiques électrocinétiques des dendrimères. Dans une deuxième partie, la structure, la morphologie et les propriétés mécaniques des films PDADMAC-PAA et leur évolution temporelle dans des conditions de vieillissement naturel ou après traitement thermique ont été déterminées par microscopie à force atomique (AFM) et analyses microspectroscopie Raman. Les résultats démontrent que les films multicouches PDADMAC-PAA de type exponentiel présentent des caractéristiques mécaniques et structurelles typiques de films polyelectrolytes multicouches à croissance linéaire. En particulier, leur relaxation lente vers un état d'équilibre est accélérée après traitement thermique à 60 °C et se révèle être intimement liée à l'instabilité de domaines de films riches en PDADMAC, épuisés en eau (faits confirmés par la théorie de la fonctionnelle de la densité) et marqués par la présence de structures caractéristiques en forme de 'donuts'. Dans une dernière partie, des résultats préliminaires sont donnés pour la dépendance de l'élasticité des films multicouches PDADMAC-PAA avec la concentration en solution de nanodendrimères. Les résultats suggèrent que ces films multicouches complexes constituent une option prometteuse pour la capture et l'élimination de nanodendrimères carboxylés présents en milieux aqueux.

**Mots-clés:** films multicouches de polyelectrolytes, nanodendrimères, électrocinétique, nanomécanique, Microscopie à Force Atomique